# Robust microvibration control and worst-case analysis for high pointing stability space missions

Valentin Preda

▶ **To cite this version:**

Valentin Preda. Robust microvibration control and worst-case analysis for high pointing stability space missions. Other. Université de Bordeaux, 2017. English. NNT : 2017BORD0785 . tel-01722860

**HAL Id: tel-01722860**
**https://theses.hal.science/tel-01722860**

Submitted on 5 Mar 2018

**HAL** is a multi-disciplinary open access archive for the deposit and dissemination of scientific research documents, whether they are published or not. The documents may come from teaching and research institutions in France or abroad, or from public or private research centers.

L'archive ouverte pluridisciplinaire **HAL**, est destinée au dépôt et à la diffusion de documents scientifiques de niveau recherche, publiés ou non, émanant des établissements d'enseignement et de recherche français ou étrangers, des laboratoires publics ou privés.

université de BORDEAUX

# THÈSE

présentée pour obtenir le grade de

## Docteur de l'Université de Bordeaux

ÉCOLE DOCTORALE DES SCIENCES PHYSIQUES ET DE L'INGÉNIEUR
SPÉCIALITÉ AUTOMATIQUE, PRODUCTIQUE, SIGNAL ET IMAGE

par

**Valentin PREDA**

---

# Robust Microvibration Control and Worst-case Analysis for High Pointing Stability Space Missions

---

Présentée et soutenue publiquement le 13 Decembre 2017

**Devant la commission d'examen formée de :**

| | | | | |
|---|---|---|---|---|
| M. | HENRY, David | Professeur | Université de Bordeaux | Directeur |
| M. | CIESLAK, Jérôme | Maître de Conférences | Université de Bordeaux | Co-encadrant |
| M. | ALAZARD, Daniel | Professeur | ISAE-SUPAERO | Rapporteur |
| M. | SENAME, Olivier | Professeur | Grenoble-INP | Rapporteur |
| M. | BENNANI, Samir | Docteur Ingénieur | Agence Spatiale Européenne | Examinateur |
| M. | FALCOZ, Alexandre | Docteur Ingénieur | Airbus Defense & Space | Examinateur |
| M. | ZOLGHADRI, Ali | Professeur | Université de Bordeaux | Président |

**Titre:** Contrôle robuste des microvibration et analyse pire cas pour les missions spatiales nécessitant une très haute stabilité en pointage

**Résumé:** Le contexte général des travaux de recherche de cette thèse concerne les problématiques liées à l'optimisation globale liée à la conception des futurs satellites d'observation terrestre et de missions scientifiques, nécessitant une très haute stabilité en pointage. Plus particulièrement, les travaux concernent le contrôle actif des modes microvibratoires. Dans une mission satellitaire d'observation terrestre, la qualité des images dépend bien évidemment des instruments de mesure optique mais également des performances de la stabilité de la ligne de visée du satellite qui peut s'avérer dégradée pour cause de microvibrations. Le contrôle des microvibrations représentent ainsi un défit technologique, conduisant l'ESA et les acteurs industriels du monde spatial, a considéré cette problématique comme hautement prioritaire pour le développement des satellites d'observation terrestre nouvelle génération. l'environnement. Malheureusement, la demande de plus en plus importante de grande stabilité de la ligne de visée pour les futures missions d'observation terrestres rend l'approche passive insuffisante. L'ESA et Airbus Defence and Space, ont donc collaborer conjointement avec l'équipe ARIA au travers de cette thèse, dans des travaux de recherche dans le domaine du contrôle actif pour palier ces problèmes. L'objectif visé est de coupler les approches passives et actives afin de rejeter à la fois les microvibrations en hautes fréquences (approche passive existant) et en basses fréquences (approche active objet des travaux de la thèse)

**Mots clés:** contrôle robuste, haute stabilité en pointage, microvibrations, analyse pire cas

---

**Title:** Robust Microvibration Control and Worst-case Analysis for High Pointing Stability Space Missions

**Abstract:** Next generation satellite missions will have to meet extremely challenging pointing stability requirements. Even low levels of vibration can introduce enough jitter in the optical elements to cause a significant reduction in image quality. The success of these projects is therefore constrained by the ability of on-board vibration isolation and optical control techniques to keep stable the structural elements of the spacecraft in the presence of external and internal disturbances. In this context, the research work presented in this thesis combines the expertise of the European Space Agency (ESA), the industry (Airbus Defence and Space) and the IMS laboratory (laboratoire de l'Intégration du Matériau au Système) with the aim of developing new generation of robust microvibration isolation systems for future space observation missions. More precisely, the thesis presents the development of an Integrated Modeling, Control and Analysis framework in which to conduct advanced studies related to reaction wheel microvibration mitigation.The thesis builds upon the previous research conducted by Airbus Defence and Space and ESA on the use of mixed active/passive microvibration mitigation techniques and provides a complete methodology for the uncertainty modeling, robust control system design and worst-case analysis of such systems for a typical satellite observation mission. It is shown how disturbances produced by on-board mechanical spinning devices can be significantly attenuated in order to improve the pointing stability of the spacecraft even in the presence of model uncertainty and other nonlinear phenomenon.

**Keywords:** robust control, high pointing stability, microvibrations, worst case analysis

---

## Unité de recherche

Laboratoire IMS, CNRS UMR5218, Adresse: 351 cours de la liberation 33405 Talence cedex

# Abstract

*Robust Microvibration Control and Worst-case Analysis*
*for High Pointing Stability Space Missions*

Next generation satellite missions will have to meet extremely challenging pointing stability requirements. Even low levels of vibration can introduce enough jitter in the optical elements to cause a significant reduction in image quality. The success of these projects is therefore constrained by the ability of on-board vibration isolation and optical control techniques to keep stable the structural elements of the spacecraft in the presence of external and internal disturbances.

In this context, the research work presented in this thesis combines the expertise of the European Space Agency (ESA), the industry (Airbus Defence and Space) and the IMS laboratory (laboratoire de l'Intégration du Matériau au Système) with the aim of developing new generation of robust microvibration isolation systems for future space observation missions. More precisely, the thesis presents the development of an Integrated Modeling, Control and Analysis framework in which to conduct advanced studies related to reaction wheel microvibration mitigation.

The thesis builds upon the previous research conducted by Airbus Defence and Space and ESA on the use of mixed active/passive microvibration mitigation techniques and provides a complete methodology for the uncertainty modeling, robust control system design and worst-case analysis of such systems for a typical satellite observation mission. It is shown how disturbances produced by mechanical spinning devices such as reaction wheels can be significantly attenuated in order to improve the pointing stability of the spacecraft even in the presence of model uncertainty and other nonlinear phenomenon.

Finally, the work introduces a new disturbance model for the multi harmonic perturbation spectrum produced by spinning reaction wheels that is suitable for both controller synthesis and worst-case analysis using modern robust control tools. This model is exploited to provide new ways of simulating the image distortions induced by such disturbances.

# Acknowledgements

First and foremost I want to thank my technical supervisor Samir Benanni from the European Space Agency. It has been an honor and a great privilege to be one of his students. He has taught me both consciously and unconsciously how to be a better researcher, a better engineer and a better person. His passion, enthusiasm, deep knowledge and strength of character was both motivational and contagious, providing a pillar of stability even during the tough times of the Ph.D. I am totally convinced that without his *Guidance, Navigation and Control* this endeavor would have been impossible and I appreciate all his contributions of time and ideas to make my experience during these last years both productive and stimulating.

I also want to extend my gratitude to my academic supervisors from the University of Bordeaux, namely David Henry and Jérôme Cieslak, for welcoming me into their team and supplying me with all the necessary resources to accomplish this project. I am thankful for their reviews, suggestions and almost endless patience with me throughout these years. Both of them have contributed immensely to my professional and my personal life and I will be forever grateful to them. I have very fond memories of my time visiting Jérôme's beautiful family in the splendid region of Dordogne and enjoying all the delicious wines and meals.

Regarding the initial data that was of great importance to this study, I want to thank Alexandre Falcoz from Airbus Defence and Space. His previous studies were critical to this project and provided a very clear direction for the thesis from the beginning. I also want to thank him for his good advice, his collaboration and thoughtful questions.

The research period at the European Space Research and Technology Centre (ESTEC) in the Netherlands was an extraordinary and life-changing experience. Here I met people with a remarkable talent for research and built long-lasting friendships. I want to thank Alain Benoit, Bénédicte Girouart, Guillermo Ortega and the rest of the AOCS and GNC Division for making me feel welcome within the group and providing me support along the journey. Special thanks go to Fabrice Boquet and René Seiler for the very useful discussions related to microvibrations and pointing stability research.

For this dissertation, I would like to thank my Ph.D. review committee members: Daniel Alazard and Olivier Sename for their time, interest, helpful comments and insightful questions. Their reviews significantly improved the quality of this manuscript. I am also grateful to Ali Zolghadri for his time presiding over the thesis defense proceedings.

My time in Bordeaux and at ESTEC was made enjoyable and unforgettable in large part due to the many friends that became a part of my life. It has been a deeply rewarding experience to meet and know so many great people from all corners of the globe. I am grateful for the time spent with my backpacking buddies in our countless wine *tasting* adventures, our awesome picnics and many memorable trips throughout France and Europe.

Lastly, I would like to thank my family for all their love and encouragement. For my parents who raised me to feel a genuine satisfaction from learning, an appreciation for quality work and supported me in all my pursuits. Thank you.

Valentin Preda

*This PhD was supported by Région Aquitaine and the European Space Agency (ESA) in the framework of ESA's Networking / Partnering Initiative program n. 4000109882/13/NL/GLC/al.*

# Table of contents

# List of figures

# List of tables

# List of acronyms

**ACS** attitude control system. 54

**ASD** amplitude spectral density. 61

**CoM** center of mass. 16–18, 24, 27, 29, 55, 87

**DoF** degree of freedom. 5, 6, 9, 18

**ESA** European Space Agency. 49, 54

**IQC** Integral Quadratic Constraints. 53, 54, 78, 79, 84, 101, 104, 107

**LFT** Linear Fractional Transformation. 16, 28, 30–32, 34–37, 41, 45, 48, 49, 51, 53, 103

**LMI** Linear Matrix Inequality. 108

**LPV** Linear Parameter Varying. 28, 54, 60, 70–74

**LTI** Linear Time Invariant. 9, 28, 78, 88, 103

**MTF** Modulation Transfer Function. 2

**OTF** Optical Transfer Function. 93–96

**PMA** proof mass actuator. 32, 33, 42, 104

**PSF** Point Spread Function. 93

**RMS** root mean square. 51, 67, 82, 86, 89

**RPE** relative pointing error. 61, 70, 75, 76, 81, 82

**RWA** reaction wheel assembly. 3, 5

# Author's list of publications

## Journals

[1] Valentin Preda, Jérôme Cieslak, David Henry, Samir Bennani, and Alexandre Falcoz. A H-infinity/mu solution for microvibration mitigation in satellites: A case study. *Journal of Sound and Vibration*, 399:21–44, jul 2017.

[2] Valentin Preda, Jérôme Cieslak, David Henry, Samir Bennani, and Alexandre Falcoz. Robust Microvibration Control and Worst-case Analysis for High Pointing Stability Space Missions. Submitted to: *International Journal of Robust and Nonlinear Control*, 2017.

## Conferences

[1] Valentin Preda, Jérôme Cieslak, David Henry, Samir Bennani, and Alexandre Falcoz. Robust Control Design in a Non-Smooth H-infinity / mu setting for Spacecraft Microvibration Attenuation. In *10th International ESA Conference on Guidance, Navigation & Control Systems*, Salzburg, Austria, may 2017. European Space Agency.

[2] Valentin Preda, Jérôme Cieslak, David Henry, Samir Bennani, and Alexandre Falcoz. LPV Control for Active Vibration Mitigation in High Stability Space Missions: A Comparative Study. In *8th IFAC Symposium on Robust Control Design*, 2015.

[3] Valentin Preda, Jérôme Cieslak, David Henry, Samir Bennani, and Alexandre Falcoz. Microvibration Attenuation based on H-infinity/LPV Theory for High Stability Space Missions. In *12th European Workshop on Advanced Control and Diagnosis (ACD 2015)*, Pilsen, Czech Republic, 2015.

[4] Valentin Preda, Jerome Cieslak, David Henry, Samir Bennani, and Alexandre Falcoz. LPV Control for Multi-harmonic Microvibration Attenuation: Application to High Stability Space Missions. *IFAC-PapersOnLine*, 48(26):127–132, 2015.

## Private presentations

[1] Robust And Adaptive Active Micro Vibration Isolation, *NPI presentations on the occasion of the 23rd Selection Board*, ESTEC, Noordwijk, 16 jun 2017

[2] Contrôle micro-vibratoire, *Séminaire applications de la commande structurée*, ONERA, Toulouse, 27 nov 2014

# Résumé en français

## R.1 Contexte

Le travail de recherche présenté dans ce mémoire, résulte d'une collaboration maintenant pérenne, entre l'équipe ARIA (Approche Robuste et Intégrée de l'Automatique) du laboratoire IMS (Intégration du Matériau au Système) de l'université de Bordeaux, Airbus Defence and Space et l'agence spatiale européenne (ESA). Les travaux menés au sein de cette collaboration visent à développer de nouveaux algorithmes de guidage, navigation, contrôle, pour améliorer les performances et l'autonomie fonctionnelle et opérationnelles des missions spatiales.

Le contexte général des travaux de recherche concerne les problématiques liées à l'optimisation globale liée à la conception des futurs satellites d'observation terrestre et de missions scientifiques, nécessitant une très haute stabilité en pointage (capacité du satellite à garder son point de visée). Plus particulièrement, les travaux concernent le contrôle actif des modes micro-vibratoires.

Dans une mission satellitaire d'observation terrestre, la qualité des images dépend bien évidemment des instruments de mesure optique (diamètre du miroir, aberrations optiques et qualité du polissage) mais également des performances de la stabilité de la ligne de visée du satellite qui peut s'avérer dégradée pour cause de micro-vibrations. La présence de ces micro-vibrations est liée aux divers éléments tournant du satellite tels que les mécanismes de rotation des panneaux solaires ou de contrôle d'orientation du satellite (on parle de contrôle d'attitude réalisé au moyen de roues inertielles).
A titre d'exemple, la figure suivante illustre les variations de la ligne de visée liés aux micro-vibrations (figure de gauche) et son impact sur la qualité de l'image prise par le satellite (figure de droite). L'image de droite résulte d'un traitement par des stations sols.

Le retour d'expérience de l'ESA et d'Airbus Defence and Space, sur les missions satellitaires les plus caractéristiques du problème de distorsion des images liée à la présence de micro-vibrations, souligne les enjeux de cette problématique, voir tableau ??.

Le contrôle des micro-vibrations représentent ainsi un défit technologique, conduisant l'ESA et les acteurs industriels du monde spatial, a considéré cette problématique comme hautement prioritaire pour le développement des satellites d'observation terrestre nouvelle génération.

Il existe à l'heure actuelle deux principes fondamentaux de contrôle des micro-vibrations :

- le contrôle dit passif: la stratégie consiste à introduire des dispositions constructives et des matériaux particuliers permettant de minimiser la transmission des vibrations à l'environnement.
- le contrôle dit actif : le concept de contrôle actif des vibrations est tout autre : l'idée est cette fois-ci, de bloquer la micro-vibration en exerçant une vibration antagoniste créée artificiellement avec des propriétés en opposition, à tout instant, relativement à la vibration indésirable, pour rendre nulle leur somme.

L'industrie spatiale aborde cette problématique en plaçant des isolateurs en élastomère au voisi-

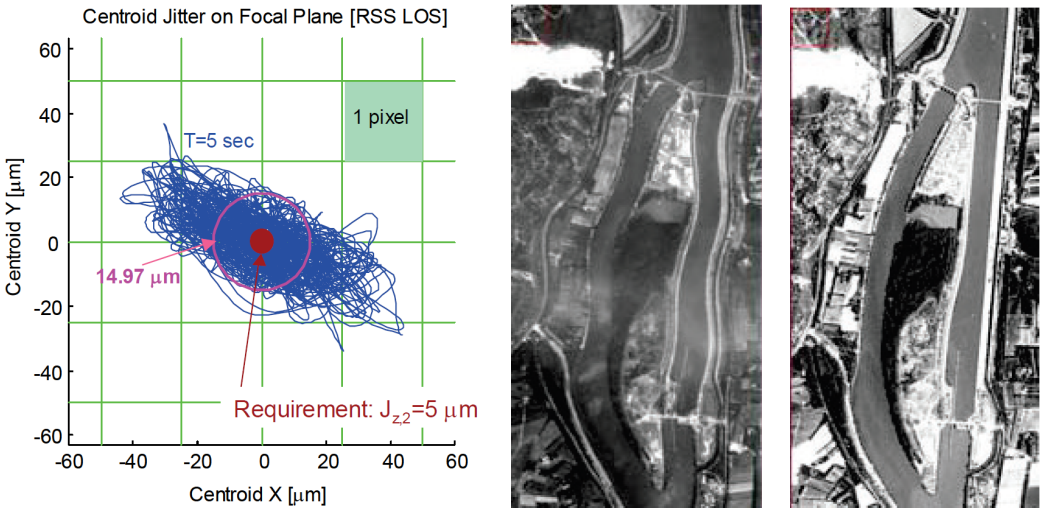


(a) (b) (c)

Figure 1: (a) Erreurs de pointage (ligne bleue) et les objectifs de performance (point rouge) (b) Effets sur la qualité de l'image (c) Résultat comparatif avec mesures correctives [CRS13]

| **Satellite** | **Mission** | **sources de micro-vibrations** |
|---|---|---|
| MTG | Observation terrestre | - roues inertielles<br>- cryocooler<br>- moteur SADM des panneaux solaires |
| Geo-oculus | Observation terrestre | - roues inertielles<br>- cryocooler |
| IXO | Mission scientifique | - roues inertielles<br>- cryocooler |

Table 1: Missions satellitaires et sources principales de micro-vibrations

nage de chaque source de micro-vibrations. Cette solution, qui a fait ses preuves puisqu'elle équipe actuellement nombre de satellites en orbite, permet de rejeter nombre de micro-vibrations. Malheureusement, la demande de plus en plus importante de grande stabilité de la ligne de visée pour les futures missions d'observation terrestres telles que les missions GAIA rend l'approche passive insuffisante.

L'ESA et Airbus Defence and Space, ont donc collaborer conjointement avec l'équipe ARIA au travers de cette thèse, dans des travaux de recherche dans le domaine du contrôle actif pour palier ces problèmes. L'objectif visé est de coupler les approches passives et actives afin de rejeter à la fois les micro-vibrations en hautes fréquences (approche passive existant) et en basses fréquences (approche active objet des travaux de la thèse).

Pour mener à bien cet objectif, un procédé expérimental représentatif de la problématique satellitaire et issu des études passées menées conjointement par l'ESA et Airbus Defence and Space sur la problématique micro-vibratoire, a été mis à notre disposition. Ce procédé, dont une illustration est donnée sur la fig. 2, constitue le support type qui a conduit aux développements méthodologiques présentés dans ce mémoire.

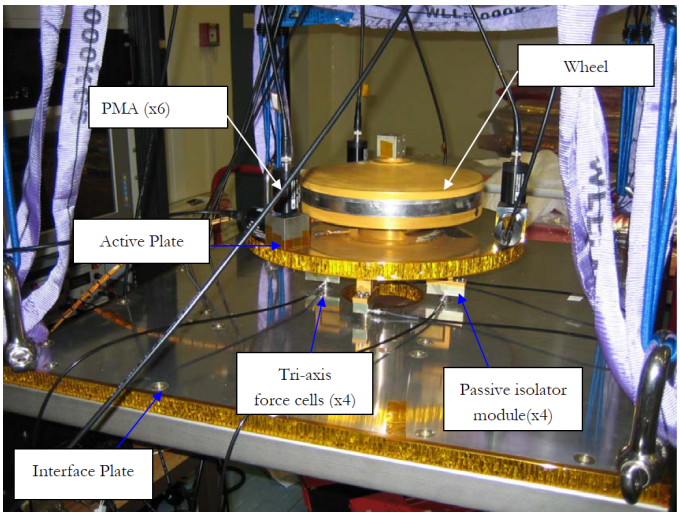


Figure 2: Illustration du procédé expérimental représentatif de la problématique satellitaire en micro-vibrations

## R.2 Contributions de la thèse

Les contributions méthodologiques des travaux de recherche présentés dans cette thèse s'articulent autour de trois axes majeurs: la modélisation, la synthèse de loi de commande robuste multivariable et l'analyse pire-cas.

### R.2.1 Contribution en modélisation

Dans nos travaux de thèse, nous abordons le problème de modélisation des phénomènes vibratoires liés à la rotation des roues inertielles, ces phénomènes étant responsables des phénomènes de micro-vibrations de la ligne de visée d'un satellite d'observation. Nous proposons un cadre méthodologique permettant d'établir un modèle dynamique d'un satellite d'observation équipé d'un système d'isolation micro-vibratoire mixte passif/actif, dont le contrôle d'attitude est réalisé à l'aide de roues inertielles. La figure suivante donne une illustration sous forme de schéma blocs du modèle proposé dans ce mémoire.

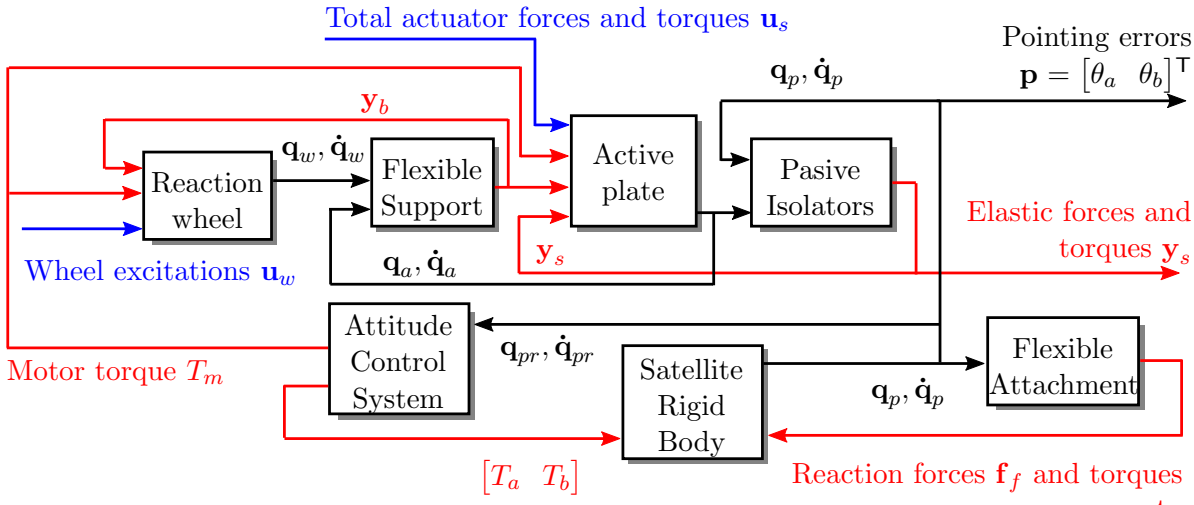


Figure 3: Schéma bloc d'un satellite d'observation équipé d'un système d'isolation micro-vibratoire mixte passif/actif et contrôler en attitude par roues inertielles

Un modèle de roue inertielle qui tient compte des couplages en phase des phénomènes multi - harmoniques, est établi dans un premier temps. La démarche est basée sur une approche géométrique.

Dans un deuxième temps, le formalisme de Lagrange est utilisé pour déduire un modèle dynamique de l'ensemble "roue inertielle - système d'isolation micro-vibratoire - satellite". L'approche proposée tient compte des modes flexibles du satellite (liés notamment aux panneaux solaires), des modes de vibrations liés aux roues inertielles (notamment le phénomène de balourd), du système passif d'isolation des micro-vibrations constitué des élastomères placés au voisinage du système de vision et enfin des modes du système actif d'isolation des micro-vibrations. Le modèle obtenu est un modèle sous forme de représentation d'état non linéaire. Une linéarisation du modèle ainsi obtenu autour de la position d'équilibre caractérisée par "vibration nulle", est alors réalisée. Cette approche se justifie par le fait que nous nous intéressons aux micro-vibrations. On montre alors que le modèle dynamique peut être formulé comme un modèle à paramètres variants dans le temps (modèles dit LPV pour l'acronyme anglo-saxon Linear Parameter Varying), paramétré par la vitesse $\Omega(t)$ des roues inertielles. Le modèle LPV étant établi dans un cadre formel, il permet de mettre en évidence les paramètres physiques du système qui sont incertains et/ou mal connus (incertitudes paramétriques). Le formalisme LFT (de l'acronyme anglo-saxon Linear Fractionnal Transformation) est alors utilisé pour séparer les incertitudes paramétriques (ces dernières étant bornées), de la partie connue du modèle. Un modèle paramétrique incertain des capteurs (12 capteurs de force) et des actionneurs (6 actionneurs PMAs, acronyme anglo-saxon de Proof Mass Actuator) est alors adjoint au modèle dynamique précédent, conduisant à un modèle dynamique du système complet à 6 entrées et 12 sorties (notées $\mathbf{y}$ et $\mathbf{u}$ sur la fig. 4). Le phénomène de saturation des actionneurs et la présence éventuelle de retards (incertains) dans ces derniers, sont également considérés. Le modèle complet est alors reformulé dans un contexte LFT. La fig. 4 donne la structure du modèle LFT obtenu.

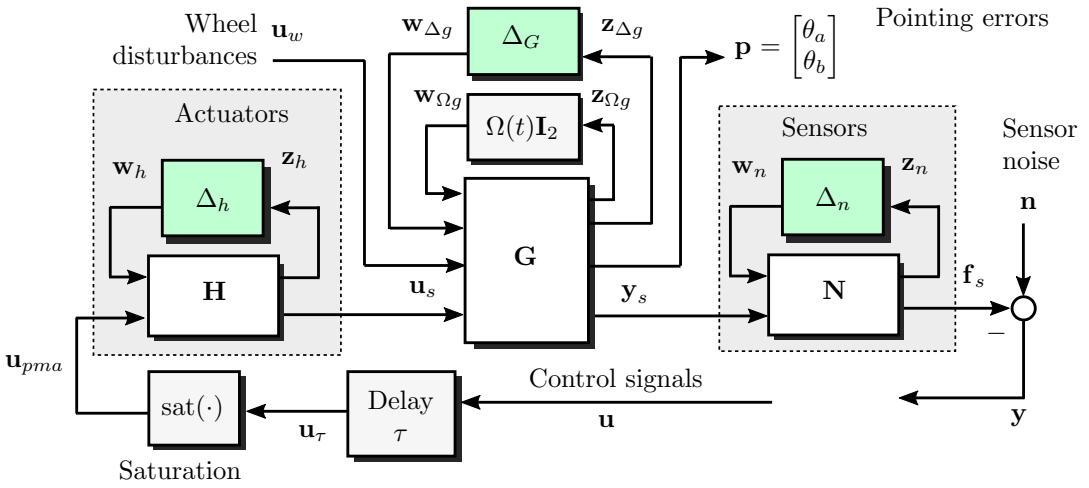


Figure 4: Modèle LFT du système complet

Ce modèle LFT obtenu étant complexe et d'ordre élevé, nous proposons une procédure de réduction de ce dernier basée sur l'analyse des modes vibratoires et sur la reformulation des incertitudes structurées sous forme additive non structurée. Le résultat obtenu conduit à un modèle de complexité moindre englobant toutes les dynamiques des phénomènes de micro-vibrations et des modes souples du système de contrôle actif. Ce dernier modèle sera alors retenu pour synthétiser le système de contrôle actif des micro-vibrations, tandis que le modèle LFT complexe original qui tient compte de tous les modes du système (y compris ceux du satellite), sera utilisé pour valider les performances du système de contrôle actif. A titre d'exemple, la fig. 5 illustre, pour les transferts $\mathbf{u}_s(1) \rightarrow \mathbf{y}_s(1)$ et $\mathbf{u}_s(4) \rightarrow \mathbf{y}_s(1)$, le tracé des gains principaux des modèles structuraux complets et réduits pour différentes valeurs d'incertitudes ainsi que les limites d'incertitude additive correspondantes.

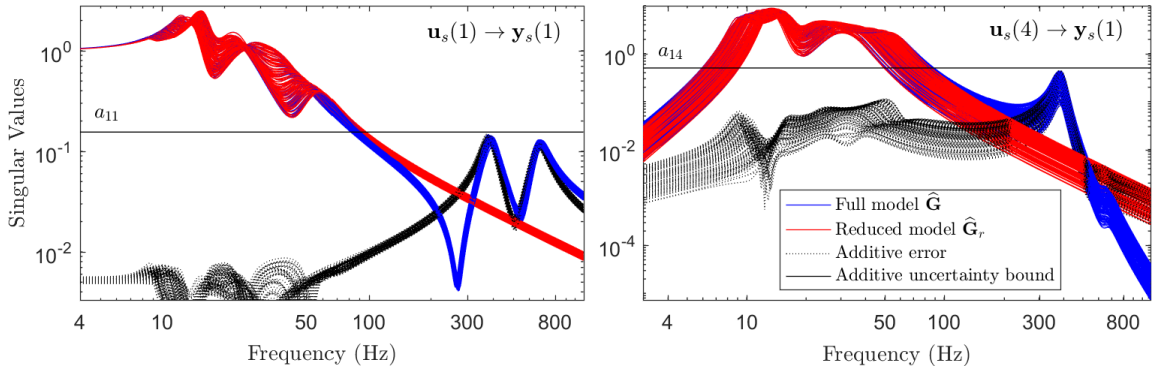


Figure 5: Gains principaux des modèles structuraux complets et réduits pour différentes valeurs d'incertitudes ainsi que les limites d'incertitude additive correspondantes

### R.2.2 Contribution en commande robuste multivariable

Dans nos travaux de thèse, nous abordons la problématique de synthèse d'un système de contrôle actif des micro-vibrations, reformulé comme un problème de commande robuste multivariable $\mathcal{H}_\infty$. Dans ce contexte, nous montrons comment l'approche $\mathcal{H}_\infty$ non lisse permet d'apporter une solution au problème.

Plus précisément, les contributions des travaux de recherche sont de deux natures, *i*) méthodologique via le choix systématique des fonctions de pondération du problème $\mathcal{H}_\infty$, et, *ii*) algorithmique via le développement d'une procédure de synthèse $\mathcal{H}_\infty$ non lisse permettant de tenir compte de la nature LPV du problème, sous l'hypothèse réaliste que l'accélération des roues inertielles restent lentes devant la bande passante de la boucle de contrôle des micro-vibrations. Cette hypothèse est d'ailleurs vérifiée *a posteriori* à l'aide de la théorie des IQC (acronyme anglo-saxon de Integral Quadratic Constraint).

#### Choix systématique des fonctions de pondération du problème $\mathcal{H}_\infty$

Le problème $\mathcal{H}_\infty$ pondéré que nous proposons pour synthétiser le système de contrôle actif des micro-vibrations, est illustré sur la fig. 6.

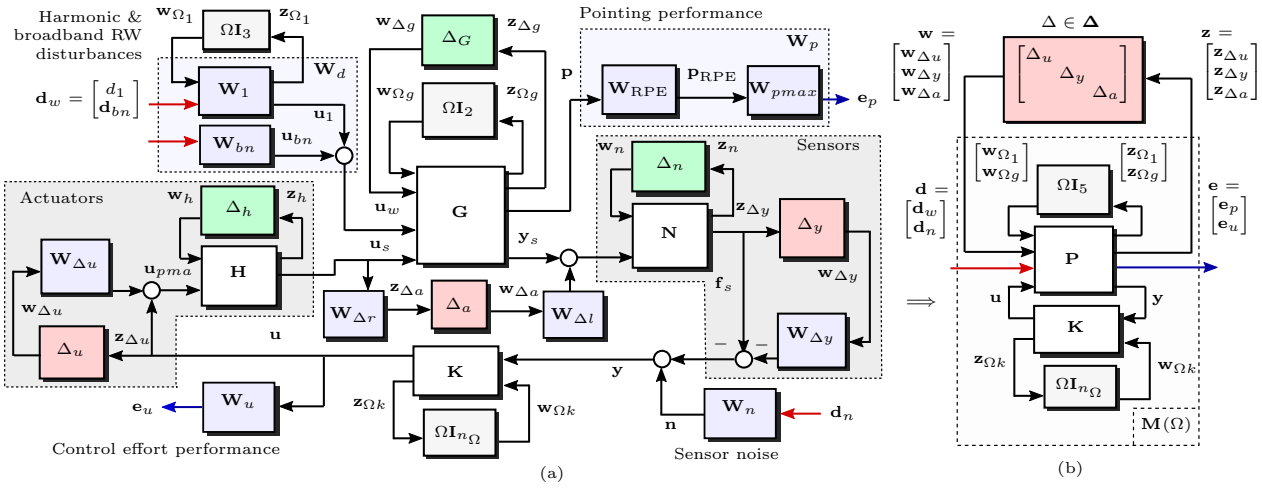


Figure 6: Problème de synthèse $\mathcal{H}_\infty$

Sur cette figure, les blocs (complexes) $\Delta_a, \Delta_u$ et $\Delta_y$ correspondent au modèle LFT d'ordre réduit,

introduits pour englober toutes les incertitudes représentées par les blocs (réels) $\Delta_G, \Delta_n$ et $\Delta_h$ correspondant au modèle LFT complet illustré sur la fig. 4. Le bloc $\Delta = \text{diag}\,(\Delta_u,\ \Delta_y,\ \Delta_a)$ couvre également les phénomènes de saturation et de retard, voir fig. 4.
Comme classiquement en théorie $\mathcal{H}_\infty$, la problématique qui se pose est le choix des pondérations permettant de fixer les objectifs de robustesse et de performance à atteindre. Comme l'illustre la fig. 6, les pondérations à choisir sont au nombre de 10, i.e. les pondérations $\mathbf{W}_{\Delta_y}, \mathbf{W}_{\Delta_u}, \mathbf{W}_{\Delta l}, \mathbf{W}_{\Delta_r}$ relatives aux erreurs de modèle, les pondérations $\mathbf{W}_n, \mathbf{W}_{bn}, \mathbf{W}_1$ relatives aux perturbations exogènes, les pondérations $\mathbf{W}_{RPE}, \mathbf{W}_{pmax}$ relatives aux performances de pointage du satellite d'observation et la pondération $\mathbf{W}_u$ relative aux objectifs sur le signal de contrôle.

• Choix des pondérations $\mathbf{W}_{\Delta_y}, \mathbf{W}_{\Delta_u}, \mathbf{W}_{\Delta l}, \mathbf{W}_{\Delta_r}$: Dans nos travaux, nous montrons que la variation de gain sur les senseurs engendrées par les incertitudes peuvent être couvertes en choisissant $\mathbf{W}_{\Delta_y} = 0.1\mathbf{I}$. Similairement, le choix suivant de $\mathbf{W}_{\Delta_u}$ permet de couvrir les dynamiques négligées sur les actionneurs ainsi que de prendre en compte les phénomènes de saturation et de retard:

$$\mathbf{W}_{\Delta u} = \Gamma(s)\ \mathbf{I}_6 \quad \text{with} \quad \begin{array}{l} \Gamma(s) = \beta + \alpha \cdot w_\tau(s) \\ \beta = 30\% \end{array} \quad \text{and} \quad \begin{array}{l} \alpha = 1 - \beta/3.465 \\ w_\tau(s) = s/\left(\tau_{max}^{-1} + s/3.465\right) \\ \tau_{max} = 1\,\text{ms} \end{array} \tag{1}$$

Typiquement le choix $\beta = 30\%$ permet de tenir compte des incertitudes multiplicatives des actionneurs PMA, et la pondération $w_\tau(s)$ permet de tenir compte du retard $\tau \in [0, \tau_{max}]$. Les pondérations $\mathbf{W}_{\Delta l} \in \mathbb{R}^{6\times 36}$ and $\mathbf{W}_{\Delta r} \in \mathbb{R}^{36\times 6}$ permettent de mettre à l'échelle $\Delta_a$ tout en couvrant l'erreur qu'il existe entre le modèle réduit et le modèle originel. On montre dans nos travaux que celles-ci peuvent être judicieusement déterminées telles que

$$\mathbf{W}_{\Delta l}\Delta_a\mathbf{W}_{\Delta r} = \begin{bmatrix} a_{11}\delta_{16} & \dots & a_{16}\delta_{16} \\ \vdots & \ddots & \vdots \\ a_{61}\delta_{66} & \dots & a_{66}\delta_{66} \end{bmatrix} \quad \text{où} \quad \Delta_a \in \left\{ \text{diag}\,(\delta_{ij}) : \begin{array}{c} \delta_{ij} \in \mathbb{C},\ |\delta_{ij}| \le 1 \\ i,j \in \{1,\dots,6\} \end{array} \right\} \subset \mathbb{C}^{36\times 36} \tag{2}$$

où les paramètres $a_{i,j} \in \{1,\dots,6\}$ représentent les erreurs entre le modèle LFT réduit et le modèle LFT originel, termes à termes.

• Choix des pondérations $\mathbf{W}_n, \mathbf{W}_{bn}, \mathbf{W}_1$: Comme assez classiquement, ces pondérations pondérant le problème $\mathcal{H}_\infty$ à gauche et prennent le sens de filtres formeurs. La pondération $\mathbf{W}_n$ est ainsi choisie comme un majorant de l'estimée de la densité spectrale de puissance du bruit de mesure. Dans nos travaux, nous faisons l'hypothèse d'un spectre des bruits de mesure, constant, d'où $\mathbf{W}_n = n_{max}\mathbf{I}_{12}$, $n_{max} = 10^{-3}\text{N}/\sqrt{\text{Hz}}$. De façon similaire, les pondérations $\mathbf{W}_{bn}$ et $\mathbf{W}_1$ sont déterminées de façon à capturer le spectre de l'harmonique de rang 1 des micro-vibrations causées par les roues inertielles et des variations autour du rang 1. Nous montrons ainsi dans nos travaux, qu'un choix judicieux pour $\mathbf{W}_{bn}$ consiste en le choix suivant,

$$\mathbf{W}_{bn} = \text{diag}\left(a_1^f\Omega_{bn}^2\,\mathbf{I}_2,\ a_1^t\Omega_{bn}^2\,\mathbf{I}_2\right), \quad \Omega_{bn} = 1\,\text{Hz},\ a_1^f = 0.785,\ a_1^t = 0.324 \tag{3}$$

où $a_1^f, a_1^t$ sont les coefficients radiaux d'harmonique de rang 1 caractérisant les micro-vibrations causées par la roue inertielle considérée, en force et en couple respectivement. $\mathbf{W}_1$ est déterminé de façon à modéliser les liens entre phase et amplitude des effets des micro-vibrations causées par la rotation des roues inertielles, selon les axes $x$ et $y$. La fig. 7 donne le schéma bloc de $\mathbf{W}_1$. Soulignons ici que nos travaux traitent également du cas des harmoniques de rang différent afin de permettre au lecteur d'étendre nos résultats au cas multi-harmoniques, c'est à dire $\forall i$, voir fig. 7. Les coefficients $a_i^f, a_i^t$ sont les coefficients radiaux d'harmonique de rang "$i$" caractérisant les micro-vibrations, en force et en couple respectivement.

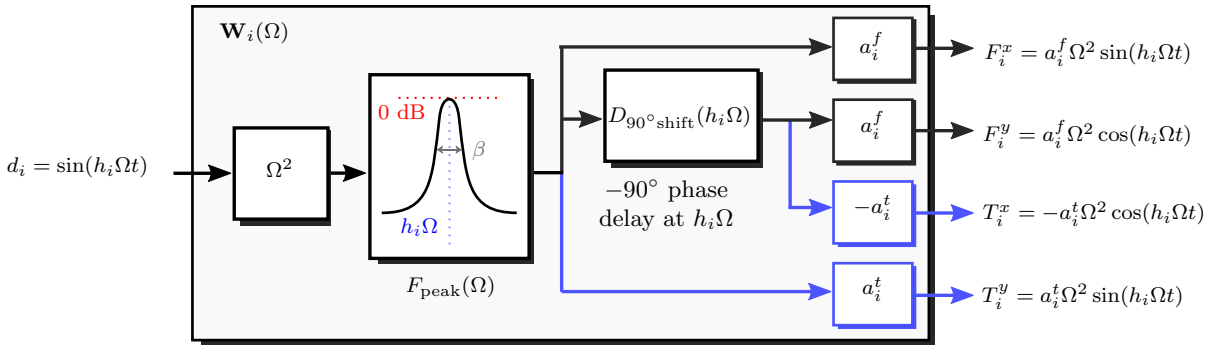


Figure 7: Schéma bloc pour la pondération $\mathbf{W}_i$ qui correspond à l'harmonique de rang "$i$".

• Choix des pondérations $\mathbf{W}_{RPE}, \mathbf{W}_{pmax}, \mathbf{W}_u$: Ces pondérations permettent de définir les objectifs de performance de pointage ($\mathbf{W}_{RPE}, \mathbf{W}_{pmax}$) et d'énergie du signal de commande $\mathbf{u}$. Pour $\mathbf{W}_u$, une pondération constante est retenue, soit $\mathbf{W}_u = u_{max}^{-1}\mathbf{I}_6$, $u_{max} = 10\,\text{V}/\sqrt{\text{Hz}}$. Dans nos travaux de thèse et sur la base des spécifications de pointage pour les satellites d'observation à haute stabilité de la ligne de visée fournies par l'ESA (voir les ouvrages de référence [ECS08] et [ECS11]), nous montrons qu'un choix judicieux des pondérations $\mathbf{W}_{RPE}$ et $\mathbf{W}_{pmax}$ est:

$$\mathbf{W}_p = \mathbf{W}_{pmax}\mathbf{W}_{\text{RPE}} \quad \text{où} \quad \begin{array}{l} \mathbf{W}_{pmax} = \epsilon_{max}^{-1}\mathbf{I}_2 \\ \epsilon_{max} = 0.65\,\text{mas}/\sqrt{\text{Hz}} \end{array} \quad ; \quad \begin{array}{l} \mathbf{W}_{\text{RPE}} = \frac{t_\Delta s\left(t_\Delta s+\sqrt{12}\right)}{(t_\Delta s)^2+6(t_\Delta s)+12}\mathbf{I}_2 \\ t_\Delta = 20\,\text{ms} \end{array} \tag{4}$$

**Synthèse du correcteur $\mathcal{H}_\infty$**

Les pondérations du problème $\mathcal{H}_\infty$ ayant été fixées, il nous reste à déterminer le correcteur LPV $\mathbf{K}(\Omega) = \mathcal{F}_l\left(\mathbf{K}, \Omega\mathbf{I}_{n_\Omega}\right)$ comme illustré sur la fig. 6. Une procédure originale $\mathcal{H}_\infty$ non lisse est pour cela proposée. Elle vise à réduire le caractère conservateur des approches $\mathcal{H}_\infty$ LPV récentes (approches polytopique ou bien LFT), en résolvant le problème d'optimisation multi-critères suivant:

$$\begin{array}{l} \text{minimise } \gamma \\ \mathbf{K}(\Omega) \in \boldsymbol{\mathcal{K}}, \\ \boldsymbol{\mathcal{D}}_s, \boldsymbol{\mathcal{D}}_1, \ldots, \boldsymbol{\mathcal{D}}_8 \in \mathbb{D} \end{array} \quad \text{tel que} \quad \begin{array}{l} \left\| \text{diag}\left( \begin{bmatrix} \boldsymbol{\mathcal{D}}_i\sqrt{\epsilon} & \\ & \boldsymbol{\mathcal{X}}(i) \end{bmatrix} \mathbf{M}(\Omega) \begin{bmatrix} \sqrt{\epsilon}\boldsymbol{\mathcal{D}}_i^{-1} & \\ & \mathbf{I} \end{bmatrix} \right) \right\|_{\mathcal{L}_{2i}} < \gamma \\ \left\| \boldsymbol{\mathcal{D}}_s \mathbf{M}_{\mathbf{w}\to\mathbf{z}}(\Omega) \boldsymbol{\mathcal{D}}_s^{-1} \right\|_{\mathcal{L}_{2i}} < 1/\nu \\ \forall \Omega \in \boldsymbol{\Omega} \qquad i \in \{1, \ldots, 8\} \end{array} \tag{5}$$

où $\boldsymbol{\mathcal{X}}(i) = \begin{bmatrix} \mathbf{0}_{1\times(i-1)} & 1 & \mathbf{0}_{1\times(8-i)} \end{bmatrix}$ et $\|\mathbf{M}\|_{\mathcal{L}_{2i}}$ représente la norme $\mathcal{L}_2$ induite de $\mathbf{M}$. Les paramètres $\epsilon, \nu$ sont utilisé pour gérer le compromis entre performance et robustesse. L'originalité de cette formulation réside dans le fait que l'on cherche simultanément un correcteur d'ordre fixé *a priori*, une dimension du bloc $\Omega\mathbf{I}_{n_\Omega}$ du correcteur LPV $\mathbf{K}(\Omega) = \mathcal{F}_l\left(\mathbf{K}, \Omega\mathbf{I}_{n_\Omega}\right)$, pas forcément égale à celle du modèle (ce qui revient à dire $n_\Omega \leq 5$) et des matrices de "$\mathcal{D}$-scaling", de telle sorte à garantir les propriétés de stabilité robuste $\forall\Omega \in \boldsymbol{\Omega}$ pour un certain niveau $\nu$ d'incertitudes maximales (i.e. $\|\Delta\|_{\mathcal{L}_{2i}} \leq \nu$) et un niveau de performance $\gamma$ pour pour un certain niveau $\epsilon/\gamma$ d'incertitudes maximales (i.e. $\|\Delta\|_{\mathcal{L}_{2i}} \leq \epsilon/\gamma$).

Enfin, nous montrons dans nos travaux de thèse qu'il est judicieux à des fins d'implantation, de retenir une structure particulière du correcteur $\mathbf{K}(\Omega)$ telle que (voir fig. 8):

$$\mathbf{K}(\Omega) = \mathbf{K}_{out}\widetilde{\mathbf{K}}(\Omega)\mathbf{K}_{in} \quad \text{où} \quad \widetilde{\mathbf{K}}(\Omega) = \mathcal{F}_l\left(\left(\begin{array}{cc|c} \mathbf{A}_0 & \mathbf{B}_0 & \mathbf{A}_\Delta \\ \mathbf{C}_0 & \mathbf{D}_0 & \mathbf{B}_\Delta \\ \hline \mathbf{C}_\Delta & \mathbf{D}_\Delta & \mathbf{0} \end{array}\right), \Omega\mathbf{I}_{n_\Omega}\right) = \left(\begin{array}{c|c} \mathbf{A}_0 + \Omega\mathbf{A}_1 & \mathbf{B}_0 + \Omega\mathbf{B}_1 \\ \hline \mathbf{C}_0 + \Omega\mathbf{C}_1 & \mathbf{D}_0 + \Omega\mathbf{D}_1 \end{array}\right) \tag{6}$$

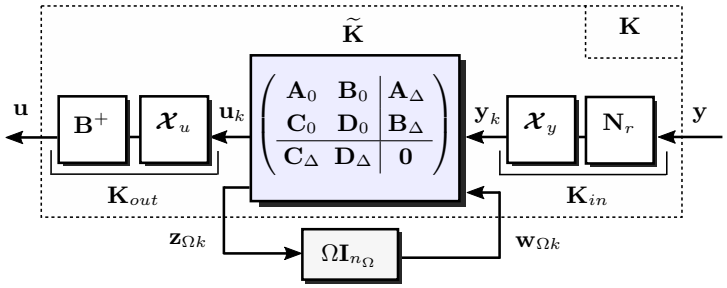


Figure 8: Structure du correcteur $\mathbf{K}(\Omega)$.

où $\mathbf{A}_1 = \mathbf{A}_\Delta \mathbf{C}_\Delta$, $\mathbf{B}_1 = \mathbf{A}_\Delta \mathbf{D}_\Delta$, $\mathbf{C}_1 = \mathbf{B}_\Delta \mathbf{C}_\Delta$ et $\mathbf{D}_1 = \mathbf{B}_\Delta \mathbf{D}_\Delta$ et $\mathcal{F}_l(\mathbf{A}, \mathbf{B})$ est le transformation fractionnaire linéaire (ou LFT) inférieure entre $\mathbf{A}$ et $\mathbf{B}$. La dimension $n_\Omega$ du bloc $\Omega \mathbf{I}_{n_\Omega}$ du correcteur LPV fixant le rang des matrices $\mathbf{A}_1, \mathbf{B}_1, \mathbf{C}_1, \mathbf{D}_1$, cela offre une paramétrisation élégante du dimensionnement de $n_\Omega$. La matrice $\mathbf{K}_{in} = \boldsymbol{\mathcal{X}}_y \mathbf{N}_r \in \mathbb{R}^{2\times 12}$ où $\boldsymbol{\mathcal{X}}_y = \begin{bmatrix} \mathbf{0}_{2\times 3} & \mathbf{I}_2 & \mathbf{0}_{2\times 1} \end{bmatrix}$ relève simplement d'une fusion des mesures par combinaison linéaire, et de façon très similaire, la matrice $\mathbf{K}_{out} = \mathbf{B}^+ \boldsymbol{\mathcal{X}}_u \in \mathbb{R}^{6\times 4}$ où $\boldsymbol{\mathcal{X}}_u = \text{diag}\left( \begin{bmatrix} \mathbf{I}_2 \\ \mathbf{0}_{1\times 2} \end{bmatrix}, \begin{bmatrix} \mathbf{I}_2 \\ \mathbf{0}_{1\times 2} \end{bmatrix} \right)$ représente une allocation du vecteur de commande, par combinaison linéaire.
On montre alors comment les outils $\mathcal{H}_\infty$ non lisse permettent de déterminer tous les paramètres du correcteur. Une procédure originale de synthèse est pour cela proposée. Cette dernière vise notamment à gérer de façon optimale (au sens de Paretto), le compromis stabilité robuste (à travers le facteur $\nu$) / performances robustes (à travers le facteur $\epsilon$). La fig. 9 illustre parfaitement ce compromis. Deux correcteurs sont particulièrement étudiés dans nos travaux: le correcteur $\mathbf{K}_{robustness}$ permettant d'assurer les meilleurs marges de stabilité robuste et le correcteur $\mathbf{K}_{performance}$ permettant d'assurer les meilleurs performances robustes.

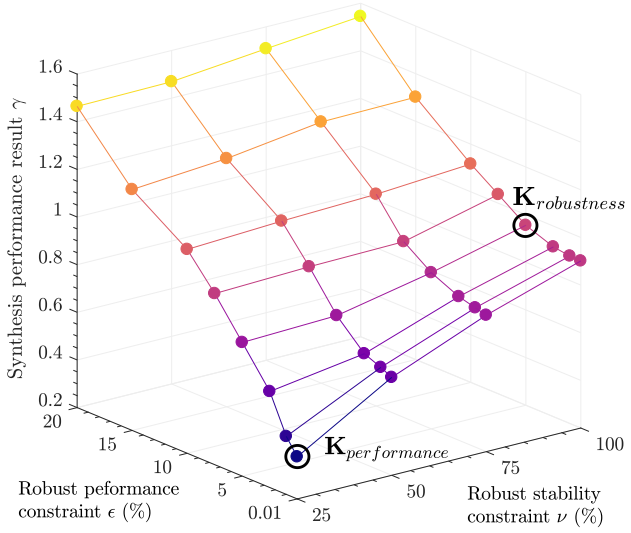


Figure 9: Famille des correcteurs synthétisés.

### Analyse des performances du système de contrôle de micro-vibrations

Des analyses de performances sont alors menées à travers une série de critères mettant en jeu la théorie de la $\mu$-analyse ainsi que celle des IQCs (acronyme anglo-saxon pour Integral Quadratic Constraints). Comme explicité précédemment, ces analyses sont menées sur le modèle complet originel.

Dans un premier, nous menons une analyse des performances nominales sur le correcteur $\mathbf{K}_{robustness}$. La fig. 10 illustre les tracés des gains principaux des transferts de $\mathbf{d}$ vers les deux

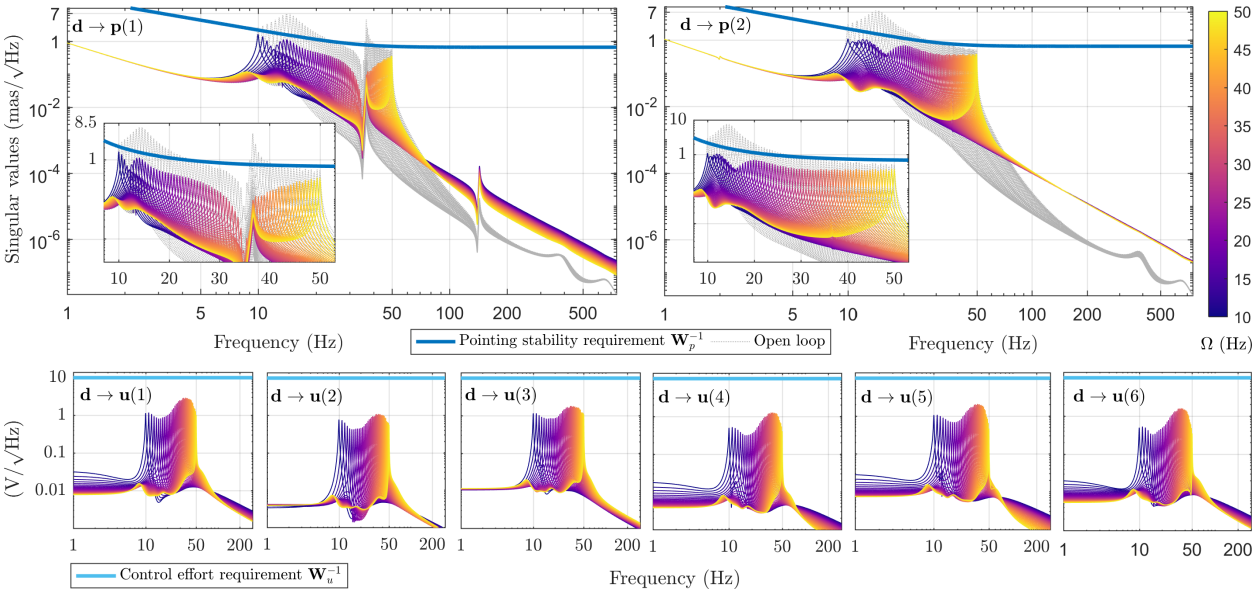


Figure 10: Gains principaux des transferts de $\mathbf{d}$ vers les deux erreurs de pointage $\mathbf{p}$ (haut) et les six commandes $[u]$ (bas). $\mathbf{K}_{robustness}$

erreurs de pointage $\mathbf{p}$ (haut) et les six commandes $[u]$ (bas) pour différentes valeurs de vitesse de rotation $\Omega$, versus les spécifications de synthèse. Afin d'apprécier le gain en performance du système de contrôle des micro-vibrations proposé, les même tracés sont superposés lorsque le système ne possède pas de système de contrôle microvibratoire (tracés en gris clair). On peut clairement apprécier sur ces tracés, le gain en performance apporté par la solution que nous avons développée. On notera également que les spécifications sur les signaux de contrôle sont satisfaites.

Dans un deuxième temps nous menons une analyse de stabilité robuste à l'aide de la procédure de $\mu$-analyse. Une analyse particulière est notamment réalisée vis-à-vis des blocs $\Delta_u, \Delta_a, \Delta_y$ pris individuellement, ainsi que pour le bloc $\Delta$ dans son intégralité, voir fig. 6 pour la définition de ces derniers blocs. L'analyse est réalisée pour un échantillonnage de la vitesse de rotation $\Omega$ assez conséquent de manière à pouvoir apprécier les résultats obtenus. La fig. 11 donne les résultats obtenus. Clairement les résultats illustrent parfaitement les marges de robustesse en stabilité de la solution que nous avons développée dans nos travaux de thèse.

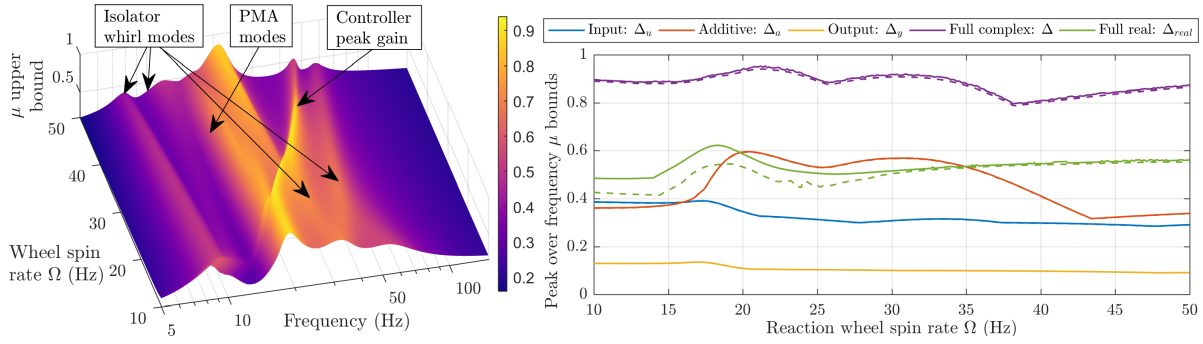


Figure 11: Marges de stabilité robuste pour $\mathbf{K}_{robustness}$

Dans un troisième temps, nous menons une analyse de compromis entre stabilité robuste et performance, dans un contexte pire-cas. L'objectif est d'illustrer l'impacte des incertitudes croissantes sur la dégradation des performances, dans un contexte pire-cas. Cette analyse est menée à l'aide de la procédure de $\mu$-analyse. La fig. 12 illustre les résultats obtenus. On y présente l'impacte sur les performances de pointage selon les deux axes, ainsi que sur les signaux de commande.

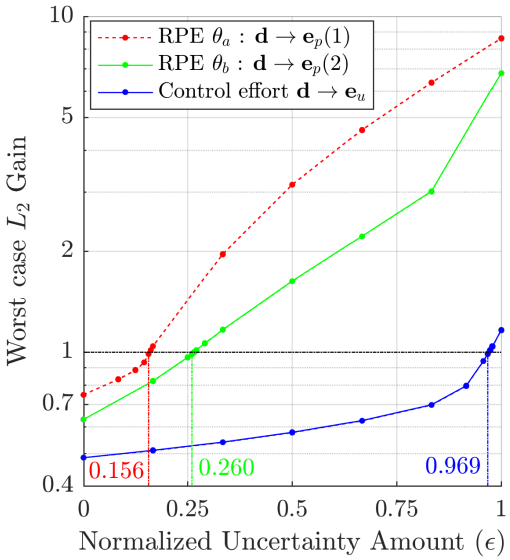


Figure 12: Illustration de l'impacte des incertitudes sur les performances (RPE = Relative Pointing Error)

Dans un quatrième temps, nous menons des analyses de performances en tenant compte de la présence de retard dans la chaîne des actionneurs PMA, des effets de saturation de ces derniers et de la nature variante dans le temps de la vitesse de rotation $\Omega(t)$. On montre alors dans nos travaux de thèse comment ce problème peut être reformulé comme un problème IQC. Etant donné la complexité du problème, ces analyses sont menées séparément, i.e. les performances $\mathcal{H}_\infty$ sont étudiées dans un premier temps, en fonction de l'accélération maximale $\dot{\Omega}_{max}$ des roues, puis en fonction du niveau de saturation $\sigma_{max}$ des actionneurs et enfin en fonction du retard maximal $\tau_{max}$. Les résultats obtenus sont donnés sur la fig. 13, de gauche à droite. Ces résultats montrent clairement que la solution de contrôle des micro-vibrations que nous avons développées, est robuste aux accélérations des roues inertielles pouvant atteindre 1 Hz/s, à la pleine échelle de saturation des actionneurs. Par contre, elle n'est pas robuste à des retards trop importants présents dans les PMAs, ce qui n'est pas surprenant.

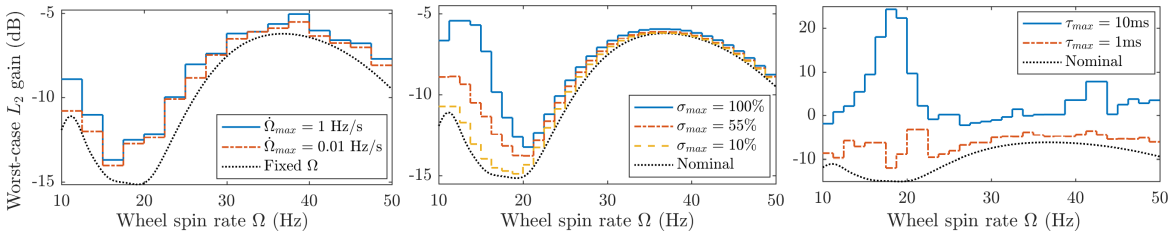


Figure 13: IQC portant sur le transfert $\mathbf{d} \rightarrow \mathbf{e}_u$ vis-à-vis de $\dot{\Omega}_{max}$ (gauche), $\sigma_{max}$ (centre) et du retard $\tau_{max}$ (droite)

Enfin, des simulations temporelles sont menées sur le système, dans des conditions nominales. Afin d'illustrer le compromis marges de stabilité robuste / performance robuste, les simulations sont conduites en utilisant, dans un premier temps, le correcteur $\mathbf{K}_{robustness}$, puis dans un deuxième temps, avec le correcteur $\mathbf{K}_{performance}$. Les résultats sont donnés sur la fig. 14. Les résultats obtenus sont sur-imposés pour une meilleure appréciation des performances obtenues. Afin d'apprécier également le gain en performance du système de contrôle des micro-vibrations proposé, les même tracés sont superposés lorsque le système ne possède pas de système de contrôle microvibratoire (tracés en gris clair). Clairement, ces tracés montrent bien l'avantage de la solution que nous proposons dans nos travaux de thèse. Ils soulignent également, et de façon non surprenante, que

dans des conditions de fonctionnement nominal, les meilleurs performances sont obtenues avec le correcteur $\mathbf{K}_{performance}$.

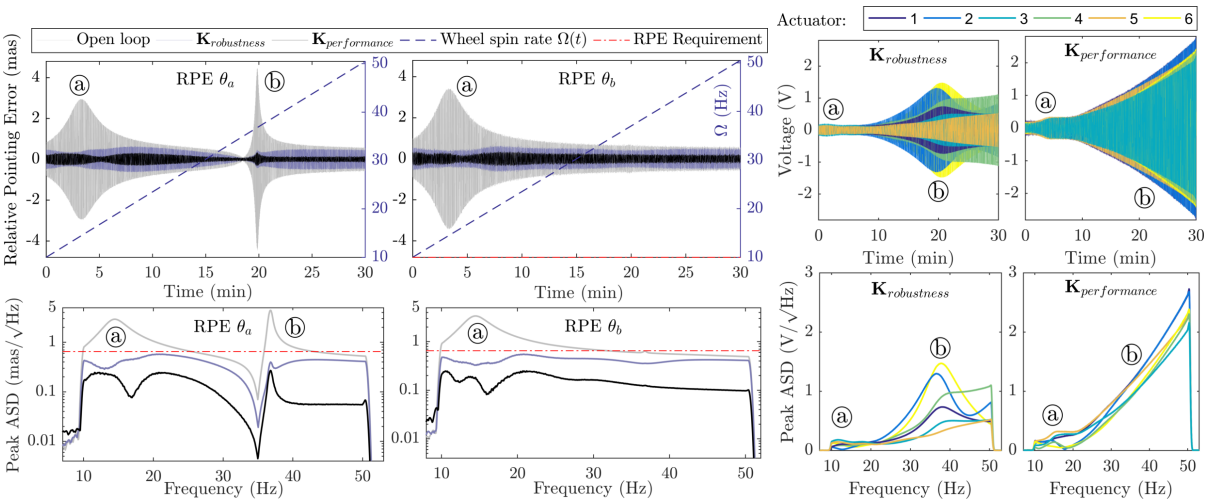


Figure 14: Simulations temporelles (conditions nominales) - (RPE = Relative Pointing Error)

### R.2.3 Contribution en analyse sur la précision de la ligne de visée et son impact sur la qualité d'imagerie

La troisième et dernière contribution de nos travaux de thèse, traite de la problématique de l'analyse des micro-vibrations sur la précision de la ligne de visée du satellite d'observation et son impact sur la qualité d'imagerie. Dans ce contexte, nous établissons une démarche méthodologique qui permet de reproduire la pire distorsion des images.

Plus précisément, nous proposons une architecture générique permettant d'analyser les effets de distorsion d'imagerie, dans un contexte pire-cas. L'architecture proposée est illustrée sur la fig. 15.

Cette architecture illustre comment les erreurs de pointage $\mathbf{e}_p$ (voir fig. 6), erreurs rappelons le qui se traduisent par des écarts de position angulaire $\theta_a$ et $\theta_b$, sont liées aux erreurs de pixel 2D, i.e. selon les axes $x$ et $y$ de l'image. Cette architecture, qui tient compte de la dynamique de la caméra, des modes flexibles et du système de contrôle du satellite (cela comprend le contrôle d'attitude et le système de contrôle de micro-vibrations), est basée sur l'hypothèse que les sources de perturbations qui causent une distorsion d'image, sont de deux natures:

- harmoniques dues aux micro-vibrations engendrées par la rotation $\Omega$ des roues inertielles. La fig. 15 fait référence à l'harmonique de rang 1 (notée $d_1$), mais nos travaux de recherche traitent du problème multi-harmonique.

- stochastiques, notée $\mathbf{d}_n$ sur la fig. 15.

L'intérêt de la structure proposée est de permettre d'avoir une approche automaticienne de la problématique de distorsion d'imagerie, en supposant que ces dernières sont la résultante d'un filtrage des entrées $\mathbf{d}$ et $\mathbf{d}_n$, moyennant la structure illustrée sur la fig. 15. Nous montrons alors que les erreurs de pixel 2D peuvent être prédites en analysant les transferts incertains $\begin{bmatrix}\mathbf{d}\\ \mathbf{d}_n\end{bmatrix} \rightarrow \mathbf{e}$ où $\mathbf{e}$ représente les erreurs de pixel 2D.

Parmi les résultats pertinents que nous avons établis dans nos travaux de thèse, nous montrons comment, dans le cas sans incertitude de modèle (i.e. $\Delta = \mathbf{0}$) et pour un angle de rotation de la caméra $\beta$ donné (voir fig. 15), les critères de norme de type $\mathcal{H}_2$ et RMS (Root Mean Square), permettent de prédire des majorants des erreurs de pixel 2D. Ces prédictions sont validées à travers

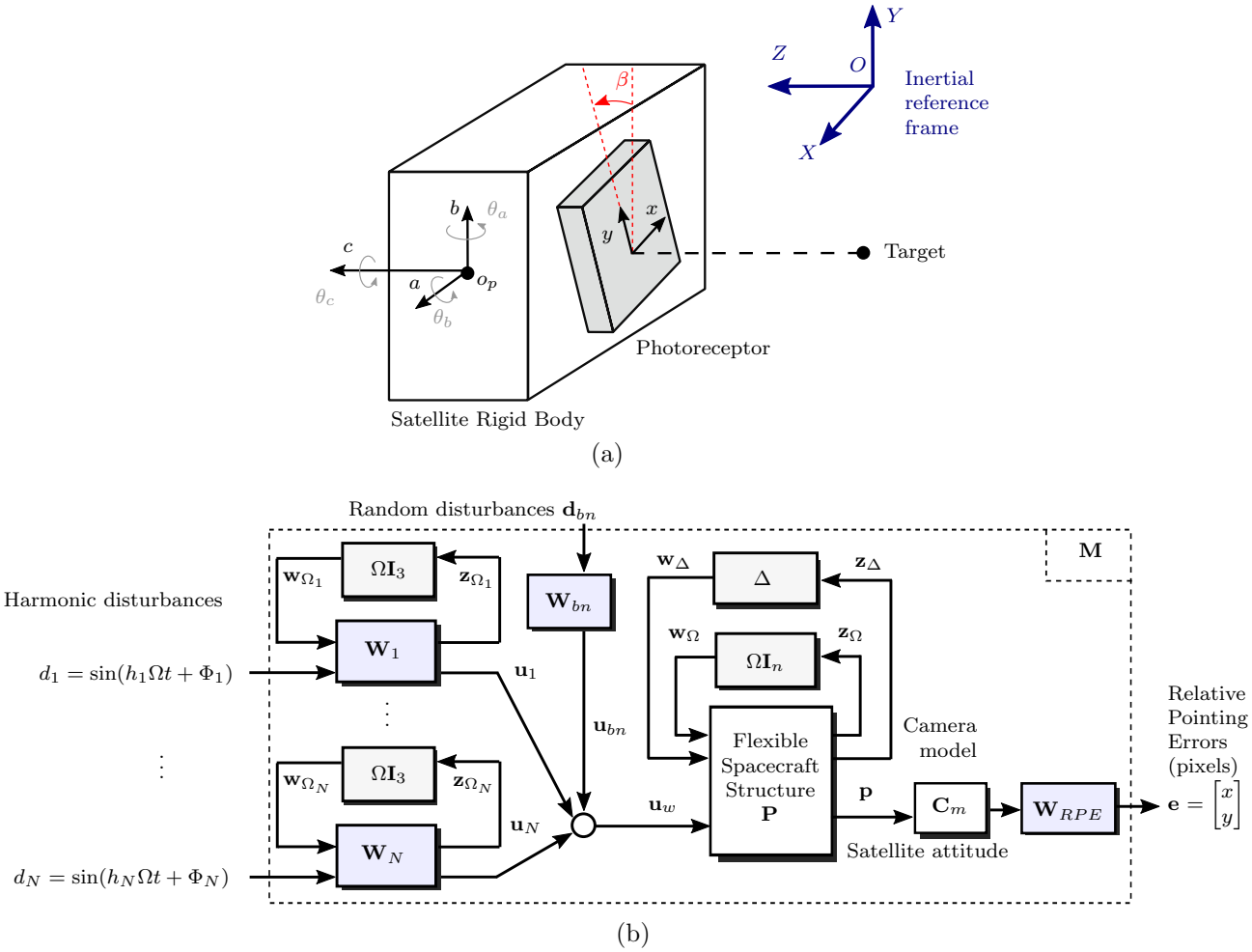


Figure 15: (a) Scène de pointage considérée. (b) Structure d'analyse de distorsion d'imagerie.

des simulations, comme l'illustre la fig. 16. Afin d'apprécier le gain en performance du système de contrôle des micro-vibration développé dans le cadre des travaux de cette thèse, les prédictions sont superposées lorsque le système ne possède pas de système de contrôle microvibratoire (tracés en gris clair). On peut clairement apprécier sur ces tracés, le caractère peut conservateur de la prédiction réalisée.

Les résultats obtenus sont alors étendus au cas incertain dans un contexte "pire-cas". On montre alors que la détermination d'un majorant des erreurs de pixel 2D pour un angle de rotation de la caméra $\beta$ donné, peut se poser comme un problème de minimisation $\mathcal{H}_2$ sous contrainte $\mathcal{H}_\infty$, de dimension infinie car paramétré par la vitesse de rotation $\Omega$ des roues inertielles. Pour résoudre le problème, nous proposons d'effectué un échantillonnage dense des incertitudes $\Delta$ et de $\Omega$ (ce qui revient à avoir une famille dense de modèle $\mathbf{M}$ comme illustré sur la fig. 15). On montre alors que le problème admet une formulation $\mathcal{H}_\infty$ non lisse. Le résultat obtenu est un majorant peu conservateur, qui est fonction de $\Omega$ et de $\beta$. Ainsi, pour $\beta \in [0, \pi]$ et pour un $\Omega$ donné, nous montrons que l'erreur de distorsion de l'image se traduit par une famille d'ellipses, fonction des incertitudes $\Delta$, et dont une approximation polytopique peut être déterminée. Bien évidemment, plus le nombre $n$ de sommets du polytope est important, moins conservatrice est l'approximation polytopique. La fig. 17 illustre ces résultats pour $\Omega = 14.44\,\text{Hz}$ (gauche) et $\Omega = 36.4\,\text{Hz}$ (droite). Les figures présentent les résultats dans le cas sans système de contrôle de micro-vibrations (tracés bleus) et avec le système de contrôle de micro-vibrations que nous avons développés dans nos travaux de thèse (tracés rouge), pour un échantillonnage de valeurs de $\Delta$. Ces résultats montrent

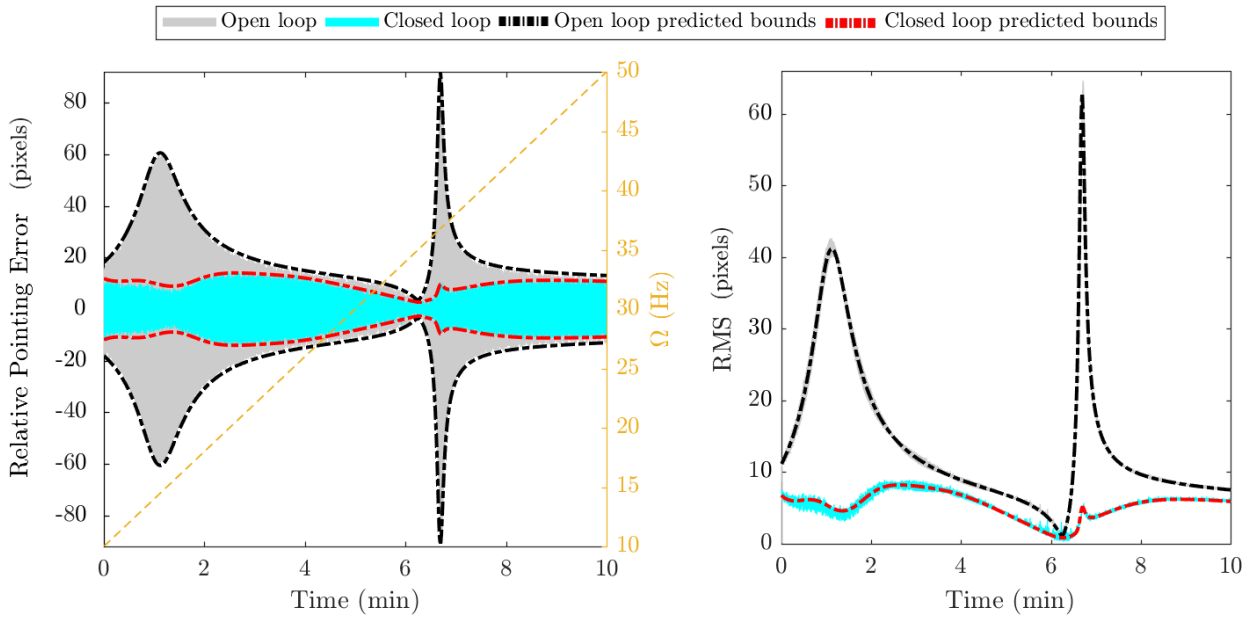


Figure 16: Prédiction des majorants des enveloppes des erreurs de pixel $\mathbf{e}(1)$. Cas nominal ($\Delta = \mathbf{0}$)

clairement qu'avec le système de contrôle de micro-vibrations, la distorsion d'image est réduite à quelques pixels. Les résultats présentés ne tiennent compte que de l'effet de l'harmonique de rang 1 des micro-vibrations et des sources de perturbations stochastiques.

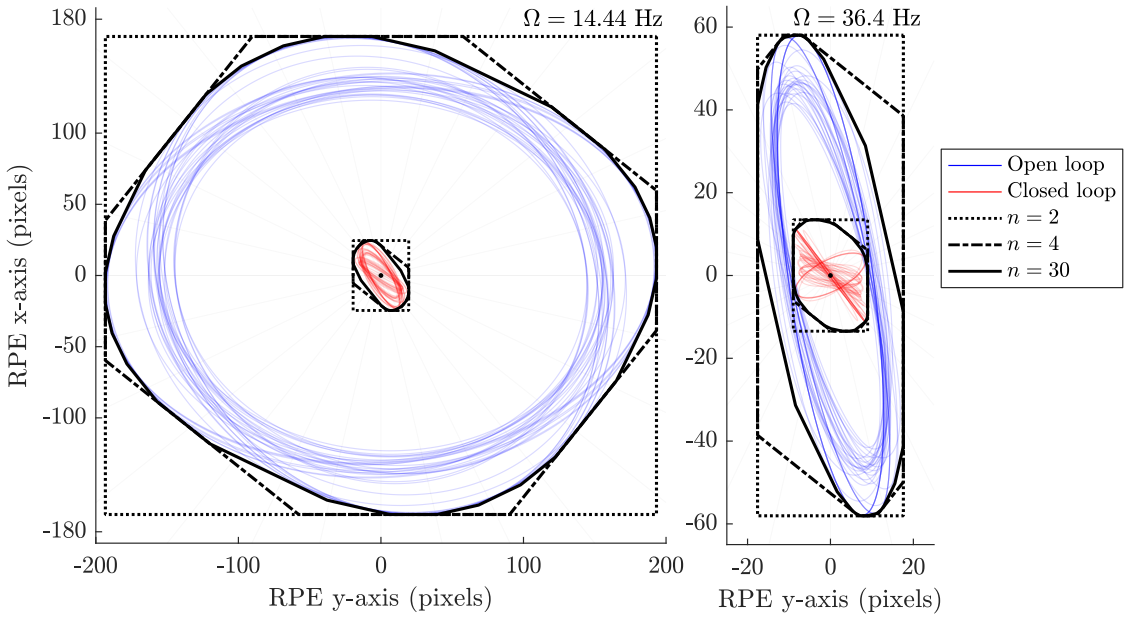


Figure 17: Majorant des erreurs de pixel et approximation polytopique

Enfin, nous montrons comment les outils de filtrage 2D telle que la fonction de transfert optique (traduction francophone de "Optical Transfer Function" **OTF**), couplée avec les majorants ainsi obtenus, peuvent être utilisés pour reconstruire l'image. L'idée est, connaissant complètement les caractéristiques des sources de distorsion (ce qui revient à dire, connaître $\mathbf{d}$ et $\mathbf{d}_n$ et le modèle $\mathbf{M}(\Omega, \Delta)$ illustré sur la fig. 15) et l'**OTF**, de pouvoir reconstruire l'image distordue. La problématique étant positionnée dans un contexte linéaire, la solution développée est basée sur une procédure de filtrage. Un exemple des résultats obtenus pour $\Omega = \{14.5, 36.75\}$ Hz est donné sur la fig. 18. Les résultats présentés ne considèrent pas le système de contrôle des micro-vibrations.

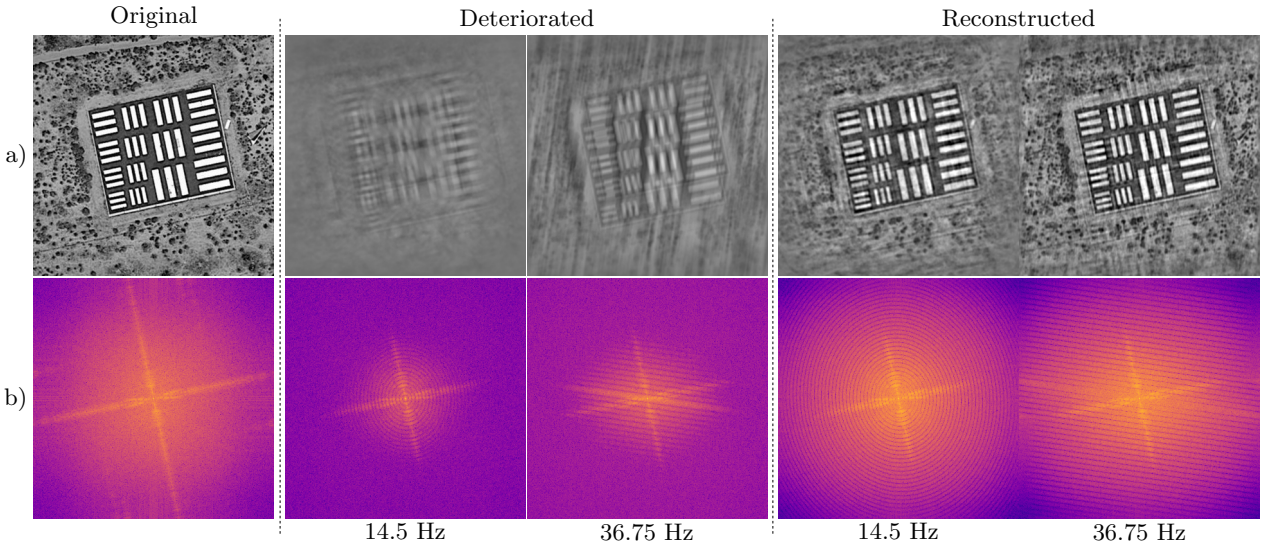


Figure 18: Reconstruction d'une image distordue. $\Omega = \{14.5,\ 36.75\}$ Hz. a) Image b) Densité Spectrale de Puissance.

---

"*Le savant n'étudie pas la nature parce que cela est utile ; il l'étudie parce qu'il y prend plaisir et il y prend plaisir parce qu'elle est belle. Si la nature n'était pas belle, elle ne vaudrait pas la peine d'être connue, la vie ne vaudrait pas la peine d'être vécue.*"

Henri Poincaré

# 1 Introduction

## 1.1 Context and motivation

Due to recent technological advancements in space based instrumentation, spacecraft mechanical vibrations have become a significant concern for earth observation, communication, space astronomy or advanced scientific missions that rely on high level of pointing stability. For instance, in the case of space based telescopes, the current tendency is to build instruments with an aperture that roughly doubles in size about every 20 years as illustrated in fig. 1.1a. A large aperture leads to a higher resolution and the ability to detect dimmer objects. Larger optical instruments usually involve bigger and more expensive launch vehicles due to the increase in weight. This provided a strong incentive for researchers and engineers to create proportionally lighter spacecraft. However, lightweight structures are also usually more flexible and therefore more susceptible to mechanical resonances induced by microvibrations. Meanwhile, due to the demand for higher resolution images, the average angular resolution of imaging sensors has been improved by a few orders of magnitude over the past decades as seen in fig. 1.1b. These changes to structural flexibility and

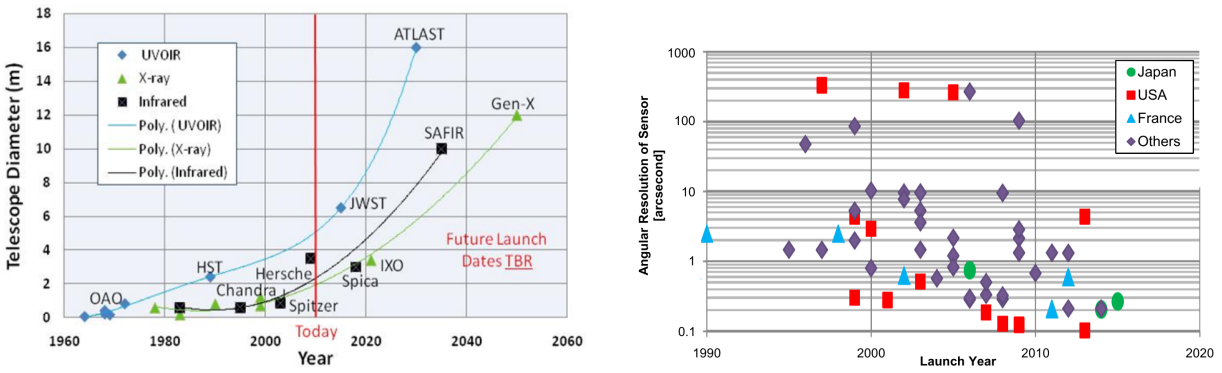


(a) (b)

Figure 1.1: (a) The growing aperture of space telescopes [LPD10]. (b) Angular resolution of recent civilian Earth observation satellites (1 arcsecond = 5 µrad) [KU14].

payload resolution progressively increase the requirements on the spacecraft pointing stability. As a result, modern earth observation and space astronomy missions have to meet extremely challenging pointing accuracy requirements. For instance, cosmic vision missions such as Euclid, Plato, Chandra X-ray Observatory or the James Webb Space Telescope require high precision pointing performance in the order of 1 mas (milliarcseconds). Similar demands also arise in geosynchronous missions like Geo-Oculus and Meteosat Third Generation or agile Low-Earth Orbit missions such as the future Sentinel-6. As line-of-sight stability requirements get tighter, mechanical vibrations become one of the key performance limiting factors. These disturbances are commonly termed microvibrations and are low-amplitude vibrations in the range of a few micro-g's ($\mu$g), that span a

wide frequency range from few Hz up to 1 kHz [CRS13]. Since spacecraft are isolated systems and operate in an environment that provides no atmospheric damping, the mechanical energy associated with these disturbances must be dissipated into the system. Moreover, satellites are constructed from very lightweight materials and microvibrations can easily be transmitted through the flexible structure towards various sensitive payloads or on-board instruments potentially causing severe performance degradation. Considering observation missions, microvibrations reduce image quality by introducing jitter motion during the exposure interval of the optical instruments. The images are impacted in two ways: *high frequency* disturbances degrade the Modulation Transfer Function (MTF) inducing image blurring, whereas *low frequency* ones degrade the geometry inducing image distortions. For example, the line of sight jitter on the detector plane shown in fig. 1.2a, introduces the significant image distortions visible in fig. 1.2b. In some cases, image distortions can be corrected on-ground by dedicated algorithms, but image blurring is definitely not rectifiable. This high/low frequency limit separation depends on the integration time: it is usually roughly equal to 0.1 times the inverse of the integration time. Hence, long integration time instruments like the ones used in scientific missions are more affected by this degradation compared to the short integration time ones used for example in low Earth orbit observation missions.

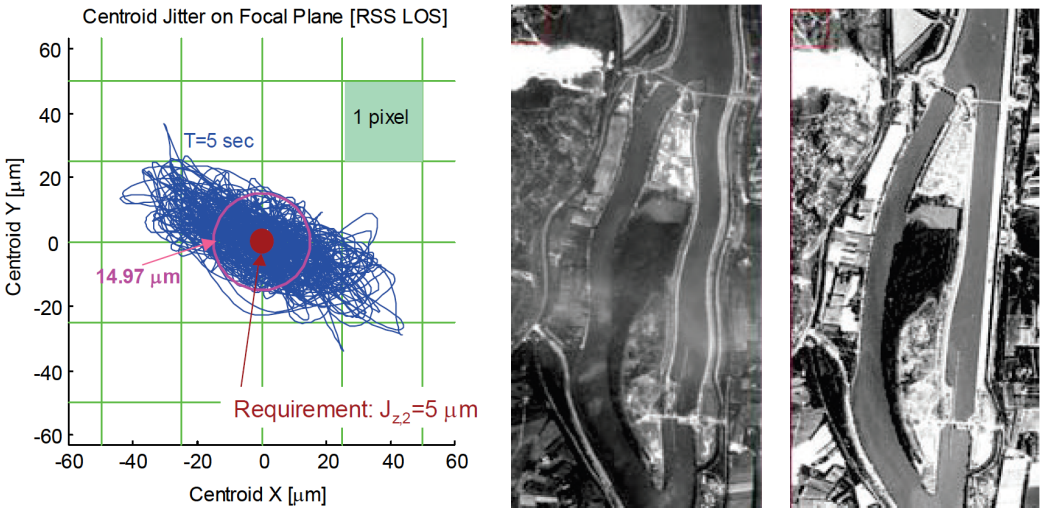


(a) (b) (c)

Figure 1.2: (a) Satellite pointing error (blue line) together with the requirement (red dot) (b) Resulting effects on image quality (c) Comparative result with corrective measures and reduced imager motion [CRS13]

### 1.1.1 Microvibration sources

Depending on their origin, microvibration disturbances that commonly occur in spacecraft are:

- **External** (or natural) perturbations that are the result of interaction between the satellite and the space environment. These include quasi-steady perturbations (such as atmospheric drag, earth gravity field gradient, magnetic field interactions, solar flux or earth albedo) or intermittent transient load (such as those occurring from micro-meteoroids and debris impacts) [CRS13].

- **Internal** disturbances that are generated by various subsystems and devices on-board modern spacecraft such as the attitude control, propulsion, avionics , electrical power, telemetry or thermal control subsystems.

In general, internal disturbances are far more important and depending on their temporal behavior can be furter classified into two broad categories:

- **Single disturbance events** also known as transient loads are intermittent impulsive disturbances with small dynamic amplitudes. Frequent causes include sudden stress release between parts with differential temperatures due to thermal expansion, micro-cracking in laminates, buckling of foils due to thermal expansion and contraction [WWE05, Wij09]. Shock type disturbances forces of this type can also be generated due to specific commands such as thrusters firing or momentum unloading [MKS07], or liquid flowing and sloshing [VGL+07, DQGL08, GV03].

- **Continuous disturbances** otherwise known as vibratory loads can be either narrowband harmonic disturbances or broadband perturbations [ZYP09]. A variety of on-board equipment such as infrared sensors, solar array drive mechanisms or cryo-coolers generate this type of microvibrations. Additional sources include electric motors, data storage devices [Bia97] or high speed rotating equipment such as momentum/reaction wheel assemblies, gyroscopes or solar array drives [SNG08].

Overall, out of all these possible sources, the ones generated by the reaction wheel assemblies (RWAs) or Control Moment Gyroscopes are usually the most significant [Bro06, LJDL15]. These mechanical spinning devices are used to achieve attitude control by acting as momentum exchange devices. Additionally, they provide a cheaper and lighter alternative to Cold Gas Micro Propulsion Systems that are currently the state of practice for very high stability missions (see for instance [FSBW07, PdBB+16]). A RWA, is typically made up of rotating flywheel that is mounted on a shaft supported by either mechanical or magnetic bearings and driven by a brushless DC motor. Inside the RWAs, the flywheels are usually arranged either symmetrically at the mid-span of the shaft or cantilevered with the flywheel at the end of the shaft, as seen in fig. 1.3. Although slightly different, both configurations share the same dynamic behavior to a large extent [Add17]. During

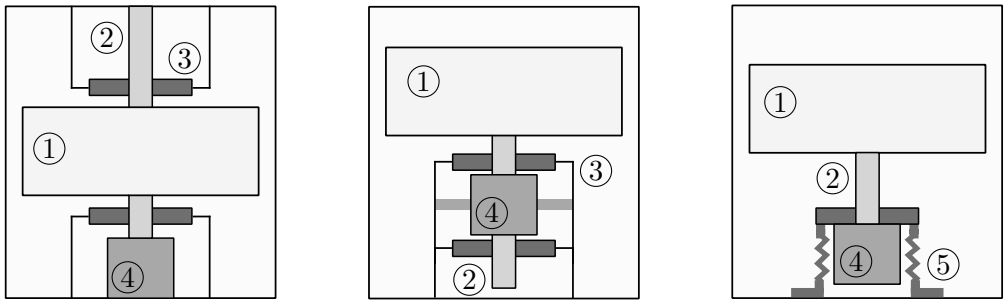


(a) (b) (c)

Figure 1.3: Possible reaction wheel configurations: a) rigid axi-symmetrical b) rigid cantilever c) flexible cantilever. ①-flywheel ②-rigid motor shaft ③-bearings ④-motor ⑤-flexible support.

manufacturing, the flywheels are precisely balanced in order to minimize the vibrations that occur during operation. Nevertheless, even with extremely tight manufacturing tolerances, these rotating devices still generate residual harmonic perturbations. The disturbances that arise in flywheels are mainly caused by static imbalance, dynamic imbalance and bearing imperfections [LMB08]. Static imbalance is caused by the offset of the center mass of the wheel spin axis. Dynamic imbalance results from the misalignment of the principal axis and the rotating axis on the wheels, while bearing disturbances are caused by irregularities in balls, races or cages [TO03]. For clarity, fig. 1.4 illustrates some of these bearing imperfections and how the static imbalance caused by the mass $m_s$ give rise to the lateral centrifugal force $\mathbf{F}_1$ rotating with the spin rate $\Omega$ of the reaction wheel. Similarly, the figure shows how the dynamic imbalanced caused by the two masses $m_d$ produces two centrifugal forces $\mathbf{F}_{d1}$ and $\mathbf{F}_{d2}$. These forces combine to create a lateral rotating torque $\mathbf{T}_1$ and zero net force on the flywheel body.

As modern space structures become increasingly more lightweight and flexible, these harmonics can be greatly amplified if they interact with the structural modes of the spacecraft, leading to an

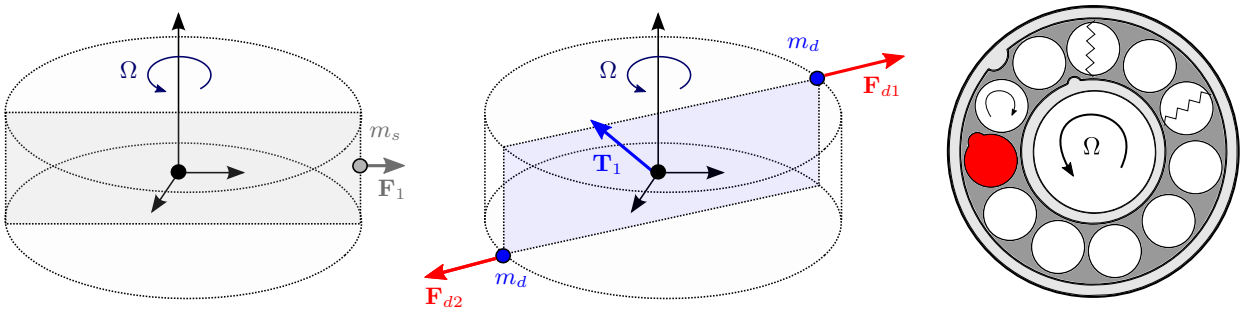


(a) (b) (c)

Figure 1.4: For a reaction wheel spinning at a constant spin rate $\Omega$: (a) Static imbalance caused my mass $m_s$ giving rise to the lateral force $\mathbf{F}_1$. (b) Dynamic imbalance caused by the two masses $m_d$ producing a combined lateral torque $\mathbf{T}_1$. (c) Example of imperfections in the flexible bearings supporting the wheel.

issue of great importance. The problem of obtaining accurate dynamical models of reaction wheel perturbations has attracted considerable research interest as evidenced by the numerous studies such as [Le17, Add17, Mas99, Has86] dedicated to this topic.

### 1.1.2 Microvibration isolation

Another very active field is the one related to microvibration isolation, especially with regards to the ones generated by reaction wheels. State-of-the-art microvibration isolation methods have been reviewed in literature by [AG03, Agr09, LJDL15, GW00] or [Ibr08]. Figure 1.5 shows the general vibration isolation architecture for a typical imaging spacecraft. In general, multiple

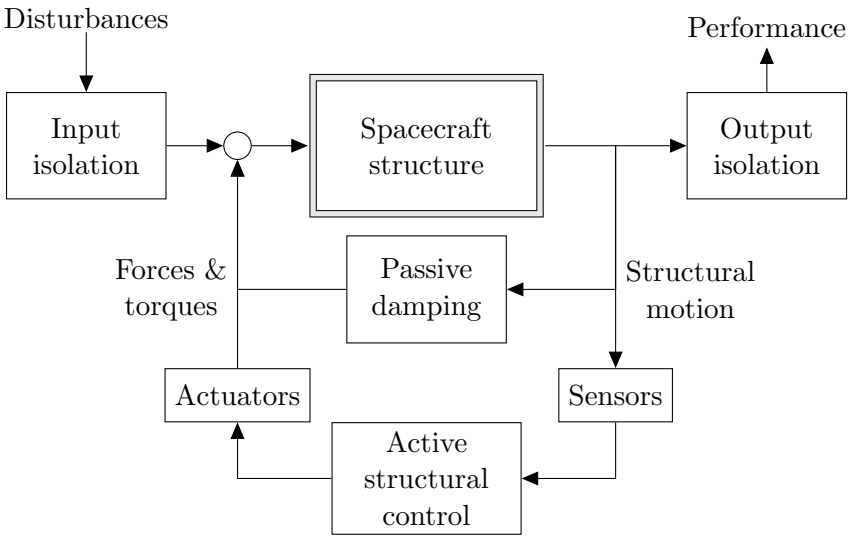


Figure 1.5: General microvibration isolation architecture.

vibration isolation techniques are used in combination to reduce the influence of microvibrations on the pointing accuracy. One method is to add passive or active damping to the spacecraft support structure and reduce the vibration response. A second approach is isolate the disturbance equipment from the other parts of the spacecraft. The third technique is to isolate sensitive payloads from the spacecraft. For space missions requiring very low jitter, the isolation strategy usually involves a combination of these techniques, as exemplified in fig. 1.6. In the case of reaction wheels, significant research effort has been invested in finding ways of reducing the impact of the generated microvibrations [LJDL15, WC03]. One of the simplest techniques is to constrain the rotational

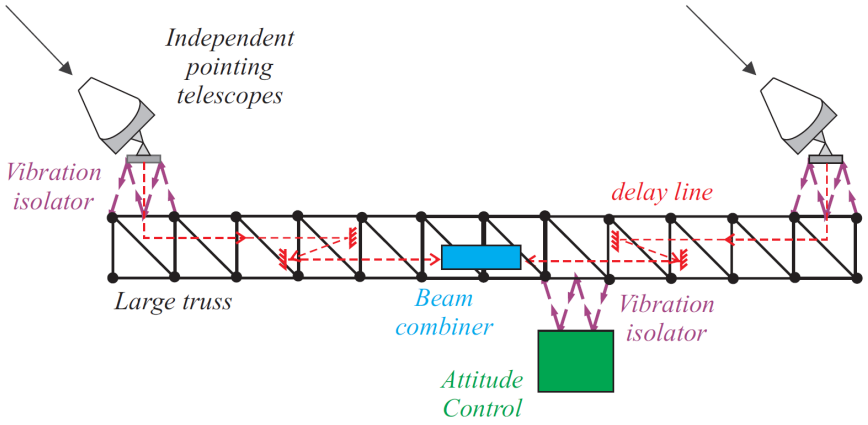


Figure 1.6: Possible vibration isolation architecture for a future interferometric mission [Pre11]

speed of the flywheels in order to avoid exciting the spacecraft's structural modes. However, this constraint becomes more demanding as structures become less rigid and their flexible modes get shifted to lower frequencies. Another promising future approach is to use magnetically suspended bearings [ZBK14] instead of ball-bearings to support the flywheels. This eliminates the direct mechanical connection and can significantly attenuate the transmitted disturbances. Although this technology is encouraging, especially for smaller satellites, it is not yet a mature, space-proven solution and the vast majority of reaction wheels still rely on traditional ball-bearings.

### Passive isolation

A much more common isolation approach involves placing isolators along the disturbance propagation path between the noise source and the instruments. Passive isolation techniques are regarded as the most mature technology for managing in-orbit vibration isolation [WHX+13] and are a common presence in aerospace applications [DC93, DCH94]. A passive isolator can be defined as a compact connection between two structures that receives no external energy or information [WC03]. From a control perspective, a passive isolator acts like a low-pass filter [GW00] and has the advantage of guaranteed stability. Inside these devices, stiffness and damping elements are used to dissipate vibrational energy and prevent the high frequency disturbances from propagating. Traditionally, for passive vibration control applications, the dissipative elements are usually visco-elastic materials, springs or hydraulic dampers isolators [Riv04].

In [KPG10, KPG12, ZL12, ZLLJ12], continuous folded beams (such as the one shown in fig. 1.7) are employed in the design of a passive isolation platform for RWA. The design of these beams is optimized and achieves simultaneously a low amplification around the critical wheel speeds and a large reduction at high frequency. The low corner frequency can be obtained by raising the number of folds and decreasing the thickness of the vertical beams.

At Airbus Defense and Space, isolators based on elastomeric materials, are the current baseline for microvibration mitigation on-board the majority of satellites [Sec13]. Recent technological improvements have made elastomer components very attractive [Lau16] due to their very light weight, their capability of withstanding launch loads without requiring a locking device (reducing weight, complexity and increasing reliability) and testability under 1-g (lower development and validation costs). Nevertheless, these apparently simple isolators actually require a deep understanding of the material properties to be compliant with all space constraints such as compatibility with the attitude control systems, thermal variations, radiation exposure, launch stresses, etc. In [VP99] a six degree of freedom (DoF) isolation of a disturbance source such as RWA or cryocooler was designed and implemented using three elastomer-based softmounts made of space-qualified silicon rubber material. The authors point out that an elastomeric material compatible with the space environment was preferred to other conventional spring/damper technology (such as [RDR+86, DWJR86, CDS96])

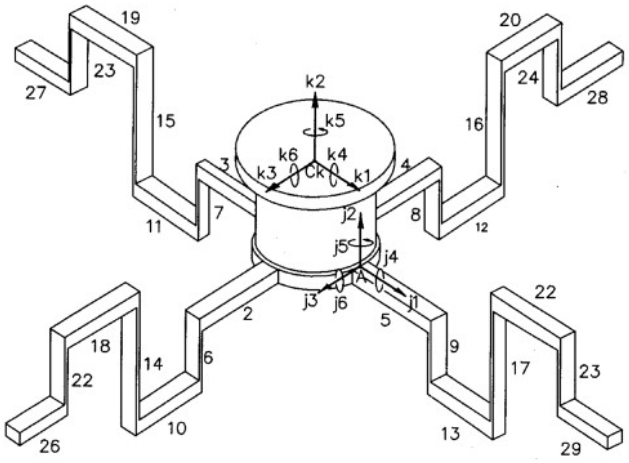


Figure 1.7: Flexible space platform using folded continuous beams [KPG10, KPG12]

for its simplicity and improved performance. Experimental tests demonstrate the attenuation in force transmissibility exceeding 20 dB above 25 Hz and 40 dB above 50 Hz.

All of the aforementioned types of passive isolators, share the same dynamic behavior in the case of small amplitude vibrations. Namely, they can be mathematically modeled as a visco-elastic connection with stiffness $k$ and damping $c$ as shown in fig. 1.8. Considering that the disturbance

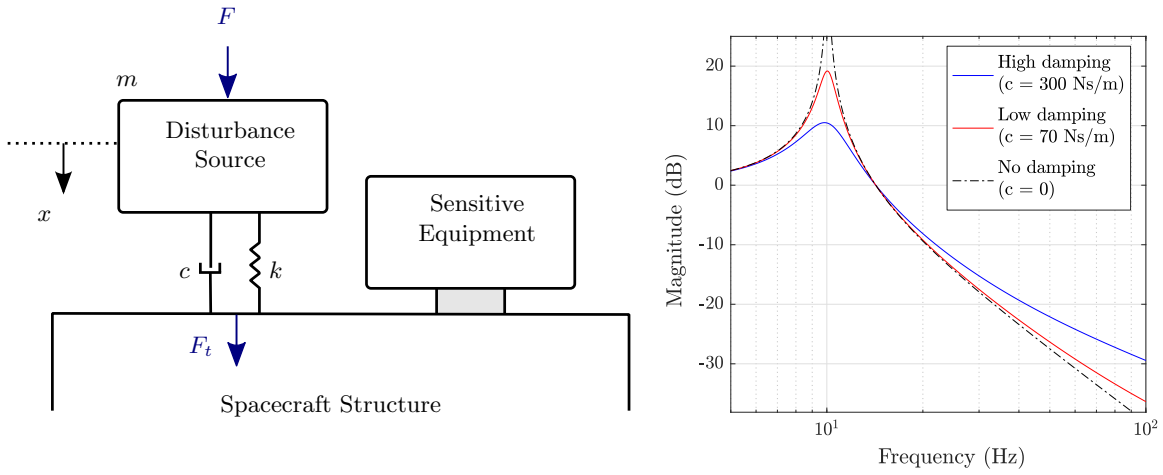


(a) (b)

Figure 1.8: (a) Model of a passive isolation system. (b) Theoretical force transmissibility for a 1-DoF passive isolator with $m = 10\,\text{kg}$, $k = 10\,000\,\text{N/m}$ and considering a fixed spacecraft.

source of mass $m$ is placed on top of the isolators and $m$ is much smaller than the supporting spacecraft structure, the relationship between the disturbance force $F$ acting on the equipment and the force $F_t$ transmitted to the structured is described with the following set of equations

$$\begin{cases} m\ddot{x} + c\dot{x} + kx = F \\ F_t = c\dot{x} + kx \end{cases} \tag{1.1}$$

where $x$ is the isolator displacement. In terms of input-output behavior, the relationship between the forces is given by the following second order transfer function:

$$H(s) = \frac{F_t(s)}{F(s)} = \frac{cs + k}{ms^2 + cs + k} \tag{1.2}$$

This function is characterized by the undamped natural frequency $\omega_n = \sqrt{\frac{k}{m}}$ and damping ratio $\xi = \frac{c}{2\sqrt{km}}$. Figure 1.8b shows the magnitude plots of this function for fixed $m$ and $k$ across different values of the damping coefficient $c$. It can be seen that increasing $c$ leads to a decrease in the peak amplification around $w_n$ together with a corresponding increase in the high-frequency roll-off. This inherent trade-off between peak amplification and high-frequency attenuation is the main limitation common to most passive isolators. Accordingly, the passive isolator performances depend on the tuning of their characteristics in terms of stiffness $k$ and damping coefficient $c$. The lower the resonance frequency, the wider the spectrum interval that is rejected. In other terms, a twice lower resonance frequency, for instance, allows for a four times stronger attenuation performance of a given high frequency perturbation component. Nevertheless, practical constraints make it unrealistic to design very soft isolators. Among them, we can cite testability on ground and less resistance of the component to launch stresses. The quality factor $Q = 1/(2\xi)$ for state-of-the-art elastomer-based isolators is about 3 to 4 (corresponding to about 24 dB amplification at resonance) and cannot be reduced further due the intrinsic damping property of the material [Sec13]. Accordingly, passive isolators not only are not able to attenuate the low frequency spectrum, but they actually introduce underdamped structure modes in the frequency range where the reaction wheel disturbances are expected to act. This explains why for missions requiring very high platform stability in a wide frequency band, passive isolation systems alone are insufficient to meet mission pointing requirements when wheels are used.

### Hybrid isolation

To compensate for the limitations of a purely passive approach and achieve broadband vibration isolation, multiple hybrid (mixed pasive/active) control strategies such as [DCH95, LLJ14, LLZ13a] have been studied in literature. Active isolation techniques rely on external actuators and sensors in order to provide control force and feedback. The idea is to rely on active vibration isolation in the low frequency range and use passive isolators to target the high frequency disturbances.

One hybrid isolation approach is to combine the passive folded continuous beams described earlier with piezoelectric actuators and sensors as shown in fig. 1.9a. Such an arrangement was used in [KPG10] to isolate microvibrations from reaction wheels in six-degrees-of-freedom. Another much more common technique is to employ an active platform driven by six active/passive hybrid struts in a hexapod configuration, such as the one illustrated in fig. 1.9b. For example, one such arrangement is used by the Jet Propulsion Laboratory within an active–passive vibration isolation platform meant for space borne interferometry missions [TCVV02]. Each of the hybrid strut is made up of a voice coil actuator in parallel with a soft spring. The springs act like passive isolators with 3 Hz break frequency guarantees that even if the active power fails, the isolation system is still operated by the passive part. The active vibration control unit uses the force measurements provided by the load cell mounted in the hybrid strut to drive the actuators. Another hexapod hybrid isolation platform is the Vibration Isolation and Suppression System (VISS) shown in fig. 1.9c which was employed to protect high precision payloads from on-board disturbances [CSD+99]. The key isolation component of VISS is a hybrid D-strut with the cross-section shown in fig. 1.9c. This strut has a passive part composed by viscous fluid in two primary bellows and interconnected by a narrow orifice between the payload and the base. The main advantage of such a passive isolator is that the damping is independent of stiffness, has no wear mechanism and exhibits large stroke.

Overall, hybrid isolation systems combine the best of both the passive and active isolation techniques. When properly used, both high and low frequency microvibrations can be effectively isolated. However, a drawback of these systems is that they require additional accessory devices such as sensors, actuators and power systems alongside a feedback control loop. If the controller is not properly designed, the system may suffer from serious spillover (due to actuator saturation for example) and stability problems.

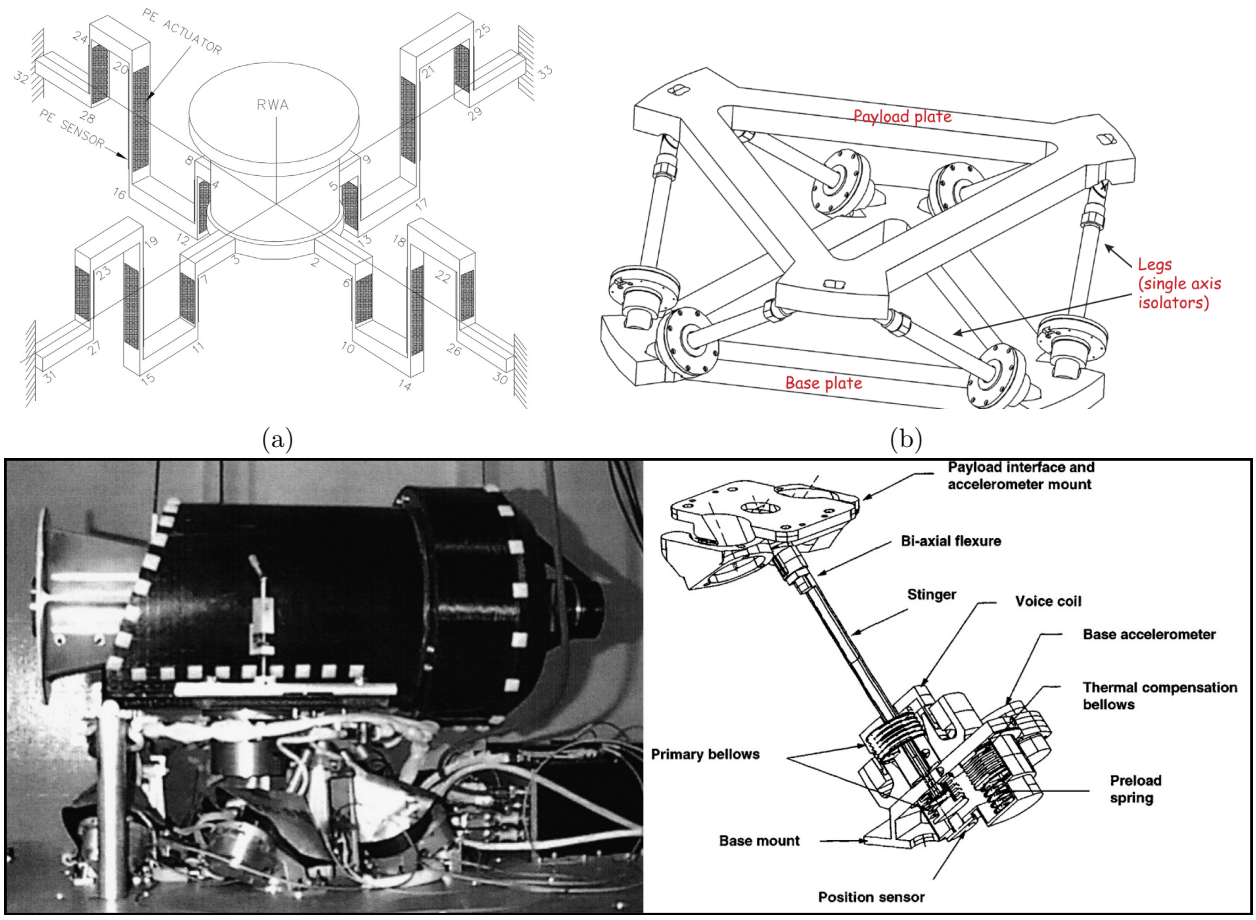


Figure 1.9: (a) Hybrid isolator consisting of folded continuous beams and smart material [KPG10]. (b) Soft isolation Stewart platform with six active actuators [PHR+07]. (c) VISS hexapod configuration with model of MWIR telescope and cross-section of the new-type hybrid D-strut [CSD+99].

### 1.1.3 Description of the ESA and Airbus D&S hybrid isolation platform

In this context, research activities at ESA and Airbus D&S have seeked to remedy the drawbacks of the flight-proven passive elastomer isolators by means of an active isolation system. One such hybrid isolation platform is the one that was initially described in [BMSL11, FBBH14, Sec13] and shown in fig. 1.10. The initial aim of this benchmark was to demonstrate the good functionality of a coupled solution composed by a passive stage and an active stage for microvibration mitigation in satellites. For these purposes, the different elements that composed the system have been dimensioned so that the setup is representative of the structure behavior of a satellite put in an orbit. The platform consists of an interface plate suspended by four springs representative of a satellite panel in free floating conditions. Instead of real reaction wheel, the benchmark made use of a dummy wheel sharing the same inertial properties of a real wheel. A perturbation source composed of a shaker was installed on the top of this dummy wheel with the aim of partially simulating the time-varying harmonic disturbances induced by a real spinning wheel. Although, the shaker and dummy wheel can't fully capture the precise nature of real reaction wheel microvibrations, the setup provided a good initial starting point to evaluate novel isolation methods in a cost effective manner. The active plate rigidly connects to the dummy wheel while the connection to the interface plate is made through four passive elastomer isolators that are used to mitigate the effect of high frequency perturbations. On the bottom of each isolator, a tri-axis force cell sensor is installed. When strained, piezoelectric elements inside these cells generate electric charges that are converted into voltages

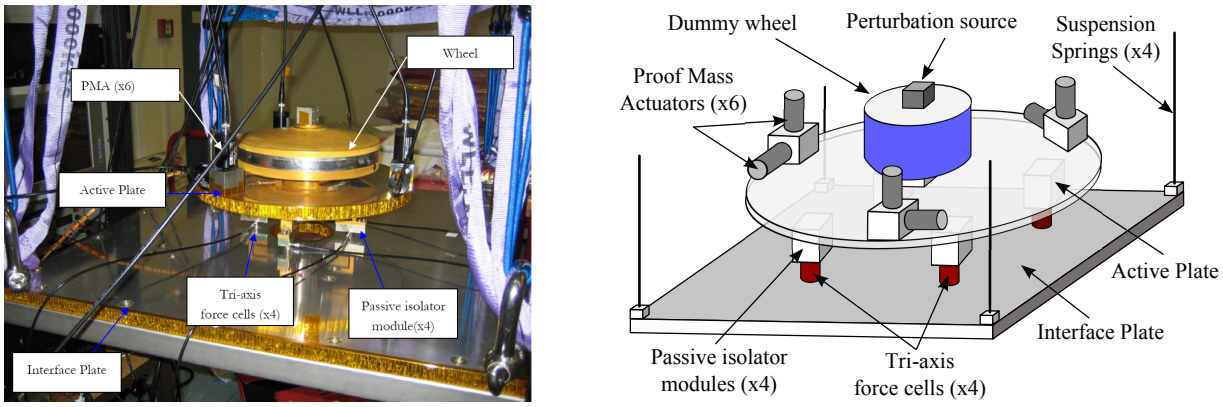


(a) (b)

Figure 1.10: (a) Airbus D&S and ESA breadboard used in preliminary studies. (b) Schematic of the same breadboard.

using charge amplifiers. The noisy force measurements are afterwards interpreted by the controller in order to mitigate low-frequency disturbances in the range of 10-50 Hz. This is accomplished using a set of six proof mass actuators that are used to actuate the active plate. These are mounted on three cubes; three along the vertical axis and three in the tangential direction and are driven by a set of six current amplifiers. The end goal is minimize the contact forces measured by the sensors and therefore the mitigate the microvibrations that get transmitted to the interface plate.

Using an Linear Time Invariant (LTI) model of this platform, experimentally identified by Airbus D&S, various controller synthesis strategies have been investigated in [BMSL11, FBBH14, Sec13] with the goal of achieving a reduction of disturbance transmissibility in all of the six DoF of at least 20 dB. The strategies were experimentally verified and include an adaptive feedforward disturbance cancelation scheme while the second one was formulated and managed in the $\mu$-synthesis framework to easily handle robust stability and performance specifications.

### 1.1.4 Motivation of the study

#### Limitations of the previous setup

One of the most important motivations for this thesis was the need to address the following list of limitations with the previous setup and control design approaches:

- the previous setup attempted to emulate the harmonic spectrum of a real reaction wheel by means of a single shaker installed on top of the dummy wheel. Although this was very useful in highlighting the potential of the isolation platform, the shaker could only induce vibrations along the mounting direction. A real reaction wheel on the other hand typically generates a complex multi-harmonic and phase correlated spectrum in both lateral and axial directions.

- a spinning reaction wheel will naturally induce a coupling between the lateral displacements of the active plate due to gyroscopic effects. Additionally, a real reaction wheel is not rigidly connected to supporting structure and typically the rotating shaft is supported by ball-bearings that have an inherent flexibility.

- the previously identified black box LTI dynamics and the associated uncertainty model offered little insight into the physical reality or the limits of achievable performance.

- due to the lack of physical insight a series of very conservative assumptions were implicitly made during the controller synthesis procedures about the nature of model uncertainty in order to safeguard against potential plant variation.

**End-to-end analysis of microvibration disturbances**

For modern space missions requiring stringent point performances, the calibration and Validation & Verification (V&V) of microvibration isolation systems is a crucial step in the overall process.

Currently, due to the reduced means of integrated flight testing for space missions, engineers have to rely almost exclusively on computer simulations, for the tuning, validation and acceptance of such systems. In the vast majority of cases, the isolation system tuning is performed using a combination of empirical and classical control approaches. For the V&V phase, the industry relies essentially on time-domain analysis techniques based on Monte-Carlo simulations. The setup of such validation techniques is rather simple. First, engineer build a highly accurate and representative simulation model. Afterwards, thousands or even millions of flight simulations are run using different values for the isolation parameters or considering multiple mission conditions. These characteristics are chosen over a set of predefined feasible values in order to ensure that all possible mission conditions are covered. This often leads to long design, development and validation times

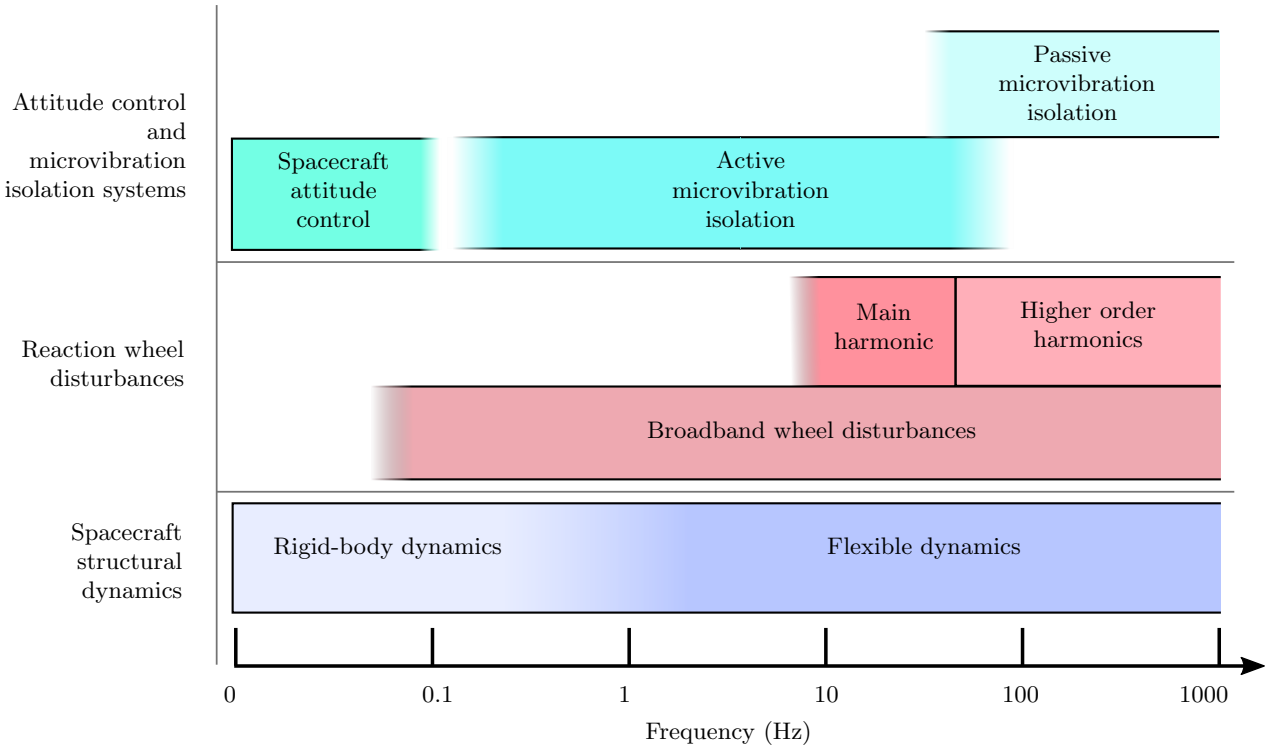


Figure 1.11: Typical frequency range for reaction wheel disturbances, spacecraft structural dynamics and the attitude & microvibration control systems.

with a lot of iterations relying on these intensive, high fidelity simulation campaigns. However, slight changes in design hypotheses and objectives lead to large redesign and verification efforts. These time domain methods have the additional shortcoming that no direct relation exists between the analysis and the control design. Requirement non-satisfaction from simulations does not typically give the designer guidelines in which direction the control laws need to be updated and many iterations are necessary to fix the non compliance while not introducing another one. In addition to these issues, the main drawback of this method is that the random choice of the parameters over their predefined range of feasible values does not imply that all the possible parameter combinations are investigated. Therefore, the method provides no rigorous guarantee concerning the stability and performance due to the observation of discrete operating points. The "certificate" that is obtained solely consists in a probability of success of the mission. These are some of the reasons why our industrial partners seek better analytical tools that aid the design and V&V of

isolation systems and provided a lot motivation for the research conducted in this thesis. The need is to build accurate and integrated models of typical mission scenarios and afterwards use the analytical tool to perform both the controller synthesis and the worst-case analysis without the need for time-domain methods.

With regards to the hybrid isolation of microvibrations produced by reaction wheels, fig. 1.11 seeks to illustrate the typical frequency range for reaction wheel disturbances, spacecraft dynamics and the attitude & microvibration control systems. The frequency ranges are organized in layers that are typically found in any space observation mission. The motivation is therefore to build a representative end-to-end model that combines all this complexity and sub-components in a common mathematical framework and afterwards use this integrated system for both controller synthesis and worst-case analysis purposes.

## 1.2 Aims and objectives

In this context, the research work presented in this thesis combines the expertise of the European Space Agency (ESA), the industry (Airbus Defence and Space) and the IMS laboratory (laboratoire de l'Intégration du Matériau au Système) with the aim of developing new generation of robust microvibration isolation systems for future space observation missions. More precisely, the goal of the thesis is the development of an Integrated Modeling, Control and Analysis (IMCA) framework in which to conduct advanced studies related to reaction wheel microvibration mitigation.

Integrated modeling should be understood in the context of this thesis as the process of building an overall system model of the spacecraft containing realistic structures, disturbances, optics, attitude control and vibration isolation models and their mutual interaction. Each of these subsystems can have an associated uncertain or parameter-dependent part that is independently identified and calibrated. Afterwards, the integrated system seamlessly assembles these sub-blocks and their corresponding uncertain or parameter-dependent components into an end-to-end model that maps disturbances to various performance signals. With the overall spacecraft model properly constructed, the thesis then seeks to demonstrate how modern robust analysis tools can be employed to truly understand the reaction wheel disturbance propagation throughout the system and also perform state-of-the-art worst case uncertainty analysis with guaranteed performance bounds. The present works also seeks new ways to simulate the image distortions induced by such disturbances. Finally, the thesis aims to highlight how these modeling and analysis capabilities can be combined with modern controller synthesis techniques to synthesize and tune advanced architectures for microvibration isolation.

To accomplish these goals, the thesis will build upon the previous research conducted by Airbus Defence and Space and ESA on the use of mixed active/passive microvibration mitigation techniques. Therefore, the main isolation architecture that will be considered in this work is the one previously described in section 1.1.3. However, it should be stressed that the methodologies and capabilities demonstrated in this thesis are not limited to this particular architecture and that the guidelines and procedures presented throughout this work can be adapted to a wide variety of other mission scenarios.

In accordance with the previously stated goals, the research activity proposed and accomplished a series of objectives that can be grouped as follows:

#### Integrated modeling

- establish an Integrated Modeling, Control and Analysis framework for a typical space observation mission composed of a flexible satellite mode, a hybrid isolation platform and a reaction wheel assembly. The integrated end-to-end uncertain system model must fully capture the disturbance propagation from the reaction wheels, through the isolation system and flexible spacecraft structure towards the sensitive instruments

- develop a new model for reaction wheel disturbance that takes into account the multi-harmonic and phase-correlated perturbations generated by a typical wheel during operation. The model must have a representation that can be easily combined with any end-to-end model in order to make non-conservative predictions about the resulting performance signals.

**Control system design**

- show how stability requirements and isolation performance objectives can be expressed as bounds on certain scaled closed-loop transfers using results from modern control theory.
- demonstrate how the integrated model together with modern controller synthesis techniques can be employed to tune the active isolation platform and deliver high performance disturbance isolation with guaranteed transmissibility or pointing performance in the presence of plant uncertainty.
- propose a methodology to easily calibrate the trade-off between robustness and performance.

**Worst case analysis**

- demonstrate how guaranteed performance bounds of the isolation architecture can be extracted using analytical worst-case analysis tools. These are used to certify the control solution with respect to model uncertainty and nonlinear phenomenon without relying on Monte-Carlo campaigns.
- introduce new methods to simulate the image distortions resulting from jitter motions in a manner that correctly handles the phase relations between the motions along each imaging axis.

## 1.3 Outline of the thesis

The content of this thesis is organized into five chapters that are illustrated in the flowchart in fig. 1.12.

Chapter 1 provided an overview of the concern about spacecraft microvibration and the need to perform the current research.

Chapter 2 introduces the integrated uncertain model for the hybrid microvibration isolation platform developed by Airbus Defence and Space and ESA. Based on this uncertain model, the chapter presents a method to tune a robust controller for active vibration isolation in order to minimize the elastic forces transmitted through the passive isolators. Finally, the robust performances of the isolation architecture are assessed using analytical tools and time domain simulations based on a nonlinear high-fidelity industrial simulator are included as a final verification step.

Chapter 3 shows how the dynamical models of the reaction wheel and microvibration isolation platform established in the previous chapter can be integrated with that of simplified model of a flexible spacecraft stabilized using an attitude control system. The end-to-end system also includes a novel disturbance model of the reaction wheel perturbations that is suitable for worst case analysis and controller design. The main goal is to establish an Integrated Modeling, Control and Analysis framework of reaction wheel perturbations for a typical space observation mission in order to guarantee improved pointing stability performance even in the presence of isolation platform uncertainties and non-linear effects.

Chapter 4 presents a method that guarantees upper bounds on the worst-case pointing errors of a general flexible spacecraft in response to reaction wheel disturbances. The chapter also includes

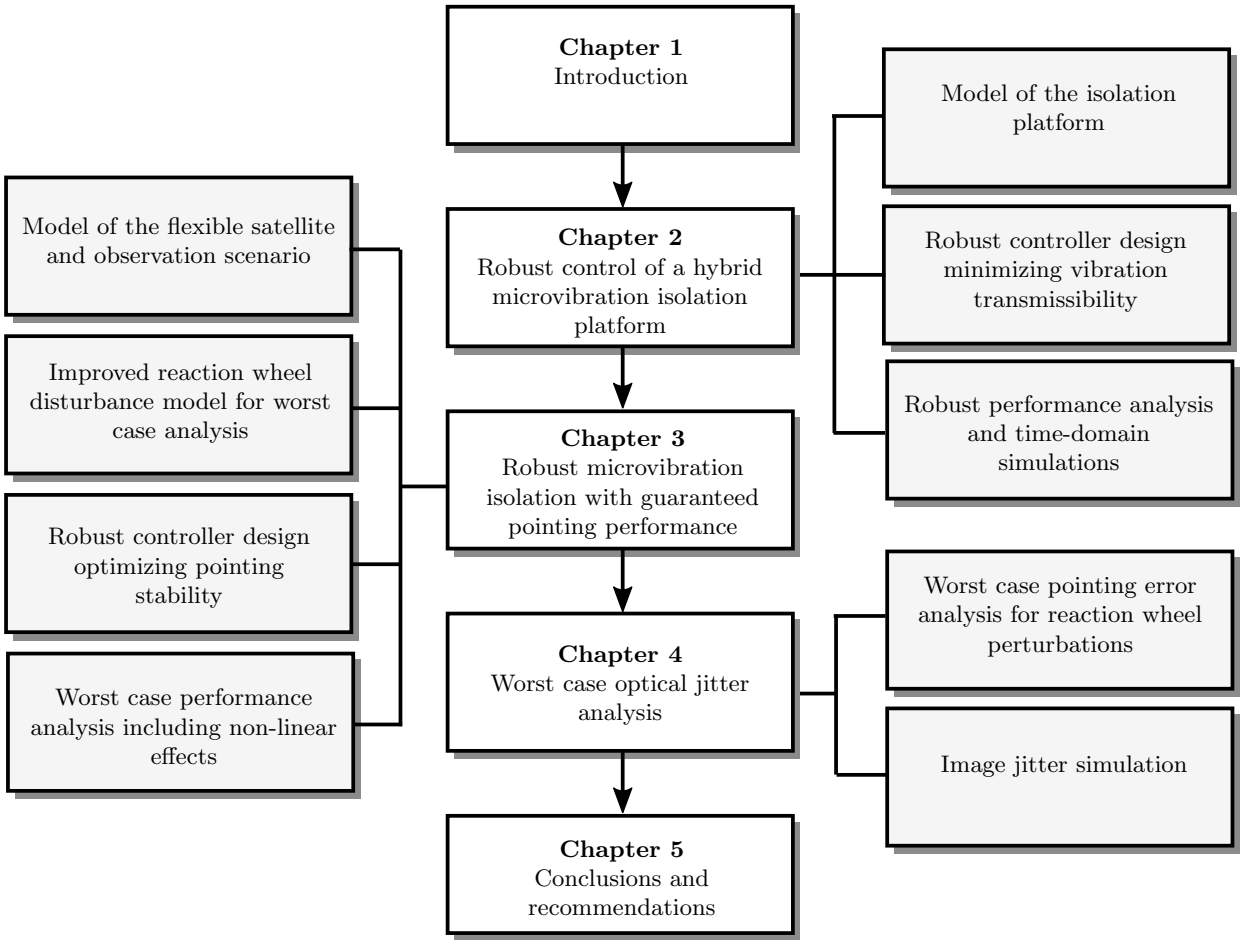


Figure 1.12: Overall structure of the thesis.

a framework to simulate the resulting image distortions based on the predicted geometry of the time-domain pointing error response.

Chapter 5 presents the main conclusions of the work performed together with recommendations for future research studies.

---

"*Somewhere, something incredible is waiting to be known.*"

Carl Sagan

# 2 Robust control of a hybrid microvibration isolation platform

## 2.1 Introduction

The previous chapter outlined the real industrial need to achieve significant microvibration isolation across the full operating range of a typical reaction wheel to meet rising pointing accuracy requirements demanded by future space observation missions. It was also shown how hybrid isolation systems can compensate for the limitations of a purely passive approach by means of an active control strategy at low frequencies. In particular, the mixed passive/active isolation platform developed by ESA and Airbus Defence and Space is outlined in section 1.1.3

Motivated by the previous research obtained using this hybrid isolation platform and the need to address the limitations of the initial design, the first objective of this chapter is to present an uncertain model of the platform that is based upon the physical equations of the system. The new model includes the dynamics of a spinning reaction supported by flexible bearings and captures the interactions between the sub-components with various uncertain parameters, in a unified way. Next, a vibration mitigation architecture is proposed and a systematic control design procedure is used to calibrate the active control solution. In order to push the system to the limits of achievable performance, the proposed controller is chosen to adapt based upon the current operating spin rate of the reaction wheel. Finally, a comprehensive robust analysis procedure based on the structured singular value $\mu$ is used to assess and certify the stability margin and robust performance of the proposed design. The frequency-dependent parametric sensitivity of the stability and performance indications is provided and used to identify the critical uncertain parameters and worst-case combinations. In this way, the classical use of expensive and time-consuming Monte Carlo campaigns can be avoided.

## 2.2 Main contributions and chapter organization

The chapter begins with section 2.3 that aims at deriving an uncertain model of the plant that is suitable for robust control synthesis and subsequent performance analysis. Section 2.4 is devoted to the aspects of synthesizing a robust controller. The various trade-offs and limitations of the synthesis procedures are highlighted. The resulting controller is thoroughly analyzed in section 2.5 by employing the structured singular value $\mu$ to assess the robust stability and robust performance of the closed-loop system. Time domain simulations based on a nonlinear high-fidelity industrial

simulator derived with the expertise of ESA and Airbus Defense & Space are included as a validation step. A summary and final concluding remarks are given in section 2.7.

## 2.3 Modeling the plant

The purpose of this section is to model the plant illustrated on fig. 2.1. The model represents an extension of the hybrid isolation that was previously described in section 1.1.3 and illustrated in fig. 1.10. More precisely, it is assumed that the dummy wheel used in previous studies was replaced by a spinning reaction wheel in cantilevered configuration that connects to the active plate using a flexible support.

Both parametric uncertainties and disturbances are taken into account. To this end, an uncertain nonlinear model of the plant is derived using the Lagrangian formalism and a Linear Fractional Transformation (LFT) model is extracted considering a Taylor expansion of each nonlinear terms.

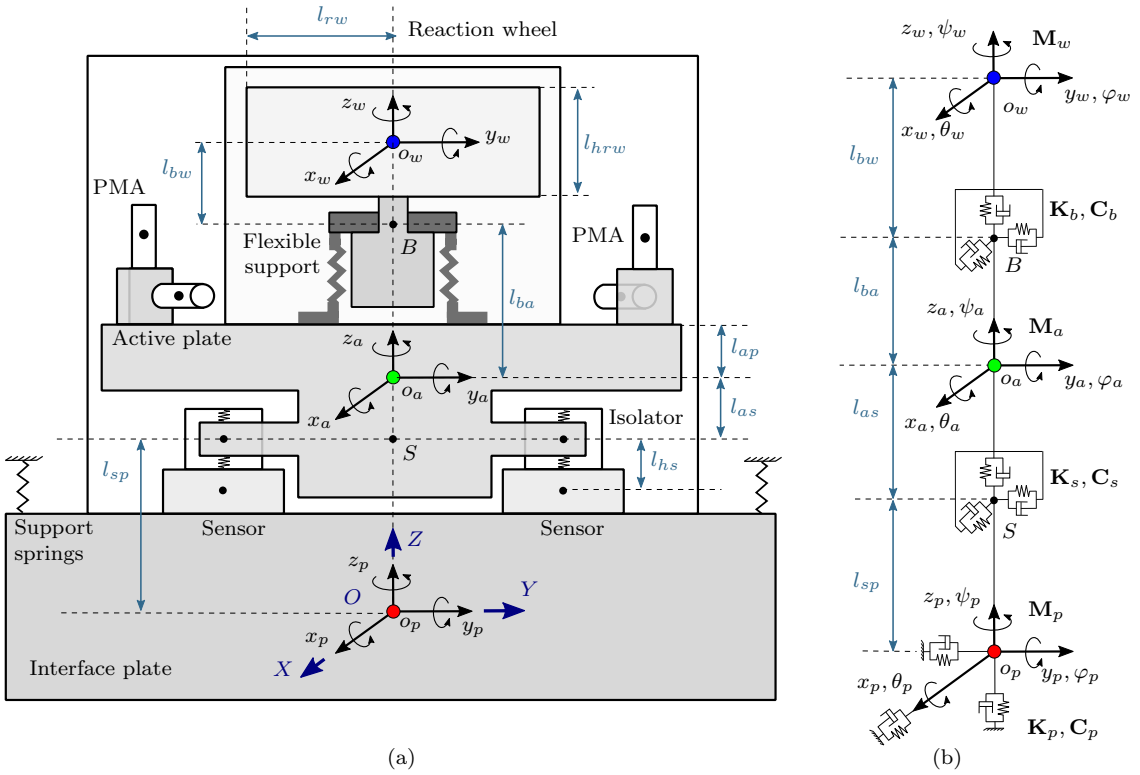


Figure 2.1: (a) Scaled illustration of the system setup with the various subcomponents (Note: only four of the six PMAs are illustrated here, while fig. 2.2 shows the locations and orientations of all six actuators). (b) Body frames, flexible connections and relative placements.

### 2.3.1 Coordinate system definitions

The dynamical model of the wheel is based on extensive works on this subject in [LLZ+13b, Kim14, ZAZ11, Mas02]. In this work, the reaction wheel is modeled as a rigid cylinder connected to the base structure through a massless shaft supported by a flexible connection. This cantilevered configuration allows the wheel to freely rotate along its shaft pointing axis while the elastic connection also allows for lateral and rocking motions of the wheel. Let $\mathcal{F}_w := (o_w; \vec{x}, \vec{y}, \vec{z})$ a body-fixed frame attached to the center of mass (CoM) of the flywheel with the $z$-axis aligned with the shaft axis

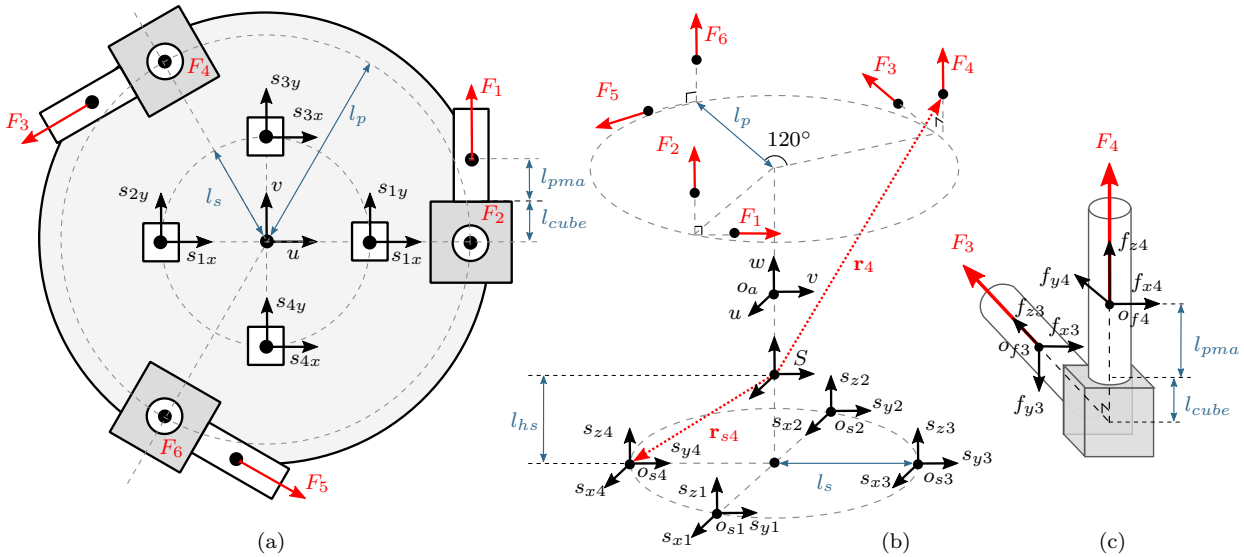


Figure 2.2: (a) Top view of actuator and sensor placement. (b) Schematic view of the reference frames (the vectors $\mathbf{r}_4$ and $\mathbf{r}_{s4}$ correspond to positions of the 4th actuator and force sensor). (c) One the three cubes with two proof-mass actuators attached.

as shown in fig. 2.1. The flywheel's displacements from the initial position are given in the inertial reference frame $\mathcal{F}_{world} := \left(O; \vec{X}, \vec{Y}, \vec{Z}\right)$ through the vector $\mathbf{q}_{wt} = \begin{bmatrix} x & y & z \end{bmatrix}^\mathsf{T}$. The wheel's body frame orientation with respect to the inertial frame is described using the y-x-z rotation sequence illustrated in fig. 2.3 and the angles $\mathbf{q}_{wr} = \begin{bmatrix} \theta_x & \theta_y & \theta_z \end{bmatrix}^\mathsf{T}$. The first one around the $Y$-axis ro-

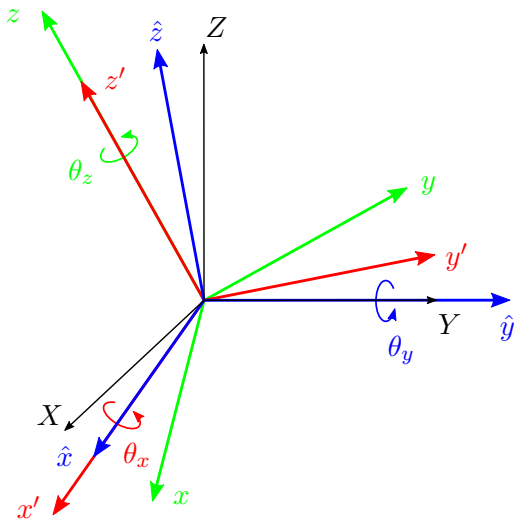


Figure 2.3: Definition of the Tait-Bryan angles and transformations from the inertial frame $XYZ$ to the reaction wheel body frame $xyz$ by means of a y-x-z rotation sequence.

tates the inertial reference frame into the intermediate frame $\hat{x}\hat{y}\hat{z}$. A subsequent rotation about the new $\hat{x}$-axis leads to the so-called rocking frame $\mathcal{F}_{wrock} := \left(o_w; \vec{x'}, \vec{y'}, \vec{z'}\right)$. This frame describes the rocking motion of wheel due to the elastic connection. A final rotation about the $z'$-axis by $\theta_z$ is used to capture the free spinning motion of the flywheel. The overall transformation matrix $\boldsymbol{\mathcal{R}}_w = \boldsymbol{\mathcal{R}}_{yxz}(\theta_x, \theta_y, \theta_z)$ from inertial to body frame is detailed in table 2.1.

In a similar fashion, both the interface and the active plate are free to translate and rotate in three dimensions. A body-fixed frame $\mathcal{F}_a := (o_a; \vec{u}, \vec{v}, \vec{w})$ is attached at the CoM of the active plate while

Table 2.1: Transformation matrices between the inertial frame and the reaction wheel body frame

| Inertial frame to body frame<br>Sequence: $XYZ \rightarrow \hat{x}\hat{y}\hat{z} \rightarrow x'y'z' \rightarrow xyz$ | | |
|---|---|---|
| From | To | Transformation matrix |
| $XYZ$ | $\hat{x}\hat{y}\hat{z}$ | $\boldsymbol{\mathcal{R}}_y(\theta_y) = \begin{bmatrix} \cos\theta_y & 0 & -\sin\theta_y \\ 0 & 1 & 0 \\ \sin\theta_y & 0 & \cos\theta_y \end{bmatrix}$ |
| $\hat{x}\hat{y}\hat{z}$ | $x'y'z'$ | $\boldsymbol{\mathcal{R}}_x(\theta_x) = \begin{bmatrix} 1 & 0 & 0 \\ 0 & \cos\theta_x & \sin\theta_x \\ 0 & -\sin\theta_x & \cos\theta_x \end{bmatrix}$ |
| $x'y'z'$ | $xyz$ | $\boldsymbol{\mathcal{R}}_z(\theta_z) = \begin{bmatrix} \cos\theta_z & \sin\theta_z & 0 \\ -\sin\theta_z & \cos\theta_z & 0 \\ 0 & 0 & 1 \end{bmatrix}$ |
| $XYZ$ | $xyz$ | $\boldsymbol{\mathcal{R}}_{yxz}(\theta_x, \theta_y, \theta_z) = \boldsymbol{\mathcal{R}}_z(\theta_z)\,\boldsymbol{\mathcal{R}}_x(\theta_x)\,\boldsymbol{\mathcal{R}}_y(\theta_y)$ |

Note: all the transformation matrices are orthonormal i.e. the inverse is equal to the transpose

the frame $\mathcal{F}_p := \left(o_p; \vec{a}, \vec{b}, \vec{c}\right)$ is fixed to the CoM of the interface plate, see fig. 2.1 for an illustration of these frames. The translational displacements from the equilibrium configuration of the two plates are specified in the inertial reference frame using the vectors $\mathbf{q}_{at} = \begin{bmatrix} u & v & w \end{bmatrix}^\mathsf{T}$ for the active plate and $\mathbf{q}_{pt} = \begin{bmatrix} a & b & c \end{bmatrix}^\mathsf{T}$ for the interface plate. The orientations are described as for the reaction wheel, by the Euler angles $\mathbf{q}_{ar} = \begin{bmatrix} \theta_u & \theta_v & \theta_w \end{bmatrix}^\mathsf{T}$ and y-x-z rotation matrix $\boldsymbol{\mathcal{R}}_a = \boldsymbol{\mathcal{R}}_{yxz}(\theta_u, \theta_v, \theta_w)$ for the active plate and $\mathbf{q}_{pr} = \begin{bmatrix} \theta_a & \theta_b & \theta_c \end{bmatrix}^\mathsf{T}$ and $\boldsymbol{\mathcal{R}}_p = \boldsymbol{\mathcal{R}}_{yxz}(\theta_a, \theta_b, \theta_c)$ for the interface plate. The total vector of generalized coordinates $\mathbf{q}$ of the mechanical system can thus be written as:

$$\mathbf{q} = \begin{bmatrix} \mathbf{q}_p^\mathsf{T} & \mathbf{q}_a^\mathsf{T} & \mathbf{q}_w^\mathsf{T} \end{bmatrix}^\mathsf{T} \in \mathbb{R}^{18} \quad \text{with} \quad \begin{aligned} \mathbf{q}_w &= \begin{bmatrix} \mathbf{q}_{wt}^\mathsf{T} & | & \mathbf{q}_{wr}^\mathsf{T} \end{bmatrix}^\mathsf{T} = \begin{bmatrix} x & y & z & | & \theta_x & \theta_y & \theta_z \end{bmatrix}^\mathsf{T} \\ \mathbf{q}_a &= \begin{bmatrix} \mathbf{q}_{at}^\mathsf{T} & | & \mathbf{q}_{ar}^\mathsf{T} \end{bmatrix}^\mathsf{T} = \begin{bmatrix} u & v & w & | & \theta_u & \theta_v & \theta_w \end{bmatrix}^\mathsf{T} \\ \mathbf{q}_p &= \begin{bmatrix} \mathbf{q}_{pt}^\mathsf{T} & | & \mathbf{q}_{pr}^\mathsf{T} \end{bmatrix}^\mathsf{T} = \begin{bmatrix} a & b & c & | & \theta_a & \theta_b & \theta_c \end{bmatrix}^\mathsf{T} \end{aligned} \tag{2.1}$$

The flexible support connecting the reaction wheel to the active plate is modeled as a single six DoF elastic connection (point $B$ in fig. 2.1) located at

$$\begin{aligned} \mathbf{r}_{wb} &= \begin{bmatrix} 0 & 0 & -l_{bw} \end{bmatrix}^\mathsf{T} \text{ in the wheel's frame } \mathcal{F}_w \text{ and} \\ \mathbf{r}_{ab} &= \begin{bmatrix} 0 & 0 & l_{ba} \end{bmatrix}^\mathsf{T} \text{ in the active plate frame } \mathcal{F}_a \end{aligned} \tag{2.2}$$

where the nominal offsets $l_{bw}$ and $l_{ba}$ are given in table 2.3. Similarly, the elasticity of the passive isolators connecting the active and interface plates is also modeled as a six DoF elastic joint (point $S$ in fig. 2.1) with coordinates

$$\begin{aligned} \mathbf{r}_{as} &= \begin{bmatrix} 0 & 0 & -l_{as} \end{bmatrix}^\mathsf{T} \text{ in the active plate frame } \mathcal{F}_a \text{ and} \\ \mathbf{r}_{ps} &= \begin{bmatrix} 0 & 0 & l_{sp} \end{bmatrix}^\mathsf{T} \text{ in the interface plate frame } \mathcal{F}_p \end{aligned} \tag{2.3}$$

### 2.3.2 Reaction wheel microvibrations

For the considered mission, the reaction wheel's time-varying spin rate $\Omega(t)$ and acceleration $\dot{\Omega}(t)$ are assumed to be bounded with:

$$\Omega(t) \in \boldsymbol{\Omega} = [10, 50] \text{ Hz (rev/s)} \quad \text{and} \quad |\dot{\Omega}(t)| \leq \dot{\Omega}_{max} = 0.01 \text{ Hz/s (rev/s}^2\text{)} \quad \forall t \geq 0 \tag{2.4}$$

**Remark 1.** *Throughout this study, $\Omega$ will also sometimes refer to a frequency value and therefore the preferred unit of measure for the wheel spin rate and acceleration will be* Hz *and* Hz/s.

As explained in the previous chapter, the unavoidable mass imbalances in the flywheel give rise to a dominant harmonic disturbance centered at the same frequency $\Omega$ as the spin rate of the flywheel. To understand the cause, the static and dynamic imbalances of the flywheel are first modeled as additional small masses $m_s$ and $m_d$ fixed to the wheel's body frame $\mathcal{F}_w$ as shown in figs. 2.1 and 2.4. Typically, the mass of these imbalances is several orders of magnitude smaller than that of the balanced flywheel. Therefore, these imbalances don't cause a significant shift of the center of mass and the principal axis of inertia when attached to the balanced wheel. In effort to extract a simple model of the system, the contribution of the mass imbalances to the kinetic energy of the system (2.12) is only as an additional mass added within the total wheel mass $m_w$. Their effect on the dynamics of the system is approximated as additional external forces $\mathbf{F}_1 = \begin{bmatrix} F_1^x & F_1^y \end{bmatrix}^\mathsf{T}$ and torques $\mathbf{T}_1 = \begin{bmatrix} T_1^x & T_1^y \end{bmatrix}^\mathsf{T}$ that are applied to the wheel's rocking frame $\mathcal{F}_{wrock} := \left(o_w; \vec{x'}, \vec{y'}, \vec{z'}\right)$ and rotate with the same instantaneous angular spin rate $\Omega$ as the flywheel. The magnitude of these forces and torques is speed dependent with $|\mathbf{F}_1| = U_s\Omega^2$ and $|\mathbf{T}_1| = U_d\Omega^2$ where $U_s = m_s l_{rw}$, $U_d = m_d l_{rw} l_{hrw}$ and $l_{rw}, l_{hrw}$ are the wheel radius and height visible in fig. 2.1. Additionally, the relative phasing between these vectors depends on the angular separation $\varphi$ between the two planes containing $m_s$ and $m_d$ as shown in fig. 2.4. Typically, a simplifying assumption is made that the mass imbalances are coplanar i.e. $\varphi = 0$ and the vectors $\mathbf{F}_1$ and $\mathbf{T}_1$ are perpendicular. With the previous considerations, the components of these disturbance vectors are given by for a constant spin rate $\Omega$ by

$$\mathbf{F}_1(t) = \begin{bmatrix} F_1^x(t) \\ F_1^y(t) \end{bmatrix} = \begin{bmatrix} U_s\Omega^2 \sin(\Omega t + \phi) \\ U_s\Omega^2 \cos(\Omega t + \phi) \end{bmatrix} \quad \text{and} \quad \mathbf{T}_1(t) = \begin{bmatrix} T_1^x(t) \\ T_1^y(t) \end{bmatrix} = \begin{bmatrix} -U_d\Omega^2 \cos(\Omega t + \phi) \\ U_d\Omega^2 \sin(\Omega t + \phi) \end{bmatrix} \tag{2.5}$$

where $\psi$ is a random phase angle. In addition to the mass imbalance disturbances, the wheel can

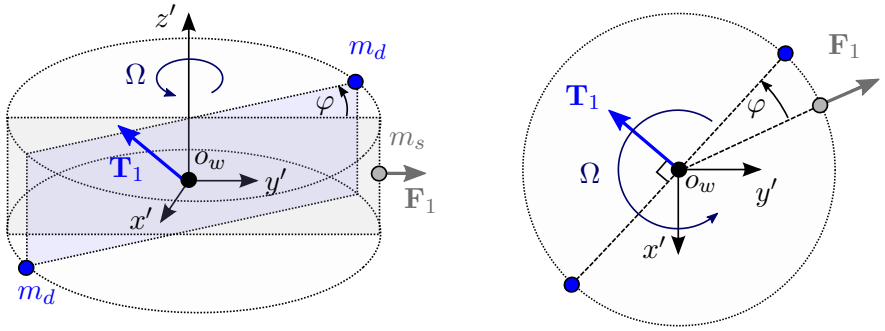


Figure 2.4: Phase relationship between the harmonic forces and torques due to the mass imbalances.

also generate other harmonics at integer or non-integer multiples of the fundamental frequency $\Omega$ as well as broadband noise [Add17, TO03, LMB08, LYH12, Kim14]. These additional perturbations are caused among other things by irregularities, lubrication and friction in the ball bearings and motor drive operation. Experimental studies given in [GMGB14, Kim14] also show that some wheels can even generate axial forces along the $z$-axis. With the prior considerations, the extended excitation vector $\mathbf{u}_w$ that combines all the forces and torques acting on the flywheel can be expressed in the wheel's rocking frame $\mathcal{F}_{wrock}$ as:

$$\begin{aligned} \mathbf{u}_w &= \begin{bmatrix} \mathbf{f}_w^\mathsf{T} & | & \mathbf{t}_w^\mathsf{T} \end{bmatrix}^\mathsf{T} = \begin{bmatrix} F_x & F_y & F_z & | & T_x & T_y & T_z \end{bmatrix}^\mathsf{T} \\ &= \begin{bmatrix} \mathbf{0}_{1\times 5} & T_m \end{bmatrix}^\mathsf{T} + \underbrace{\begin{bmatrix} F_{xbn} & F_{ybn} & F_{zbn} & | & T_{xbn} & T_{ybn} & T_{zbn} \end{bmatrix}^\mathsf{T}}_{\mathbf{u}_{bn}} + \sum_{i=1}^{N} \underbrace{\begin{bmatrix} F_i^x & F_i^y & F_i^z & | & T_i^x & T_i^y & 0 \end{bmatrix}^\mathsf{T}}_{\mathbf{u}_i} \end{aligned} \tag{2.6}$$

where $T_m$ represents the control torque supplied by the motor, $\mathbf{u}_{bn}$ is the stochastic broadband noise and $\mathbf{u}_i$ is the $i$-th out of a total of $N$ harmonic disturbances with

$$\begin{bmatrix} F_i^x(t) \\ F_i^y(t) \\ F_i^z(t) \end{bmatrix} = \begin{bmatrix} a_i^f \Omega^2 \sin\left(h_i \Omega t + \phi_i^f\right) \\ a_i^f \Omega^2 \cos\left(h_i \Omega t + \phi_i^f\right) \\ a_i^{fz} \Omega^2 \cos\left(h_i \Omega t + \phi_i^{fz}\right) \end{bmatrix} \quad \begin{bmatrix} T_i^x(t) \\ T_i^y(t) \end{bmatrix} = \begin{bmatrix} -a_i^t \Omega^2 \cos\left(h_i \Omega t + \phi_i^t\right) \\ a_i^t \Omega^2 \sin\left(h_i \Omega t + \phi_i^t\right) \end{bmatrix} \tag{2.7}$$

where $h_i$ is the harmonic number (in the case of the main harmonic $h_1 = 1$), $a_i^f$, $a_i^t$, $a_i^{fz}$ are harmonic amplitude coefficients and $\phi_i^f$, $\phi_i^t$, $\phi_i^{fz}$ are random phase angles. For the main harmonic disturbance generated by coplanar mass imbalances, the following relationships hold:

$$a_1^f = U_s = m_s l_{rw} \quad ; \quad a_1^t = U_d = m_d l_{rw} l_{hrw} \quad ; \quad \phi_1^f = \phi_1^t \tag{2.8}$$

Both the harmonic coefficients $a_i^f$, $a_i^t$, $a_i^{fz}$, $\phi_i^f$, $\phi_i^t$, $\phi_i^{fz}$ and a stochastic model for the broadband noise $\mathbf{u}_{bn}$ can be estimated from experimental data [Mas99, LKM+07, LMB08, Kim14]. With this in mind and for the considering wheel harmonics given in table 2.3, the spectrogram of the reaction wheel's axial force disturbance $F_x$ is shown in fig. 2.5 for a linear variation of the spin rate within $\Omega \in [10, 50]$ Hz over a 8 min period. The peaks corresponding to each of the 4 harmonics are clearly visible and highlighted in the figure.

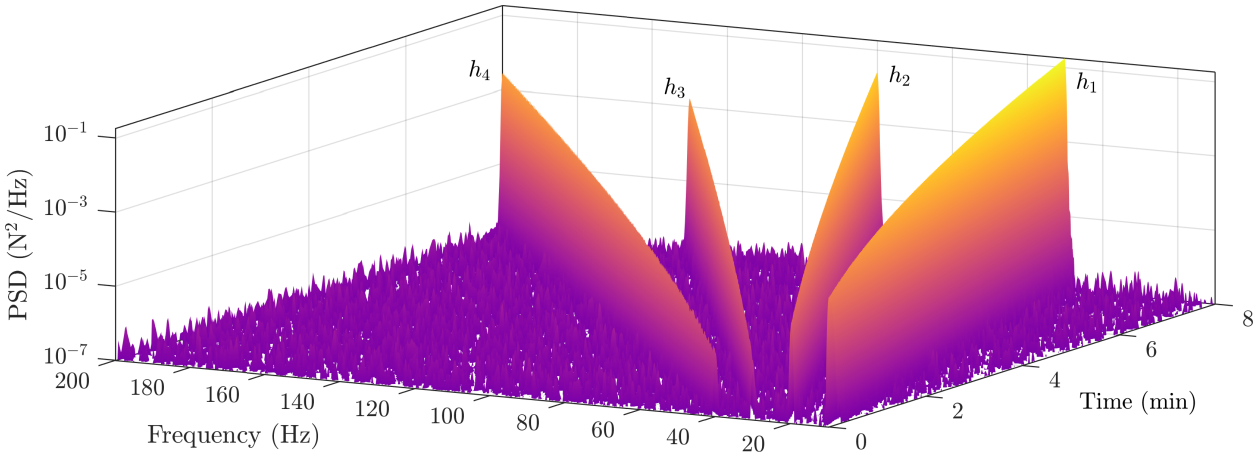


Figure 2.5: Spectrogram of the reaction wheel's axial force disturbance $F_x$ for a linear variation of the spin rate within $\Omega \in [10, 50]$ Hz over a 8 min period (Note: only the four dominant harmonic components $(h_1, \ldots, h_4)$ have been included in the model while in reality the number of harmonics can be much higher).

### 2.3.3 Equations of motion using Lagrangian formalism

The dynamics of the overall setup with generalized coordinates $\mathbf{q}$ is completely described using energy principles from classical mechanics by the following set of Lagrange equation:

$$\begin{aligned} \frac{d}{dt}\left(\frac{\partial \boldsymbol{\mathcal{L}}_{total}(\mathbf{q}, \dot{\mathbf{q}})}{\partial \dot{\mathbf{q}}}\right) - \frac{\partial \boldsymbol{\mathcal{L}}_{total}(\mathbf{q}, \dot{\mathbf{q}})}{\partial \mathbf{q}} + \frac{\partial \boldsymbol{\mathcal{D}}_{dissipative}(\dot{\mathbf{q}})}{\partial \dot{\mathbf{q}}} &= \boldsymbol{\mathcal{Q}}(\mathbf{q}, \dot{\mathbf{q}}) \\ \boldsymbol{\mathcal{L}}_{total}(\mathbf{q}, \dot{\mathbf{q}}) &= \boldsymbol{\mathcal{T}}_{kinetic}(\mathbf{q}, \dot{\mathbf{q}}) - \boldsymbol{\mathcal{V}}_{potential}(\mathbf{q}) \end{aligned} \tag{2.9}$$

where $\dot{\mathbf{q}}$ represents the first derivative of the generalized coordinate with respect to time $t$, $\boldsymbol{\mathcal{L}}_{total}$ is the Lagrangian, $\boldsymbol{\mathcal{T}}_{kinetic}$ the total kinetic energy, $\boldsymbol{\mathcal{V}}_{potential}$ the potential energy, $\boldsymbol{\mathcal{D}}_{dissipative}$ the dissipative function and $\boldsymbol{\mathcal{Q}}$ the vector of external generalized forces.

### Kinetic energy

The total kinetic energy $\mathcal{T}_{kinetic}$ is the sum of the translational and the rotational of the flywheel, active plate and interface plate. With reference to figs. 2.1 and 2.3, the angular velocity vector of the reaction wheel $\boldsymbol{\omega}_w$ is equal to the sum of the angular velocity $\dot{\theta}_y$ about the $Y$-axis, $\dot{\theta}_x$ about the $\hat{x}$-axis and $\dot{\theta}_z$ about the $z'$-axis. Employing the transformation matrices defined in table 2.1, the angular velocity vector in the body frame can be written as

$$\begin{aligned}\boldsymbol{\omega}_w &= \begin{bmatrix}0\\0\\\Omega\end{bmatrix} + \boldsymbol{\mathcal{R}}_z(\theta_z)\begin{bmatrix}\dot{\theta}_x\\0\\0\end{bmatrix} + \boldsymbol{\mathcal{R}}_z(\theta_z)\boldsymbol{\mathcal{R}}_x(\theta_x)\begin{bmatrix}0\\\dot{\theta}_y\\0\end{bmatrix} = \begin{bmatrix}\dot{\theta}_x\cos\theta_z + \dot{\theta}_y\cos\theta_x\sin\theta_z\\ \dot{\theta}_y\cos\theta_x\cos\theta_z - \dot{\theta}_x\sin\theta_z\\ \Omega - \dot{\theta}_y\sin\theta_x\end{bmatrix}\\ &= \underbrace{\begin{bmatrix}\cos\theta_z & \cos\theta_x\sin\theta_z & 0\\ -\sin\theta_z & \cos\theta_x\cos\theta_z & 0\\ 0 & -\sin\theta_x & 1\end{bmatrix}}_{\boldsymbol{\mathcal{W}}(\theta_x,\theta_y,\theta_z)}\underbrace{\begin{bmatrix}\dot{\theta}_x\\\dot{\theta}_y\\\Omega\end{bmatrix}}_{\dot{\mathbf{q}}_{wr}} \qquad \text{where } \Omega = \dot{\theta}_z \text{ denotes the wheel spin rate}\end{aligned} \tag{2.10}$$

As previosuly mentioned, the orientations of the two plates is described using the same rotational sequence as for the flywheel. Therefore, the angular velocities of the active plate $\boldsymbol{\omega}_a$ and of the interface plate $\boldsymbol{\omega}_p$ in the respective body frames are equal to

$$\boldsymbol{\omega}_a = \boldsymbol{\mathcal{W}}(\theta_u,\theta_v,\theta_w)\,\dot{\mathbf{q}}_{ar} \qquad \text{and} \qquad \boldsymbol{\omega}_p = \boldsymbol{\mathcal{W}}(\theta_a,\theta_b,\theta_c)\,\dot{\mathbf{q}}_{pr} \tag{2.11}$$

It is now possible to write the total kinetic energy of the system as

$$\begin{aligned}\mathcal{T}_{kinetic}(\mathbf{q},\dot{\mathbf{q}}) &= \frac{1}{2}\Bigg(\underbrace{m_w\dot{\mathbf{q}}_{wt}^{\mathsf{T}}\dot{\mathbf{q}}_{wt} + \boldsymbol{\omega}_w^{\mathsf{T}}\mathbf{J}_w\boldsymbol{\omega}_w}_{\text{Reaction wheel}} + \underbrace{m_a\dot{\mathbf{q}}_{at}^{\mathsf{T}}\dot{\mathbf{q}}_{at} + \boldsymbol{\omega}_a^{\mathsf{T}}\mathbf{J}_a\boldsymbol{\omega}_a}_{\text{Active plate}} + \underbrace{m_p\dot{\mathbf{q}}_{pt}^{\mathsf{T}}\dot{\mathbf{q}}_{pt} + \boldsymbol{\omega}_p^{\mathsf{T}}\mathbf{J}_p\boldsymbol{\omega}_p}_{\text{Interface plate}}\Bigg)\\ &= \frac{1}{2}\dot{\mathbf{q}}^{\mathsf{T}}\boldsymbol{\mathcal{M}}(\mathbf{q},\dot{\mathbf{q}})\,\dot{\mathbf{q}}\end{aligned} \tag{2.12}$$

where $\boldsymbol{\mathcal{M}}$ is the generalized mass matrix, $m_w$, $m_a$ and $m_p$ are the masses of the flywheel, active and interface plate respectively while $\mathbf{J}_w$, $\mathbf{J}_a$, $\mathbf{J}_p$ denote the corresponding body frame inertia tensors. Taking into account the rotational symmetries of each object, these tensors are given by

$$\mathbf{J}_w = \operatorname{diag}\begin{pmatrix}J_{rr} & J_{rr} & J_{zz}\end{pmatrix} \quad \mathbf{J}_a = \operatorname{diag}\begin{pmatrix}J_{uu} & J_{vv} & J_{ww}\end{pmatrix} \quad \mathbf{J}_p = \operatorname{diag}\begin{pmatrix}J_{aa} & J_{bb} & J_{cc}\end{pmatrix} \tag{2.13}$$

**Remark 2.** *The inertial properties of the active plate given by $m_a$ and $\mathbf{J}_a$ and center of mass location are calculated with the assumption that the proof mass actuators are rigidly connected to the plate and part of same composite object.*

### Potential energy and disipations

The potential energy of the system is stored as elastic energy in the flexible wheel support, elastomer isolators and the springs supporting the interface plate. Similarly, damping also occurs within these interconnecting elements. To calculate the potential energy $\mathcal{V}_{potential}$ and the dissipation $\boldsymbol{\mathcal{D}}_{dissipative}$, it is necessary to first calculate the relative displacements and relative velocities between the system components. It can be safely assumed, in the context of microvibration applications, that except for the wheel angle $\theta_z$, the angular displacements are of small magnitude [LJDL15, ZAZ11, LLZ13a]. Considering the relative offsets (2.2), the linearized displacements $\mathbf{q}_{\Delta b}$ occurring at the elastic connection between the flywheel and the active plate can be written in the inertial frame as:

$$\begin{aligned}\mathbf{q}_{\Delta b} &= (\mathbf{q}_{wt} + \mathbf{r}_{wb}\times\mathbf{q}_{wr}) - (\mathbf{q}_{at} + \mathbf{r}_{ab}\times\mathbf{q}_{ar})\\ &= \boldsymbol{\mathcal{T}}(\mathbf{r}_{wb})\mathbf{q}_w - \boldsymbol{\mathcal{T}}(\mathbf{r}_{ab})\mathbf{q}_a\end{aligned} \tag{2.14}$$

$$\text{where} \quad \boldsymbol{\mathcal{T}}(\mathbf{r}) = \begin{bmatrix} \mathbf{I}_3 & [\mathbf{r}]_\times \\ \mathbf{0}_3 & \mathbf{I}_3 \end{bmatrix} \quad \text{and} \quad [\mathbf{r}]_\times = \begin{bmatrix} 0 & -z & y \\ z & 0 & -x \\ -y & x & 0 \end{bmatrix} \quad \text{for} \quad \mathbf{r} = \begin{bmatrix} x \\ y \\ z \end{bmatrix} \tag{2.15}$$

Similarly, for the passive isolators connecting the active and interface plates, the extension of elastic connection is equal to:

$$\mathbf{q}_{\Delta s} = \boldsymbol{\mathcal{T}}(\mathbf{r}_{as})\mathbf{q}_a - \boldsymbol{\mathcal{T}}(\mathbf{r}_{ps})\mathbf{q}_p \tag{2.16}$$

For clarity, these elastic extensions for small rotations are shown in fig. 2.6. Lastly, it is assumed

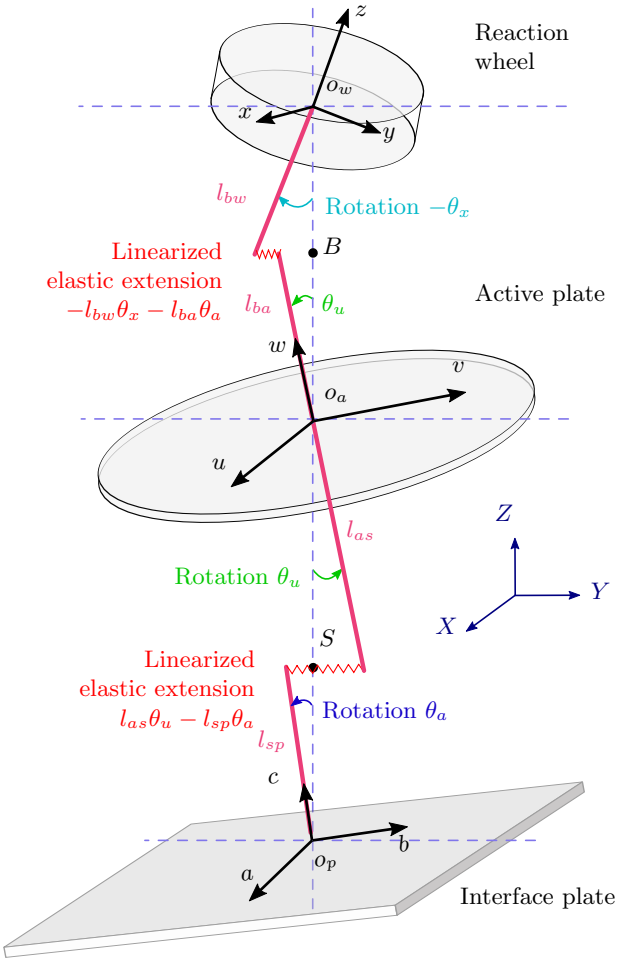


Figure 2.6: Example of linearized extensions of the elastic connections in the inertial reference caused by small rotations.

that the elastic energy due to the suspension springs of the interface plate depends only on the plate's generalized displacement vector $\mathbf{q}_p$. Additionally, classical damping is assumed for all the elastic connections. With this previous consideration, the potential energy $\boldsymbol{\mathcal{V}}_{potential}(\mathbf{q})$ and the dissipation function $\boldsymbol{\mathcal{D}}_{dissipative}(\dot{\mathbf{q}})$ of the system can be written as

$$\begin{aligned} \boldsymbol{\mathcal{V}}_{potential}(\mathbf{q}) &= \frac{1}{2}\left(\mathbf{q}_{\Delta b}^\mathsf{T}\mathbf{K}_b\mathbf{q}_{\Delta b} + \mathbf{q}_{\Delta s}^\mathsf{T}\mathbf{K}_s\mathbf{q}_{\Delta s} + \mathbf{q}_p^\mathsf{T}\mathbf{K}_p\mathbf{q}_p\right) = \mathbf{q}^\mathsf{T}\left(\boldsymbol{\Upsilon}^\mathsf{T}\mathbf{K}\boldsymbol{\Upsilon}\right)\mathbf{q} \\ \boldsymbol{\mathcal{D}}_{dissipative}(\dot{\mathbf{q}}) &= \frac{1}{2}\left(\dot{\mathbf{q}}_{\Delta b}^\mathsf{T}\mathbf{C}_b\dot{\mathbf{q}}_{\Delta b} + \dot{\mathbf{q}}_{\Delta s}^\mathsf{T}\mathbf{C}_s\dot{\mathbf{q}}_{\Delta s} + \dot{\mathbf{q}}_p^\mathsf{T}\mathbf{C}_p\dot{\mathbf{q}}_p\right) = \dot{\mathbf{q}}^\mathsf{T}\left(\boldsymbol{\Upsilon}^\mathsf{T}\mathbf{C}\boldsymbol{\Upsilon}\right)\dot{\mathbf{q}} \end{aligned} \tag{2.17}$$

where $\mathbf{K}_b, \mathbf{K}_s, \mathbf{K}_p$ are the stiffness matrices and $\mathbf{C}_b, \mathbf{C}_s, \mathbf{C}_p$ are the damping matrices given by (the numerical values of the elements of these matrices are listed in table 2.3):

$$\begin{aligned}
\mathbf{K}_b &= \operatorname{diag}\begin{pmatrix} k_x & k_y & k_z & k_{\theta x} & k_{\theta y} & 0 \end{pmatrix} & \mathbf{C}_b &= \operatorname{diag}\begin{pmatrix} c_x & c_y & c_z & c_{\theta x} & c_{\theta y} & 0 \end{pmatrix} \\
\mathbf{K}_s &= \operatorname{diag}\begin{pmatrix} k_u & k_v & k_w & k_{\theta u} & k_{\theta v} & k_{\theta w} \end{pmatrix} & \mathbf{C}_s &= \operatorname{diag}\begin{pmatrix} c_u & c_v & c_w & c_{\theta u} & c_{\theta v} & c_{\theta w} \end{pmatrix} \\
\mathbf{K}_p &= \operatorname{diag}\begin{pmatrix} k_a & k_b & k_c & k_{\theta a} & k_{\theta b} & k_{\theta c} \end{pmatrix} & \mathbf{C}_p &= \operatorname{diag}\begin{pmatrix} c_a & c_b & c_c & c_{\theta a} & c_{\theta b} & c_{\theta c} \end{pmatrix}
\end{aligned} \tag{2.18}$$

$$\text{and} \quad \begin{aligned} \boldsymbol{\mathcal{K}} &= \operatorname{diag}\begin{pmatrix} \mathbf{K}_p & \mathbf{K}_s & \mathbf{K}_b \end{pmatrix} \\ \boldsymbol{\mathcal{C}} &= \operatorname{diag}\begin{pmatrix} \mathbf{C}_p & \mathbf{C}_s & \mathbf{C}_b \end{pmatrix} \end{aligned} ; \qquad \boldsymbol{\Upsilon} = \begin{bmatrix} \mathbf{I}_6 & \mathbf{0}_6 & \mathbf{0}_6 \\ -\boldsymbol{\mathcal{T}}(\mathbf{r}_{ps}) & \boldsymbol{\mathcal{T}}(\mathbf{r}_{as}) & \mathbf{0}_6 \\ \mathbf{0}_6 & -\boldsymbol{\mathcal{T}}(\mathbf{r}_{ab}) & \boldsymbol{\mathcal{T}}(\mathbf{r}_{wb}) \end{bmatrix} \tag{2.19}$$

Note that, the matrices $\mathbf{K}_b, \mathbf{C}_b$ have the elements connecting the axial rotations $\theta_x, \theta_w$ and velocities $\dot{\theta}_x, \dot{\theta}_w$ null due to the fact that the flywheel is considered free to rotate without friction or elastic forces along its $z$-axis. The matrices $\mathbf{K}_s, \mathbf{C}_s$ depend on the physical characteristics and topology of the passive isolators and can be identified experimentally up to a certain accuracy. For example, consider the $k_{\theta u}$ parameter associated with the rotational stiffness of the joint and assume that each of the four passive isolators (arranged as shown in figs. 2.1 and 2.2) behaves like a linear spring with stiffness $\frac{k}{4}$. A virtual rotation of angle $\delta$ between the active and interface plates as seen in fig. 2.7 would produce a corresponding extension of the two springs by a factor of $l_s\delta$. This in turn would generate two elastic forces $F_\delta = l_s\frac{k}{4}\delta$ that give rise to a total torque $T_\delta = 2l_sF_\delta = l_s^2\frac{k}{2}\delta = k_{\theta_u}\delta$ applied to both plates. The vector $\mathbf{y}_s$ of elastic forces $\mathbf{f}_s = \begin{bmatrix} F_{su} & F_{sv} & F_{sw} \end{bmatrix}^\mathsf{T}$ and torques

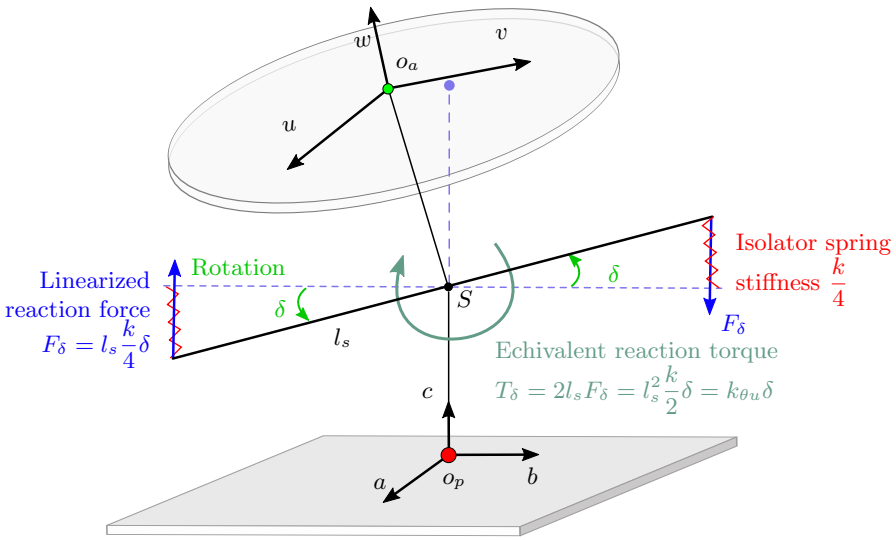


Figure 2.7: Derivation of the rotational stiffness $k_{\theta u}$ for the passive isolators by considering small virtual rotational displacements.

$\mathbf{t}_s = \begin{bmatrix} T_{su} & T_{sv} & T_{sw} \end{bmatrix}^\mathsf{T}$ between the active plate and the interface plate, results from (2.17) and has the following expression in the inertial frame

$$\mathbf{y}_s = \begin{bmatrix} \mathbf{f}_s^\mathsf{T} & | & \mathbf{t}_s^\mathsf{T} \end{bmatrix}^\mathsf{T} = \begin{bmatrix} F_{su} & F_{sv} & F_{sw} & | & T_{su} & T_{sv} & T_{sw} \end{bmatrix}^\mathsf{T} = \mathbf{K}_s\mathbf{q}_{\Delta s} + \mathbf{C}_s\dot{\mathbf{q}}_{\Delta s} \tag{2.20}$$

$$= \boldsymbol{\mathcal{S}}\left(\boldsymbol{\mathcal{K}}\boldsymbol{\Upsilon}\,\mathbf{q} + \boldsymbol{\mathcal{C}}\boldsymbol{\Upsilon}\,\dot{\mathbf{q}}\right) \tag{2.21}$$

where $\boldsymbol{\mathcal{S}} = \begin{bmatrix} \mathbf{0}_6 & \mathbf{I}_6 & \mathbf{0}_6 \end{bmatrix}$ is a selection matrix. The purpose of the control architecture will be to reconstruct this vector using the noisy sensor measurements and generate an appropriate control signal to significantly attenuate each component of $\mathbf{y}_s$ in the presence of external disturbances. This will be discussed in detail in the following sections.

### External forces

It is now necessary to determine each component of the vector $\boldsymbol{\mathcal{Q}}(\mathbf{q}, \dot{\mathbf{q}})$ of external generalized forces in (2.9). To do this, it is first noted that the external forces and torques acting on the system are due to disturbances generated by the spinning reaction wheel, the actuator forces and the torque applied by the motor.

As explained in (2.6), the vector $\mathbf{u}_w = \begin{bmatrix} F_x & F_y & F_z & | & T_x & T_y & T_z \end{bmatrix}^\mathsf{T}$ of reaction wheel forces and torques is applied directly to the CoM of the flywheel. The $T_z$ component combining the motor torque as well as the torque ripple disturbance is applied with equal magnitude but opposite directions to the flywheel and the active plate bodies. The main harmonic is the focus of this chapter and the additional disturbances are all lumped into a stochastic broadband disturbance $\mathbf{u}_{bn}$ without explicitly modeling their sources physically.

In the case of the six actuators, each one generates an axial force along the direction they are mounted on to active plate (see fig. 2.2). However, in order to derive the structural dynamics of the overall system, the actual topology of the actuators will be considered in a later section of this chapter. For now, it is assumed that the combined actuators can directly apply the following overall force $\mathbf{f}_{as} = \begin{bmatrix} F_{asu} & F_{asv} & F_{asw} \end{bmatrix}^\mathsf{T}$ and torque vector $\mathbf{t}_{as} = \begin{bmatrix} T_{asu} & T_{asv} & T_{asw} \end{bmatrix}^\mathsf{T}$ to the active plate at the passive isolator elastic connection $S$:

$$\mathbf{u}_s = \begin{bmatrix} \mathbf{f}_{as}^\mathsf{T} & | & \mathbf{t}_{as}^\mathsf{T} \end{bmatrix}^\mathsf{T} = \begin{bmatrix} F_{asu} & F_{asv} & F_{asw} & | & T_{asu} & T_{asv} & T_{asw} \end{bmatrix}^\mathsf{T} \tag{2.22}$$

In this way, both the actuator inputs $\mathbf{u}_s$ and the ouputs $\mathbf{y}_s$ are defined in the same frame and are said to be collocated.

Let $F_k$ represent the $k$-th external forces applied at the position $\mathbf{r}_k(\mathbf{q})$ of the system where $\mathbf{q}$ is the generalized coordinate vector as defined in (2.1). Using the principle of virtual work from Lagrangian mechanics, the generalized force vector $\boldsymbol{\mathcal{Q}}(\mathbf{q}) \in \mathbb{R}^{18}$ can be calculated as follows

$$\boldsymbol{\mathcal{Q}}(\mathbf{q}) = \begin{bmatrix} \mathcal{Q}_1(\mathbf{q}) & \dots & \mathcal{Q}_{18}(\mathbf{q}) \end{bmatrix}^\mathsf{T} \quad \text{with} \quad \mathcal{Q}_i(\mathbf{q}) = \sum_k F_k \cdot \frac{\partial \mathbf{r}_k(\mathbf{q})}{\partial q_i} \quad ; \quad i = \{1, \dots, 18\} \tag{2.23}$$

where $q_i$ represents the $i$-th generalized coordinate.

### Linearized equations of motion

Using (2.12), (2.17) and (2.23), the Lagrange equations (2.9) can be written as:

$$\boldsymbol{\mathcal{M}}(\mathbf{q}, \dot{\mathbf{q}})\, \ddot{\mathbf{q}} + \left( \boldsymbol{\mathcal{G}}(\mathbf{q}, \dot{\mathbf{q}}) + \boldsymbol{\Upsilon}^\mathsf{T} \boldsymbol{\mathcal{C}} \boldsymbol{\Upsilon} \right) \dot{\mathbf{q}} + \boldsymbol{\Upsilon}^\mathsf{T} \boldsymbol{\mathcal{K}} \boldsymbol{\Upsilon}\, \mathbf{q} = \boldsymbol{\mathcal{Q}}(\mathbf{q}) \tag{2.24}$$

The elements $\boldsymbol{\mathcal{G}}_{ij}$ with $i, j = \{1, \dots, 18\}$ of the gyroscopic matrix $\boldsymbol{\mathcal{G}}$ are calculated from the elements $\boldsymbol{\mathcal{M}}_{ij}$ of the mass matrix $\boldsymbol{\mathcal{M}}$ as follows [TN85]:

$$\boldsymbol{\mathcal{G}}_{ij}(\mathbf{q}, \dot{\mathbf{q}}) = \sum_{k=1}^{18} \frac{1}{2} \left( \frac{\partial \boldsymbol{\mathcal{M}}_{ij}(\mathbf{q}, \dot{\mathbf{q}})}{\partial \mathbf{q}_k} + \frac{\partial \boldsymbol{\mathcal{M}}_{ik}(\mathbf{q}, \dot{\mathbf{q}})}{\partial \mathbf{q}_j} - \frac{\partial \boldsymbol{\mathcal{M}}_{jk}(\mathbf{q}, \dot{\mathbf{q}})}{\partial \mathbf{q}_i} \right) \dot{\mathbf{q}}_k \quad ; \quad i, j = \{1, \dots, 18\} \tag{2.25}$$

where $\dot{\mathbf{q}}_k$ represents the $k$-th component of the state vector $\mathbf{q}$. Except for the wheel spin angle $\theta_z$, the other generalized displacements in $\mathbf{q}$ are of small amplitude, i.e. if the state vector is partitioned as $\mathbf{q} = \begin{bmatrix} \boldsymbol{\eta}^\mathsf{T} & \theta_z \end{bmatrix}^\mathsf{T}$ then $\boldsymbol{\eta} \approx \mathbf{0}$. The dynamics is heavily influenced by the gyroscopic effects due to the reaction wheel spinning with velocity $\Omega = \dot{\theta}_z$. Hence, the nonlinear matrices in (2.24) can be

linearized by performing a Taylor expansion of each term in the neighborhood of $\boldsymbol{\eta} = \mathbf{0}$ and $\dot{\boldsymbol{\eta}} = \mathbf{0}$. The higher-order terms are ignored, except for those related to the wheel spin $\Omega$ and the resulting linear model is given below

$$\begin{cases} \boldsymbol{\mathcal{M}}\ddot{\mathbf{q}} + \left(\boldsymbol{\mathcal{G}}(\Omega) + \boldsymbol{\Upsilon}^\mathsf{T}\boldsymbol{\mathcal{C}}\boldsymbol{\Upsilon}\right)\dot{\mathbf{q}} + \boldsymbol{\Upsilon}^\mathsf{T}\boldsymbol{\mathcal{K}}\boldsymbol{\Upsilon}\mathbf{q} = \boldsymbol{\mathcal{Q}}\begin{bmatrix}\mathbf{u}_w \\ \mathbf{u}_s\end{bmatrix} \\ \mathbf{y}_s = \boldsymbol{\mathcal{S}}\begin{bmatrix}\boldsymbol{\mathcal{K}}\boldsymbol{\Upsilon} & \boldsymbol{\mathcal{C}}\boldsymbol{\Upsilon}\end{bmatrix}\begin{bmatrix}\mathbf{q} \\ \dot{\mathbf{q}}\end{bmatrix} \end{cases} \tag{2.26}$$

where

$$\boldsymbol{\mathcal{M}} = \operatorname{diag}\left(\underbrace{\begin{bmatrix} m_p\mathbf{I}_3 & \\ & \mathbf{J}_p\end{bmatrix}}_{\mathbf{M}_p}, \underbrace{\begin{bmatrix} m_a\mathbf{I}_3 & \\ & \mathbf{J}_a\end{bmatrix}}_{\mathbf{M}_a}, \underbrace{\begin{bmatrix} m_w\mathbf{I}_3 & \\ & \mathbf{J}_w\end{bmatrix}}_{\mathbf{M}_w}\right)$$

$$\boldsymbol{\mathcal{G}}(\Omega) = \operatorname{diag}\left(\mathbf{0}_{15}\,,\ \begin{bmatrix} 0 & \Omega J_{zz} \\ -\Omega J_{zz} & 0\end{bmatrix},\ 0\right) \qquad \boldsymbol{\mathcal{Q}} = \left[\begin{array}{c|c} \begin{bmatrix}\mathbf{0}_{12\times 5} \\ \mathbf{I}_5 \\ \mathbf{0}_{1\times 5}\end{bmatrix} & \begin{bmatrix}\mathbf{0}_{11\times 1} \\ -1 \\ \mathbf{0}_{5\times 1} \\ 1\end{bmatrix} \end{array}\quad \begin{bmatrix}\mathbf{0}_6 \\ \boldsymbol{\mathcal{T}}(\mathbf{r}_{as})^\mathsf{T} \\ \mathbf{0}_6\end{bmatrix}\right] \tag{2.27}$$

The input-output behavior is described through a $\Omega$-dependent system model $\widehat{\mathbf{G}}(\Omega)$ with 12 inputs $\begin{bmatrix}\mathbf{u}_w \\ \mathbf{u}_s\end{bmatrix}$, 6 outputs $\mathbf{y}_s$ and 36 states $\begin{bmatrix}\mathbf{q} \\ \dot{\mathbf{q}}\end{bmatrix}$ having the following representation

$$\widehat{\mathbf{G}}(\Omega) := \begin{cases} \begin{bmatrix}\dot{\mathbf{q}} \\ \ddot{\mathbf{q}}\end{bmatrix} = \underbrace{\begin{bmatrix} \mathbf{0} & \mathbf{I} \\ -\boldsymbol{\mathcal{M}}^{-1}\widetilde{\boldsymbol{\mathcal{K}}} & -\boldsymbol{\mathcal{M}}^{-1}\left(\widetilde{\boldsymbol{\mathcal{C}}} + \boldsymbol{\mathcal{G}}(\Omega)\right)\end{bmatrix}}_{\in\mathbb{R}^{36\times 36}}\begin{bmatrix}\mathbf{q} \\ \dot{\mathbf{q}}\end{bmatrix} + \underbrace{\begin{bmatrix}\mathbf{0} \\ \boldsymbol{\mathcal{M}}^{-1}\boldsymbol{\mathcal{Q}}\end{bmatrix}}_{\in\mathbb{R}^{36\times 12}}\begin{bmatrix}\mathbf{u}_w \\ \mathbf{u}_s\end{bmatrix} \\ \mathbf{y}_s = \underbrace{\widetilde{\boldsymbol{\mathcal{S}}}}_{\in\mathbb{R}^{6\times 36}}\begin{bmatrix}\mathbf{q} \\ \dot{\mathbf{q}}\end{bmatrix} \end{cases} \tag{2.28}$$

where $\widetilde{\boldsymbol{\mathcal{K}}} = \boldsymbol{\Upsilon}^\mathsf{T}\boldsymbol{\mathcal{K}}\boldsymbol{\Upsilon}$, $\widetilde{\boldsymbol{\mathcal{C}}} = \boldsymbol{\Upsilon}^\mathsf{T}\boldsymbol{\mathcal{C}}\boldsymbol{\Upsilon}$, $\widetilde{\boldsymbol{\mathcal{S}}} = \boldsymbol{\mathcal{S}}\begin{bmatrix}\boldsymbol{\mathcal{K}}\boldsymbol{\Upsilon} & \boldsymbol{\mathcal{C}}\boldsymbol{\Upsilon}\end{bmatrix}$. The previous dynamical system can be written in a more compact form as

$$\widehat{\mathbf{G}}(\Omega) := \left(\begin{array}{cc|c} \mathbf{0} & \mathbf{I} & \mathbf{0} \\ -\boldsymbol{\mathcal{M}}^{-1}\widetilde{\boldsymbol{\mathcal{K}}} & -\boldsymbol{\mathcal{M}}^{-1}\left(\widetilde{\boldsymbol{\mathcal{C}}} + \boldsymbol{\mathcal{G}}(\Omega)\right) & \boldsymbol{\mathcal{M}}^{-1}\boldsymbol{\mathcal{Q}} \\ \hline \multicolumn{2}{c|}{\widetilde{\boldsymbol{\mathcal{S}}}} & \mathbf{0} \end{array}\right) \quad \text{with} \quad \mathbf{y}_s = \widehat{\mathbf{G}}(\Omega)\begin{bmatrix}\mathbf{u}_w \\ \mathbf{u}_s\end{bmatrix} \tag{2.29}$$

where the notation $\left(\begin{array}{c|c}\mathbf{A} & \mathbf{B} \\ \hline \mathbf{C} & \mathbf{D}\end{array}\right)$ denotes the dynamical system: $\mathbf{C}\,(s\mathbf{I} - \mathbf{A})^{-1}\,\mathbf{B} + \mathbf{D}$. Since the system matrices contain rational combinations of uncertain parameters and the wheel spin rate $\Omega$ is considered time-varying and part of the system state (i.e. an endogenous parameter), it follows that $\widehat{\mathbf{G}}$ is an uncertain quasi Linear Parameter-Varying (qLPV) system scheduled by $\Omega$.

The numerical values of the system parameters are provided in table 2.3 together with the uncertainty ranges. The singular values of the transfer from wheel disturbances $\mathbf{u}_w$ to the isolator contact forces and torques $\mathbf{y}_s$ are shown in fig. 2.8a for various values of uncertain system parameters and for different reaction wheel speeds spin rates $\Omega \in \{10, 30, 50\}$ Hz. The peaks in the singular values below 2 Hz correspond to the flexible modes due to the suspension springs attached to the interface plate. Similarly, the modes in the $[5, 60]$ Hz region are the result of the passive isolators while the higher frequency resonances above 200 Hz are caused by the flexibility in the reaction wheel support (in this case corresponding to the flexible wheel bearings supporting the wheel's shaft). Some of the flexible modes form pairs deemed positive and negative whirl modes that separate due

to gyroscopic effects with increasing values of $\Omega$. This effect can be highlighted using the so-called Campbell diagram included in fig. 2.8b. This plot shows the shift in the modal frequencies of the system (2.29) as a function of $\Omega$. The image focuses on the isolator modes in the $[6, 50]$ Hz region where active isolation is desired. It is visible that the gyroscopic effect has no influence on the axial and torsional isolator modes corresponding to movements along and around the $w$-axis of the active plate. On the other hand, the nonzero terms in the gyroscopic matrix $\mathcal{G}$ introduce coupling between the lateral and rocking motions along and around the $u$ and $v$ body axes.

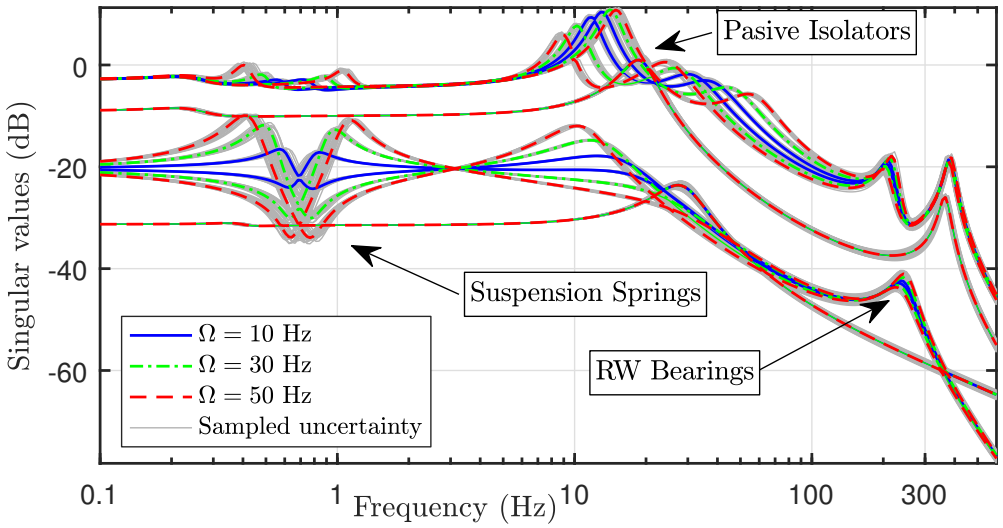


(a)

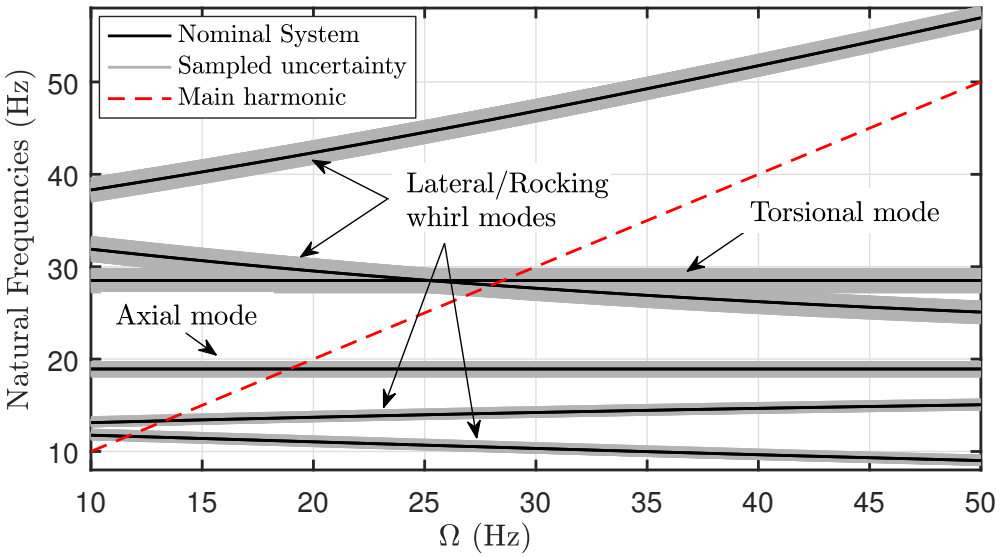


(b)

Figure 2.8: For multiple values of the uncertain parameters: (a) Singular values of the transfer from wheel disturbances to the isolator contact forces and torques $\mathbf{u}_w \to \mathbf{y}_s$ for $\Omega \in \{10, 30, 50\}$ Hz. (b) Campbell diagram showing the main harmonic disturbance frequency as well as the shift in the natural frequencies of the system within the control bandwidth [10,50] Hz as a function of the wheel spin rate $\Omega$.

In order to develop a deeper intuition of the overall system, the dynamical model (2.26) can be rewritten in terms of the governing equation of each subsystem. These equations are given in table 2.2 and also shown as a block diagram in fig. 2.9. This provides a more modular approach to system analysis and enables the possibility to quickly adapt the model to new configurations

Table 2.2: Dynamical equations the system subcomponents

| Subsystem | Governing equation |
|---|---|
| Reaction wheel | $\mathbf{M}_w\ddot{\mathbf{q}}_w + \text{diag}\left(\mathbf{0}_3,\ \Omega\begin{bmatrix}0 & J_{zz}\\ -J_{zz} & 0\end{bmatrix}, 0\right)\dot{\mathbf{q}}_w = \mathbf{u}_w - \boldsymbol{\mathcal{T}}(\mathbf{r}_{wb})^\mathsf{T}\mathbf{y}_b$ |
| Wheel motor | $J_{zz}\dot{\Omega} = T_m + T_{zbn} = T_z = \begin{bmatrix}\mathbf{0}_{1\times5} & 1\end{bmatrix}\mathbf{u}_w$ |
| Wheel support (Flexible bearings) | $\mathbf{y}_b = \mathbf{K}_b\mathbf{q}_{\Delta b} + \mathbf{C}_b\dot{\mathbf{q}}_{\Delta b}$ with $\mathbf{q}_{\Delta b} = \boldsymbol{\mathcal{T}}(\mathbf{r}_{wb})\mathbf{q}_w - \boldsymbol{\mathcal{T}}(\mathbf{r}_{ab})\mathbf{q}_a$ |
| Active plate | $\mathbf{M}_a\ddot{\mathbf{q}}_a = \boldsymbol{\mathcal{T}}(\mathbf{r}_{as})^\mathsf{T}(\mathbf{y}_s + \mathbf{u}_s) - \boldsymbol{\mathcal{T}}(\mathbf{r}_{ab})^\mathsf{T}\mathbf{y}_b - \begin{bmatrix}\mathbf{0}_{5\times1}\\ 1\end{bmatrix}\underbrace{\begin{bmatrix}\mathbf{0}_{1\times5} & 1\end{bmatrix}\mathbf{u}_w}_{T_z}$ |
| Passive Isolator | $\mathbf{y}_s = \mathbf{K}_s\mathbf{q}_{\Delta s} + \mathbf{C}_s\dot{\mathbf{q}}_{\Delta s}$ with $\mathbf{q}_{\Delta s} = \boldsymbol{\mathcal{T}}(\mathbf{r}_{as})\mathbf{q}_a - \boldsymbol{\mathcal{T}}(\mathbf{r}_{ps})\mathbf{q}_p$ |
| Interface plate | $\mathbf{M}_p\ddot{\mathbf{q}}_p + \mathbf{C}_p\dot{\mathbf{q}}_p + \mathbf{K}_p\mathbf{q}_p = -\boldsymbol{\mathcal{T}}(\mathbf{r}_{ps})^\mathsf{T}\mathbf{y}_s$ |

Dimensions: $\mathbf{M}_w, \mathbf{M}_a, \mathbf{M}_p, \mathbf{K}_b, \mathbf{K}_s, \mathbf{K}_p, \mathbf{C}_b, \mathbf{C}_s, \mathbf{C}_p \in \mathbb{R}^{6\times6}$ ; $\mathbf{q}_w, \mathbf{q}_a, \mathbf{q}_p, \mathbf{u}_w, \mathbf{y}_b, \mathbf{y}_s \in \mathbb{R}^6$

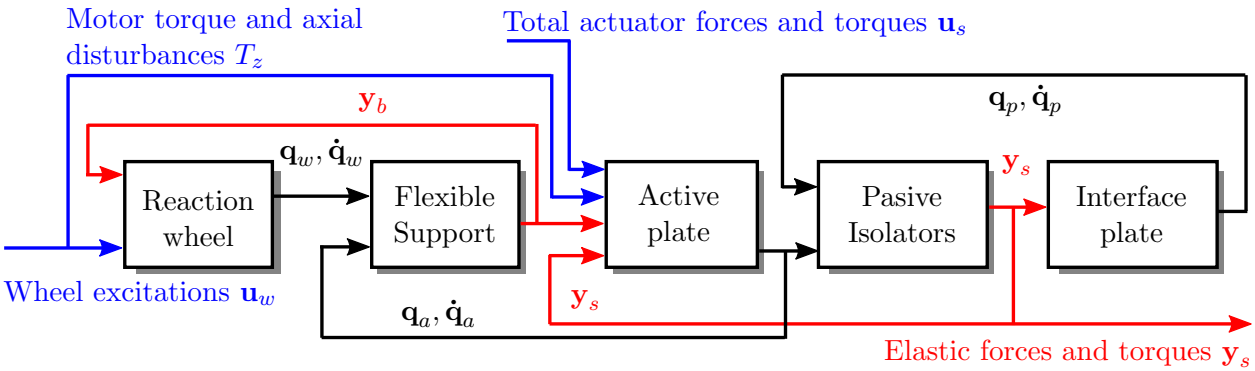


Figure 2.9: System block diagram of the structural equations of motion. Input forces and torques, Elastic forces and torques , Generalized displacements and velocities.

by replacing some of the component blocks. This will be exploited in the next chapter where the dynamical model of the interface plate is replaced with that of a flexible satellite. Analyzing table 2.2 the following facts can be stated:

- due to the offsets $l_{bw}$, $l_{ba}$, $l_{as}$, $l_{sp}$ between the elastic connections and the CoM of the different subcomponents, the lateral translations of the wheel, active and interface plates, i.e. the states $\begin{bmatrix}x & u & a\end{bmatrix}$ in $\mathbf{q}$ are coupled to the rotations $\begin{bmatrix}\theta_x & \theta_u & \theta_a\end{bmatrix}$. Similarly, the translations $\begin{bmatrix}y & v & b\end{bmatrix}$ are coupled to the rotations $\begin{bmatrix}\theta_y & \theta_v & \theta_b\end{bmatrix}$.
- the angular rotations $\theta_x$ and $\theta_y$ of the flywheel are also coupled due to the gyroscopic torques dependent of the spin axis inertia $J_{zz}$ and the wheel spin rate $\Omega$. As the wheel is elastically connected to the active plate, the rocking motions of both the active and interface plates get coupled as a result. This explains the multiple whirl modes seen in the Campbell diagram from fig. 2.8b.
- from the motor equation it follows that the wheel acceleration is proportional to $T_z/J_{zz}$ and therefore the reaction wheel spin rate $\Omega$ acts like an integrator of the total applied torque

signal $T_z = T_m + T_{zbn}$, i.e. $\Omega(T) = \frac{1}{J_{zz}} \int_0^T T_z(t)\, dt$. If the motor torque $T_m$ is assumed to be an exogenous signal, this integrator introduces an uncontrollable and unstable pole at zero in the overall system $\widehat{\mathbf{G}}(\Omega)$. One solution to stabilize this pole is to add an attitude control loop such that the motor torque is dependent on the axial displacement and velocity of the interface plate, i.e. $T_m = K_q\theta_c + C_q\dot{\theta}_c$ where $K_q, C_q \in \mathbb{R}$ are the tunable parameters of the attitude controller. This will be the method of choice in the subsequent chapter, where the dynamical model of the interface plate will be substituted with a flexible satellite. In practice however, the flywheel axial inertia $J_{zz}$ is considerably higher than the total applied torque signal $T_z$ and therefore the factor $T_z/J_{zz}$ is very small. This corresponds to small accelerations (see (2.4)) in the reaction wheel, i.e. the $\dot{\Omega} \approx 0$ and the wheel can be assumed to spin at a constant rate $\Omega$ in order to simplify the subsequent developments present in this chapter. With the previous assumption, the motor equation $J_{zz}\dot{\Omega} = T_z$ together with the axial rotation $\theta_z$ of the wheel can be eliminated from the system state $\mathbf{q}$ in (2.26) and (2.29) and table 2.2. Subsequently, $\Omega$ is considered an exogenous scheduling parameter that only influences the values of the gyroscopic matrix $\boldsymbol{\mathcal{G}}(\Omega)$ in the previous equations. With these considerations, the previously quasi Linear Parameter Varying (LPV) system (2.29) becomes a standard LPV system the wheel rate is no longer part of the system state $\begin{bmatrix}\mathbf{q}^\mathsf{T} & \dot{\mathbf{q}}^\mathsf{T}\end{bmatrix}^\mathsf{T}$. Furthermore, the new LPV system remains open-loop stable for any choice in the spin rate $\Omega$ or other structural parameters.

### 2.3.4 Extracting the models based on Linear Fractional Transformations

LFTs play a fundamental role in modern robust control as they provide an elegant and unified means to model real or complex uncertain or varying parameters, LTI uncertainties, sector nonlinearities, saturations, time delays, deadzones, or more general nonlinear operators [BR16, HO06, DPZ91]. The main idea is to separate the known part of the process model from the unknown by expressing the process model as a feedback connection of a nominal plant and the uncertainty description. In this way, an LFT describes a model set and the real process model is assumed to lie within this set. Algebraic operations between LFT models such as series, parallel or feedback interconnections preserve the LFT structure. Efficient tools exist to automate the LFT extraction process (see for instance [BR16, Mag06]). The goal of this section is to present the method used to derive the LFT representation of the uncertain and time-varying structural dynamics model given in (2.26) and (2.29) and also introduce the uncertain sensor and actuator models. The combined LFT models will then provide the basis for robust controller synthesis that is addressed in section 2.4 and $\mu$-based performance analysis, that will be addressed in section 2.5.

#### Structural model of the plant

Coming back to the structural model (2.26), it can be observed that $\widehat{\mathbf{G}}(\Omega)$ depends on a certain number of parameters that are uncertain or time-varying. The list of these parameters is given in table 2.3. Let $\boldsymbol{\Phi}$ denote the set of these parameters. Each parameter $\Phi_\bullet \in \boldsymbol{\Phi}$ can be written in normalized form as $\Phi_\bullet = \Phi_\bullet^0 + v_\bullet\delta_\bullet$ where $\Phi_\bullet^0 \in \mathbb{R}$ is the nominal value, $\delta_\bullet$ is a normalized uncertain parameter associated with $\Phi_\bullet$ having $|\delta_\bullet| \leq 1$ and $v_\bullet \in \mathbb{R}$ is used to define the uncertainty range. Assuming that the wheel's axial moment of inertial $J_{zz}$ has a known value, the uncertain parameter dependent matrices $\boldsymbol{\mathcal{M}}, \boldsymbol{\mathcal{C}}, \boldsymbol{\mathcal{G}}, \boldsymbol{\mathcal{K}}, \boldsymbol{\Upsilon}, \boldsymbol{\Upsilon}^\mathsf{T}, \mathbf{Q}$ in (2.26) are all affine in $\boldsymbol{\Phi}$. These matrices can thus be written as the following minimal LFTs by employing the so-called Morton's method [Mor85, HO06]

Table 2.3: Nominal values and uncertainty ranges of the plant parameters.

| Subsystem | Parameter | Description | Value / Uncertainty |
|---|---|---|---|
| Reaction Wheel | $\boldsymbol{\Omega}$ | Spin rate range | $[10, 50]$ Hz (rev/s) |
| | $\dot{\Omega}_{max}$ | Maximum acceleration | 0.01 Hz/s (rev/s$^2$) |
| | $m_w$ | Mass | 5.9 kg $\pm$ 1% |
| | $\begin{bmatrix} J_{rr} & J_{zz} \end{bmatrix}$ | Radial and axial moments of inertia | $\begin{bmatrix} 0.063 & 0.075 \end{bmatrix}$ kg m$^2$ |
| | $[U_s \;\; U_d]$ | Static and dynamic imbalances | $[0.716$ g cm $\;\; 29.24$ g cm$^2]$ |
| | $\begin{bmatrix} h_1 & \dots & h_4 \end{bmatrix}$ | harmonic numbers | $\begin{bmatrix} 1 & 2 & 3 & 4 \end{bmatrix}$ |
| | $\begin{bmatrix} a_1^f & \dots & a_4^f \end{bmatrix}$ | multi-harmonic radial force coefficients | $\begin{bmatrix} 0.785 & 0.298 & 0.078 & 0.104 \end{bmatrix}$ |
| | $\begin{bmatrix} a_1^{fz} & \dots & a_4^{fz} \end{bmatrix}$ | multi-harmonic axial force coefficients | $\begin{bmatrix} 0.08 & 0.03 & 0.008 & 0.01 \end{bmatrix}$ |
| | $\begin{bmatrix} a_1^t & \dots & a_4^t \end{bmatrix}$ | multi-harmonic radial torque coefficients | $\begin{bmatrix} 0.324 & 0.074 & 0.03 & 0.012 \end{bmatrix}$ |
| Flexible Wheel support (ball bearings) | $l_{bw}$ | Distance from reaction wheel CoM to elastic support connection | 6 cm $\pm$ 1% |
| | $l_{ba}$ | Distance from active plate CoM to elastic support connection | 0.94 cm $\pm$ 1% |
| | $k_x,\ k_y,\ k_z$ | Translational stiffness coefficients | $7.861 \times 10^6$ N/m $\pm$ 5% |
| | $c_x,\ c_y,\ c_z$ | Translational damping coefficients | 200 N s/m $\pm$ 10% |
| | $k_{\theta x},\ k_{\theta y}$ | Rotational stiffness coefficients | $3.7 \times 10^4$ Nm/rad $\pm$ 5% |
| | $c_{\theta x},\ c_{\theta y}$ | Rotational damping coefficients | 0.942 Nm s/rad $\pm$ 10% |
| Proof Mass Actuators | $m_{pma}$ | Mass of proof-mass | 25.5 g |
| | $k_{pma}$ | Stiffness coefficient | 226.5 N/m $\pm$ 5% |
| | $c_{pma}$ | Damping coefficient | 1.2 N s/m $\pm$ 10% |
| | $T_{pma}$ | Amplification factor | 3.16 N/V $\pm$ 5% |
| | $l_p$ | Placement radius | 17.5 cm $\pm$ 0.1 mm |
| | $d\theta,\ d\phi$ | Force direction uncertainty | $\pm$0.06 rad |
| Active Plate | $m_a$ | Total mass including actuators | 2.02 kg $\pm$ 2% |
| | $J_{uu},\ J_{vv}$ | Moments of inertia about $u$ and $v$ axes | 31.6 g m$^2$ $\pm$ 2% |
| | $J_{ww}$ | Moment of inertia about $w$ axis | 128.9 g m$^2$ $\pm$ 2% |
| Isolators | $l_{as}$ | Distance from active plate CoM to isolator connection | 9.18 cm $\pm$ 1% |
| | $l_{sp}$ | Distance from interface plate CoM to isolator connection | 4.2 cm $\pm$ 1% |
| | $k_u,\ k_v,\ k_w$ | Translational stiffness coefficients | $1.013 \times 10^5$ N/m $\pm$ 15% |
| | $c_u,\ c_v,\ c_w$ | Translational damping coefficients | 256 N s/m $\pm$ 10% |
| | $k_{\theta u},\ k_{\theta v},\ k_{\theta w}/2$ | Rotational stiffness coefficients | $2.026 \times 10^3$ Nm/rad $\pm$ 15% |
| | $c_{\theta u},\ c_{\theta v},\ c_{\theta w}/2$ | Rotational damping coefficients | 5.12 Nm s/rad $\pm$ 10% |
| Interface Plate | $m_p$ | Mass | 70 kg $\pm$ 2% |
| | $J_{aa},\ J_{bb}$ | Moments of inertia about $a$ and $b$ axes | 6.3 kg m$^2$ $\pm$ 5% |
| | $J_{cc}$ | Moment of inertia about $c$ axis | 6.47 kg m$^2$ $\pm$ 5% |
| Suspension springs | $k_a, k_b, k_c$ | Translational stiffness coefficients | 202.6 N/m $\pm$ 15% |
| | $c_a, c_b, c_c$ | Translational damping coefficients | 76.7 N s/m $\pm$ 15% |
| | $k_{\theta a}, k_{\theta b}, k_{\theta c}/2$ | Rotational stiffness coefficients | 101.3 Nm/rad $\pm$ 15% |
| | $c_{\theta a}, c_{\theta b}, c_{\theta c}/2$ | Rotational damping coefficients | 5.12 Nm s/rad $\pm$ 10% |
| Sensors | $l_s$ | Sensor/Isolator configuration radius | 10 cm |
| | $l_{hs}$ | Distance from sensors to isolator location | 5.12 cm $\pm$ 10% |

Note: Due to industrial confidentiality some of the numerical values have been modified. Reaction wheel parameters and flexible ball bearing properties are adapted from [Kim14]. Actuator parameters and isolator properties are derived from the work done in [Sec13].

detailed in appendix A.1:

$$\begin{array}{llll}\boldsymbol{\mathcal{M}}(\boldsymbol{\Phi}) = \mathcal{F}_u\left(\boldsymbol{\mathcal{M}}, \Delta_m\right) & \boldsymbol{\mathcal{C}}(\boldsymbol{\Phi}) = \mathcal{F}_u\left(\boldsymbol{\mathcal{C}}, \Delta_c\right) & \boldsymbol{\mathcal{G}}(\boldsymbol{\Phi}) = \mathcal{F}_u\left(\boldsymbol{\mathcal{G}}, \Omega\,\mathbf{I}_2\right) & \boldsymbol{\mathcal{Q}}(\boldsymbol{\Phi}) = \mathcal{F}_u\left(\boldsymbol{\mathcal{Q}}, \Delta_q\right) \\ \boldsymbol{\mathcal{K}}(\boldsymbol{\Phi}) = \mathcal{F}_u\left(\boldsymbol{\mathcal{K}}, \Delta_k\right) & \boldsymbol{\Upsilon}(\boldsymbol{\Phi}) = \mathcal{F}_u\left(\boldsymbol{\Upsilon}, \Delta_\Upsilon\right) & \boldsymbol{\Upsilon}^\mathsf{T}(\boldsymbol{\Phi}) = \mathcal{F}_u\left(\boldsymbol{\Upsilon}^\mathsf{T}, \Delta_\Upsilon\right) & \end{array}$$

$$\text{with} \begin{cases} \Delta_m = \operatorname{diag}\left(\delta_{m_a} \quad \delta_{m_p} \quad \delta_{J_{rr}} \quad \delta_{J_{rr}} \quad \delta_{J_{uu}} \quad \delta_{J_{vv}} \quad \delta_{J_{ww}} \quad \delta_{J_{aa}} \quad \delta_{J_{bb}} \quad \delta_{J_{cc}}\right) \\ \Delta_c = \operatorname{diag}\left(\delta_{c_x} \quad \delta_{c_y} \quad \delta_{c_z} \quad \delta_{c_u} \quad \delta_{c_v} \quad \delta_{c_w} \quad \delta_{c_a} \quad \delta_{c_b} \quad \delta_{c_c}\right) \\ \Delta_k = \operatorname{diag}\left(\delta_{k_x} \quad \delta_{k_y} \quad \delta_{k_z} \quad \delta_{k_u} \quad \delta_{k_v} \quad \delta_{k_w} \quad \delta_{k_a} \quad \delta_{k_b} \quad \delta_{k_c}\right) \\ \Delta_\Upsilon = \operatorname{diag}\left(\delta_{l_{bw}}\mathbf{I}_2 \quad \delta_{l_{ba}}\mathbf{I}_2 \quad \delta_{l_{as}}\mathbf{I}_2 \quad \delta_{l_{sp}}\mathbf{I}_2\right) \\ \Delta_q = \delta_{l_{as}}\mathbf{I}_2 \end{cases} \quad ; \quad \delta_\bullet \in \mathbb{R} : |\delta_\bullet| \leq 1 \tag{2.30}$$

where $\mathcal{F}_u$ denotes the upper LFT. The multiplicity of the time-varying spin rate $\Omega$ in the LFT description of the gyroscopic matrix $\boldsymbol{\mathcal{G}}(\boldsymbol{\Phi}) = \mathcal{F}_u\left(\boldsymbol{\mathcal{G}}, \Omega\,\mathbf{I}_2\right)$ is 2 and equal to the rank of the $\boldsymbol{\mathcal{G}}$ matrix from (2.29).

Using the definitions (2.30), the block diagram of the system described by (2.26) is drawn as seen in fig. 2.10 using the LFT form (2.30) of each parameter dependent matrix. Individual blocks are assembled into an overall system LFT using standard algebraic operations. The output vector $\mathbf{y}_s$ of interconnecting forces and torques at the isolator location can thus be expressed as follows

$$\mathbf{y}_s = \underbrace{\mathcal{F}_u\left(\mathbf{G}, \begin{bmatrix} \Omega\,\mathbf{I}_2 & \\ & \Delta_G \end{bmatrix}\right)}_{\widehat{\mathbf{G}}(\Omega)} \begin{bmatrix} \mathbf{u}_w \\ \mathbf{u}_s \end{bmatrix} \quad \text{with} \quad \Delta_G = \operatorname{diag}\left(\Delta_m \quad \Delta_c \quad \Delta_k \quad \Delta_\Upsilon \quad \Delta_\Upsilon \quad \Delta_q\right) \in \boldsymbol{\Delta}_G \subset \mathbb{R}^{46\times 46} \tag{2.31}$$

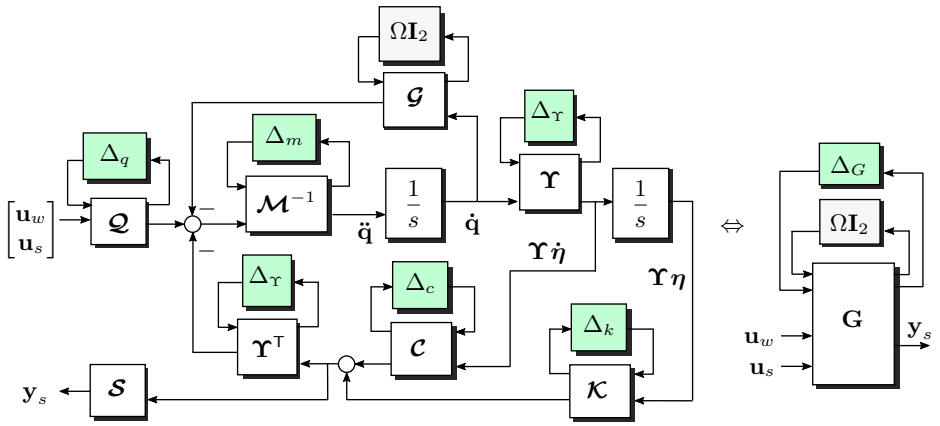


Figure 2.10: LFT representation of the multi-body mechanical system.

### Sensor model

The vector $\mathbf{y}_s$ of coupling joint forces and torques between the active plate and the satellite body is registered by the set of four tri-axis force cells placed underneath the passive isolators and connected to the base structure. These force cells use piezoelectric elements to convert strains into electric charges that are subsequently transformed into voltage signals using charge amplifiers. This enable direct monitoring of the forces transmitted to the base structure by the disturbance equipment. Figure 2.11 shows the Kistler 3-axis piezoelectric force cells that were used in this study. Let $\mathcal{F}_{s1\ldots4} := (o_{s1\ldots4}; \vec{s}_{x1\ldots4}, \vec{s}_{y1\ldots4}, \vec{s}_{z1\ldots4})$ denote the reference frames aligned with each of the sensors measurement axes (see fig. 2.2). The coordinates $\mathbf{r}_{s1\ldots4}$ of these frames relative to the location of

the passive isolator connection $S$ are

$$\left[\begin{array}{c|c|c|c} \mathbf{r}_{s1} & \mathbf{r}_{s2} & \mathbf{r}_{s3} & \mathbf{r}_{s4} \end{array}\right] = \left[\begin{array}{c|c|c|c} l_s & -l_s & 0 & 0 \\ 0 & 0 & l_s & -l_s \\ -l_{hs} & -l_{hs} & -l_{hs} & -l_{hs} \end{array}\right] \tag{2.32}$$

as show in fig. 2.2 for $\mathbf{r}_{s4}$. The corresponding force measurements in each of these frames are $\mathbf{s}_{1\ldots4} = \begin{bmatrix} s^x_{1\ldots4} & s^y_{1\ldots4} & s^z_{1\ldots4} \end{bmatrix}^\mathsf{T}$. Assuming zero torques at the contact points of the sensors, the elastic forces and torques $\mathbf{y}_s(t) \in \mathbb{R}^6$ at the isolator location $S$ can be reconstructed from the sensor measurement vector $\mathbf{f}_s(t) = \begin{bmatrix} \mathbf{s}_1^\mathsf{T} & \mathbf{s}_2^\mathsf{T} & \mathbf{s}_3^\mathsf{T} & \mathbf{s}_4^\mathsf{T} \end{bmatrix}^\mathsf{T} \in \mathbb{R}^{12}$ through the following relationship:

$$\mathbf{y}_s = \begin{bmatrix} \mathbf{I}_3 & \mathbf{I}_3 & \mathbf{I}_3 & \mathbf{I}_3 \\ [\mathbf{r}_{s1}]_\times & [\mathbf{r}_{s2}]_\times & [\mathbf{r}_{s3}]_\times & [\mathbf{r}_{s4}]_\times \end{bmatrix} \mathbf{f}_s = \mathbf{N}_r \mathbf{f}_s \tag{2.33}$$

In order to assess the influence of sensor placement misknowledge and measurement noise on the closed-loop system, the inverse problem is to determine the projection matrix $\widehat{\mathbf{N}}$ such that for a given force and torque combination $\mathbf{y}_s$, the corresponding sensor force vector $\mathbf{f}_s$ is given by:

$$\mathbf{f}_s = \widehat{\mathbf{N}} \mathbf{y}_s \tag{2.34}$$

Since the matrix $\mathbf{N}_r$ has linearly independent rows, $\widehat{\mathbf{N}}$ can be computed as a right-inverse of $\mathbf{N}_r$, i.e.

$$\widehat{\mathbf{N}} = \mathbf{N}_r^\mathsf{T} (\mathbf{N}_r \mathbf{N}_r^\mathsf{T})^{-1} \quad \text{with} \quad \mathbf{N}_r \widehat{\mathbf{N}} = \mathbf{I}_6$$

$$\widehat{\mathbf{N}} = \frac{1}{4} \begin{bmatrix} 1 & 0 & -2\,l_{hs}\,l_s^{-1} & 1 & 0 & 2\,l_{hs}\,l_s^{-1} & 1 & 0 & 0 & 1 & 0 & 0 \\ 0 & 1 & 0 & 0 & 1 & 0 & 0 & 1 & -2\,l_{hs}\,l_s^{-1} & 0 & 1 & 2\,l_{hs}\,l_s^{-1} \\ 0 & 0 & 1 & 0 & 0 & 1 & 0 & 0 & 1 & 0 & 0 & 1 \\ 0 & 0 & 0 & 0 & 0 & 0 & 0 & 0 & 2\,l_s^{-1} & 0 & 0 & -2\,l_s^{-1} \\ 0 & 0 & -2\,l_s^{-1} & 0 & 0 & 2\,l_s^{-1} & 0 & 0 & 0 & 0 & 0 & 0 \\ 0 & l_s^{-1} & 0 & 0 & -l_s^{-1} & 0 & -l_s^{-1} & 0 & 0 & l_s^{-1} & 0 & 0 \end{bmatrix}^\mathsf{T} \tag{2.35}$$

The offset $l_{hs}$ is assumed to be uncertain in the range given in table 2.3 and therefore $\widehat{\mathbf{N}}$ is used to capture how this uncertainty propagates to the sensor forces $\mathbf{f}_s$. For a fixed value of $l_s$, the matrix $\widehat{\mathbf{N}}$ is affine in $l_{hs}$ and can be written in minimal LFT form as:

$$\widehat{\mathbf{N}} = \mathcal{F}_u(\mathbf{N}, \Delta_n) \quad \text{where} \quad \Delta_n = \delta_{ds}\mathbf{I}_3 \in \mathbf{\Delta}_n \subset \mathbb{R}^{3\times3} \quad \text{and} \quad |\delta_{hs}| \leq 1 \tag{2.36}$$


Figure 2.11: Kistler 3-axis piezoelectric force cell used on the breadboard.

### Actuator model

As mentioned previously, the setup is actuated by a set of six electromagnetic proof-mass actuators arranged. These are mounted on top of the active plate on set of three cubes with three actuators

perpendicular to the plate and three in the tangential direction (see fig. 2.2). Each of these actuators is made out of a reaction mass $m_{pma}$ connected at the base through a visco-elastic joint with stiffness $k_{pma}$ and damping $c_{pma}$. A force $f$ on the proof-mass $m_{pma}$ and on the base structure is generated by a moving-coil transducer modeled as a static gain $T_{pma}$ with input voltage $u_{pma} \in [-10,\ 10]$ V. Considering $x_{pma}$ to be the displacement from the equilibrium position of the proof-mass, a schematic of actuator is shown in fig. 2.12b. For each of the six actuators, the mapping between input voltage $u_{pma1\ldots6}$ and the corresponding output forces $F_{1\ldots6}$ can be described by the following high-pass second order filters $H(s)$ with natural frequency $\omega_{pma}$ and damping ratio $\xi_{pma}$:

$$H(s) = \frac{T_{pma}s^2}{s^2 + 2\xi_{pma}\omega_{pma}s + \omega_{pma}^2} \quad \text{where} \quad \omega_{pma} = \sqrt{\frac{k_{pma}}{m_{pma}}} \qquad \xi_{pma} = \frac{c_{pma}}{2\sqrt{k_{pma}m_{pma}}} \tag{2.37}$$

The breadboard analyzed in this study is equipped with Wilcoxon F5B actuators (fig. 2.12a) that have the nominal natural frequency $\omega_{pma} \approx 15$ Hz within the control bandwidth 10-50 Hz. Therefore, the actuator dynamics must be included in the overall system model to account for the phase loss and overshoot occurring around $\omega_{pma}$. As the system contains six actuators, the voltage inputs

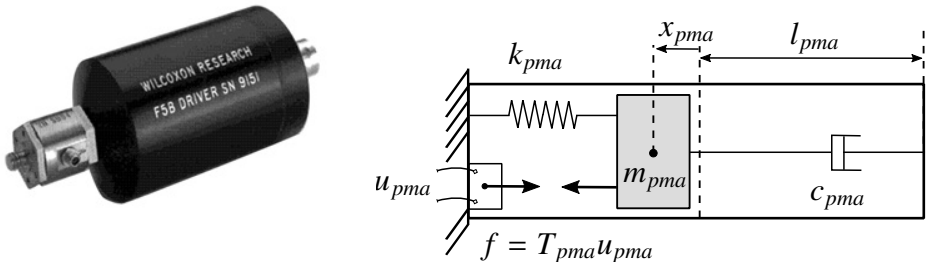


(a) (b)

Figure 2.12: (a) Proof-mass actuator used on the breadboard (Wilcoxon F5B). (b) Schematic of the actuator.

and mass displacements can be aggregated into the vectors $\mathbf{u}_{pma}(t) = \begin{bmatrix} u_{pma1} & \ldots & u_{pma6} \end{bmatrix}^\mathsf{T} \in \mathbb{R}^6$ and $\mathbf{x}_{pma}(t) \in \mathbb{R}^6$, respectively. Additionally, the parameters $m_{pma}, c_{pma}, k_{pma}, T_{pma}$ defined for each actuator combine into the following diagonal matrices:

$$\mathbf{M}_{pma} = m_{pma}\mathbf{I}_6 \quad \mathbf{C}_{pma} = c_{pma}\mathbf{I}_6 \quad \mathbf{K}_{pma} = k_{pma}\mathbf{I}_6 \quad \mathbf{T}_{pma} = T_{pma}\mathbf{I}_6 \tag{2.38}$$

The actuators and voltage supplier unit also contribute with uncertain delays of varying size. To account for this, uncertain time invariant delays $\tau_{1\ldots6} \in [0.1,\ 1]$ ms at the input of each of the six proof mass actuator (PMA) actuators are considered in this work and modeled as the following first-order Padé approximation:

$$e^{-s\tau_i} \approx \frac{-\tau_i s + 2}{\tau_i s + 2}, \quad \tau_i \in [0.01,\ 1] \text{ ms} \quad \text{for} \quad i = \{1, \ldots, 6\} \tag{2.39}$$

The bode diagram of a single PMA together with the time-delay is shown in fig. 2.13 for different samples of the uncertain parameters. It can be seen how the introduction of the uncertain time-delay causes a significant uncertain phase shift above 30 Hz. The uncertain delays are next structed as an LFT model following the same procedure as the one for the plant model (2.30). This boils down to the setup illustrated in fig. 2.14 with $\text{diag}\begin{bmatrix} \tau_1^{-1} & \ldots & \tau_6^{-1} \end{bmatrix} = \mathcal{F}_u\left(\mathbf{D}_{\tau^{-1}}, \Delta_\tau\right)$ and $\Delta_\tau = \text{diag}\begin{pmatrix} \delta_{\tau_1} & \ldots & \delta_{\tau_6} \end{pmatrix}$, $\delta_{\tau_{1\ldots6}} \in \mathbb{R} : |\delta_{\tau_{1\ldots6}}| \leq 1$. This resulting LFT provides the mapping between inputs $\mathbf{u}_{pma}(t) \in \mathbb{R}^6$ to delayed actuator signals $\mathbf{u}_\tau(t) \in \mathbb{R}^6$. The next step is now to connect the actuator model to the structural model of the setup illustrated in fig. 2.10. Therefore, it is necessary to express the link that maps voltage inputs $\mathbf{u}_{pma}$ to the resulting actuator forces

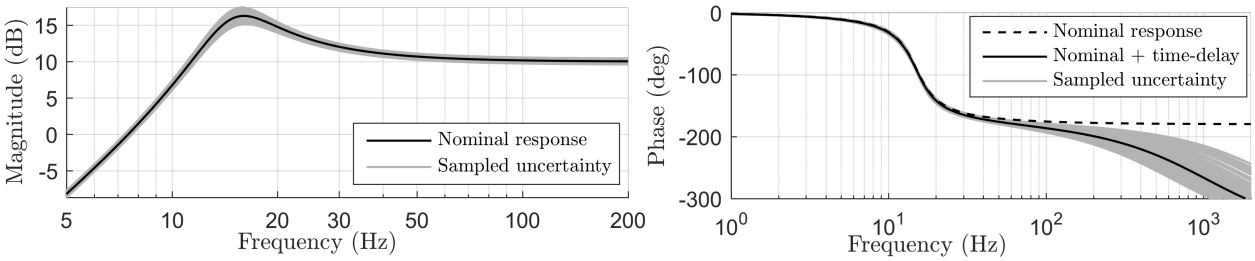


Figure 2.13: Bode diagram for the uncertain PMA model mapping input voltage to transmitted force.

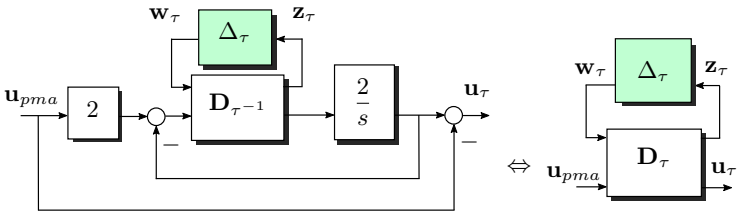


Figure 2.14: LFT form of the first order Padé approximation of the time delay.

and torques $\mathbf{u}_s = \begin{bmatrix}\mathbf{f}_{as}^\mathsf{T} & \mathbf{t}_{as}^\mathsf{T}\end{bmatrix}^\mathsf{T}$ at the isolator connection $S$. To proceed, let $\mathcal{F}_{fi} := (o_{fi}; \vec{f}_{xi}, \vec{f}_{yi}, \vec{f}_{zi})$ with $i = \{1, \ldots, 6\}$ be a set of frames corresponding to each of the PMAs and centered at the points where the forces $F_i$ are applied to the supporting cube. Each of the $\mathcal{F}_{fi}$ frames is aligned with the $\vec{f}_{zi}$-axis along the direction of the applied forces and $\vec{f}_{xi}$ pointing towards the exterior of the plate. The following set of position vectors $\mathbf{r}_i$ give the location of the frames $\mathcal{F}_{fi}$ relative to the isolator connection $S$:

$$\left[\,\mathbf{r}_1 \,\middle|\, \mathbf{r}_2 \,\middle|\, \ldots \,\middle|\, \mathbf{r}_6\,\right] = \left[\begin{array}{c|c|c|c|c|c} l_p & l_p & \left(-l_p - \sqrt{3}h_2\right)/2 & -l_p/2 & \left(\sqrt{3}h_2 - l_p\right)/2 & -l_p/2 \\ h_2 & 0 & \left(\sqrt{3}l_p - h_2\right)/2 & l_p\sqrt{3}/2 & \left(\sqrt{3}l_p - h_2\right)/2 & -l_p\sqrt{3}/2 \\ h_1 & h_1 + h_2 & h_1 & h_1 + h_2 & h_1 & h_1 + h_2 \end{array}\right] \tag{2.40}$$

with $h_1 = l_{cube} + l_{ap} + l_{as}$ and $h_2 = l_{pma} + l_{cube}$. The frames $\mathcal{F}_{f3}$ and $\mathcal{F}_{f4}$ together with the vector $\mathbf{r}_4$ are illustrated in fig. 2.2. To calculate the forces and torques produced by the actuators at the isolator connection $S$, namely $\mathbf{u}_s = \begin{bmatrix}\mathbf{f}_{as}^\mathsf{T} & \mathbf{t}_{as}^\mathsf{T}\end{bmatrix}^\mathsf{T}$, the forces $F_i$ generated by the PMAs in their respective $\mathcal{F}_{fi}$ frames are first rotated to the active plate frame $\mathcal{F}_a$ using the following rotation matrix:

$$\boldsymbol{\mathcal{R}}_{\mathcal{F}_{fi}\to\mathcal{F}_a} = \boldsymbol{\mathcal{R}}_{yxz}\left(d\phi_i,\ \ \theta_i + d\theta_i,\ \ \psi_i\right)^\mathsf{T} \tag{2.41}$$

where $\psi_{1\ldots6} = \{0, 0, 2/3\pi, 2/3\pi, 4/3\pi, 4/3\pi\}$ and $\theta_{1\ldots6} = \{0, -\pi/2, 0, -\pi/2, 0, -\pi\}$ are used to represent the nominal orientation of each actuator and $d\theta_i$ together with $d\phi_i$ reflect small angle deviations (see table 2.3) around this nominal direction. Afterwards, the rotated force vectors are projected into actuator forces and torques at the passive isolator as follows:

$$\begin{aligned}\mathbf{u}_s = \begin{bmatrix}\mathbf{f}_{as} \\ \mathbf{t}_{as}\end{bmatrix} &= \sum_{i=1}^{6} \begin{bmatrix}\mathbf{I}_3 \\ [\mathbf{r}_i]_\times\end{bmatrix} \underbrace{\left(\boldsymbol{\mathcal{R}}_{\mathcal{F}_{fi}\to\mathcal{F}_a}\begin{bmatrix}0\\0\\1\end{bmatrix}\right)}_{\mathbf{g}_i} F_i \\ &= \underbrace{\begin{bmatrix}\mathbf{I}_3 & \mathbf{I}_3 & \ldots & \mathbf{I}_3 \\ [\mathbf{r}_1]_\times & [\mathbf{r}_2]_\times & \ldots & [\mathbf{r}_6]_\times\end{bmatrix}\begin{bmatrix}\mathbf{g}_1 & & \\ & \ddots & \\ & & \mathbf{g}_6\end{bmatrix}}_{\mathbf{B}\in\mathbb{R}^{6\times6}}\begin{bmatrix}F_1 \\ \vdots \\ F_6\end{bmatrix}\end{aligned} \tag{2.42}$$

Here, $\mathbf{g}_{1\ldots6}$ are unit vectors giving the uncertain direction of each PMA in the active plate frame $\mathcal{F}_a$. As the uncertain angles $d\theta_i$ and $d\phi_i$ are small, the vectors $\mathbf{g}_{1\ldots6}$ are linearized to the following

values:

$$\begin{bmatrix}\mathbf{g}_1 & \mathbf{g}_2 & \cdots & \mathbf{g}_6\end{bmatrix} = \left[\begin{array}{c|c|c|c|c|c} d\phi_1 & d\phi_2 & \frac{\sqrt{3}-d\phi_3}{2} & \frac{\sqrt{3}\,d\theta_4-d\phi_4}{2} & \frac{\sqrt{3}-d\phi_5}{2} & \frac{\sqrt{3}\,d\theta_6-d\phi_6}{2} \\ 1 & -d\theta_2 & \frac{\sqrt{3}\,d\phi_3-1}{2} & \frac{d\theta_4+\sqrt{3}\,d\phi_4}{2} & \frac{1-\sqrt{3}\,d\phi_5}{2} & \frac{d\theta_6-\sqrt{3}\,d\phi_6}{2} \\ d\theta_1 & 1 & d\theta_3 & 1 & d\theta_5 & 1 \end{array}\right] \tag{2.43}$$

The full actuator model combines the actuator and delay models (2.37) and (2.39) with the projection matrices (2.42) and (2.43) and provides the full mapping between voltage signals $\mathbf{u}$ and the vector $\mathbf{u}_s$ of actuator forces and torques at the passive isolator connection. This mapping can now be put into a LFT form by first drawing the block diagram of the each uncertain subsystem. Let

$$\mathbf{\Phi}_p = \{m_{pma_{1\ldots6}},\ c_{pma_{1\ldots6}},\ k_{pma_{1\ldots6}},\ k_{pma_{1\ldots6}},\ T_{pma_{1\ldots6}},\ \theta_{1\ldots6},\ \phi_{1\ldots6},\ h_1,\ h_2,\ l_p\} \tag{2.44}$$

be the set of uncertain parameters of all the six actuator. Following the same reasoning as for the structural model of the plant in (2.30), the uncertain matrices from (2.38) and (2.42) can be written as

$$\begin{aligned}
&\mathbf{M}_{pma}(\mathbf{\Phi}_p) = \mathcal{F}_u\left(\mathbf{M}_{pma}, \Delta_{m_p}\right) \quad \mathbf{C}_{pma}(\mathbf{\Phi}_p) = \mathcal{F}_u\left(\mathbf{C}_{pma}, \Delta_{c_p}\right) \quad \mathbf{K}_{pma}(\mathbf{\Phi}_p) = \mathcal{F}_u\left(\mathbf{K}_{pma}, \Delta_{k_p}\right) \\
&\mathbf{T}_{pma}(\mathbf{\Phi}_p) = \mathcal{F}_u\left(\mathbf{T}_{pma}, \Delta_{t_p}\right) \qquad \mathbf{B}(\mathbf{\Phi}_p) = \mathcal{F}_u\left(\mathbf{B}, \Delta_b\right) \\
&\Delta_{m_p} = \mathrm{diag}\left(\delta_{m_{pma1}} \quad \ldots \quad \delta_{m_{pma6}}\right) \qquad \Delta_{c_p} = \mathrm{diag}\left(\delta_{c_{pma1}} \quad \ldots \quad \delta_{c_{pma6}}\right) \\
&\Delta_{k_p} = \mathrm{diag}\left(\delta_{k_{pma1}} \quad \ldots \quad \delta_{k_{pma6}}\right) \qquad \Delta_{l_p} = \mathrm{diag}\left(\delta_{T_{pma1}} \quad \ldots \quad \delta_{T_{pma6}}\right) \\
&\Delta_b = \mathrm{diag}\left(\delta_{h_1} \quad \delta_{h_2} \quad \delta_{l_p} \quad \delta_{d\theta_1} \quad \ldots \quad \delta_{d\theta_6} \quad \delta_{d\phi_1} \quad \ldots \quad \delta_{d\phi_6}\right)
\end{aligned} \tag{2.45}$$

with $\delta_\bullet \in \mathbb{R} : |\delta_\bullet| \leq 1$ being the normalized uncertain parameter corresponding to each element of the set $\mathbf{\Phi}_p$. Finally, the uncertainties at block level are grouped into the block $\Delta_h$ as illustrated in fig. 2.15, which provides the LFT model of the actuators:

$$\mathbf{u}_s = \underbrace{\mathcal{F}_u\left(\mathbf{H}, \Delta_h\right)}_{\hat{\mathbf{H}}} \mathbf{u}_{pma} \quad \text{with} \quad \Delta_h = \mathrm{diag}\left(\Delta_\tau \quad \Delta_{m_p} \quad \Delta_{k_p} \quad \Delta_{c_p} \quad \Delta_{l_p} \quad \Delta_b\right) \in \mathbf{\Delta}_h \subset \mathbb{R}^{42\times42} \tag{2.46}$$

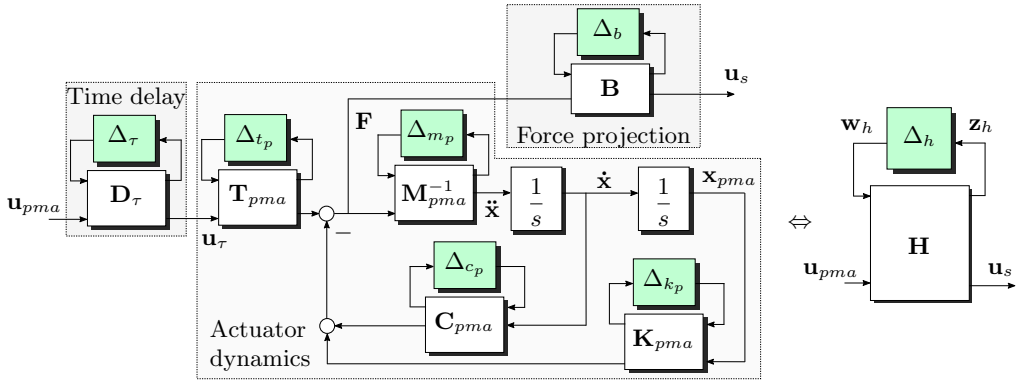


Figure 2.15: Block diagram and LFT of the actuator model including the time-delay and force projection matrices.

### LFT model of the complete system

Combining the LFT models of the actuators (see fig. 2.15), the platform (see fig. 2.10) and the sensors (see (2.36)) leads to a new overall setup illustrated on fig. 2.16a and defined according to:

$$\begin{aligned} \mathbf{f}_n &= \widehat{\mathbf{N}}\widehat{\mathbf{G}}(\Omega) \begin{bmatrix} \mathbf{u}_w \\ \widehat{\mathbf{H}}\mathbf{u}_{pma} \end{bmatrix} - \mathbf{n} \\ &= \mathcal{F}_u\left(\mathbf{N}, \Delta_n\right)\ \mathcal{F}_u\left(\mathbf{G}, \begin{bmatrix} \Omega\,\mathbf{I}_2 & \\ & \Delta_G \end{bmatrix}\right) \begin{bmatrix} \mathbf{u}_w \\ \mathcal{F}_u\left(\mathbf{H}, \Delta_h\right)\mathbf{u}_{pma} \end{bmatrix} - \mathbf{n} \end{aligned} \tag{2.47}$$

with the combined real uncertainty set:

$$\Delta_{real} = \text{diag}\left(\Delta_G \quad \Delta_n \quad \Delta_h\right) \in \mathbf{\Delta}_{real} \subset \mathbb{R}^{91\times 91} \tag{2.48}$$

To highlight the frequency behavior of this overall model, fig. 2.16b illustrates the open-loop singular values of the transfer between $\mathbf{u}_{pma}$ and $\mathbf{f}_n$ for the wheel spin rates $\Omega \in \{10, 30, 50\}$ Hz and various values of the $\Delta$ blocks. It can be seen on this figure that the gain rolls off by 20 dB/dec in the low frequency due to the actuators and that the actuator resonances around 15 Hz combine with the isolator flexible modes in the mid frequency range.

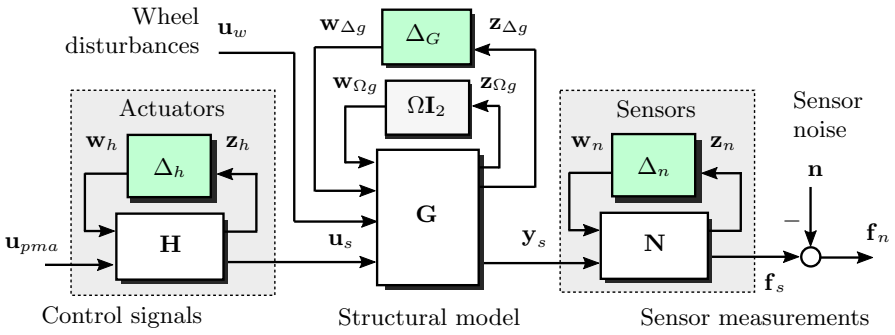


(a)

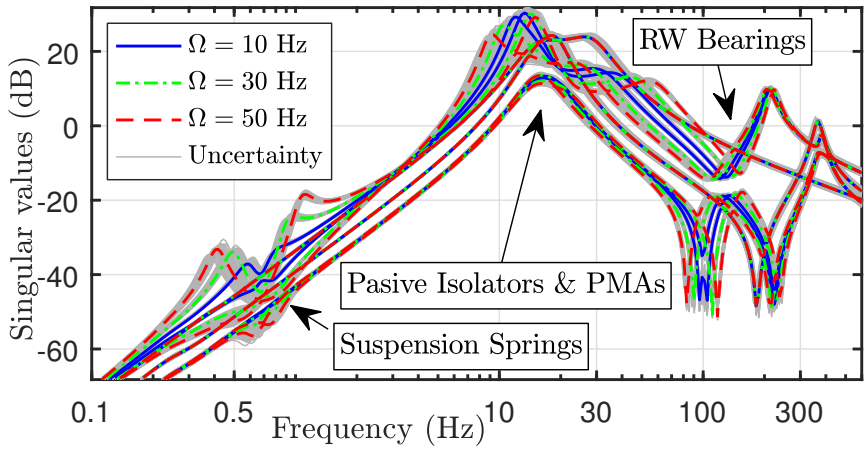


(b)

Figure 2.16: (a) Open loop interconnection (total number of states = 30). (b) Singular values of the open-loop transfer $\mathbf{u}_{pma} \to \mathbf{f}_n$ from actuator inputs to sensor outputs for the wheel spin rates $\Omega \in \{10, 30, 50\}$ Hz.

## 2.4 Controller design

### 2.4.1 Requirements, control architecture and problem formulation

As previously stated, the active control strategy should complement the passive solution and provide microvibration mitigation in the low frequency range corresponding to reaction wheel operating speeds specified in (2.4). Therefore, the challenge is now to design a controller that uses the force measurements $\mathbf{f}_n$ to generate a control signal $\mathbf{u}_{pma}(t) \in \mathbb{R}^6$ in such a way as to achieve the following requirements for all $\Omega \in \mathbf{\Omega} = [10, 50]$ Hz:

**(R1)** ***Robust harmonic disturbance attenuation*:** The aim is to guarantee in the worst case at least 20 dB decrease in force transmissibility and at least 10 dB in torque transmissibility around $\Omega$. This frequency corresponds to the main harmonic disturbance generated by the spinning reaction wheel due to mass imbalances [Bro06, LS89, ZLLL12, LLZ+13b, EM02, Mas02]. This performance goal should be achieved despite all uncertainties and delays affecting the system. The solution should have minimal impact on the torque signal $T_m$ generated by the reaction wheel and used in attitude control. Additionally, the controller, during operation, should not severely degrade the disturbance transmissibility outside the main harmonic frequency $\Omega$.

**(R2)** ***Robust stability*:** The solution must guarantee closed-loop stability $\forall \Omega \in \mathbf{\Omega}$ and for all considered uncertainties.

**(R3)** ***Actuator limitations*:** The control signal voltages should stay within limits (absolute values below $u_{max} = 10\,\mathrm{V}$) and not saturate the actuators.

The LFT model (2.47) is used for that purposes. Due to the fact that the wheel speed $\Omega$ is assumed to be known, it is proposed to use this parameter to adapt a gain-scheduling policy depending on the current speed of the reaction wheel so that it admits the following structure

$$\mathbf{K}(\Omega) = \mathbf{K}_\mu \, \widehat{\mathbf{K}}_\Omega(\Omega) \, \mathbf{N}_r = \mathbf{K}_\mu \mathcal{F}_u \left( \mathbf{K}_\Omega, \Omega \, \mathbf{I}_{12} \right) \mathbf{N}_r \tag{2.49}$$

where $\mathbf{N}_r$ is the nominal value of the projection matrix given in (2.33) that maps sensor measurements to forces and torques at the passive isolator connection. $\widehat{\mathbf{K}}_\Omega(\Omega)$ forms the known parameter-dependent part of the overall controller used to adjust the attenuation requirements and reconfigure the overall controller $\mathbf{K}$, based on the known operating speed $\Omega$ of the reaction wheel in order to reject only the main harmonic disturbance $\mathbf{u}_1$ of the reaction wheel (see (2.6) for the harmonic disturbance model). Its definition is addressed in the following subsection. Thus, the synthesis problem turns out to be the design of $\mathbf{K}_\mu$. This is tackled using the $\mathcal{H}_\infty/\mu$ theory. More precisely, nonsmooth optimization techniques [Apk11, AN07] are used for the design of $\mathbf{K}_\mu$ and $\mu$ analysis techniques [PD93, FTD91, ZDGO96] are used to perform a deeper analysis of the computed design solution. Two LFT models are derived from (2.47) for that purposes:

- The first reduced LFT is for controller synthesis purposes. The technique mainly consists in introducing two complex uncertainty blocks $\Delta_u$ and $\Delta_y$ so that they provide a crude coverage of the real uncertainty set $\Delta_{real} = \mathrm{diag}\left(\Delta_G \;\; \Delta_n \;\; \Delta_h\right) \in \mathbf{\Delta}_{real}$. The reduced LFT model then consists in removing the blocks $\Delta_h, \Delta_G, \Delta_n$, that is, the design is done considering only $\Delta_u$ and $\Delta_y$.

- The second LFT is for robust stability assessment, robust performance and worst-case analysis purpose. Thus, the complete and fully representative LFT model illustrated in fig. 2.17 is used for that purpose. Details on the definition of the $\Delta$ block for that purposes are given later in section 2.4.2.

To synthesize $\mathbf{K}_\mu$, the requirements **R1-R3** are first formulated within the $\mathcal{H}_\infty$ setting, that is, the design objectives are formulated in terms of loop shapes, i.e., of desired gain responses for the appropriate closed-loop transfer functions. The shaping objectives are then turned into uniform bounds by means of the shaping filters. This setup is illustrated on fig. 2.17 where $\mathbf{W}_\bullet$ refer to the shaping filters, also called weighting functions.

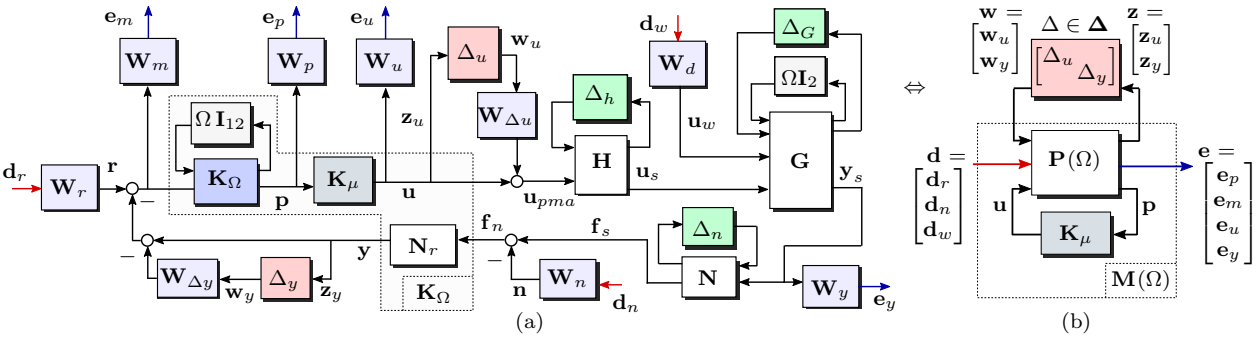


Figure 2.17: (a) Weighted closed-loop system interconnection. (b) Synthesis structure considering only the complex uncertainty blocks. Weighting functions, Real uncertainty, Complex uncertainty.

### 2.4.2 Requirements formulation within the $\mathcal{H}_\infty/\mu$ framework

In order to design a control law that accommodates the requirements given in the previous section, the synthesis problem is recast into the $\mathcal{H}_\infty/\mu$ framework. For the necessary mathematical background related to $\mathcal{H}_\infty/\mu$ concepts, including the recent nonsmooth approaches, the reader is invited to refer to the non exhaustive list of references [PD93, GA94, ZDGO96, Apk11, ADN15]. In this context, the synthesis problem is turned into an optimization problem of the worst-case $\mathcal{L}_2$ induced norm between different closed-loop signals scaled by so-called weighting functions.

#### Closed-loop transfer functions

To understand the link between the weighting functions and the various performance objectives, the closed-loop interconnection $\mathbf{M}(\Omega) = \mathcal{F}_l(\mathbf{P}(\Omega), \mathbf{K}_\mu)$ is first deduced from the setup shown in fig. 2.17 using the reduced LFT model. In other words the block $\Delta$ depicted in fig. 2.17 takes the expression

$$\Delta = \operatorname{diag}\begin{pmatrix}\Delta_u & \Delta_y\end{pmatrix} \in \mathbf{\Delta} \subset \mathbb{C}^{12\times 12} \tag{2.50}$$

With this model, the general interconnection matrix $\mathbf{P}(\Omega)$ can be partitioned as follows:

$$\begin{bmatrix}\mathbf{z}\\ \hline \mathbf{e}\\ \hline \mathbf{p}\end{bmatrix} = \underbrace{\left[\begin{array}{c|c|c} \mathbf{P}_{\mathbf{w}\to\mathbf{z}} & \mathbf{P}_{\mathbf{d}\to\mathbf{z}} & \mathbf{P}_{\mathbf{u}\to\mathbf{z}} \\ \hline \mathbf{P}_{\mathbf{w}\to\mathbf{e}} & \mathbf{P}_{\mathbf{d}\to\mathbf{e}} & \mathbf{P}_{\mathbf{u}\to\mathbf{e}} \\ \hline \mathbf{P}_{\mathbf{w}\to\mathbf{p}} & \mathbf{P}_{\mathbf{d}\to\mathbf{p}} & \mathbf{P}_{\mathbf{u}\to\mathbf{p}} \end{array}\right]}_{\mathbf{P}(\Omega)} \begin{bmatrix}\mathbf{w}\\ \hline \mathbf{d}\\ \hline \mathbf{u}\end{bmatrix} \quad \text{and} \quad \mathbf{w} = \Delta\mathbf{z} \tag{2.51}$$

where $\mathbf{e} = \begin{bmatrix}\mathbf{e}_p^\mathsf{T} & \mathbf{e}_m^\mathsf{T} & \mathbf{e}_u^\mathsf{T} & \mathbf{e}_y^\mathsf{T}\end{bmatrix}^\mathsf{T}$ represents the performance signals, $\mathbf{d} = \begin{bmatrix}\mathbf{d}_r^\mathsf{T} & \mathbf{d}_n^\mathsf{T} & \mathbf{d}_w^\mathsf{T}\end{bmatrix}^\mathsf{T}$ the disturbances and $\mathbf{w} = \begin{bmatrix}\mathbf{w}_u^\mathsf{T} & \mathbf{w}_y^\mathsf{T}\end{bmatrix}^\mathsf{T}$ with $\mathbf{z} = \begin{bmatrix}\mathbf{z}_u^\mathsf{T} & \mathbf{z}_y^\mathsf{T}\end{bmatrix}^\mathsf{T}$ the uncertainty channels. With the notation:

$$\mathbf{y}_s = \widehat{\mathbf{G}}(\Omega)\begin{bmatrix}\mathbf{I} & \\ & \widehat{\mathbf{H}}\end{bmatrix}\begin{bmatrix}\mathbf{u}_w \\ \mathbf{u}_{pma}\end{bmatrix} = \begin{bmatrix}\mathbf{G}_d(\Omega) & \mathbf{G}_u(\Omega)\end{bmatrix}\begin{bmatrix}\mathbf{u}_w \\ \mathbf{u}_{pma}\end{bmatrix} \text{ where } \mathbf{y}_s(t), \mathbf{u}_w(t), \mathbf{u}_{pma}(t) \in \mathbb{R}^6 \quad (2.52)$$

the augmented open-loop system interconnection matrix $\mathbf{P}(\Omega)$ becomes:

$$\begin{bmatrix}\mathbf{z}_{\Delta u} \\ \mathbf{z}_{\Delta y} \\ \hline \mathbf{e}_p \\ \mathbf{e}_m \\ \mathbf{e}_u \\ \mathbf{e}_y \\ \hline \mathbf{p}\end{bmatrix} = \underbrace{\operatorname{diag}\left(\begin{array}{c}\mathbf{I} \\ \mathbf{I} \\ \hline \mathbf{W}_p\widehat{\mathbf{K}}_\Omega \\ \mathbf{W}_m \\ \mathbf{W}_u \\ \mathbf{W}_y \\ \hline \widehat{\mathbf{K}}_\Omega\end{array}\right)\left[\begin{array}{cc|cc|c} \mathbf{0} & \mathbf{0} & \mathbf{0} & \mathbf{0} & \mathbf{I} \\ \mathbf{G}_u & \mathbf{0} & \mathbf{0} & \mathbf{G}_d & \mathbf{G}_u \\ \hline -\mathbf{G}_u & \mathbf{I} & \mathbf{I} & -\mathbf{G}_d & -\mathbf{G}_u \\ -\mathbf{G}_u & \mathbf{I} & \mathbf{I} & -\mathbf{G}_d & -\mathbf{G}_u \\ \mathbf{0} & \mathbf{0} & \mathbf{0} & \mathbf{0} & \mathbf{I} \\ \mathbf{G}_u & \mathbf{0} & \mathbf{0} & \mathbf{G}_d & \mathbf{G}_u \\ \hline -\mathbf{G}_u & \mathbf{I} & \mathbf{I} & -\mathbf{G}_d & -\mathbf{G}_u \end{array}\right]\operatorname{diag}\left(\begin{array}{c}\mathbf{W}_{\Delta u} \\ \mathbf{W}_{\Delta y} \\ \hline \begin{bmatrix}\mathbf{W}_r \mid \mathbf{N}_r\mathbf{W}_n\end{bmatrix} \\ \mathbf{W}_d \\ \hline \mathbf{I}\end{array}\right)}_{\mathbf{P}(\Omega)}\begin{bmatrix}\mathbf{w}_{\Delta u} \\ \mathbf{w}_{\Delta y} \\ \hline \begin{bmatrix}\mathbf{d}_r \\ \mathbf{d}_n\end{bmatrix} \\ \mathbf{d}_w \\ \hline \mathbf{u}\end{bmatrix} \quad (2.53)$$

where the dependency on the wheel spin rate $\Omega$ in certain transfers was omitted for clarity. Let $\mathbf{S}_i = (\mathbf{I} + \mathbf{K}_\mu\widehat{\mathbf{K}}_\Omega\mathbf{G}_u)^{-1}$ and $\mathbf{S}_o = (\mathbf{I} + \mathbf{G}_u\mathbf{K}_\mu\widehat{\mathbf{K}}_\Omega)^{-1}$ denote the input and output sensitivity functions. Similarly, the input complementary sensitivity $\mathbf{T}_i$ and output complementary sensitivity $\mathbf{T}_o$ are defined such that $\mathbf{S}_i + \mathbf{T}_i = \mathbf{I}$ and $\mathbf{S}_o + \mathbf{T}_o = \mathbf{I}$. With the previous definitions, the closed-loop $\mathbf{M}(\Omega) = \left[\begin{array}{c|c}\mathbf{M}_{\mathbf{w}\to\mathbf{z}} & \mathbf{M}_{\mathbf{d}\to\mathbf{z}} \\ \hline \mathbf{M}_{\mathbf{w}\to\mathbf{e}} & \mathbf{M}_{\mathbf{d}\to\mathbf{e}}\end{array}\right] = \mathcal{F}_l(\mathbf{P}, \mathbf{K}_\mu)$ can be written as:

$$\begin{bmatrix}\mathbf{z}_{\Delta u} \\ \mathbf{z}_{\Delta y} \\ \hline \mathbf{e}_p \\ \mathbf{e}_m \\ \mathbf{e}_u \\ \mathbf{e}_y\end{bmatrix} = \underbrace{\operatorname{diag}\left(\begin{array}{c}\mathbf{I} \\ \mathbf{I} \\ \hline \mathbf{W}_p\widehat{\mathbf{K}}_\Omega \\ \mathbf{W}_m \\ \mathbf{W}_u \\ \mathbf{W}_y\end{array}\right)\left[\begin{array}{cc|cc} -\mathbf{T}_i & \mathbf{S}_i\mathbf{K}_\mu\widehat{\mathbf{K}}_\Omega & \mathbf{S}_i\mathbf{K}_\mu\widehat{\mathbf{K}}_\Omega & \mathbf{S}_i\mathbf{K}_\mu\widehat{\mathbf{K}}_\Omega\mathbf{G}_d \\ \mathbf{G}_u\mathbf{S}_i & \mathbf{T}_o & \mathbf{T}_o & \mathbf{S}_o\mathbf{G}_d \\ \hline -\mathbf{G}_u\mathbf{S}_i & \mathbf{S}_o & \mathbf{S}_o & -\mathbf{S}_o\mathbf{G}_d \\ -\mathbf{G}_u\mathbf{S}_i & \mathbf{S}_o & \mathbf{S}_o & -\mathbf{S}_o\mathbf{G}_d \\ -\mathbf{T}_i & \mathbf{S}_i\mathbf{K}_\mu\widehat{\mathbf{K}}_\Omega & \mathbf{S}_i\mathbf{K}_\mu\widehat{\mathbf{K}}_\Omega & \mathbf{S}_i\mathbf{K}_\mu\widehat{\mathbf{K}}_\Omega\mathbf{G}_d \\ \mathbf{G}_u\mathbf{S}_i & \mathbf{T}_o & \mathbf{T}_o & \mathbf{S}_o\mathbf{G}_d\end{array}\right]\operatorname{diag}\left(\begin{array}{c}\mathbf{W}_{\Delta u} \\ \mathbf{W}_{\Delta y} \\ \hline \begin{bmatrix}\mathbf{W}_r \mid \mathbf{N}_r\mathbf{W}_n\end{bmatrix} \\ \mathbf{W}_d\end{array}\right)}_{\mathbf{M}(\Omega)=\mathcal{F}_l(\mathbf{P}(\Omega),\mathbf{K}_\mu)}\begin{bmatrix}\mathbf{w}_{\Delta u} \\ \mathbf{w}_{\Delta y} \\ \hline \begin{bmatrix}\mathbf{d}_r \\ \mathbf{d}_n\end{bmatrix} \\ \mathbf{d}_w\end{bmatrix} \quad (2.54)$$

### Robust stability and performance requirements

If the nominal system (i.e. the block $\mathbf{M}_{\mathbf{d}\to\mathbf{e}}(\Omega)$ in (2.54)) is stable $\forall\Omega \in \boldsymbol{\Omega}$, then the stability of this loop is conditioned by the existence of $(\mathbf{I} - \mathbf{M}_{\mathbf{w}\to\mathbf{z}}(\Omega)\Delta)^{-1}$. This is assessed by evaluating $\mu_{\boldsymbol{\Delta}}\left(\mathbf{M}_{\mathbf{w}\to\mathbf{z}}(\Omega, j\omega)\right)$, where $\mu_{\boldsymbol{\Delta}}(\cdot)$ represents the structured singular value [PD93] defined for a complex matrix $\mathbf{M} \in \mathbb{C}^{m\times m}$ and a set of uncertainties $\Delta \in \boldsymbol{\Delta}$ as:

$$\mu_{\boldsymbol{\Delta}}(\mathbf{M}) = 1/\min\left\{\|\Delta\|_{\mathcal{L}_{2i}} : \Delta \in \boldsymbol{\Delta}, \det(\mathbf{I} - \mathbf{M}\Delta) = 0\right\} \quad (2.55)$$

where $\|\Delta\|_{\mathcal{L}_{2i}}$ denotes the $\mathcal{L}_2$-induced norm (also called $\mathcal{L}_2$ gain) of $\Delta$. If no $\Delta \in \boldsymbol{\Delta}$ makes $\mathbf{I} - \mathbf{M}\Delta$ singular, then $\mu_{\boldsymbol{\Delta}}(\mathbf{M}) := 0$. Following this definition and under the assumption that the nominal system $\mathbf{M}_{\mathbf{d}\to\mathbf{e}}(\Omega)$ is stable for all fixed $\Omega \in \boldsymbol{\Omega}$, then $\mathcal{F}_u(\mathbf{M}(\Omega), \Delta)$ is stable $\forall\Delta \in \boldsymbol{\Delta}, \|\Delta\|_{\mathcal{L}_{2i}} < \nu$ if and only if: $\mu_{\boldsymbol{\Delta}}\left(\mathbf{M}_{\mathbf{w}\to\mathbf{z}}(\Omega, j\omega)\right) < 1/\nu \ ; \ \forall\, \omega \in \mathbb{R}, \Omega \in \boldsymbol{\Omega}$. In this context, $\mu_{\boldsymbol{\Delta}}$ gives a measure of the smallest structured uncertainty $\Delta$ that causes closed-loop instability for any frequency $\omega \in \mathbb{R}$ and wheel rate $\Omega \in \boldsymbol{\Omega}$. Moreover, the $\mathcal{L}_2$ gain of this destabilizing perturbation is exactly $1/\mu_{\boldsymbol{\Delta}}$. This fact will be used to impose the robust stability requirement during the synthesis phase and afterwards to evaluate the stability margin of the loop with respect to different uncertainty structures in the analysis phase. However, due to its nonconvex character $\mu_{\boldsymbol{\Delta}}$ can be difficult

to compute exactly and in order to include these criteria into the control design procedures, $\mu_{\mathbf{\Delta}}$ is replaced with a more conservative upper bound. In this case, the closed-loop system (2.54) is guaranteed to remain stable for any fixed spin rate $\Omega \in \mathbf{\Omega}$ and $\forall \Delta \in \mathbf{\Delta}, \|\Delta\|_{\mathcal{L}_{2i}} < \nu$ if

$$\left( \sup_{\omega \in \mathbb{R}} \mu_{\mathbf{\Delta}} \left( \mathbf{M}_{\mathbf{w} \to \mathbf{z}}(\Omega, j\omega) \right) \leq \inf_{\boldsymbol{\mathcal{D}} \in \mathbb{D}} \left\| \boldsymbol{\mathcal{D}} \mathbf{M}_{\mathbf{w} \to \mathbf{z}}(\Omega) \boldsymbol{\mathcal{D}}^{-1} \right\|_{\mathcal{L}_{2i}} \right) < 1/\nu \quad \forall \Omega \in \mathbf{\Omega} \tag{2.56}$$

where the so-called $D$-scaling matrices $\boldsymbol{\mathcal{D}}$ belong to a set $\mathbb{D}$ such that for any $\boldsymbol{\mathcal{D}} \in \mathbb{D}$ and $\Delta \in \mathbf{\Delta}$ the condition $\boldsymbol{\mathcal{D}}\Delta = \Delta\boldsymbol{\mathcal{D}}$ holds [DPZ91]. This result can also be adapted in order to assess the robust performance requirements **(R2)**. As such, the worst case $\mathcal{L}_2$ gain of the closed-loop system along the transfer $\mathbf{d} \to \mathbf{e}(i)$ remains below $\gamma$ for any $\Omega \in \mathbf{\Omega}$ and $\forall \Delta \in \mathbf{\Delta}$; $\|\Delta\|_{\mathcal{L}_{2i}} \leq \epsilon/\gamma$ with fixed $\epsilon \in [0, 1]$ if and only if

$$\mu_{\mathbf{\Delta}_{RP}} \left( \begin{bmatrix} \sqrt{\epsilon}\mathbf{I} \end{bmatrix} \left[ \begin{array}{c|c} \mathbf{M}_{\mathbf{w} \to \mathbf{z}}(\Omega, j\omega) & \mathbf{M}_{\mathbf{d} \to \mathbf{z}}(\Omega, j\omega) \\ \hline \mathbf{M}_{\mathbf{w} \to \mathbf{e}(i)}(\Omega, j\omega) & \mathbf{M}_{\mathbf{d} \to \mathbf{e}(i)}(\Omega, j\omega) \end{array} \right] \begin{bmatrix} \sqrt{\epsilon}\mathbf{I} \end{bmatrix} \right) < \gamma \quad \forall\, \omega \in \mathbb{R}, \Omega \in \mathbf{\Omega} \tag{2.57}$$

where the set $\mathbf{\Delta}_{RP} = \mathrm{diag}\left(\mathbf{\Delta}, \mathbf{\Delta}_{perf}\right)$ combines the original model uncertainty $\Delta \in \mathbf{\Delta}$ with the set $\Delta_{perf} \in \mathbf{\Delta}_{perf}$ ; $\|\Delta_{perf}\|_{\mathcal{L}_{2i}} < 1$ of fictitious full complex perturbations closing the performance channels $\mathbf{d} \to \mathbf{e}(i)$. As for the robust stability constraint, the requirement is replaced during the design phase with the following upper bound:

$$\left( \begin{array}{l} \sup\limits_{\Delta \in \mathbf{\Delta}, \|\Delta\|_{\mathcal{L}_{2i}} \leq \epsilon/\gamma} \left\| \mathcal{F}_u \left( \mathbf{M}(\Omega), \Delta \right)_{\mathbf{d} \to \mathbf{e}(i)} \right\|_{\mathcal{L}_{2i}} \leq \\ \inf\limits_{\boldsymbol{\mathcal{D}} \in \mathbb{D}} \left\| \begin{bmatrix} \boldsymbol{\mathcal{D}}\sqrt{\epsilon}\mathbf{I} \end{bmatrix} \left[ \begin{array}{c|c} \mathbf{M}_{\mathbf{w} \to \mathbf{z}}(\Omega) & \mathbf{M}_{\mathbf{d} \to \mathbf{z}}(\Omega) \\ \hline \mathbf{M}_{\mathbf{w} \to \mathbf{e}(i)}(\Omega) & \mathbf{M}_{\mathbf{d} \to \mathbf{e}(i)}(\Omega) \end{array} \right] \begin{bmatrix} \sqrt{\epsilon}\boldsymbol{\mathcal{D}}^{-1}\mathbf{I} \end{bmatrix} \right\|_{\mathcal{L}_{2i}} \end{array} \right) < \gamma \quad ; \quad \forall \Omega \in \mathbf{\Omega} \tag{2.58}$$

### 2.4.3 Weighting functions selection and definition of the pre-filter $\widehat{\mathbf{K}}_{\Omega}(\Omega)$

The objective is now to select appropriate values for the weighting functions $\mathbf{W}_{\bullet}$.

The uncertainty matrix $\Delta_u = \mathrm{diag}\left(\delta_{u_1} \dots \delta_{u_6}\right), \delta_{u_\bullet} \in \mathbb{C}, |\delta_{u_\bullet}| \leq 1$ together with the weight $\mathbf{W}_{\Delta u}$ behave as input multiplicative uncertainty $(\mathbf{I}_6 + \mathbf{W}_{\Delta u}\Delta_u)$ acting at the input of the actuator block. The weight $\mathbf{W}_{\Delta u}$ is chosen to provide an upper bound on the multiplicative uncertainty due to the maximum time-delay $\tau_0$ as explained in [WLS94]. An additional 5% multiplicative uncertainty is added to account for the uncertainty in the actuator gains $T_{pma}$ and other unaccounted input uncertainties. Similarly, the weight $\mathbf{W}_{\Delta y}$ together with the uncertainty block $\Delta_y \in \mathbb{C}^{6\times 6}, \|\Delta_y\|_{\mathcal{L}_{2i}} \leq 1$ account for 5% multiplicative output uncertainty in the forces and torques vector $\mathbf{y}$. As the uncertain matrix $\Delta_y$ is chosen as full block, for cross couplings between the output channels are also considered with this uncertainty description. These cross-couplings can result for example from sensor placement uncertainty. With these considerations, $\mathbf{W}_{\Delta u}$ and $\mathbf{W}_{\Delta y}$ are chosen as:

$$\mathbf{W}_{\Delta u} = \left( \frac{\tau_0 s}{1 + \tau_0 s/3.465} + 0.05 \right) \mathbf{I}_6 \quad \text{and} \quad \mathbf{W}_{\Delta y} = 0.05\, \mathbf{I}_6 \tag{2.59}$$

**Remark 3.** *The resulting uncertain dynamics provided by $\Delta$ with the weights $\mathbf{W}_{\Delta u}$ and $\mathbf{W}_{\Delta y}$ defines a model set chosen large enough to include several important uncertainties such as uncertain time-delays, uncertain actuator gains and sensor placement as well as variations in mass, stiffness and damping coefficients. Although this is an approximation of the true uncertainty set, the input uncertainty model captures the dominant uncertainties of the system and allows for a simpler weight tuning process.*

As a preliminary step, all external disturbances are scaled based on the expected maximum values. The sensor measurement noise $\mathbf{n}(t) \in \mathbb{R}^{12}$ is considered to affect each of the twelve sensor measurements independently and in equal measure.

Based on the sensitivity limit of the piezoelectric sensors and the associated signal-to-noise ratio, it is assumed that each of the force measurements will be corrupted by additive zero-mean white gaussian noise with an upper bound of $n_{max} = 10^{-3}\text{N}/\sqrt{\text{Hz}}$ on its amplitude spectral density. In this case, the weight $\mathbf{W}_n$ is fixed to

$$\mathbf{W}_n = n_{max}\mathbf{I}_{12} \quad ; \quad n_{max} = 10^{-3}\text{N}/\sqrt{\text{Hz}} \tag{2.60}$$

in order to scale the normalized unit white noise signal $\mathbf{d}_n$ and thus capture the maximum measurement noise spectrum.

Similarly, the matrix $\mathbf{W}_d$ is used to scale the normalized reaction wheel disturbance vector $\mathbf{d}_w$. According to the wheel perturbation model (2.6) and considering a maximum $\Omega = 50$ Hz, the maximum disturbances are 0.7 N for radial forces $\begin{bmatrix} F_x & F_y \end{bmatrix}$, 0.3 Nm for radial torques $\begin{bmatrix} T_x & T_y \end{bmatrix}$, 0.35 N for axial forces $F_z$ and 0.2 Nm for the motor torques jitter $T_{zbn}$ . The weight $\mathbf{W}_d$ is therefore chosen as:

$$\mathbf{W}_d = \text{diag}\begin{pmatrix} 0.7\,\text{N} & 0.7\,\text{N} & 0.35\,\text{N} & 0.3\,\text{Nm} & 0.3\,\text{Nm} & 0.2\,\text{Nm} \end{pmatrix} \tag{2.61}$$

It was previously shown that the open-loop system (2.52) is stable and that the transfer matrix from reaction wheel disturbance $\mathbf{u}_w$ to transmitted forces and torques $\mathbf{y}_s$ is given by $\mathbf{G}_d(\Omega)$.

Based on this transfer matrix and the reaction wheel disturbance model in (2.6), the weight $\mathbf{W}_y$ is chosen as the inverse of the maximum transmitted forces and torques $\mathbf{y}_s$ observed during open-loop simulations for typical reaction wheel speed profiles $\Omega(t)$. In this way, the outputs $\mathbf{e}_y = \mathbf{W}_y\mathbf{y}_s$ are scaled to one for all the considered open-loop scenarios by using the following weight values:

$$\mathbf{W}_y = \text{diag}\begin{pmatrix} 1.4\,\text{N} & 1.4\,\text{N} & 0.16\,\text{N} & 0.19\,\text{Nm} & 0.19\,\text{Nm} & 0.2\,\text{Nm} \end{pmatrix}^{-1} \tag{2.62}$$

This corresponds to a maximum transmitted lateral forces $F_{su}$, $F_{sv}$ of 1.4 N, lateral torques $T_{su}$, $T_{sv}$ of 0.19 Nm, axial force $F_{sw}$ of 0.16 N and axial torque $T_{sw}$ of 0.2 Nm.

Let the disturbance rejection requirement be now considered. The closed-loop transfer between wheel disturbances $\mathbf{d}_w$ and sensor noise $\mathbf{d}_n$ to the scaled output forces and torques $\mathbf{e}_y = \mathbf{W}_y\mathbf{y}_s$ is given by:

$$\mathbf{d}_w \to \mathbf{e}_y = \mathbf{W}_y\mathbf{S}_o\mathbf{G}_d\mathbf{W}_d \quad \text{and} \quad \mathbf{d}_n \to \mathbf{e}_y = \mathbf{W}_y\mathbf{T}_o\mathbf{N}_r\mathbf{W}_n \tag{2.63}$$

It should be noted that the output sensitivity function $\mathbf{S}_o$ also appears in the transfer from the references $\mathbf{d}_r$ to weighted error outputs $\mathbf{e}_p$ given by $\mathbf{d}_r \to \mathbf{e}_p = \mathbf{W}_p\widehat{\mathbf{K}}_\Omega\mathbf{S}_o\mathbf{W}_r$. Therefore, the disturbance requirement will be enforced by shaping the sensitivity $\mathbf{S}_o$ through an appropriate choice of the weighting functions $\mathbf{W}_r$ and $\mathbf{W}_p\widehat{\mathbf{K}}_\Omega$.

During controller operation, the reference signal $\mathbf{d}_r$ is always kept at $\mathbf{d}_r = \mathbf{0}$ and it is thus introduced purely as a mathematical tool to enforce the proper shape of $\mathbf{S}_o$ through the selection of the filters $\mathbf{W}_p$, $\widehat{\mathbf{K}}_\Omega$ and $\mathbf{W}_r$. In this case, the weight $\mathbf{W}_r$ is chosen as

$$\mathbf{W}_r = \mathbf{W}_y^{-1} \tag{2.64}$$

and has the role of scaling the reference $\mathbf{d}_r$ based the maximum open-loop values of the transmitted forces and torques. The weight $\mathbf{W}_p$ is used to set a lower bound on the desired closed-loop disturbance attenuation level. This leads to the following choice of $\mathbf{W}_p$:

$$\mathbf{W}_p = \text{diag}\begin{pmatrix} 20 & 20 & 20 & 10 & 10 & 10 \end{pmatrix}\text{dB} \cdot \mathbf{W}_r^{-1} \tag{2.65}$$

It corresponds to a desired attenuation of at least 20 dB in the force transmissibility and 10 dB for torque transmissibility. The term $\mathbf{W}_r^{-1}$ is used to scale back the signals $\mathbf{d}_r$.

Coming back to the pre-filter $\widehat{\mathbf{K}}_\Omega(\Omega)$, it is used to reject only the main harmonic disturbance of the reaction wheel as explained previously. Therefore, $\widehat{\mathbf{K}}_\Omega(\Omega)$ is chosen to filter each of its six input channels through unit gain second order bandpass filters parameterized by the wheel speed $\Omega$ i.e.

$$\widehat{\mathbf{K}}_\Omega(\Omega) = w_\Omega(s)\mathbf{I}_6 \quad ; \quad w_\Omega(s) = \frac{Bs}{s^2 + Bs + \Omega^2} = \mathcal{F}_u\left(\left[\begin{array}{cc|c} -B & -\Omega & B \\ \Omega & 0 & 0 \\ \hline 1 & 0 & 0 \end{array}\right], \frac{1}{s}\mathbf{I}_2\right) \tag{2.66}$$

where the bandwidth $B$ refers to the width in rad/s between the upper and lower cut-off frequencies at which the gain of the filter is down 3 dB from its response at the central frequency $\Omega$. This parameter is also related to the Q-factor $Q$, damping ratio $\xi$ and attenuation rate $\alpha$ of the bandpass filter through the following relationship:

$$B = \Omega/Q = 2\xi\Omega = 2\alpha \tag{2.67}$$

A decrease in $B$ forces the filter to become narrower, increasing its Q-factor and putting more emphasis on the frequencies around $\Omega$. For performance reasons, it is desired to maximize this bandwidth and therefore ensure that a larger region around the main harmonic $\Omega$ is attenuated. However, due to Bode's integral theorem, also known as the waterbed effect, an unavoidable consequence of improving the disturbance attenuation around some frequencies is disturbance amplification at other frequencies [RLD10]. As such, the filter's bandwidth can't be set arbitrarily high without severely impacting the disturbance transmissibility outside of $\Omega$. Additionally, the bandwidth can't be set too low as this will induce a low attenuation rate $\alpha$ and a slow convergence of the filter. To accommodate these constraints and maximize performance, the bandwidth $B$ can be considered as function of $\Omega$. Replacing $B$ in (2.66) with the affine dependency $B(\Omega) = b_A + b_M\Omega$, leads to:

$$\begin{aligned} w_\Omega(s) &= \mathcal{F}_u\left(\left[\begin{array}{cc|c} -b_A & 0 & b_A \\ 0 & 0 & 0 \\ \hline 1 & 0 & 0 \end{array}\right] + \left[\begin{array}{cc|c} -b_M & -1 & \\ 1 & 0 & \\ \hline 0 & 0 & \end{array}\right] \Omega\mathbf{I}_2 \left[\begin{array}{cc|c} 1 & 0 & 0 \\ 0 & 1 & -b_M \end{array}\right], \frac{1}{s}\mathbf{I}_2\right) \\ &= \mathcal{F}_u\Big(\overline{w}_\Omega(s), \Omega\,\mathbf{I}_2\Big) \quad \text{with} \quad \overline{w}_\Omega(s) = \mathcal{F}_u\left(\left[\begin{array}{cc|ccc} -b_A & 0 & -b_M & -1 & b_A \\ 0 & 0 & 1 & 0 & 0 \\ \hline 1 & 0 & 0 & 0 & 0 \\ 0 & 1 & 0 & 0 & -b_M \\ 1 & 0 & 0 & 0 & 0 \end{array}\right], \frac{1}{s}\mathbf{I}_2\right) \end{aligned} \tag{2.68}$$

Combining six $w_\Omega(s)$ into the overall pre-filter $\widehat{\mathbf{K}}_\Omega(\Omega)$, leads to the following LFT description:

$$\widehat{\mathbf{K}}_\Omega(\Omega) = w_\Omega(s)\mathbf{I}_6 = \mathcal{F}_u\left(\widehat{\mathbf{K}}_\Omega, \Omega\,\mathbf{I}_{12}\right) \tag{2.69}$$

Let $B_{20}(\Omega)$ and $B_{10}(\Omega)$ be defined as the bandwidths in Hz around $\Omega$ where the response of $\widehat{\mathbf{K}}_\Omega(\Omega)$ drops by 20 dB and 10 dB respectively from the response at $\Omega$. The bandwidths therefore correspond to the regions around $\Omega$ where the force and respectively the torque attenuation requirements introduced through $\mathbf{W}_p\widehat{\mathbf{K}}_\Omega(\Omega)$ drop to 0 dB. For the current setup, the choice was made to fix $b_M = 1/150$ and $b_A = 0.01$. For this parameter choice, the attenuation bandwidth $B_{10}$ is around 0.24 Hz at $\Omega = 10$ Hz and grows to 1.86 Hz at $\Omega = 50$ Hz as shown in fig. 2.18.

To control the maximum amplification due to the waterbed effect, the output performance channel $\mathbf{e}_m$ is introduced, see fig. 2.17 if necessary. The transfer from the references $\mathbf{d}_r$ to $\mathbf{e}_m$ is given by

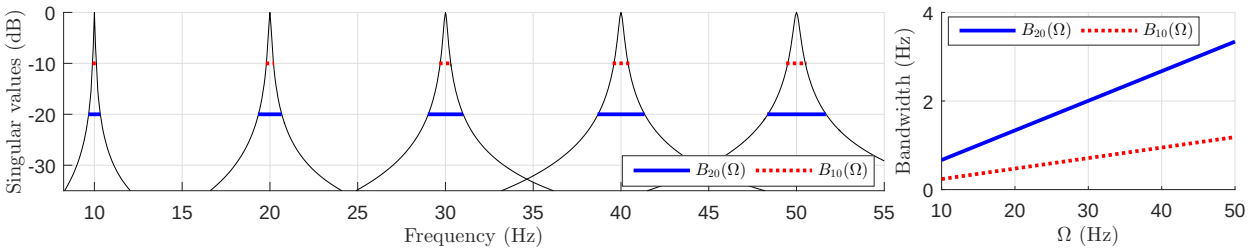


Figure 2.18: Singular values of $\widehat{\mathbf{K}}_\Omega(\Omega)$ and the corresponding attenuation bandwidths $B_{10}(\Omega)$ and $B_{20}(\Omega)$ for different $\Omega \in [10, 50]$ Hz.

$\mathbf{d}_r \to \mathbf{e}_m = \mathbf{W}_m \mathbf{S}_o \mathbf{W}_r$. The filter $\mathbf{W}_m$ is thus used to place an upper bound on the $\mathbf{S}_o$, thereby limiting the disturbance amplification outside the main harmonic $\Omega$. At high frequencies outside the controller bandwidth $\|\mathbf{S}_o\|_{\mathcal{L}_{2i}} \approx 1$ and it follows that $\mathbf{W}_m$ needs at least to satisfy the following inequality $\|\mathbf{W}_m \mathbf{N}_r \mathbf{W}_n\|_{\mathcal{L}_{2i}} < 1$. With the previous considerations in mind, an upper bound of 6 dB disturbances amplification for each channel is imposed with the following weight choice:

$$\mathbf{W}_m = 6\,\text{dB} \cdot \mathbf{W}_r^{-1} \tag{2.70}$$

Finally, the last weight $\mathbf{W}_u$ is used to take into account the maximum actuator effort requirement. Reaction wheel disturbances impact the PMA signals though the transfer matrix $\mathbf{d}' \to \mathbf{u}_s = \mathbf{S}_i \mathbf{K}_\mu \widehat{\mathbf{K}}_\Omega \mathbf{G}_d$. The function $\mathbf{S}_i \mathbf{K}_\mu \widehat{\mathbf{K}}_\Omega$ also appears inside the transfer from the references $\mathbf{d}_r$ to $\mathbf{e}_u$ given by $\mathbf{d}_r \to \mathbf{e}_u = \mathbf{W}_u \mathbf{S}_i \mathbf{K}_\mu \widehat{\mathbf{K}}_\Omega \mathbf{W}_r$. The weight $\mathbf{W}_u$ is chosen as the following bandpass filter:

$$\mathbf{W}_u = \left( \frac{1}{u_{max}} \cdot \underbrace{\frac{s + \alpha\omega_1}{s + \omega_1}}_{\text{Low pass}} \cdot \underbrace{\frac{\alpha s + \omega_2}{s + \omega_2}}_{\text{High pass}} \right) \mathbf{I}_6 \quad \text{with} \quad u_{max} = 10\text{V} \quad \text{and} \quad \begin{array}{l} \alpha = 20 \\ \omega_1 = 30 \times 10^{-2}\,\text{Hz} \\ \omega_2 = 30 \times 10^{2}\,\text{Hz} \end{array} \tag{2.71}$$

This choice enforces an upper bound $u_{max} = 10\,\text{V}$ on each component of the actuator signal vector $\mathbf{u}$ within the control bandwidth $[10, 50]\,\text{Hz}$ and also guarantees that these signals are attenuated by least $\alpha = 20$, at both high and low frequencies.

For clarity, the singular values for the $\widehat{\mathbf{K}}_\Omega$, $\mathbf{W}_u$ and $\mathbf{W}_{\Delta u}$ weights are illustrated in fig. 2.19.

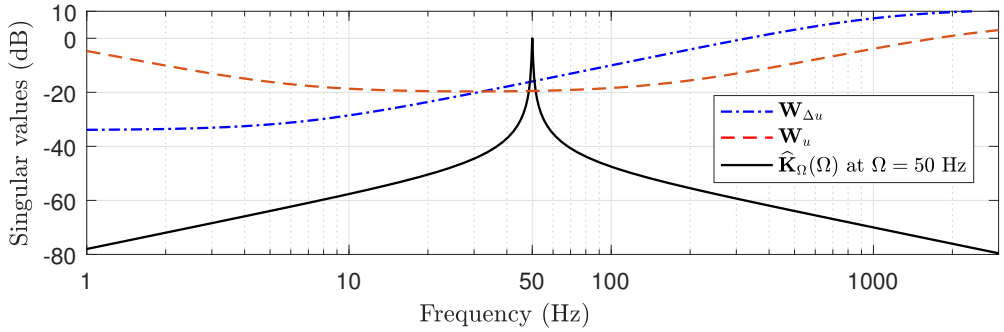


Figure 2.19: Singular values for the control effort weight $\mathbf{W}_u$, the input uncertainty weight $\mathbf{W}_{\Delta u}$ and the pre-filter $\widehat{\mathbf{K}}_\Omega$ at $\Omega = 50\,\text{Hz}$.

### 2.4.4 Controller synthesis procedure

From $\mu$ theory, it follows that:

1. the closed-loop (2.54) illustrated in fig. 2.17 is robustly stable for all uncertainties $\Delta$ if

$$\inf_{\boldsymbol{\mathcal{D}}\in\mathbb{D}} \left\|\boldsymbol{\mathcal{D}}\mathbf{M}_{\mathbf{w}\to\mathbf{z}}\boldsymbol{\mathcal{D}}^{-1}\right\|_{\mathcal{L}_{2i}} = \inf_{\boldsymbol{\mathcal{D}}\in\mathbb{D}} \left\|\boldsymbol{\mathcal{D}}\begin{bmatrix}-\mathbf{T}_i & \mathbf{S}_i\mathbf{K}_\mu\widehat{\mathbf{K}}_\Omega \\ \mathbf{G}_u\mathbf{S}_i & \mathbf{T}_o\end{bmatrix}\mathbf{W}_\Delta\boldsymbol{\mathcal{D}}^{-1}\right\|_{\mathcal{L}_{2i}} < 1 \tag{2.72}$$

where $\mathbf{W}_\Delta = \operatorname{diag}\begin{pmatrix}\mathbf{W}_{\Delta u} & \mathbf{W}_{\Delta y}\end{pmatrix}$ and $\boldsymbol{\mathcal{D}} \in \mathbb{D}$ is known as the $D$-scaling matrix that commutes with $\Delta$, i.e. $\boldsymbol{\mathcal{D}}\Delta = \Delta\boldsymbol{\mathcal{D}}$; $\forall\Delta \in \boldsymbol{\Delta}, \boldsymbol{\mathcal{D}} \in \mathbb{D}$.

2. the nominal disturbance rejection requirement for each component $\mathbf{e}_p(i)$ of the performance output channel $\mathbf{e}_p$ is achieved whenever the following following constraint holds:

$$\|\mathbf{d}_r \to \mathbf{e}_p(i)\|_{\mathcal{L}_{2i}} = \left\|\boldsymbol{\mathcal{X}}(i)\mathbf{W}_p\widehat{\mathbf{K}}_\Omega\mathbf{S}_o\mathbf{W}_r\right\|_{\mathcal{L}_{2i}} < 1 \quad , \quad i = \{1,\dots,6\} \tag{2.73}$$

Here, $\boldsymbol{\mathcal{X}}(i) = \begin{bmatrix}\mathbf{0}_{1\times(i-1)} & 1 & \mathbf{0}_{1\times(6-i)}\end{bmatrix}$ is a selection vector used to select the $i$-th channel.

3. the disturbance attenuation requirements (2.73) achieve robust performance on the $i$-th channel with $i = \{1,\dots,6\}$ for all $\Delta \in \boldsymbol{\Delta}$ if

$$\inf_{\boldsymbol{\mathcal{D}}_i\in\mathbb{D}} \left\|\operatorname{diag}\left(\frac{\boldsymbol{\mathcal{D}}_i}{\boldsymbol{\mathcal{X}}(i)\mathbf{W}_p\widehat{\mathbf{K}}_\Omega}\right)\left[\begin{array}{cc|c} -\mathbf{T}_i & \mathbf{S}_i\mathbf{K}_\mu\widehat{\mathbf{K}}_\Omega & \mathbf{S}_i\mathbf{K}_\mu\widehat{\mathbf{K}}_\Omega \\ \mathbf{G}_u\mathbf{S}_i & \mathbf{T}_o & \mathbf{T}_o \\ \hline -\mathbf{G}_u\mathbf{S}_i & \mathbf{S}_o & \mathbf{S}_o \end{array}\right]\operatorname{diag}\left(\frac{\mathbf{W}_\Delta\boldsymbol{\mathcal{D}}_i^{-1}}{\mathbf{W}_r}\right)\right\|_{\mathcal{L}_{2i}} < 1 \tag{2.74}$$

where $\boldsymbol{\mathcal{D}}_i$ are the D-scales that commute with $\Delta$.

4. the maximum disturbance amplification requirements on each component of $\mathbf{e}_m$ is given by:

$$\|\mathbf{d}_r \to \mathbf{e}_m(i)\|_{\mathcal{L}_{2i}} = \|\boldsymbol{\mathcal{X}}(i)\mathbf{W}_m\mathbf{S}_o\mathbf{W}_r\|_{\mathcal{L}_{2i}} < 1 \quad , \quad i = \{1,\dots,6\} \tag{2.75}$$

5. for each of the six actuators the nominal actuator effort requirement is given by

$$\|\mathbf{d}_r \to \mathbf{e}_u(i)\|_{\mathcal{L}_{2i}} = \left\|\boldsymbol{\mathcal{X}}(i)\mathbf{W}_u\mathbf{S}_i\mathbf{K}_\mu\widehat{\mathbf{K}}_\Omega\mathbf{W}_r\right\|_{\mathcal{L}_{2i}} < 1 \quad , \quad i = \{1,\dots,6\} \tag{2.76}$$

These constraints can be solved using the nonsmooth $\mathcal{H}_\infty$ optimization approach, i.e. combining the above formulated requirements, the problem to be solved can be formulated according to:

$$\begin{aligned} \underset{\mathbf{K}_\mu\ \boldsymbol{\mathcal{D}}\ \boldsymbol{\mathcal{D}}_i}{\text{minimize}} \quad \gamma \quad \text{s.t.} \quad & \left\|\boldsymbol{\mathcal{D}}\mathbf{M}_{\mathbf{w}\to\mathbf{z}}\boldsymbol{\mathcal{D}}^{-1}\right\|_{\mathcal{L}_{2i}} < 1 \\ & \left\|\operatorname{diag}\left(\begin{bmatrix}\boldsymbol{\mathcal{D}}_i & \\ & \boldsymbol{\mathcal{X}}(i)\end{bmatrix}\begin{bmatrix}\mathbf{M}_{\mathbf{w}\to\mathbf{z}} & \mathbf{M}_{\mathbf{w}\to\mathbf{d}} \\ \mathbf{M}_{\mathbf{w}\to\mathbf{e}} & \mathbf{M}_{\mathbf{d}\to\mathbf{e}}\end{bmatrix}\begin{bmatrix}\boldsymbol{\mathcal{D}}_i^{-1} & \\ & \mathbf{I}\end{bmatrix},\dots,\boldsymbol{\mathcal{X}}(j)\mathbf{M}_{\mathbf{d}\to\mathbf{e}}\right)\right\|_{\mathcal{L}_{2i}} < \gamma \\ & i = \{1,\dots,6\} \quad j = \{7,\dots,18\} \quad \forall\Omega \in \boldsymbol{\Omega} \end{aligned} \tag{2.77}$$

The constraint $\left\|\boldsymbol{\mathcal{D}}\mathbf{M}_{\mathbf{w}\to\mathbf{z}}\boldsymbol{\mathcal{D}}^{-1}\right\|_{\mathcal{L}_{2i}} < 1$ ensures robust stability while $\left\|\begin{bmatrix}\boldsymbol{\mathcal{D}}_i & \boldsymbol{\mathcal{X}}(i)\end{bmatrix}\mathbf{M}\begin{bmatrix}\boldsymbol{\mathcal{D}}_i^{-1} & \\ & \mathbf{I}\end{bmatrix}\right\|_{\mathcal{L}_{2i}} < \gamma$ and $\|\boldsymbol{\mathcal{X}}(j)\mathbf{M}_{\mathbf{d}\to\mathbf{e}}\|_{\mathcal{L}_{2i}} < \gamma$ are used to guarantee a minimum robust performance level $\gamma$ for the $\mathbf{e}_p$ performance channels and a minimum nominal performance level $\gamma$ for the $\mathbf{e}_m$ and $\mathbf{e}_u$ channels, see fig. 2.17 for the meaning of these signals if necessary. When $\gamma < 1$ all the required objectives are achieved.

As it is formulated, problem (2.77) does not admit a solution since it is required for the constraints to be satisfied over an infinite number of frequencies $\Omega \in \boldsymbol{\Omega}$. A solution to this problem consists in using a griding approach, leading the constraints to be finite which is suitable for the nonsmooth $\mathcal{H}_\infty$ technique, the problem being reformulated in a multi-model manner. Furthermore, one the issues with the nonsmooth $\mathcal{H}_\infty$ tool is that it is highly dependent on the initial conditions and does not guarantee convergence to a global minimum. However, by employing the following procedure, satisfactory results are obtained:

**Step 1:** Let $\overline{\mathbf{\Omega}}$ be grid across the domain of the scheduling parameter $\mathbf{\Omega} = [10, 50]$ Hz.

**Step 2:** For each $\Omega_j \in \overline{\mathbf{\Omega}}$, synthesize a full order nominal controller $\mathbf{K}_j$ using standard $\mathcal{H}_\infty$ algorithms, i.e solve:

$$\underset{\mathbf{K}_j}{\text{minimize}} \quad \gamma \quad \text{s.t.} \quad \|\mathbf{M}_{\mathbf{d}\to\mathbf{e}}(\Omega_j)\|_{\mathcal{L}_{2i}} < \gamma$$

**Step 3:** Perform a balanced model reduction of each $\mathbf{K}_j$. The resulting reduced controllers $\overline{\mathbf{K}}_j$ are of order 20.

**Step 4:** With each controller $\overline{\mathbf{K}}_j$ initialize the optimization problem (2.77) and solve it over the finite grid $\overline{\mathbf{\Omega}}$. The $D$-scales are used as optimization variables with a fixed structure compatible with the $\Delta$ block. The resulting performance level is $\gamma_j$ for each controller.

**Step 5:** Initialize (2.77) with the the best performing controller from the previous step (i.e. lowest $\gamma_j$) and the associated D-scales. Consider $\Omega$ an uncertain parameter and optimize using the nonsmooth parametric robust controller design technique proposed in [ADN15].

**Result:** The resulting controller $\mathbf{K}_\mu$ has 20 states and achieves a closed-loop performance of $\gamma = 0.878$.

The singular values of $\mathbf{K}_\mu$ and those of $\mathbf{K}_\mu\widehat{\mathbf{K}}_\Omega(\Omega)$ (which represents the overall vibration mitigation controller from (2.49)) are shown[1] in fig. 2.20 for $\Omega \in \{10, 30, 50\}$Hz. As expected, the controller has the highest gain around the central frequency $\Omega$. This helps to guarantee that the output sensitivity $\mathbf{S}_o = (\mathbf{I} + \mathbf{G}_u\mathbf{K}_\mu\widehat{\mathbf{K}}_\Omega(\Omega))^{-1}$ has low gain around $\Omega$ and hence comforts the disturbance rejection requirements (2.74). Additionally, it can be seen that the controller gains roll off at both high and low frequency as dictated by the control effort requirements (2.76) and by the robust stability condition (2.72). Since the associated performance level $\gamma = 0.878$ is below unity, the

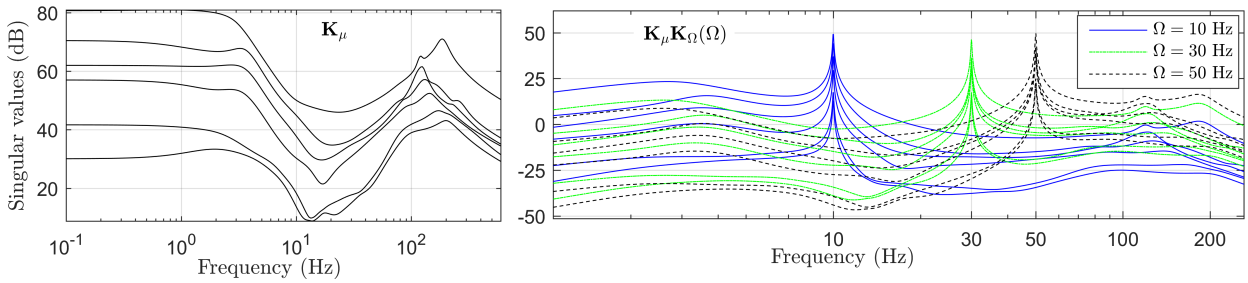


Figure 2.20: Singular values of $\mathbf{K}_\mu$ (left) and $\mathbf{K}_\mu\widehat{\mathbf{K}}_\Omega(\Omega)$ (right) for the spin rates $\Omega \in \{10, 30, 50\}$ Hz.

required robust stability and performance requirements are achieved for the reduced uncertainty structure $\Delta = \text{diag}\begin{pmatrix}\Delta_u & \Delta_y\end{pmatrix}$. However, there is no guarantee that robust stability and performance are achieved once the uncertainties $\Delta_h, \Delta_G$ and $\Delta_n$ are included. This problem is addressed in the following sections.

## 2.5 Stability and performance analysis

In this section, robust stability, robust performance and worst case analysis are addressed to evaluate the ability of the obtained controller to achieve the desired specifications. As explained

[1]Note that only three values of $\Omega$ are considered in figs. 2.20 to 2.22 to provide an improved readability. The analysis however has been done for across a much denser grid over frequencies

previously, the LFT model illustrated on fig. 2.17 is used for that purpose without any kind of reduction. However, nominal performance is first assessed since it exhibits interesting properties of the controller.

### Nominal performance

Nominal performances are assessed by fixing $\Delta = 0$ and examining the singular values of the closed-loop transfer from $\mathbf{d} = \begin{bmatrix}\mathbf{d}_r^\mathsf{T} & \mathbf{d}_n^\mathsf{T} & \mathbf{d}_w^\mathsf{T}\end{bmatrix}^\mathsf{T}$ to each component of the performance channels $\mathbf{e}_p$, $\mathbf{e}_m$ and $\mathbf{e}_u$. The results are shown in fig. 2.21 for different values of $\Omega$. It can be observed that the maximum singular values of each transfer is less than one for each $\Omega$. Therefore, it follows that the requirements **R1-R3** are met, see section 2.4.1.

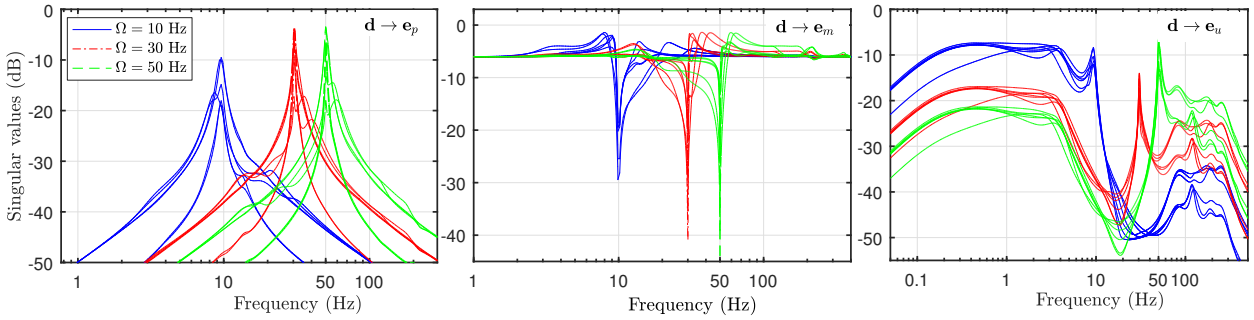


Figure 2.21: Singular values of the nominal transfer from external disturbances $\mathbf{d}$ to the performance channels $\mathbf{e}_p$, $\mathbf{e}_m$ and $\mathbf{e}_u$ for $\Omega \in \{10, 30, 50\}$ Hz.

The nominal disturbance attenuation capability of the solution can also be visualized by considering the transfer from the disturbances $\mathbf{d}$ to the components of the transmitted forces and torques vector $\mathbf{y}_s$ defined in (2.20). The singular value plots for these transfers are shown in fig. 2.22 for $\Omega \in \{10, 30, 50\}$Hz and overlaid with the open-loop responses. It is clear that the proposed solution significantly decreases the transmissibility in the region of $\Omega$ around the main harmonic disturbance. The amplifications due to the waterbed effect around $\Omega$ are within the desired 6 dB bounds.

### Robust stability assessment

Following the structured singular value ($\mu$) theory, robust stability for a given $\Omega$ is assessed by calculating $\mu_{\mathbf{\Delta}}\left(\mathbf{M}_{\mathbf{w}\to\mathbf{z}}(\Omega,\omega)\right), \forall\omega \in \mathbb{R}$ where $\mathbf{\Delta}$ is the structure associated to the uncertainty block $\Delta = \text{diag}\begin{pmatrix}\Delta_h & \Delta_G & \Delta_n\end{pmatrix} \in \mathbf{\Delta}$ and $\mathbf{M}_{\mathbf{w}\to\mathbf{z}}$ is deduced from fig. 2.17 in a similar manner to (2.54). In this case, robust stability is achieved over all $\Delta \in \mathbf{\Delta}$ if and only if $\sup_\omega \mu_{\mathbf{\Delta}}\left(\mathbf{M}_{\mathbf{w}\to\mathbf{z}}(\Omega,\omega)\right) < 1$. Figure 2.23 shows the $\mu$ (upper bound) plot across a grid of 50 values of $\Omega \in \mathbf{\Omega}$ and for frequencies $\omega \in [0.1,\ 600]$ Hz covering the whole dynamical range of the system. It can be seen that $\mu_{\mathbf{\Delta}}\left(\mathbf{M}_{\mathbf{w}\to\mathbf{z}}(\Omega,\omega)\right) < 1, \forall\omega$ at each sampled value of $\Omega$. Robust stability is therefore guaranteed for any $\Delta \in \mathbf{\Delta}$ at those speeds. It can be noted too that the $\mu$ function peaks in the frequencies adjacent to the $\Omega$. Accurate $\mu_{\mathbf{\Delta}}\left(\mathbf{M}_{\mathbf{w}\to\mathbf{z}}(\Omega,\omega)\right)$ is thus calculated in this region, both upper and lower bounds. The results are shown in fig. 2.24 for $\Omega = 10$ Hz (top-left) and $\Omega = 50$ Hz (bottom-left). The right part of the figure illustrates the parametric sensitivities plots of $\mu_{\mathbf{\Delta}}\left(\mathbf{M}_{\mathbf{w}\to\mathbf{z}}(\Omega,\omega)\right)$ with respect to each normalized parameter $\delta_\bullet$ that appears in $\Delta$ , i.e. the so called $\mu$-sensitivity functions. These plots provide a valuable tool to identify which parameters have the most impact on the stability margin in a certain frequency range. In the interest of clarity, only the parameters

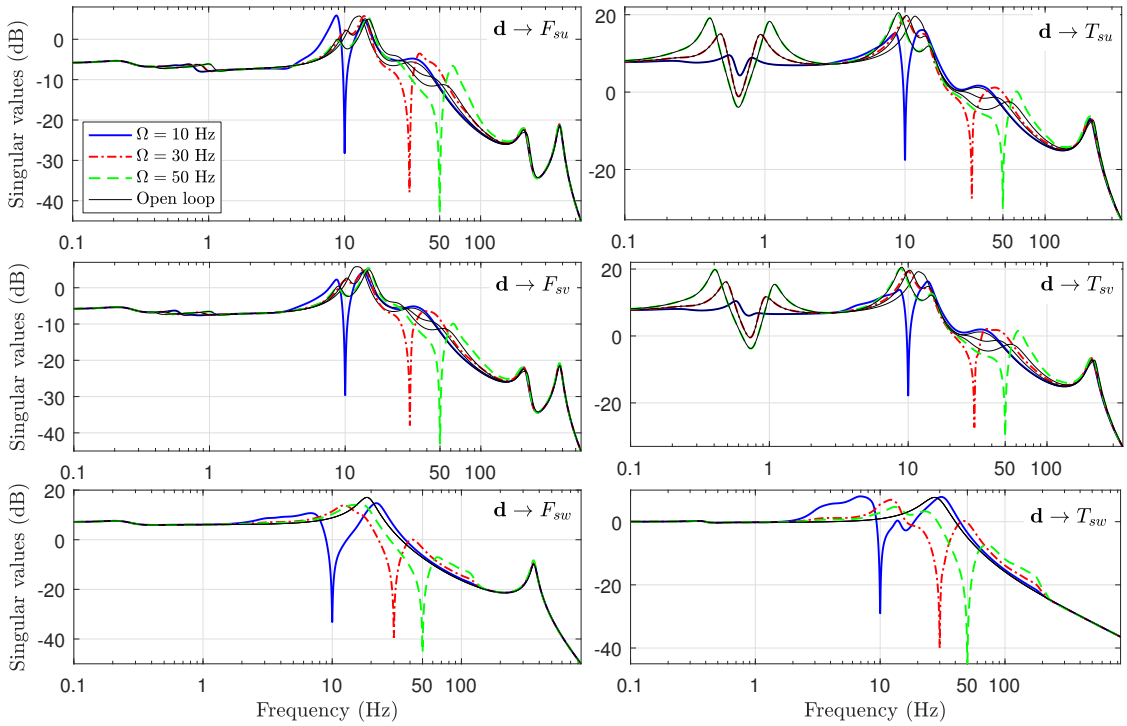


Figure 2.22: Closed-loop nominal force and torque transmissibility: singular values from the total disturbance vector $\mathbf{d}$ to each of the elastic forces and torques between the active and interface plates i.e. $\mathbf{y}_s = \left[\mathbf{f}_s^\mathsf{T} \;\middle|\; \mathbf{t}_s^\mathsf{T}\right]^\mathsf{T} = \left[F_{su} \;\; F_{sv} \;\; F_{sw} \;\middle|\; T_{su} \;\; T_{sv} \;\; T_{sw}\right]^\mathsf{T}$.

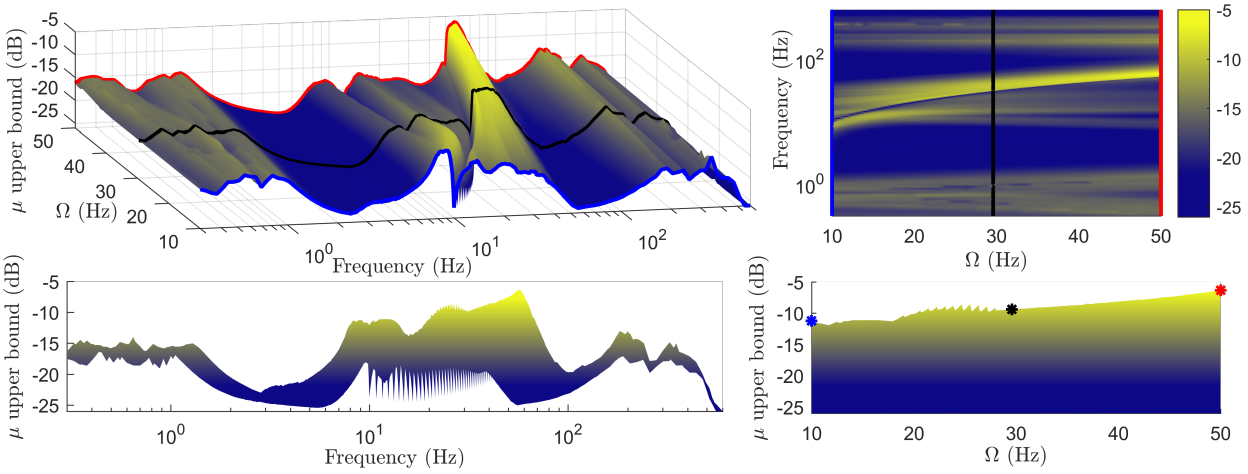


Figure 2.23: Robust stability $\mu$-plots for $\Omega \in [10, 50]$ Hz.

with the highest sensitivity gains are plotted, in decreasing order of importance. Examining these plots, it can be seen that when $\Omega = 10$ Hz, the margin is about 9 dB and is strongly influenced by uncertainties in the actuator gains $T_{pma_\bullet}$ and orientations $\phi_\bullet$. At $\Omega = 50$ Hz the margin drops to around 5 dB, mainly due to the fact that as the controller bandwidth increases, the uncertain time delays $\tau_\bullet$ play a much higher role.

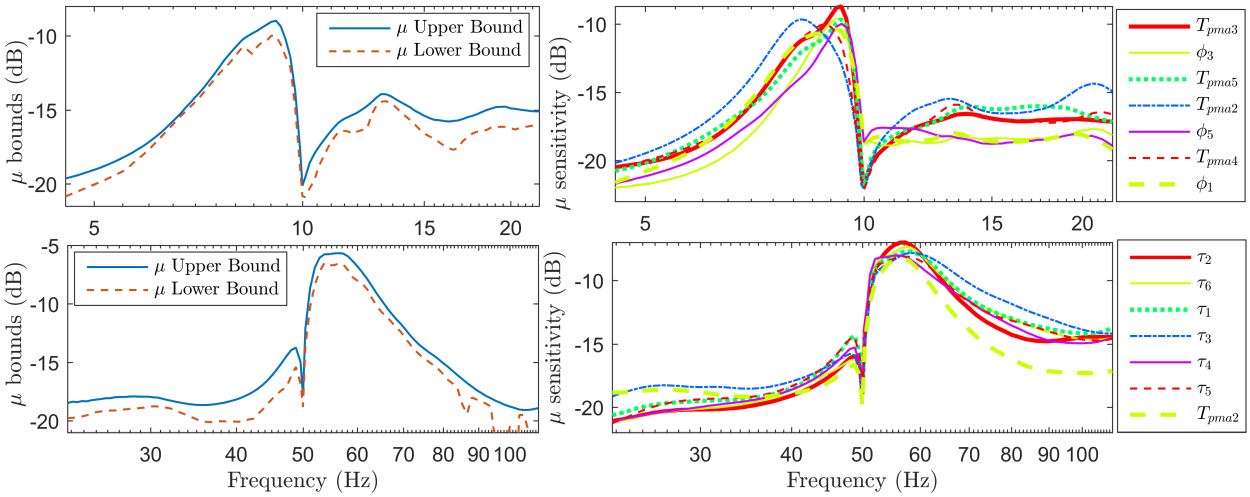


Figure 2.24: Robust stability $\mu$-bounds and $\mu$ sensitivty plots for $\Omega = 10$Hz (top) and $\Omega = 50$Hz (bottom).

### Robust performance

To study the degradation of the nominal performance under the influence of the uncertainty bock $\Delta$, the $\mu$ function is evaluated for the transfers from the performance input $\mathbf{d} = \begin{bmatrix}\mathbf{d}_r^\mathsf{T} & \mathbf{d}_n^\mathsf{T} & \mathbf{d}_w^\mathsf{T}\end{bmatrix}^\mathsf{T}$ to each component of the performance channels $\mathbf{e}_p$, $\mathbf{e}_m$ and $\mathbf{e}_u$. The results are shown in fig. 2.25 for multiple $\Omega \in \mathbf{\Omega}$. As all $\mu$-functions are less than one for each component of $\mathbf{e}_p$ and $\mathbf{e}_u$, it

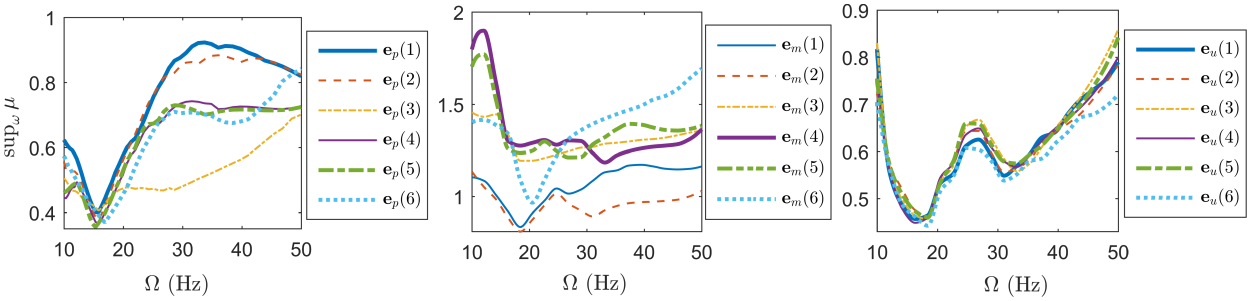


Figure 2.25: Robust performance results: upper bounds on $\mu_{\mathbf{\Delta}_{RP}}$ for the transfers from disturbance $\mathbf{d}$ to performance channels $\mathbf{e}_p$, $\mathbf{e}_m$ and $\mathbf{e}_u$ for $\Omega \in \mathbf{\Omega}$.

follows that the requirements on disturbance attenuation $\|\mathbf{d} \to \mathbf{e}_p\|_{\mathcal{L}_{2i}} < 1$ and control signal effort $\|\mathbf{d} \to \mathbf{e}_m\|_{\mathcal{L}_{2i}} < 1$ hold for any $\Delta \in \mathbf{\Delta}$. On the other hand, it can be observed that the $\mu$-function is higher than one for some components of $\mathbf{e}_m(i)$ corresponding to the maximum disturbance amplification requirements $\|\mathbf{d} \to \mathbf{e}_m\|_{\mathcal{L}_{2i}} < 1$. This is an expected and acceptable side effect due to the fact that the controller synthesis procedure prioritized robust performance only for the disturbance attenuation performance channels $\mathbf{e}_p$.

To get deeper insight into these situations, let us consider as an example, the robust performance degradation on $\mathbf{e}_m$ for the channel $\mathbf{d} \to \mathbf{e}_m(4)$ at $\Omega = 50$ Hz. The signal $\mathbf{e}_m(4)$ corresponds to the maximum disturbance amplification for the transmitted torque $T_{su}$. The plot of the $\mu$-function for this transfer are shown in fig. 2.26 together with the associated parametric sensitivities. These plots reveal that the performance degradation is primarily caused by uncertainties in the directions $\phi_\bullet$ of the actuators and the associated time-delays $\tau_\bullet$.

### Worst-case analysis

Finally, the worst case gain across all uncertainties $\Delta \in \mathbf{\Delta}$ is calculated based on algorithms described in [PBLJ00]. The worst case upper bound together with the worst case normalized parametric combination $\Delta_{wc}$ are shown in fig. 2.26. For clarity, only the most sensitive parameters are included. For this $\Delta_{wc}$, the $\mathcal{H}_\infty$ norm on closed-loop transfer $\mathbf{d} \to \mathbf{e}_m$ peaks to about 1 dB in the 52-60 Hz region. According to the definition of $\mathbf{W}_m$ from (2.70), this corresponds to about 7 dB amplification, compared to the open-loop case, for disturbances in the same frequency range.

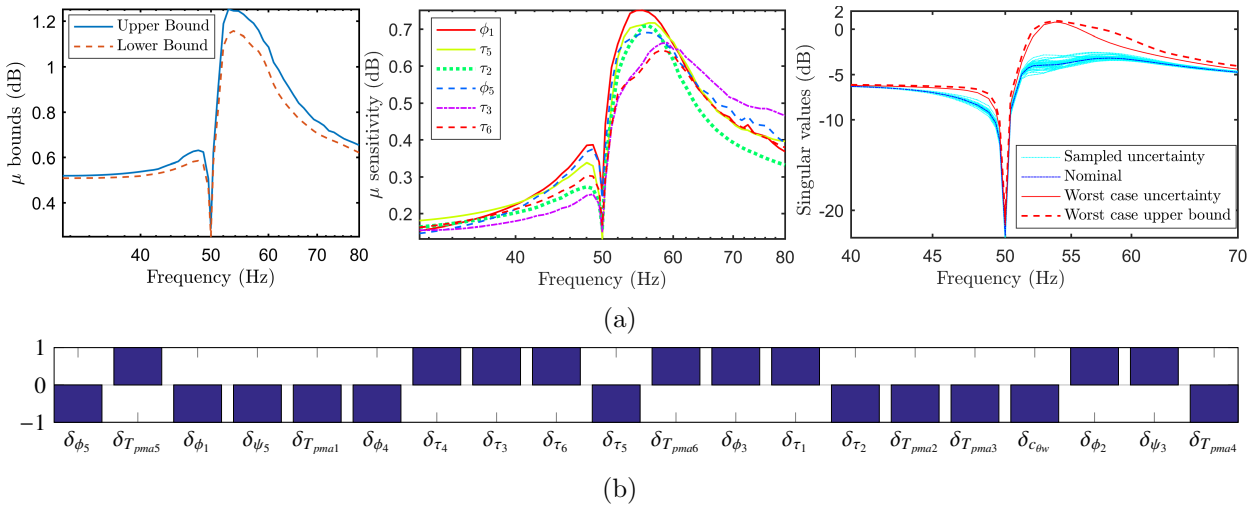


(a)

(b)

Figure 2.26: (a) Robust performance, $\mu$ sensitivities and worst case gains for the $\mathbf{d} \to \mathbf{e}_m(4)$ transfer at $\Omega = 50$ Hz. (b) The combination $\Delta_{wc}$ of normalized parameter values corresponding to the worst case gain.

### Numerical issues about $\mu$ computations

Given the number of uncertainties provided in table 2.3, it is clear that the LFT size is quite large which complicates the computation of the $\mu$-functions presented in the above sections. For robust stability analysis, $\Delta$ is given by $\Delta = \text{diag}\begin{pmatrix}\Delta_h & \Delta_G & \Delta_n\end{pmatrix}$ where $\Delta_h$ is a diagonal matrix of 42 real scalars (see figs. 2.14 and 2.15 and (2.45)), $\Delta_G$ is a diagonal matrix of 46 real scalars (see fig. 2.10 and (2.30) and (2.31)) and $\Delta_n$ is a diagonal matrix of 3 real scalars (see (2.36)). Therefore, $\Delta$ is a diagonal block composed of 91 real scalars. For robust performance assessment, it is required to add an additional full complex block $\Delta_{perf} \in \mathbb{C}^{24\times 24}$ that closes the performance transfer $\mathbf{d} \to \mathbf{e}$, leading the $\Delta$ block to be of total dimension 115.

To prevent numerical difficulties to compute $\mu$ (especially for robust stability assessment since $\Delta$ is a pure real block), a complex part is added to $\Delta$ since it is well known that the presence of a complex block improves the lower bound computations of the structured singular value $\mu$. For this purpose, the low values of complex uncertainties are added to the global uncertainty block by using $\Delta_u$ and $\Delta_y$ and fixing the associated weighting functions $\mathbf{W}_{\Delta u}$ and $\mathbf{W}_{\Delta y}$ to the low values i.e. $\mathbf{W}_{\Delta u} = \mathbf{W}_{\Delta y} = 10^{-3}\,\mathbf{I}_6$. This means that an additional 0.1% of input and output complex uncertainty is introduced. Although this introduces a slight conservatism to the lower bound calculations, it greatly improves the numerical stability during the calculations.

With the uncertainty structure in place, the computation of $\mu$ follows the two following steps:

- first, the upper bound of $\mu$ and the $\mu$-sensitivity functions, are computed using a fast upper bound algorithm, see for instance [LTD00]. The $\mu$-sensitivities are *a posteriori* checked and a subset of the uncertain parameters for which the $\mu$-sensitivities are the highest, is identified. This enables to eliminate the uncertain parameters that have minimal influence on $\mu$. 30 uncertain parameters are typically eliminated.
- In a second step, the upper bound is computed using the balanced/AMI technique [YND95, YD96], for a greater accuracy.

Following this approach, the calculation of $\mu$ does not pose a significant numerical problem for fig. 2.23. For the plots in fig. 2.24, it is required to compute an accurate value of both the upper and lower bounds. Thus, the upper bound is computed using a LMI formulation. With regards to the lower bound, it is switched to greatest accuracy by using a power algorithm with randomly reinitializing its iteration 3 times, see [YD90, YND95]. This procedure is of course considerably more time consuming. Figures 2.25 and 2.26 are obtained using the same procedure.

## 2.6 Nonlinear simulations

The microvibration mitigation strategy, derived in the previous sections, is subsequently implemented within a high-fidelity nonlinear simulator developed with the expertise of Airbus Defence and Space and the European Space Agency (ESA).

The presented simulation corresponds to the following scenario: The reaction wheel accelerates from $\Omega = 10\,\text{Hz}$ at time $t = 0\,\text{s}$ to $\Omega = 50\,\text{Hz}$ at $t = 220\,\text{s}$ using a constant motor torque applied at $t \in [10, 210]\text{s}$. The aim is to evaluate the time-domain closed-loop performances of the proposed controller for a time-varying wheel rate. These performances will be subsequently compared with the ones previously predicted using structured singular value analysis in section 2.5.

Following the reaction wheel disturbance model given in (2.6), the simulation includes the wheel's static and dynamic mass imbalances that produce the main harmonic perturbation. Additionally, to account for the full disturbance model, the main harmonic axial perturbation (component $F_1^z$ from (2.6)) as well as the broadband disturbances $\mathbf{u}_{bn}$ (see (2.6)) are added to the simulation. The sensor block is implemented as the LFT (2.36). In this case, the twelve force measurements $\mathbf{f}_s(t) \in \mathbb{R}^{12}$ from (2.34) are corrupted by first passing unit white noise through the sensor noise model $\mathbf{W}_n$ given in (2.60) and generating the appropiate sensor noise signal $\mathbf{n}(t) \in \mathbb{R}^{12}$. As explained in (2.47), the noise vector $\mathbf{n}$ this is subsequently subtracted from the measurements $\mathbf{f}_s$.

To highlight the benefits of the proposed isolation approach, the simulation results presented in fig. 2.27 show the transmitted forces $\mathbf{y}_s(1\ldots3) = \begin{bmatrix} F_{su} & F_{sv} & F_{sw} \end{bmatrix}^\mathsf{T}$ and torques $\mathbf{y}_s(4\ldots6) = \begin{bmatrix} T_{su} & T_{sv} & T_{sw} \end{bmatrix}^\mathsf{T}$ in both open-loop and closed-loop together with the six actuator control values $\mathbf{u}_{pma}$. In order to simplify the analysis of the simulations results, all the signals in fig. 2.27 are normalized prior to plotting, using the normalization factors provided in table 2.4. These factors correspond to the maximum open-loop values for the transmitted forces and torques as well as the maximum admissible control signal voltage in the case of the actuators. Examining fig. 2.27, it can

Table 2.4: Normalization factors used for the simulations plots.

| | Forces $\mathbf{y}_s(1\ldots3)$ | | | Torques $\mathbf{y}_s(4\ldots6)$ | | | Actuator inputs |
|---|---|---|---|---|---|---|---|
| Signal | $F_{su}$ | $F_{sv}$ | $F_{sw}$ | $T_{su}$ | $T_{sv}$ | $T_{sw}$ | $\mathbf{u}_{pma}(\bullet)$ |
| Normalized by | 1.4 N | 1.4 N | 0.16 N | 0.19 Nm | 0.19 Nm | 0.2 Nm | 10 V |

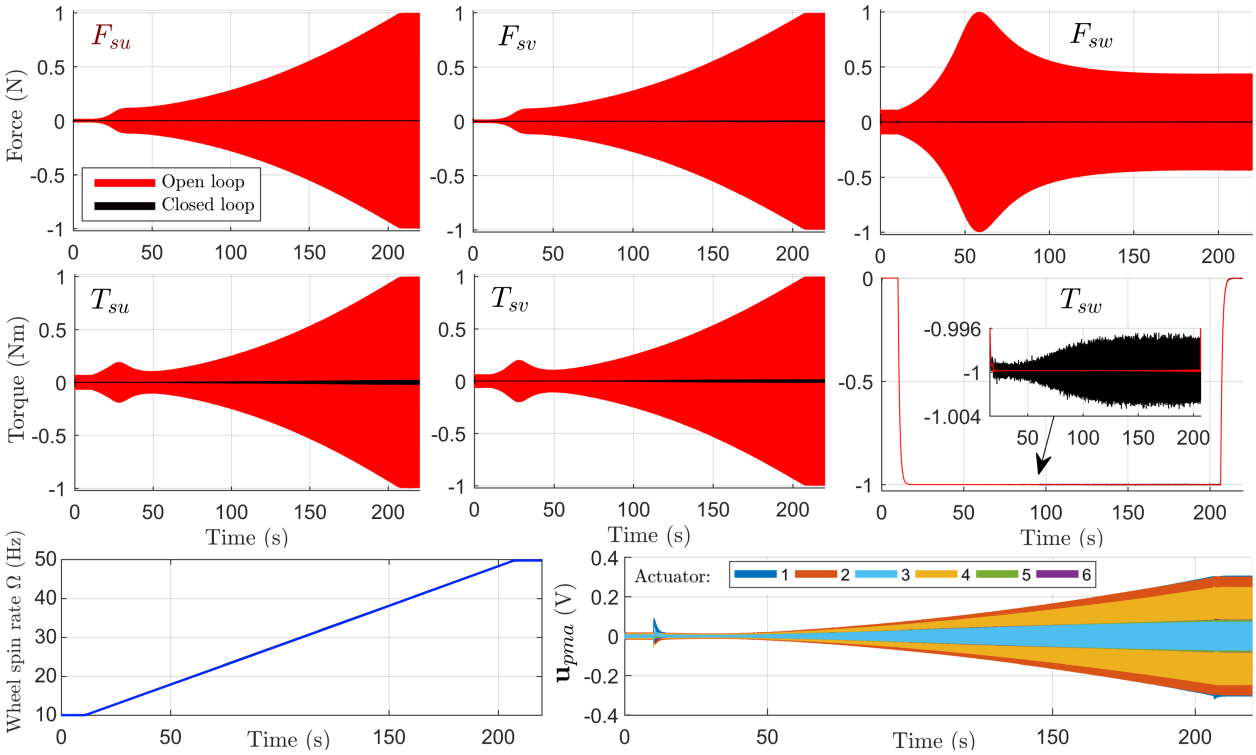


Figure 2.27: Time-domain simulation results displaying the normalized transmitted forces (top), torques (middle) and control signals (bottom) in both open and closed-loop scenarios for a variable spin rate $\Omega(t) \in \mathbf{\Omega}$ under nominal conditions (the uncertain parameters fixed to $\Delta = \mathbf{0}$).

be seen that controller significantly attenuates the transmitted lateral and axial disturbances using acceptable actuator effort (amplitude peaking around 30% of the saturation limit). At the same time, minimal distortions are introduced into the transmitted reaction wheel torque $\mathbf{y}_s(6) = T_{sw}$ during closed-loop operations. In order to better understand the attenuation performances in the frequency domain, fig. 2.28 shows the power spectral density plots of the normalized transmitted forces and torques previously shown in fig. 2.27. From these plots, it becomes apparent that

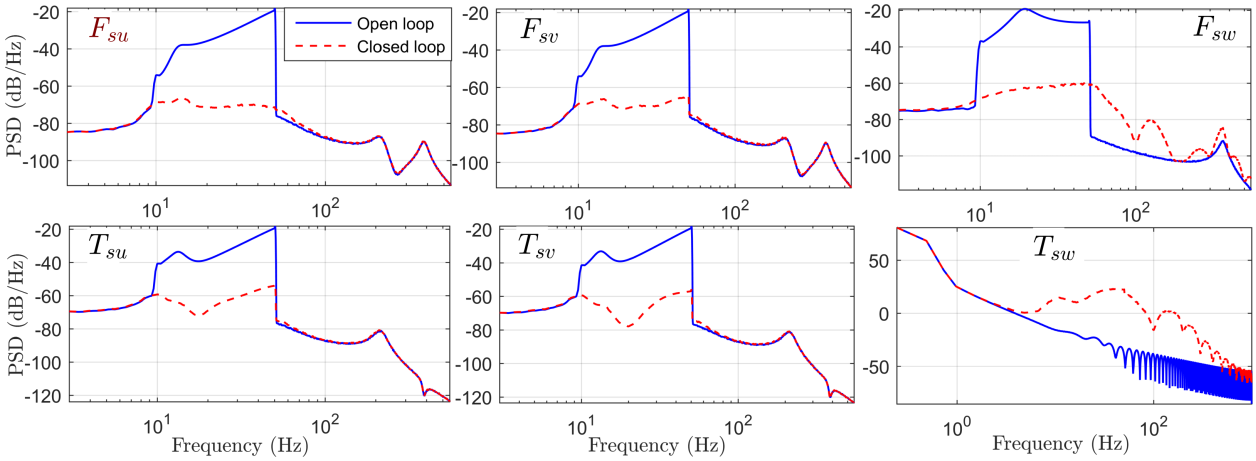


Figure 2.28: Power spectral densities of the normalized transmitted forces and torques shown in fig. 2.27.

both the transmitted forces and lateral torques are attenuated by at least 20 dB within the main harmonic range of $\mathbf{\Omega} = [10, 50]$ Hz. Therefore, both the isolation performance and the controller effort requirements introduced in section 2.4.1 are successfully met in this simulation scenario.

Next, the worst-case predictions obtained in section 2.5 are verified by adjusting the simulator parameters according to the worst-case parameter combination $\Delta_{wc}$ previously shown in fig. 2.26b. The system is then driven at a constant spin rate $\Omega = 50\,\text{Hz}$ and the transmitted torques $\mathbf{y}_s(4) = T_{su}$ for the nominal and worst-case closed-loop scenarios are compared with those obtained from the open-loop. The time-domain and root mean square (RMS) values are shown in fig. 2.29 together with the power spectral densities of each signal. The spectral content is in line with the predictions made earlier in section 2.5 with the largest peak occurring around the main harmonic $\Omega$. Compared to the nominal case, the worst-case peak in disturbance amplification around the main harmonic is clearly visible within the $52 - 60\text{Hz}$ frequency range. However, since the broadband disturbance level is fairly low, this amplification effect is barely visible in the time-domain as a slight increase in the RMS value. The effectiveness of $\mu$-tools in predicting worst-case performance and finding

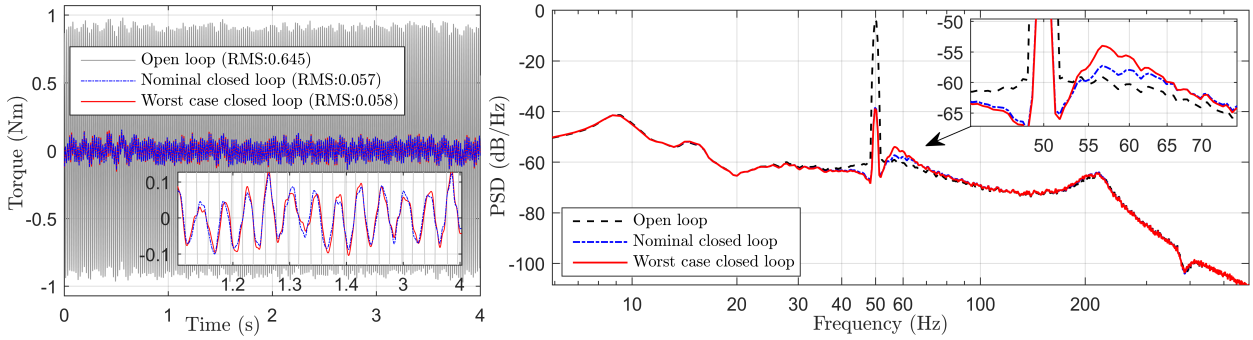


Figure 2.29: Normalized transmitted torque $T_{su}$ (left) and the corresponding power spectral density (right) for a constant spin rate $\Omega(t) = 50\,\text{Hz}$ in open-loop, nominal closed-loop as well as closed-loop with the worst-case parameter combination $\Delta_{wc}$.

particular problematic parameter combinations is therefore emphasized by these results.

## 2.7 Conclusions

This chapter addresses the development of a mixed active-passive microvibration mitigation solution capable of attenuating the transmitted vibrations generated by reaction wheels to a satellite structure. A representative benchmark developed with the support of the European Space Agency and Airbus Defence and Space, serves as a support for testing the approach. The chapter also covers modeling and design issues as well as a deep analysis of the solution within the $\mathcal{H}_\infty/\mu$ setting. A representative LFT model is developed starting from the nonlinear uncertain model of the plant, derived using Lagrangian formalism. The model captures the gyroscopic nature of the system, actuator dynamics, feedback-loop delays and uncertainties in the various components in a unified way. The design requirements are translated in the $\mathcal{H}_\infty/\mu$ framework using a comprehensive weighting function selection procedure, based on the physical characteristics and limitations of the system. The resulting controller is capable of providing significant disturbance attenuation in the frequency band of interest. The stability margins and robust performance of the proposed solution is evaluated using the structured singular value $\mu$. The most important uncertain physical parameters affecting the stability and performance of the overall system, are identified by performing local $\mu$ tests for a sufficient number of fixed values of reaction wheel speeds across the operating envelope. A worst-case analysis procedure is presented to assess the maximum disturbance amplification due to controller action. Nonlinear time-domain simulations, using the high-fidelity simulator, are used to demonstrate the capabilities of the proposed microvibration mitigation solution and to confirm the worst-case predictions made using $\mu$-tools. Based on these promising results, these methods

will be adapted in the next chapter to provide a systematic methodology for the control system design and analysis to guarantee pointing performance within typical space observation mission.

---

" *An expert is a person who has made all the mistakes that can be made in a very narrow field.* "

Niels Bohr

# 3 Robust microvibration isolation with guaranteed pointing performance

## 3.1 Introduction

Based upon the mixed passive/active isolation architecture and the techniques presented in chapter 2, the aim of this chapter is to highlight how these methods can be adapted to provide a systematic methodology for the uncertainty modeling, control system design and verification of microvibration isolation space systems for a typical space observation mission. Central to these efforts is the development of a novel integrated end-to-end uncertain system model that fully captures the disturbance propagation from the reaction wheels, through the isolation system and flexible spacecraft structure towards the sensitive instruments. The model of isolation setup is afterwards integrated with the simplified structural model of a flexible spacecraft driven by a reaction wheel. The resulting overall plant is an uncertain model derived analytically, with some parameter values based upon previous experimental results. The aim of this model is to provide a realistic benchmark for evaluating various active control strategies while at the same time capturing the main inherent complexities of the problem. Based on the deep understanding of the system provided by this model, robust synthesis and analysis procedures are systematically performed using modern mathematical tools such as $\mu$-analysis, structured $\mathcal{H}_\infty$ and Integral Quadratic Constraints (IQC) Analysis. This way, guaranteed stability and performance bounds are obtained, and the system dynamics can be pushed to the limits of achievable performance.

### 3.1.1 Contributions and chapter organization

In line with the previously stated goals, the main work covering the whole system design is organized into three parts: modeling, synthesis and analysis. The first part (section 3.2) introduces the system model that will form the basis for subsequent controller design and analysis sections. The linearized equations of motion previously obtained in section 2.3.3 are therefore updated to include the dynamical model of a flexible satellite stabilized by an attitude control system. As in the previous chapter, the model is subsequently merged with that of the sensors and actuators and rewritten in a LFT form (section 3.2.3) for robust design and analysis. The global LFT model captures the various parametric uncertainties as well gyroscopic effects in a unified manner and is used to analyze the end-to-end propagation of microvibrations towards the pointing errors of

the satellite. The model forms the basis for the second part of the chapter (section 3.3) which is dedicated to the design of the robust controller that manages the active isolation within the overall mixed microvibration attenuation strategy. Section 3.3.1 details the robust stability and performance objectives which are afterwards expressed in section 3.3.2 as bounds on the worst-case $\mathcal{L}_2$ gains of certain scaled closed-loop transfers. To accomplish this, weighting functions explained in section 3.3.3 are used to specify the frequency domain profile of external disturbances and also set the desired bounds on the pointing stability and actuator control signals. The weights include a novel model for the multi harmonic perturbation spectrum produced by a reaction wheel spinning at a particular rate. By also considering the relative phasing between the disturbance forces and torques, the model is used to make non conservative predictions about the resulting pointing error spectrum. This fact is exploited in section 3.3.4 where a detailed robust synthesis procedure is presented. Here, a number of LPV controllers, scheduled by the wheel spin rate, are designed for different levels of system uncertainty in order to push the predicted closed-loop pointing error spectrum below the required maximum threshold. Lastly, the third part of the chapter (section 3.4) details a rigorous analysis procedure used to validate the proposed control solution. The analysis relies on modern tools such as structured singular value and IQCs in order to obtain robust performance and stability margin certificates and expedite the validation and verification of the proposed control law without relying on extensive and time-consuming Monte Carlo campaigns. Time domain nonlinear simulations performed on a high-fidelity multi-body simulator developed with the expertise of ESA and Airbus Defence and Space are used to demonstrate the capabilities of the isolation setup and also verify the worst-case prediction obtained using an analysis based on the structured singular value.

## 3.2 System modeling

### 3.2.1 Description of the mission scenario

A schematic of the considered satellite setup is shown in fig. 3.1. The setup represents an extension of the isolation architecture described in chapter 2 where the dynamical model of the interface plate is replaced with that of a flexible satellite. For clarity, an overview of the interconnected system is shown in fig. 3.2. The end goal is to reduce the impact of wheel disturbances on the pointing stability of the spacecraft stabilized by an attitude control system (ACS). For the considered pointing scenario, this corresponds to minimizing the rotational displacements $\theta_a$, $\theta_b$ of the satellite rigid body around the $\vec{a}$ and $\vec{b}$ axes during the exposure time $t_\Delta$ of the optical instrument.

### 3.2.2 Equations of motion

As mentioned before, the fundamental change compared to the structural model presented in section 2.3.3 is the fact that the dynamical model of the interface plate is replaced with a six degree of freedom rigid body model of a satellite body connected to a flexible attachment and stabilized by an attitude control system. The governing equations for these new subsystems is outlined in this section.

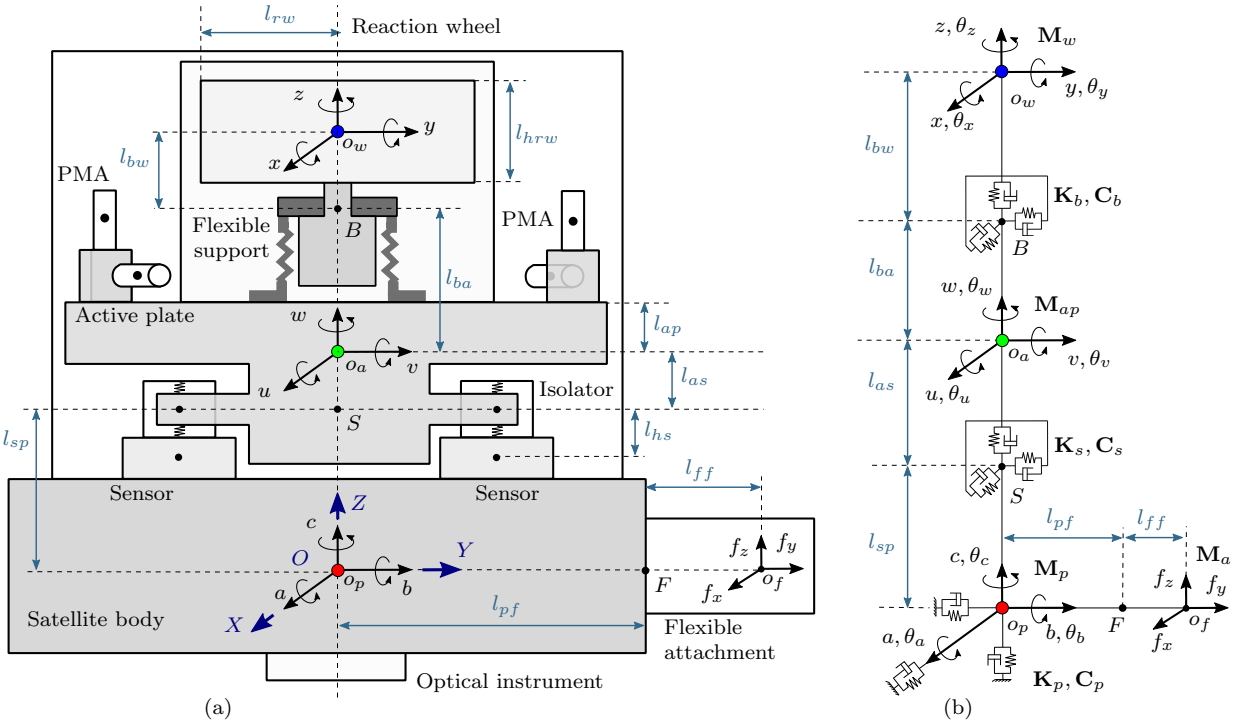


Figure 3.1: (a) Scaled illustration of the system setup with the various subcomponents (Note: only four of the six PMAs are illustrated here, while fig. 2.2 shows the locations and orientations of all six actuators). (b) Body frames, flexible connections and relative placements.

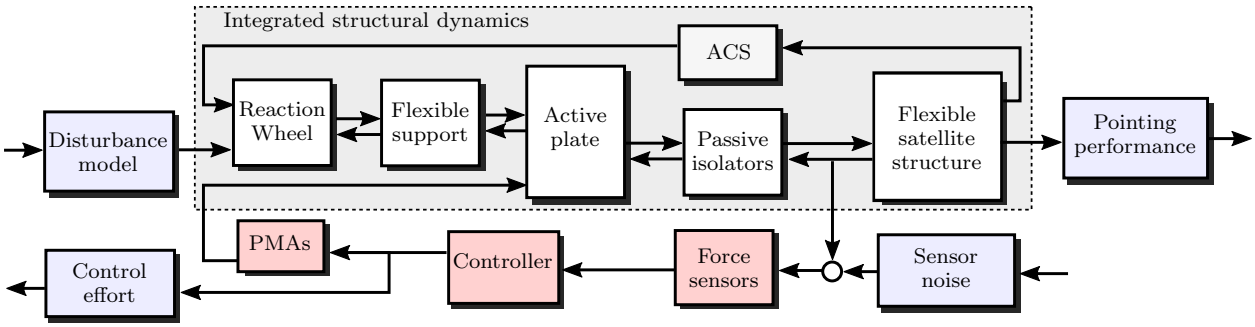


Figure 3.2: Overall system interconnection.

### Flexible satellite model

A corresponding body-fixed frame $\mathcal{F}_p := (o_p; \vec{a}, \vec{b}, \vec{c})$ is attached at center of mass (CoM) of the main satellite body. The matrix $\mathbf{M}_p = \begin{bmatrix} m_p \mathbf{I}_3 & \mathbf{0} \\ \mathbf{0} & \mathbf{J}_p \end{bmatrix}$ represents the generalized mass matrix of the rigid body combining the mass $m_p$ and moment of inertia tensor $\mathbf{J}_p$ in this body frame. As done for the interface plate in the previous chapter, the displacement of the satellite's rigid body CoM relative to the initial position is given in this inertial frame $\mathcal{F}_{world} := (O; \vec{X}, \vec{Y}, \vec{Z})$ by the vector $\mathbf{q}_{pt} = \begin{bmatrix} a & b & c \end{bmatrix}^\mathsf{T}$ while the orientation is described using the Euler angles $\mathbf{q}_{pr} = \begin{bmatrix} \theta_a & \theta_b & \theta_c \end{bmatrix}^\mathsf{T}$ and the y-x-z rotation matrix $\boldsymbol{\mathcal{R}}_p = \boldsymbol{\mathcal{R}}_{yxz}(\theta_a, \theta_b, \theta_c)$ (see table 2.1 for the matrix expression). Therefore, the combined generalized displacements of the satellite body are contained in the state vector $\mathbf{q}_p = \left[\begin{array}{c|c} \mathbf{q}_{pt}^\mathsf{T} & \mathbf{q}_{pr}^\mathsf{T} \end{array}\right]^\mathsf{T} = \left[\begin{array}{ccc|ccc} a & b & c & \theta_a & \theta_b & \theta_c \end{array}\right]^\mathsf{T}$. A flexible attachment connects to the main satellite body at a point $F$ having coordinates $\mathbf{r}_f = \begin{bmatrix} 0 & l_{pf} & 0 \end{bmatrix}^\mathsf{T}$ in $\mathcal{F}_p$. Fixed to the CoM of this attachment, a frame $\mathcal{F}_{flex} := (o_f; \vec{f}_x, \vec{f}_y, \vec{f}_z)$ is introduced such that the connection point $F$ has

coordinates $\mathbf{r}_{mf} = \begin{bmatrix} 0 & -l_{ff} & 0 \end{bmatrix}^\mathsf{T}$ in $\mathcal{F}_{flex}$. The flexible attachment generates reaction forces $\mathbf{f}_f$ and torques $\mathbf{t}_f$ due to the accelerations $\ddot{\mathbf{q}}_p$ of the satellite's rigid body. These forces and torques are applied to the satellite body in the frame $\mathcal{F}_p$ and the relationship can be described by employing the following cantilever hybrid model [GACC14, MCCCMC01]:

$$\begin{cases} \ddot{\boldsymbol{\eta}}_f + \underbrace{\operatorname{diag}\left(2\xi_f\omega_k\right)}_{\mathbf{C}_f}\dot{\boldsymbol{\eta}}_f + \underbrace{\operatorname{diag}\left(\omega_k^2\right)}_{\mathbf{K}_f}\boldsymbol{\eta}_f = -\mathbf{L}_{fp}^\mathsf{T}\ddot{\mathbf{q}}_p \\ \begin{bmatrix} \mathbf{f}_f^\mathsf{T} & \mathbf{t}_f^\mathsf{T} \end{bmatrix}^\mathsf{T} = \mathbf{M}_f\ddot{\mathbf{q}}_p + \mathbf{L}_f\ddot{\boldsymbol{\eta}}_f \end{cases} ; \quad \begin{matrix} k = \{1, \dots, n_k\} \\ n_k = 4 \end{matrix} \tag{3.1}$$

where $\omega_{1\dots n_k}$ are the modal frequencies with damping $\xi_f$ and the vector $\boldsymbol{\eta}_f(t) \in \mathbb{R}^{n_k}$ combines the displacements of all the $n_k = 4$ flexible modes. Let $m_f$ is the attachment mass and $\mathbf{J}_f$ the moment of inertia tensor in the attachment frame $\mathcal{F}_{flex}$ (with values provided in table 3.1), then the matrix $\mathbf{M}_f = \boldsymbol{\mathcal{T}}(\mathbf{r}_{mf} - \mathbf{r}_f)^\mathsf{T}\begin{bmatrix} {}^{m_f}\mathbf{I}_3 & \mathbf{0} \\ \mathbf{0} & \mathbf{J}_f \end{bmatrix}\boldsymbol{\mathcal{T}}(\mathbf{r}_{mf} - \mathbf{r}_f)$ represents the generalized mass matrix of the appendage expressed in frame $\mathcal{F}_p$ of the satellite rigid body. Here, the matrix $\boldsymbol{\mathcal{T}}(\mathbf{r}_{mf} - \mathbf{r}_f)$, with the expression provided in (2.15), is used to transport the generalized mass matrix of the appendage from the body frame $\mathcal{F}_{flex}$ of the flexible attachment into the body frame $\mathcal{F}_p$ of the satellite rigid body (see [GACC14] for details). The modal participation matrix $\mathbf{L}_f$ of the appendage in the frame $\mathcal{F}_p$ of the main satellite body can be deduced from the modal participation matrix $\mathbf{L}_a$ at the connection point $F$ (see table 3.1 for the value) by the following relationship $\mathbf{L}_f = \boldsymbol{\mathcal{T}}(\mathbf{r}_f)^\mathsf{T}\mathbf{L}_a$. Finally, the elasticity due to the passive isolators is modeled by a flexible 6 DoF joint (labeled as $S$ in fig. 2.1). Let $\mathbf{r}_{ps} = \begin{bmatrix} 0 & 0 & -l_{sp} \end{bmatrix}^\mathsf{T}$ be the coordinates of this connection in $\mathcal{F}_p$ and let $\mathbf{y}_s = \begin{bmatrix} \mathbf{f}_s^\mathsf{T} & | & \mathbf{t}_s^\mathsf{T} \end{bmatrix}^\mathsf{T} = \begin{bmatrix} F_{su} & F_{sv} & F_{sw} & | & T_{su} & T_{sv} & T_{sw} \end{bmatrix}^\mathsf{T}$ denote the elastic forces $\mathbf{f}_s$ and torques $\mathbf{t}_s$ applied to the satellite at this location. The over dynamics combining the main satellite body and the flexible attachment are therefore governed by the following set of equations

$$\begin{bmatrix} \mathbf{I}_{n_k} & \mathbf{L}_f^\mathsf{T} \\ \mathbf{L}_f & \mathbf{M}_p + \mathbf{M}_f \end{bmatrix}\begin{bmatrix} \ddot{\boldsymbol{\eta}}_f \\ \ddot{\mathbf{q}}_p \end{bmatrix} + \begin{bmatrix} \mathbf{C}_f & \mathbf{0} \\ \mathbf{0} & \mathbf{0} \end{bmatrix}\begin{bmatrix} \dot{\boldsymbol{\eta}}_f \\ \dot{\mathbf{q}}_p \end{bmatrix} + \begin{bmatrix} \mathbf{K}_f & \mathbf{0} \\ \mathbf{0} & \mathbf{0} \end{bmatrix}\begin{bmatrix} \boldsymbol{\eta}_f \\ \mathbf{q}_p \end{bmatrix} = \begin{bmatrix} \mathbf{0}_{(3+n_k)\times 2} \\ \mathbf{I}_2 \\ \mathbf{0}_{1\times 2} \end{bmatrix}\begin{bmatrix} T_a \\ T_b \end{bmatrix} - \begin{bmatrix} \mathbf{0} \\ \boldsymbol{\mathcal{T}}(\mathbf{r}_{ps})^\mathsf{T} \end{bmatrix}\begin{bmatrix} \mathbf{f}_s \\ \mathbf{t}_s \end{bmatrix} \tag{3.2}$$

where $T_a$, $T_b$ are the torques supplied by the attitude control system around the $\vec{a}$ and $\vec{b}$ axes of the satellite.

### Attitude Control System

An Attitude Control System (ACS) is used to stabilize and control the rotational movement of the entire spacecraft. The control law assumes that angular displacements $\mathbf{q}_{pr}$ and angular rates $\dot{\mathbf{q}}_{pr}$ of the main rigid satellite body are available for measurement. Based on these values, the ACS is implemented using a set of three independent controllers for each axis, similar to the one described in [GACC14]. The three control torques $\mathbf{t}_{acs}$ supplied by the ACS are therefore given by

$$\mathbf{t}_{acs} = \begin{bmatrix} T_a & T_b & T_m \end{bmatrix}^\mathsf{T} = \mathbf{K}_{acs}\mathbf{q}_{pr} + \mathbf{C}_{acs}\dot{\mathbf{q}}_{pr} \tag{3.3}$$

where the numerical values of the diagonal matrices $\mathbf{K}_{acs}$ and $\mathbf{C}_{acs}$ are provided in table 3.1. These matrices have been tuned as a preliminary step based on the static inertia of the spacecraft with the goal of providing a nominal critically damped response for each of the control axis with a settling time of about 40 s. The control torques $T_a$ and $T_b$ around the $\vec{a}$ and $\vec{b}$ axes of the spacecraft are assumed to be applied directly to the main satellite body as given in (3.2). The torque $T_m$ supplied by the reaction wheel motor is applied both to the flywheel as well as to the active plate (see table 2.2). This torque is afterwards transmitted to the satellite rigid body through the visco-elastic passive isolator connection (2.20) and used for attitute control along the $\vec{c}$ axis.

Table 3.1: Parameters values of the flexible satellite system

| | | |
|---|---|---|
| **Satellite main body and Attitude Control System** | | |
| $m_p$ | mass | $200\,\mathrm{kg}$ |
| $\mathbf{J}_p$ | moment of inertia tensor in body frame $\mathcal{F}_p$ | $\begin{bmatrix} 200 & 10 & 5 \\ 10 & 800 & 8 \\ 5 & 8 & 800 \end{bmatrix}\mathrm{kg\,m^2}$ |
| $\mathrm{diag}\,(\mathbf{K}_{acs}, \mathbf{C}_{acs})$ | ACS controller values | $\mathrm{diag}(\begin{smallmatrix} 10 & 5 & 8 & 27 & 10 & 31 \end{smallmatrix}) \times 10^2$ |
| $\begin{bmatrix} l_{pf} & l_{ff} & l_{sp} \end{bmatrix}$ | distances to connection points | $\begin{bmatrix} 25 & 25 & 28.38 \end{bmatrix}\mathrm{cm}$ |
| **Flexible attachment** | | |
| $m_f$ | mass | $10\,\mathrm{kg}$ |
| $\mathbf{J}_f$ | moment of inertia tensor in body frame $\mathcal{F}_{flex}$ | $\mathrm{diag}(\begin{smallmatrix} 700 & 20 & 1000 \end{smallmatrix})\,\mathrm{kg\,m^2}$ |
| $\begin{bmatrix} \omega_1 & \dots & \omega_4 \end{bmatrix}$ | frequencies of the flexible modes | $\begin{bmatrix} 0.8 & 2 & 35 & 140 \end{bmatrix}\mathrm{Hz} \pm 2\%$ |
| $\xi_f$ | damping ratio of the flexible modes | 0.005 |
| $\mathbf{L}_a$ | modal participation factors at the base $F$ of the flexible attachment | $\begin{bmatrix} -3 & 0 & 0 & 0 \\ 0 & 0 & 0 & 0 \\ 0 & 0 & 5 & 4 \\ 0 & 0 & 90 & 62 \\ 0 & 14 & 0 & 0 \\ 119 & 0 & 0 & 0 \end{bmatrix}$ |

The parameters were adapted from the model introduced in [GACC14].

#### Reaction wheel

The complete reaction wheel disturbance model explained in section 2.3.2 is slightly adapted for the mission scenario considered in this chapter. More precisely in order to reduce model complexity the axial force and torque disturbances $\begin{bmatrix} F_i^z & F_{zbn} & T_{zbn} \end{bmatrix}$ from (2.6) are ignored as these don't play a significant role in the overall pointing performance. Considering that the motor torque $T_m$ is provided by the attitude control system (3.3) , the new reaction wheel force and torque disturbance vector $\mathbf{u}_w$ can be expressed in the wheel's rocking frame $\mathcal{F}_{wrock}$ as

$$\mathbf{u}_w = \begin{bmatrix} F_x & F_y & | & T_x & T_y \end{bmatrix}^\mathsf{T} = \underbrace{\begin{bmatrix} F_{xbn} & F_{ybn} | & T_{xbn} & T_{ybn} \end{bmatrix}^\mathsf{T}}_{\mathbf{u}_{bn}} + \sum_{i=1}^{N} \underbrace{\begin{bmatrix} F_i^x & F_i^y & | & T_i^x & T_i^y \end{bmatrix}^\mathsf{T}}_{\mathbf{u}_i} \tag{3.4}$$

where $\mathbf{u}_{bn} \in \mathbb{R}^4$ represents the stochastic broadband noise and $\mathbf{u}_i$ is the $i$-th out of a total of $N$ harmonic disturbances with

$$\begin{aligned} F_i^x(t) &= a_i^f \Omega^2 \sin\left(h_i \Omega t + \phi_i^f\right) & T_i^x(t) &= -a_i^t \Omega^2 \cos\left(h_i \Omega t + \phi_i^t\right) \\ F_i^y(t) &= a_i^f \Omega^2 \cos\left(h_i \Omega t + \phi_i^f\right) & T_i^y(t) &= a_i^t \Omega^2 \sin\left(h_i \Omega t + \phi_i^t\right) \end{aligned} \tag{3.5}$$

where $h_i$ is the harmonic number, $a_i^f$,$a_i^t$ are harmonic amplitude coefficients from table 2.3 and $\phi_i^f$,$\phi_i^t$ are random phase angles.

### 3.2.3 LFT modeling

#### Integrated structural dynamics

The combined dynamics of the reaction wheel, active plate, flexible wheel support and passive isolators previously provided in table 2.2 are now combined with the dynamics of the flexible

satellite (3.1) and attitude control system (3.3) into the integrated model shown in fig. 3.3. Similar

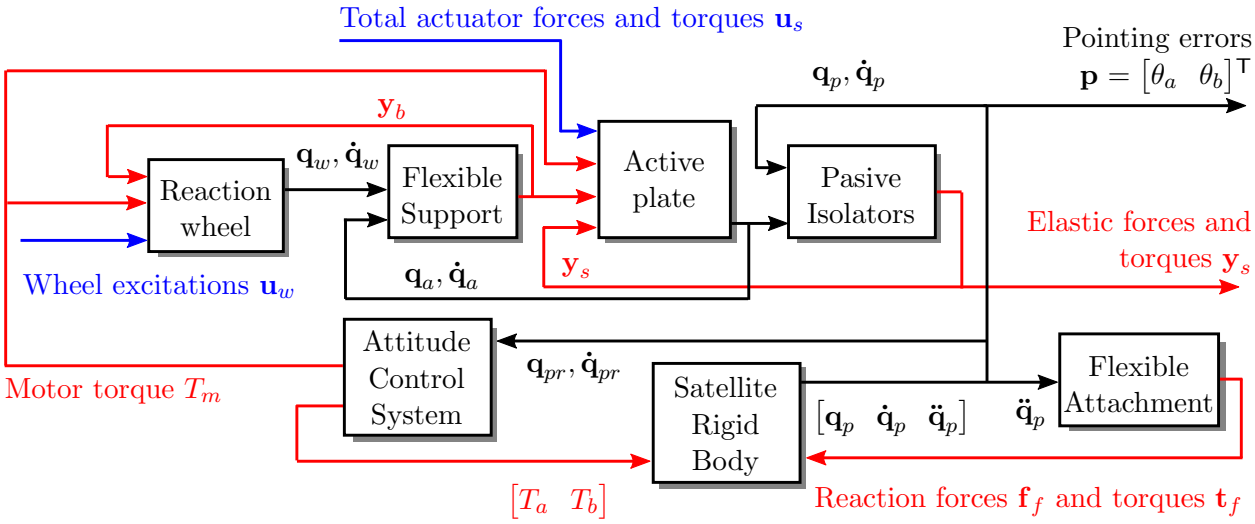


Figure 3.3: System block diagram of the structural equations of motion. Input forces and torques, Connective forces and torques , Generalized displacements and velocities.

to (2.26), the overall equations can be rewritten as

$$\begin{cases} \boldsymbol{\mathcal{M}}\ddot{\mathbf{q}} + (\boldsymbol{\mathcal{C}} + \Omega\boldsymbol{\mathcal{G}})\,\dot{\mathbf{q}} + \boldsymbol{\mathcal{K}}\mathbf{q} = \boldsymbol{\mathcal{Q}} \begin{bmatrix} \mathbf{u}_w \\ \mathbf{u}_s \end{bmatrix} \\ \begin{bmatrix} \mathbf{p} \\ \mathbf{y}_s \end{bmatrix} = \boldsymbol{\mathcal{S}} \begin{bmatrix} \mathbf{q} \\ \dot{\mathbf{q}} \end{bmatrix} \end{cases} \tag{3.6}$$

where the matrices $\boldsymbol{\mathcal{M}}$,$\boldsymbol{\mathcal{C}}$,$\boldsymbol{\mathcal{G}}$,$\boldsymbol{\mathcal{K}}$,$\boldsymbol{\mathcal{Q}}$,$\boldsymbol{\mathcal{S}}$ represent the mass, damping, gyroscopic, stiffness, input and output matrices combing each of the uncertain system parameters. The precise expressions of these is omitted but can be deduced by merging the previous subcomponent equations as done in section 2.3.3. The expression of the overall system state is

$$\mathbf{q}(t) = [\boldsymbol{\eta}_f^\mathsf{T} \quad \mathbf{q}_p^\mathsf{T} \quad \mathbf{q}_a^\mathsf{T} \quad \mathbf{q}_w^\mathsf{T}]^\mathsf{T} \in \mathbb{R}^{22} \tag{3.7}$$

and the pointing error vector

$$\mathbf{p}(t) = [\theta_a \quad \theta_b]^\mathsf{T} \in \mathbb{R}^2 \tag{3.8}$$

contains the rotational displacements of the main satellite body around the $\vec{a}$ and $\vec{b}$ axes. As in (2.22), the vector $\mathbf{u}_s(t) \in \mathbb{R}^6$ combines the total actuator forces $\mathbf{f}_{as}$ and torques $\mathbf{t}_{as}$ applied to the active plate at the passive isolator location, i.e.

$$\mathbf{u}_s = [\mathbf{f}_{as}^\mathsf{T} \;\mid\; \mathbf{t}_{as}^\mathsf{T}]^\mathsf{T} = [F_{asu} \quad F_{asv} \quad F_{asw} \;\mid\; T_{asu} \quad T_{asv} \quad T_{asw}]^\mathsf{T} \tag{3.9}$$

Similar to (2.29), the input-output behavior of these equations of motion can be described through a $\Omega$-dependent system model $\widehat{\mathbf{G}}(\Omega)$ with 12 inputs $\begin{bmatrix} \mathbf{u}_w \\ \mathbf{u}_s \end{bmatrix}$, 8 outputs $\begin{bmatrix} \mathbf{p} \\ \mathbf{y}_s \end{bmatrix}$ and 44 states $\begin{bmatrix} \mathbf{q} \\ \dot{\mathbf{q}} \end{bmatrix}$ having the following representation:

$$\widehat{\mathbf{G}}(\Omega) := \begin{cases} \begin{bmatrix} \dot{\mathbf{q}} \\ \ddot{\mathbf{q}} \end{bmatrix} = \underbrace{\begin{bmatrix} \mathbf{0} & \mathbf{I} \\ -\boldsymbol{\mathcal{M}}^{-1}\boldsymbol{\mathcal{K}} & -\boldsymbol{\mathcal{M}}^{-1}(\boldsymbol{\mathcal{C}} + \boldsymbol{\mathcal{G}}(\Omega)) \end{bmatrix}}_{\in \mathbb{R}^{44\times 44}} \begin{bmatrix} \mathbf{q} \\ \dot{\mathbf{q}} \end{bmatrix} + \underbrace{\begin{bmatrix} \mathbf{0} \\ \boldsymbol{\mathcal{M}}^{-1}\boldsymbol{\mathcal{Q}} \end{bmatrix}}_{\in \mathbb{R}^{44\times 12}} \begin{bmatrix} \mathbf{u}_w \\ \mathbf{u}_s \end{bmatrix} \\ \begin{bmatrix} \mathbf{p} \\ \mathbf{y}_s \end{bmatrix} = \underbrace{\boldsymbol{\mathcal{S}}}_{\in \mathbb{R}^{8\times 44}} \begin{bmatrix} \mathbf{q} \\ \dot{\mathbf{q}} \end{bmatrix} \end{cases} \tag{3.10}$$

Or in a more compact form as:

$$\widehat{\mathbf{G}}(\Omega) := \left(\begin{array}{cc|c} \mathbf{0} & \mathbf{I} & \mathbf{0} \\ -\boldsymbol{\mathcal{M}}^{-1}\boldsymbol{\mathcal{K}} & -\boldsymbol{\mathcal{M}}^{-1}(\boldsymbol{\mathcal{C}}+\Omega\boldsymbol{\mathcal{G}}) & \boldsymbol{\mathcal{M}}^{-1}\boldsymbol{\mathcal{Q}} \\ \hline \boldsymbol{\mathcal{S}} & & \mathbf{0} \end{array}\right) \quad \text{with} \quad \begin{bmatrix}\mathbf{p}\\ \mathbf{y}_s\end{bmatrix} = \widehat{\mathbf{G}}(\Omega)\begin{bmatrix}\mathbf{u}_w\\ \mathbf{u}_s\end{bmatrix} \tag{3.11}$$

The $\widehat{\mathbf{G}}(\Omega)$ system is subsequently expressed in LFT form[1] as a feedback interconnection between a fixed LTI part $\mathbf{G}$ and a structured block containting the time-varying spin rate $\Omega$ and all the real uncertain parameters i.e.

$$\widehat{\mathbf{G}}(\Omega) = \mathcal{F}_u\left(\mathbf{G}, \begin{bmatrix}\Omega\mathbf{I}_2 & \\ & \Delta_G\end{bmatrix}\right) \text{ with } \Delta_G \in \boldsymbol{\Delta}_G = \{\text{diag}\,(\delta_\bullet \mathbf{I}_{n_\bullet}) : \delta_\bullet \in \mathbb{R}, |\delta_\bullet| \leq 1\} \subset \mathbb{R}^{39\times 39} \tag{3.12}$$

where the block $\Delta_G$ combines all the normalized uncertain parameters $\delta_\bullet$ and their multiplicity $n_\bullet$. These parameters are those given in the previous chapter in (2.31) except for $\{\delta_{m_p}, \delta_{c_a}, \delta_{c_b}, \delta_{c_c}, \delta_{k_a}, \delta_{k_b}, \delta_{k_c}\}$ as these uncertain parameters are related to the interface plate and suspension spring models that were replaced, in this chapter, by the flexible satellite model.

Figure 3.4 includes both a block diagram of the original mechanical model (3.6) as well as the corresponding LFT (3.12). In order to highlight the gyroscopic effects and flexibles modes of

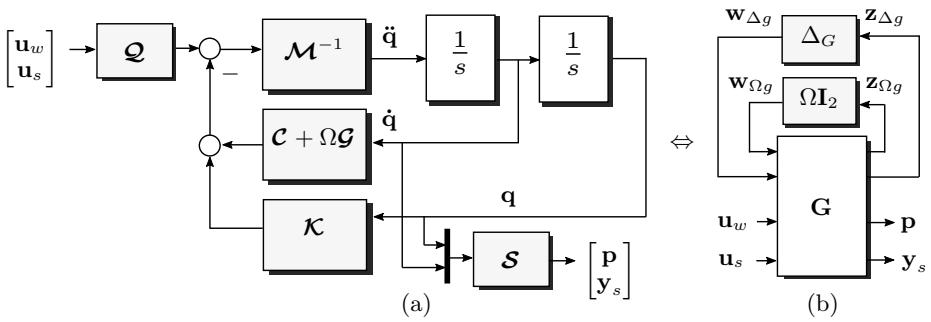


Figure 3.4: (a) Structural model of the flexible spacecraft and attitude control system. (b) Mechanical model in LFT form.

the overall mechanical system, fig. 3.5a contains the singular values from the wheel disturbances $\mathbf{u}_w$ towards one of the satellite pointing errors $\mathbf{p}(1) = \theta_a$ for different fixed $\Omega \in \boldsymbol{\Omega}$. The peaks correspond to the flexible modes i.e. poles of $\widehat{\mathbf{G}}(\Omega)$ and can be separated based on their natural frequency into three regions. The low-frequency modes below 1 Hz are due to Attitude Control System while the high frequency modes above 100 Hz result from the flexibility in the wheel support (i.e. the ball-bearings) and some satellite attachment modes. The control bandwidth spans the mid-frequency range $[10, 50]$ Hz corresponding to the wheel spin rate range $\boldsymbol{\Omega}$ where most of the harmonic disturbance energy is concentrated. One of the modes in this region is due to the flexible attachment (around 36.5 Hz) while others arise due to the flexibility in the passive isolators. The coupled lateral and rocking motions of the active plate, resting on top of the flexible passive isolators, forms pairs of gyroscopic modes (whirl modes) that significantly shift their natural frequency based on $\Omega$. The effect is illustrated in fig. 3.5b using the Campbell diagram. This plot shows the natural frequency of the poles within the control bandwidth for different fixed reaction wheel spin rates $\Omega \in \boldsymbol{\Omega} = [10, 50]$Hz.

[1] see section 2.3.4 for a more in-depth description of the LFT extraction process.

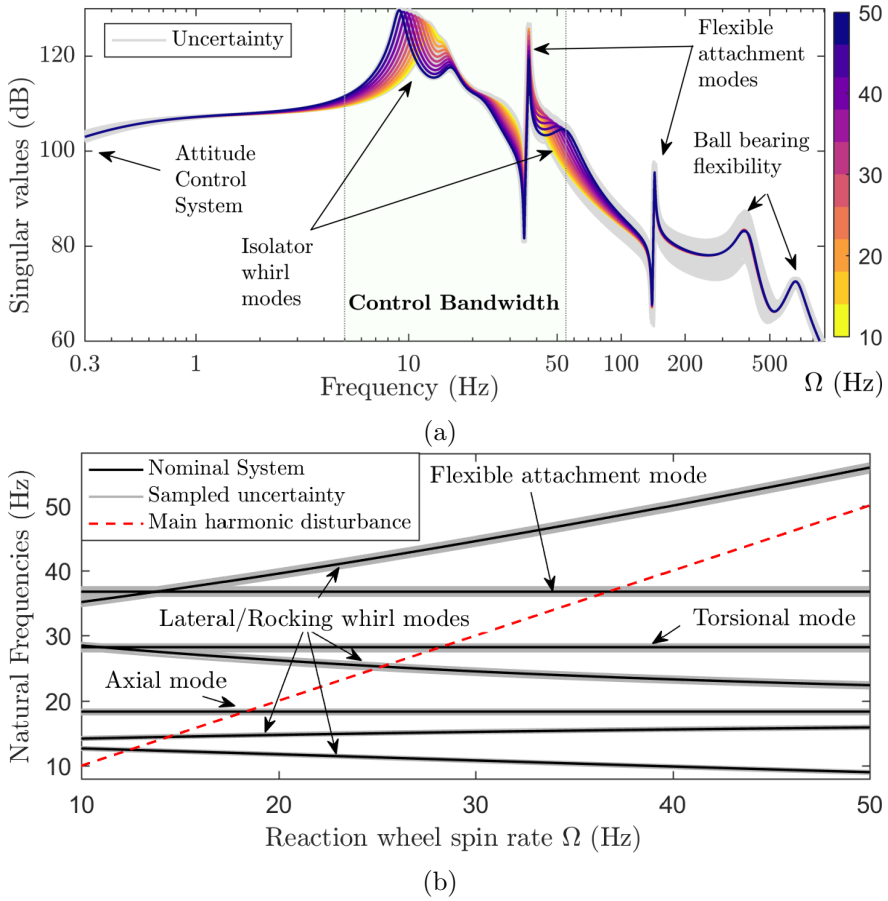


Figure 3.5: For different $\Omega \in \mathbf{\Omega}$ and uncertainty values: (a) Singular values between wheel disturbance inputs $\mathbf{u}_w$ and the pointing error $\mathbf{p}(1) = \theta_a$ ; (b) Campbell diagram showing the frequency shift of whirl modes within the control bandwidth.

## 3.3 Performance objectives and controller design

### 3.3.1 Control architecture and system requirements

The LFT models obtained in the previous section, can be merged into the overall control architecture shown in fig. 3.6 with the combined real parametric uncertainty

$$\Delta_{real} \in \mathbf{\Delta}_{real} := \text{diag}\left(\mathbf{\Delta}_G, \mathbf{\Delta}_n, \mathbf{\Delta}_h\right) \subset \mathbb{R}^{84\times 84} \tag{3.13}$$

where $\mathbf{\Delta}_G \subset \mathbb{R}^{39\times 39}$, $\mathbf{\Delta}_n \subset \mathbb{R}^{3\times 3}$ and $\mathbf{\Delta}_h \subset \mathbb{R}^{42\times 42}$ represent the uncertainty sets corresponding to the dynamical model of the flexible structure $\widehat{\mathbf{G}}(\Omega) = \mathcal{F}_u\left(\mathbf{G}, \begin{bmatrix} \Omega\mathbf{I}_2 & \\ & \Delta_G \end{bmatrix}\right)$ from (3.12), the sensor projection matrix $\widehat{\mathbf{N}} = \mathcal{F}_u\left(\mathbf{N}, \Delta_n\right)$ from (2.36) and respectively the actuator block $\widehat{\mathbf{H}} = \mathcal{F}_u\left(\mathbf{H}, \Delta_h\right)$ from (2.46).

The challenge is now to design the active control strategy that complements the passive isolators and insures that a set of robust performance and robust stability objectives are met for all the considered variable wheel rates $\Omega(t) \in \mathbf{\Omega}$ given in (2.4). To accomplish this, the proposed solution relies on a LPV controller $\mathbf{K}(\Omega(t))$ scheduled by the spin rate $\Omega(t)$ and written in LFT form as $\mathbf{K}(\Omega) = \mathcal{F}_l\left(\mathbf{K}, \Omega(t)\mathbf{I}_{n_\Omega}\right)$. This controller is used to generate an adequate control signal $\mathbf{u}(t) \in \mathbb{R}^6$ based upon the sensor outputs $\mathbf{y} = \mathbf{f}_s + \mathbf{n}$ corrupted by the noise $\mathbf{n}(t) \in \mathbb{R}^{12}$ . The control problem takes into account the presence of uncertain time delays $\tau \in [0, \tau_{max}]$ with $\tau_{max} = 1\,\text{ms}$

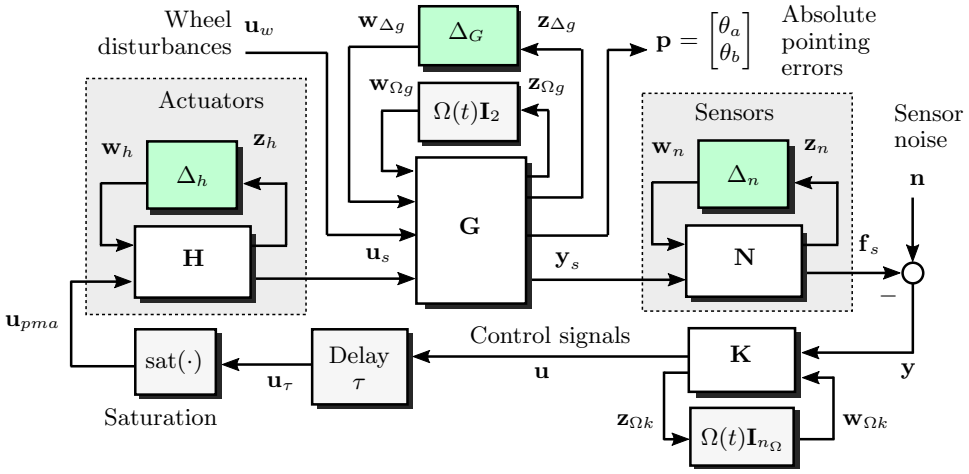


Figure 3.6: Close-loop system interconnection combining the LFT models of the sensors, flexible structure and PMA actuators.

and saturation nonlinearities sat(·) in each of the control channels. The requirements that need to be satisfied for all time-varying $\Omega(t) \in \mathbf{\Omega}$ is given below:

**(R1)** ***Robust stability*:** Closed-loop stability must be guaranteed with respect to all considered parametric uncertainties, time-delays and saturations in order to achieve the reliability demanded by a space certified technology.

**(R2)** ***Robust pointing stability and control effort performance*:** The primary performance goal is to attenuate the wheel microvibrations and guarantee that the amplitude spectral densities (ASDs) of the satellite's relative pointing errors (RPEs) are pushed below a target value of $\epsilon_{max} = 0.65\,\text{mas}/\sqrt{\text{Hz}}$. The RPE index is also known as the pointing stability and is defined [ECS08, ECS11] as the angular separation between the instantaneous pointing direction $\mathbf{p} = \begin{bmatrix}\theta_a & \theta_b\end{bmatrix}^\mathsf{T}$ and the short-time average pointing direction during a given time period (in this case equal to the exposure time of the optical instrument $t_\Delta = 20\,\text{ms}$). Additionally, in order to avoid excessive actuator degradation over the lifespan of the mission, the amplitude spectal density of the control signals must be kept below the limit $u_{max} = 10\,\text{V}/\sqrt{\text{Hz}}$ imposed by the manufacturer. Both of these requirements must be ensured even in the presence of a significant subset of model uncertainty, time-delay or saturation effects.

### 3.3.2 Requirements formulation within the $\mathcal{H}_\infty/\mu$ framework

#### Closed-loop transfer functions

Consider the proposed synthesis interconnection illustrated in fig. 3.7 that is based on the architecture previously shown in fig. 3.6. In order to reduce the computational burden of the synthesis

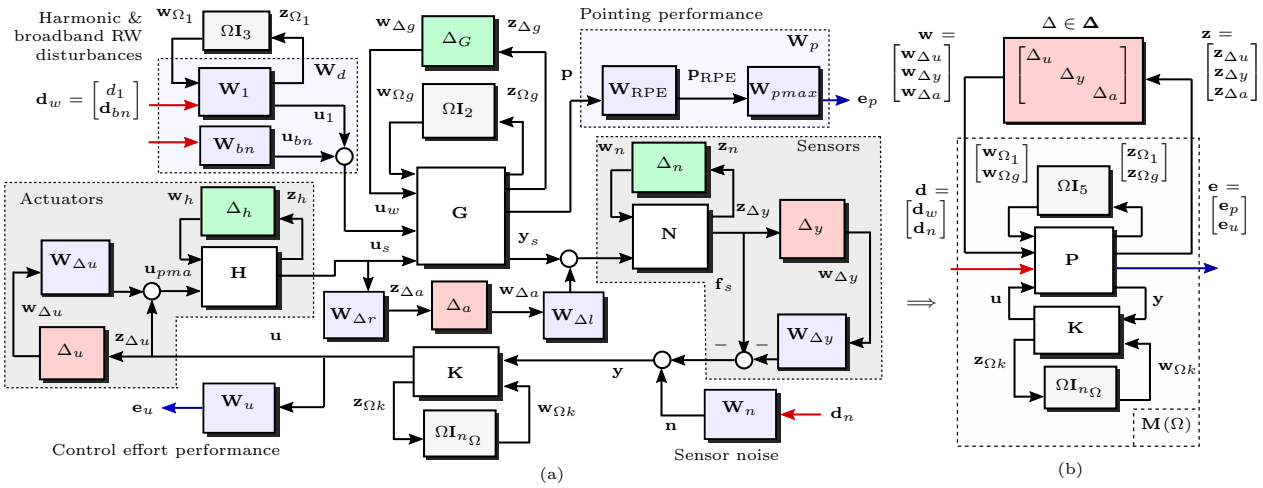


Figure 3.7: (a) Diagram of the weighted closed-loop system interconnection. (b) Synthesis structure considering only the complex uncertainty blocks. Weighting functions, Real uncertainty, Complex uncertainty.

procedure, several new complex diagonal uncertainty blocks are introduced and aggregated into:

$$\Delta = \text{diag}\left(\Delta_u,\ \Delta_y,\ \Delta_a\right) \in \mathbf{\Delta} \subset \mathbb{C}^{54\times 54} \quad \text{with} \quad \mathbf{\Delta} = \left\{\text{diag}\left(\delta_\bullet\right) : \delta_\bullet \in \mathbb{C}, |\delta_\bullet| \leq 1\right\} \tag{3.14}$$

The new complex uncertainty set $\mathbf{\Delta}$ is used to provide a low order approximation of the real uncertainty set $\mathbf{\Delta}_{real}$ as well as covering the worst-case effects of the saturation and delay blocks. The weighting functions are labeled as $\mathbf{W}_\bullet$ and depending on their role can be classified into three types:

(a) input weights $\mathbf{W}_n$ and $\mathbf{W}_d(\Omega) = \begin{bmatrix}\mathbf{W}_1(\Omega) & \mathbf{W}_{bn}\end{bmatrix}$ that are used to scale normalized disturbance signals to match the spectral content of sensor and wheel disturbances

(b) performance weights $\mathbf{W}_p = \mathbf{W}_{pmax}\mathbf{W}_{RPE}$ and $\mathbf{W}_u$ used to place upper bounds on the spectral content of the pointing error and actuator control signals

(c) uncertainty weights $\mathbf{W}_{\Delta u}$,$\mathbf{W}_{\Delta y}$,$\mathbf{W}_{\Delta l}$ and $\mathbf{W}_{\Delta r}$ used to appropriately scale the complex uncertainty blocks.

Before detailing each of weights, it is useful to calculate the closed-loop transfer functions. To simplify the subsequent equations, consider the notations

$$\begin{bmatrix}\mathbf{p}\\ \mathbf{f}_s\end{bmatrix} = \begin{bmatrix}\mathbf{I} & \mathbf{0}\\ \mathbf{0} & \widehat{\mathbf{N}}\end{bmatrix}\widehat{\mathbf{G}}(\Omega)\begin{bmatrix}\mathbf{I} & \mathbf{0}\\ \mathbf{0} & \widehat{\mathbf{H}}\end{bmatrix}\begin{bmatrix}\mathbf{u}_w\\ \mathbf{u}\end{bmatrix} = \begin{bmatrix}\mathbf{G}_{pd}(\Omega) & \mathbf{G}_{pu}(\Omega)\\ \mathbf{G}_{yd}(\Omega) & \mathbf{G}_{yu}(\Omega)\end{bmatrix}\begin{bmatrix}\mathbf{u}_w\\ \mathbf{u}\end{bmatrix} \tag{3.15}$$

where $\widehat{\mathbf{N}}$ and $\widehat{\mathbf{H}}$ are the sensor and actuator models given in (2.36) and (2.46) while $\widehat{\mathbf{G}}(\Omega)$ is the integrated structural model from (3.11). Examining fig. 3.7, the general open-loop interconnection can be written in terms of the complex uncertainty channels $\mathbf{w} = \begin{bmatrix}\mathbf{w}_{\Delta u}^\mathsf{T} & \mathbf{w}_{\Delta y}^\mathsf{T} & \mathbf{w}_{\Delta a}^\mathsf{T}\end{bmatrix}^\mathsf{T}$ and $\mathbf{z} = \begin{bmatrix}\mathbf{z}_{\Delta u}^\mathsf{T} & \mathbf{z}_{\Delta y}^\mathsf{T} & \mathbf{z}_{\Delta a}^\mathsf{T}\end{bmatrix}^\mathsf{T}$ together with the perturbations $\mathbf{d} = \begin{bmatrix}d_1 & \mathbf{d}_{bn}^\mathsf{T} & | & \mathbf{d}_n^\mathsf{T}\end{bmatrix}^\mathsf{T} = \begin{bmatrix}\mathbf{d}_w^\mathsf{T} & | & \mathbf{d}_n^\mathsf{T}\end{bmatrix}^\mathsf{T}$ and

performance channels $\mathbf{e} = \begin{bmatrix}\mathbf{e}_p^\mathsf{T} & \mathbf{e}_u^\mathsf{T}\end{bmatrix}^\mathsf{T}$ as

$$\left[\begin{array}{c}\mathbf{z}_{\Delta u}\\ \mathbf{z}_{\Delta y}\\ \mathbf{z}_{\Delta a}\\ \hline \mathbf{e}_p\\ \mathbf{e}_u\\ \hline \mathbf{y}\end{array}\right] = \underbrace{\operatorname{diag}\left(\begin{array}{c}\mathbf{I}\\ \mathbf{I}\\ \mathbf{W}_{\Delta r}\widehat{\mathbf{H}}\\ \hline \mathbf{W}_p\\ \mathbf{W}_u\\ \hline \mathbf{I}\end{array}\right)\left[\begin{array}{ccc|cc|c}\mathbf{0} & \mathbf{0} & \mathbf{0} & \mathbf{0} & \mathbf{0} & \mathbf{I}\\ \mathbf{G}_{yu}(\Omega) & \mathbf{0} & \mathbf{0} & \mathbf{G}_{yd}(\Omega) & \mathbf{0} & \mathbf{G}_{yu}(\Omega)\\ \mathbf{0} & \mathbf{0} & \mathbf{0} & \mathbf{0} & \mathbf{0} & \mathbf{I}\\ \hline \mathbf{G}_{pu}(\Omega) & \mathbf{0} & \mathbf{0} & \mathbf{G}_{pd}(\Omega) & \mathbf{0} & \mathbf{G}_{pu}(\Omega)\\ \mathbf{0} & \mathbf{0} & \mathbf{0} & \mathbf{0} & \mathbf{0} & \mathbf{I}\\ \hline -\mathbf{G}_{yu}(\Omega) & \mathbf{I} & \mathbf{I} & -\mathbf{G}_{yd}(\Omega) & \mathbf{I} & -\mathbf{G}_{yu}(\Omega)\end{array}\right]\operatorname{diag}\left(\begin{array}{c}\mathbf{W}_{\Delta u}\\ \mathbf{W}_{\Delta y}\\ \widehat{\mathbf{N}}\mathbf{W}_{\Delta l}\\ \hline \mathbf{W}_d(\Omega)\\ \mathbf{W}_n\\ \hline \mathbf{I}\end{array}\right)}_{\mathbf{P}(\Omega)}\left[\begin{array}{c}\mathbf{w}_{\Delta u}\\ \mathbf{w}_{\Delta y}\\ \mathbf{w}_{\Delta a}\\ \hline \mathbf{d}_w\\ \mathbf{d}_n\\ \hline \mathbf{u}\end{array}\right] \tag{3.16}$$

where $\mathbf{P}(\Omega)$ can also be written in LFT form as $\mathbf{P}(\Omega) = \mathcal{F}_u\left(\mathbf{P}, \Omega\mathbf{I}_5\right)$ by combining, as pictured in fig. 3.7, the $\Omega$ blocks in the LFT descriptions of $\mathbf{W}_d(\Omega)$ and $\widehat{\mathbf{G}}(\Omega)$. The controller $\mathbf{K}(\Omega)$ can now be used to close the control channels such that $\mathbf{u} = \mathbf{K}(\Omega)\mathbf{y}$. Let $\mathbf{S}_i(\Omega) = \left[\mathbf{I} + \mathbf{K}(\Omega)\mathbf{G}_{yu}(\Omega)\right]^{-1}$ and $\mathbf{T}_i(\Omega) = \mathbf{I} - \mathbf{S}_i(\Omega)$ denote the Input Sensitivity and the Input Complementary Sensitivity functions. Similarly, the functions $\mathbf{S}_o(\Omega) = \left[\mathbf{I} + \mathbf{G}_{yu}(\Omega)\mathbf{K}(\Omega)\right]^{-1}$ and $\mathbf{T}_o(\Omega) = \mathbf{I} - \mathbf{S}_o(\Omega)$ represent the Output and Output Complementary Sensitivity functions. With the previous considerations, the closed-loop interconnection matrix $\mathbf{M}(\Omega) = \left[\begin{array}{c|c}\mathbf{M}_{\mathbf{w}\to\mathbf{z}}(\Omega) & \mathbf{M}_{\mathbf{d}\to\mathbf{z}}(\Omega)\\ \hline \mathbf{M}_{\mathbf{w}\to\mathbf{e}}(\Omega) & \mathbf{M}_{\mathbf{d}\to\mathbf{e}}(\Omega)\end{array}\right] = \mathcal{F}_l\left(\mathbf{P}(\Omega), \mathbf{K}(\Omega)\right)$ has the following expression

$$\left[\begin{array}{c}\mathbf{z}_{\Delta u}\\ \mathbf{z}_{\Delta y}\\ \mathbf{z}_{\Delta a}\\ \hline \mathbf{e}_p\\ \mathbf{e}_u\end{array}\right] = \underbrace{\operatorname{diag}\left(\begin{array}{c}\mathbf{I}\\ \mathbf{I}\\ \mathbf{W}_{\Delta r}\widehat{\mathbf{H}}\\ \hline \mathbf{W}_p\\ \mathbf{W}_u\end{array}\right)\left[\begin{array}{ccc|cc}-\mathbf{T}_i & \mathbf{S}_i\mathbf{K} & \mathbf{S}_i\mathbf{K} & -\mathbf{S}_i\mathbf{K}\mathbf{G}_{yd} & \mathbf{S}_i\mathbf{K}\\ \mathbf{G}_{yu}\mathbf{S}_i & \mathbf{T}_o & \mathbf{T}_o & \mathbf{S}_o\mathbf{G}_{yd} & \mathbf{T}_o\\ -\mathbf{T}_i & \mathbf{S}_i\mathbf{K} & \mathbf{S}_i\mathbf{K} & -\mathbf{S}_i\mathbf{K}\mathbf{G}_{yd} & \mathbf{S}_i\mathbf{K}\\ \hline \mathbf{G}_{pu}\mathbf{S}_i & \mathbf{G}_{pu}\mathbf{S}_i\mathbf{K} & \mathbf{G}_{pu}\mathbf{S}_i\mathbf{K} & \mathbf{G}_{pd} - \mathbf{G}_{pu}\mathbf{S}_i\mathbf{K}\mathbf{G}_{yd} & \mathbf{G}_{pu}\mathbf{S}_i\mathbf{K}\\ -\mathbf{T}_i & \mathbf{S}_i\mathbf{K} & \mathbf{S}_i\mathbf{K} & -\mathbf{S}_i\mathbf{K}\mathbf{G}_{yd} & \mathbf{S}_i\mathbf{K}\end{array}\right]\operatorname{diag}\left(\begin{array}{c}\mathbf{W}_{\Delta u}\\ \mathbf{W}_{\Delta y}\\ \widehat{\mathbf{N}}\mathbf{W}_{\Delta l}\\ \hline \mathbf{W}_d\\ \mathbf{W}_n\end{array}\right)}_{\mathbf{M}(\Omega) = \mathcal{F}_l\left(\mathbf{P}(\Omega), \mathbf{K}(\Omega)\right)}\left[\begin{array}{c}\mathbf{w}_{\Delta u}\\ \mathbf{w}_{\Delta y}\\ \mathbf{w}_{\Delta a}\\ \hline \mathbf{d}_w\\ \mathbf{d}_n\end{array}\right] \tag{3.17}$$

where the dependency on $\Omega$ of the various functions was omitted in order to improve readability. Finally, closing the uncertainty channels $\mathbf{w}$ and $\mathbf{z}$ around $\Delta$ provides the closed-loop mapping $\mathbf{e} = \mathcal{F}_u\left(\mathbf{M}(\Omega), \Delta\right)\mathbf{d} = \left[\mathbf{M}_{\mathbf{d}\to\mathbf{e}}(\Omega) + \mathbf{M}_{\mathbf{w}\to\mathbf{e}}(\Omega)\Delta\left(\mathbf{I} - \mathbf{M}_{\mathbf{w}\to\mathbf{z}}(\Omega)\Delta\right)^{-1}\mathbf{M}_{\mathbf{d}\to\mathbf{z}}(\Omega)\right]\mathbf{d}$ between the normalized disturbance signals $\mathbf{d}$ and performance outputs $\mathbf{e}$ in the presence of uncertainties.

### Model reduction

As defined in (3.10), the number of states of the LPV system $\widehat{\mathbf{G}}(\Omega)$ is equal to 44. Due to its large size, such a system can pose serious numerical difficulties if directly used in most robust control synthesis algorithms. This is why, in order to obtain a low-order LFT model that is more suitable for synthesis, a model reduction procedure is introduced. Coupled with an additive uncertainty model, this is used to provide a simplified representation within the desired control bandwidth 10-50 Hz corresponding to the RWA spin range $\boldsymbol{\Omega}$.

Let $\boldsymbol{\Phi} = \begin{bmatrix}\phi_1 & \phi_2 & \dots & \phi_n\end{bmatrix} \in \mathbb{R}^{n\times n}, n = 22$ be the mass-normalized modal matrix of the mechanical system $\widehat{\mathbf{G}}$ calculated for the nominal values of $\boldsymbol{\mathcal{M}}$ and $\boldsymbol{\mathcal{K}}$ and assuming no damping, i.e $\boldsymbol{\mathcal{C}} = \boldsymbol{\mathcal{G}} = \mathbf{0}_n$. Each of the $n$ mode shapes $\phi_\bullet$ has an associated modal frequency $\omega_\bullet$ and the matrix $\boldsymbol{\Phi}$ satisfies, for nominal values of $\boldsymbol{\mathcal{M}}$ and $\boldsymbol{\mathcal{K}}$, the following relationships:

$$\boldsymbol{\Phi}^\mathsf{T}\boldsymbol{\mathcal{M}}\boldsymbol{\Phi} = \mathbf{I}_n, \quad \left(\boldsymbol{\mathcal{K}} - \omega_i^2\boldsymbol{\mathcal{M}}\right)\phi_i = 0, \quad \boldsymbol{\Phi}^\mathsf{T}\boldsymbol{\mathcal{K}}\boldsymbol{\Phi} = \operatorname{diag}\left(\omega_i^2\right) \quad \text{for} \quad i \in \{1, \dots, n\} \tag{3.18}$$

In this case, $\mathbf{q} = \boldsymbol{\Phi}\boldsymbol{\eta}$ can be used to describe the state $\mathbf{q}$ of the system in terms of the modal coordinates $\boldsymbol{\eta}(t) \in \mathbb{R}^n$. Consider now a partitioning $\boldsymbol{\Phi} = \begin{bmatrix}\boldsymbol{\Phi}_r & \boldsymbol{\Phi}_t\end{bmatrix}$ and $\boldsymbol{\eta} = \begin{bmatrix}\boldsymbol{\eta}_r^\mathsf{T} & \boldsymbol{\eta}_t^\mathsf{T}\end{bmatrix}^\mathsf{T}$ where $\boldsymbol{\Phi}_r \in \mathbb{R}^{n\times n_r}$ contains the $n_r$ modal vectors to be retained and $\boldsymbol{\Phi}_t$ those that will be truncated. The

original system state $\mathbf{q} = \mathbf{\Phi}_r \boldsymbol{\eta}_r + \mathbf{\Phi}_t \boldsymbol{\eta}_t$ corresponding to the system (3.6) and the input-output model $\widehat{\mathbf{G}}(\Omega)$ is therefore approximated with a reduced state $\mathbf{q}_r = \mathbf{\Phi}_r \boldsymbol{\eta}_r \in \mathbb{R}^{n_r}$.

Following this procedure, the original system $\widehat{\mathbf{G}}(\Omega)$ with 44 states $\begin{bmatrix}\mathbf{q}^\mathsf{T} & \dot{\mathbf{q}}^\mathsf{T}\end{bmatrix}^\mathsf{T}$ shown in (3.10) was converted into a reduced order system $\widehat{\mathbf{G}}_r(\Omega)$ with just 14 states $\begin{bmatrix}\mathbf{q}_r^\mathsf{T} & \dot{\mathbf{q}}_r^\mathsf{T}\end{bmatrix}^\mathsf{T}$ and defined as:

$$\underbrace{\mathcal{F}_u\left(\mathbf{G}_r, \begin{bmatrix}\Omega\mathbf{I}_2 & \\ & \Delta_G\end{bmatrix}\right)}_{\widehat{\mathbf{G}}_r(\Omega)} = \left(\begin{array}{cc|c} \mathbf{0} & \mathbf{I} & \mathbf{0} \\ -\boldsymbol{\mathcal{G}}_r^{-1}\boldsymbol{\mathcal{K}}_r & -\boldsymbol{\mathcal{M}}_r^{-1}\left(\boldsymbol{\mathcal{C}}_r + \Omega\boldsymbol{\mathcal{G}}_r\right) & \boldsymbol{\mathcal{M}}_r^{-1}\boldsymbol{\mathcal{Q}}_r \\ \hline \boldsymbol{\mathcal{S}}_r & & \mathbf{0} \end{array}\right) \quad ; \tag{3.19}$$

$$\boldsymbol{\mathcal{M}}_r = \mathbf{\Phi}_r^\mathsf{T}\boldsymbol{\mathcal{M}}\mathbf{\Phi}_r \quad \boldsymbol{\mathcal{C}}_r = \mathbf{\Phi}_r^\mathsf{T}\boldsymbol{\mathcal{C}}\mathbf{\Phi}_r \quad \boldsymbol{\mathcal{G}}_r = \mathbf{\Phi}_r^\mathsf{T}\boldsymbol{\mathcal{G}}\mathbf{\Phi}_r$$
$$\boldsymbol{\mathcal{K}}_r = \mathbf{\Phi}_r^\mathsf{T}\boldsymbol{\mathcal{K}}\mathbf{\Phi}_r \quad \boldsymbol{\mathcal{Q}}_r = \mathbf{\Phi}_r^\mathsf{T}\boldsymbol{\mathcal{Q}} \quad \boldsymbol{\mathcal{S}}_r = \boldsymbol{\mathcal{S}}\ \mathrm{diag}\left(\mathbf{\Phi}_r, \mathbf{\Phi}_r\right)$$

In order to quantify the modeling errors introduced by this truncation, let $a_{ij} \in \mathbb{R};\ \ i,j \in \{1,\ldots,6\}$ represent the upper bounds on the additive errors between $\widehat{\mathbf{G}}$ and $\widehat{\mathbf{G}}_r$ along each of the possible signal paths $\mathbf{u}_s(i) \to \mathbf{y}_s(j)$ and across all parametric uncertainties $\Delta_G \in \boldsymbol{\Delta}_G$ and $\Omega \in \boldsymbol{\Omega}$, i.e.

$$\sup_{\Delta\in\boldsymbol{\Delta}_G,\ \Omega\in\boldsymbol{\Omega}} \left\| \left(\widehat{\mathbf{G}}(\Omega) - \widehat{\mathbf{G}}_r(\Omega)\right)_{\mathbf{u}_s(i)\to\mathbf{y}_s(j)} \right\|_{\mathcal{L}_{2i}} \leq a_{ij} \quad ; \quad i,j \in \{1,\ldots,6\} \tag{3.20}$$

The computation of the worst-case upper bounds $a_{ij}$ has been done using the standard $\mu$ algorithms described in [PBLJ00] that are based on the relation given in (2.58) and are implemented in MATLAB as the the command wcgain. For clarity, these additive errors and the associated upper bounds are shown in fig. 3.8 for two different transfers of the models $\widehat{\mathbf{G}}$ and $\widehat{\mathbf{G}}_r$. It can be seen that this simple additive bounds covers all the high frequency dynamics outside of the control bandwidth while also accounting for system variations in the mid and low frequency ranges.

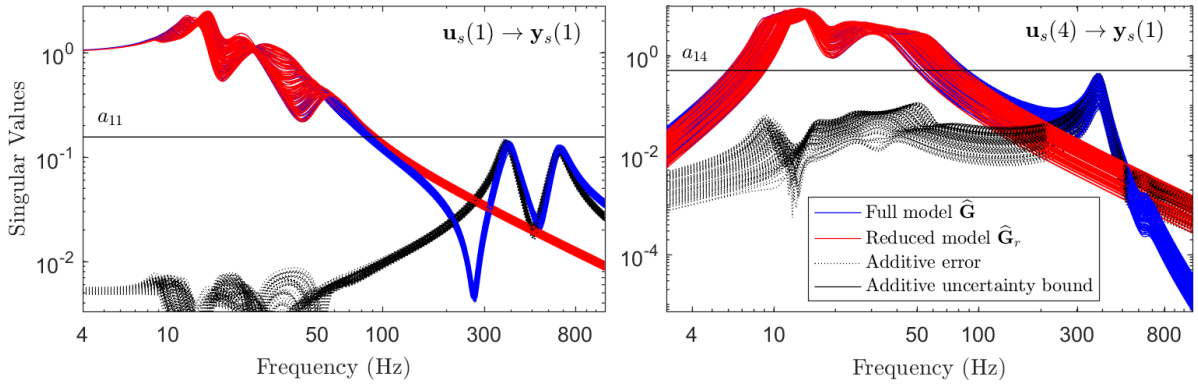


Figure 3.8: Singular values of the full and reduced structural models for different uncertainty values and wheel rates together with the corresponding additive uncertainty bounds.

### 3.3.3 Weighting function selection

The goal of this section is to explain in a systematic fashion how the weights $\mathbf{W}_\bullet$ were selected to convert the design requirements introduced in section 3.3.1 into the conditions aggregated in table 3.2 that are based upon the definitions (2.56) and (2.58).

Table 3.2: System requirements and the corresponding $\mathcal{H}_\infty/\mu$ criteria used for synthesis and analysis

| System requirements | Equivalent analysis criteria | Synthesis condition |
|---|---|---|
| **(R1)** Stability for $\|\Delta\|_{\mathcal{L}_{2i}} \leq \nu$ | $\sup_{\omega\in\mathbb{R}} \mu_{\mathbf{\Delta}}\left(\mathbf{M}_{\mathbf{w}\to\mathbf{z}}(\Omega, j\omega)\right) < 1/\nu$ | $\inf_{\boldsymbol{\mathcal{D}}\in\mathbb{D}} \left\|\boldsymbol{\mathcal{D}}\mathbf{M}_{\mathbf{w}\to\mathbf{z}}(\Omega)\boldsymbol{\mathcal{D}}^{-1}\right\|_{\mathcal{L}_{2i}} < 1/\nu$ |
| **(R2)** Performance for $\|\Delta\|_{\mathcal{L}_{2i}} \leq \epsilon$<br>Amplitude Spectral Densities:<br>RPE $_{t_\Delta=20\,\mathrm{ms}} < 0.65\,\mathrm{mas}/\sqrt{\mathrm{Hz}}$<br>Actuators $< 10\,\mathrm{V}/\sqrt{\mathrm{Hz}}$ | $\sup_{\substack{\Delta\in\mathbf{\Delta},\\ \|\Delta\|_{\mathcal{L}_{2i}}\leq\epsilon}} \left\|\mathcal{F}_u\left(\mathbf{M}(\Omega),\Delta\right)_{\mathbf{d}\to\mathbf{e}(i)}\right\|_{\mathcal{L}_{2i}} < 1$<br>for $i \in \{1,\ldots,8\}$ | $\inf_{\boldsymbol{\mathcal{D}}\in\mathbb{D}} \left\|\begin{bmatrix}\boldsymbol{\mathcal{D}}\sqrt{\epsilon} \\ \boldsymbol{\mathcal{X}}(i)\end{bmatrix}\mathbf{M}(\Omega)\begin{bmatrix}\sqrt{\epsilon}\boldsymbol{\mathcal{D}}^{-1} \\ \mathbf{I}\end{bmatrix}\right\|_{\mathcal{L}_{2i}} < 1$<br>with $\boldsymbol{\mathcal{X}}(i) = \begin{bmatrix}\mathbf{0}_{1\times(i-1)} & 1 & \mathbf{0}_{1\times(8-i)}\end{bmatrix}$ |

for all $\Omega \in \mathbf{\Omega}$ with $\epsilon, \nu \in [0,1]$; $\boldsymbol{\mathcal{D}} \in \mathbb{D}$ and $\boldsymbol{\mathcal{D}}\Delta = \Delta\boldsymbol{\mathcal{D}}$.

### Uncertainty weights

Firstly, the weights $\mathbf{W}_{\Delta\bullet}$ are used to scale the blocks $\mathbf{M}_{\mathbf{w}\to\mathbf{z}}(\Omega)$, $\mathbf{M}_{\mathbf{d}\to\mathbf{z}}(\Omega)$, $\mathbf{M}_{\mathbf{w}\to\mathbf{e}}(\Omega)$ in (3.17) and therefore the set of complex uncertainties $\Delta \in \mathbf{\Delta}$ over which the robust stability/performance requirements should be enforced. In order to comply with the conditions summarized in table 3.2, any increase in $\mathbf{W}_{\Delta\bullet}$, covering a larger uncertainty set, must be accompanied by a corresponding decrease in the maximum gains of some closed-loop functions, such as $\mathbf{T}_i$, $\mathbf{S}_i\mathbf{K}$, $\mathbf{T}_o$ that are scaled by that particular weight. Satisfying these requirements, places an upper limit on the maximum achievable disturbance rejection performance as the function $\mathbf{S}_i\mathbf{K}$ also appears in the closed-loop propagation $\mathbf{M}_{\mathbf{d}_w\to\mathbf{e}_p}$ from wheel disturbances $\mathbf{d}_w$ towards the pointing stability indicator $\mathbf{e}_p$. To maximize performance, it is therefore necessary to cover the possible plant model variations with smallest uncertainty set using low magnitude weights $\mathbf{W}_{\Delta\bullet}$. As such, the space of gain variations produced by uncertainties in the sensor placement matrix $\widehat{\mathbf{N}} = \mathcal{F}_u\left(\mathbf{N}, \Delta_n\right)$ defined in (2.35) is covered using with the weight $\mathbf{W}_{\Delta y} = 0.1\,\mathbf{I}_{12}$ that scales the normalized complex uncertainty block $\Delta_y$ with $\|\Delta_y\|_{\mathcal{L}_{2i}} \leq 1$. The choice accounts for a maximum 10% multiplicative uncertainty in each of the force sensor measurements. Similarly, the uncertainty model of the actuators is shaped by:

$$\mathbf{W}_{\Delta u} = \Gamma(s)\,\mathbf{I}_6 \quad \text{with} \quad \begin{array}{l}\Gamma(s) = \beta + \alpha\cdot w_\tau(s) \\ \beta = 30\%\end{array} \quad \text{and} \quad \begin{array}{l}\alpha = 1 - \beta/3.465 \\ w_\tau(s) = s/\left(\tau_{max}^{-1} + s/3.465\right) \\ \tau_{max} = 1\,\mathrm{ms}\end{array} \tag{3.21}$$

such that $|\Gamma(j\omega)| \geq \max\left(\beta, |w_\tau(j\omega)|\right)\ \ \forall\omega \in \mathbb{R}$. Here, $\beta = 30\%$ is used to account for input multiplicative uncertainty in each of the PMA actuators, covering unmodeled dynamics and saturations effects, while $w_\tau(s)$ provides an additional over-bound on the multiplicative uncertainty due to the uncertain time-delay $\tau \in [0, \tau_{max}]$ (see [WLS94] for additional details). Finally, the weights $\mathbf{W}_{\Delta l} \in \mathbb{R}^{6\times 36}$ and $\mathbf{W}_{\Delta r} \in \mathbb{R}^{36\times 6}$ are used to scale the additive uncertainty $\Delta_a$ and cover the truncation errors resulting from the model reduction and also account for structural uncertainty within the control bandwidth. These weights are directly chosen based on the additive errors bounds $a_{ij}$ calculated in (3.20), such that:

$$\mathbf{W}_{\Delta l}\Delta_a\mathbf{W}_{\Delta r} = \begin{bmatrix} a_{11}\delta_{16} & \ldots & a_{16}\delta_{16} \\ \vdots & \ddots & \vdots \\ a_{61}\delta_{66} & \ldots & a_{66}\delta_{66}\end{bmatrix} \quad \text{with} \quad \Delta_a \in \left\{\mathrm{diag}\left(\delta_{ij}\right) : \begin{array}{c}\delta_{ij}\in\mathbb{C},\ |\delta_{ij}|\leq 1 \\ i,j\in\{1,\ldots,6\}\end{array}\right\} \subset \mathbb{C}^{36\times 36} \tag{3.22}$$

### Input weights and disturbance source modeling

The input weight $\mathbf{W}_n \in \mathbb{R}^{12\times 12}$ is used to scale the Amplitude Spectral Density (ASD) of the unit spectral density signal $\mathbf{d}_n$ such that $\mathbf{n} = \mathbf{W}_n\mathbf{d}_n$ approximates the maximum sensor noise observed

in typical operations. As previously done in (2.60), the choice was made to fix

$$\mathbf{W}_n = n_{max}\mathbf{I}_{12} \quad ; \quad n_{max} = 10^{-3}\mathrm{N}/\sqrt{\mathrm{Hz}} \tag{3.23}$$

based on the sensor's signal-to-noise characteristic, corresponding to an upper bound of $n_{max}$ on the noise spectrum for each of the twelve sensor measurement channels.

In the same way, the weight $\mathbf{W}_d(\Omega)$ is used to capture the spectral content of the disturbances $\mathbf{u}_w$ introduced by wheel into the satellite structure and given in (3.4). Following this previous definition, the weight is decomposed into the broadband and tonal components i.e.

$$\mathbf{u}_w = \underbrace{\mathbf{W}_{bn}\mathbf{d}_{bn}}_{\text{broadband noise } \mathbf{u}_{bn}} + \sum_{i=1}^{N} \underbrace{\mathbf{W}_i(\Omega)d_i}_{\text{i-th harmonic } \mathbf{u}_i} \tag{3.24}$$

$$= \left[\mathbf{W}_1(\Omega) \ \ldots \ \mathbf{W}_N(\Omega) \mid \mathbf{W}_{bn}\right]\left[d_1 \ \ldots \ d_N \mid \mathbf{d}_{bn}^{\mathsf{T}}\right]^{\mathsf{T}} = \mathbf{W}_d(\Omega)\mathbf{d}_w \tag{3.25}$$

where $\mathbf{d}_{bn}$ and $d_i$ are white noise signals with unit spectral density. The broadband disturbance model $\mathbf{W}_{bn} \in \mathbb{R}^{4\times 4}$ is fixed to:

$$\mathbf{W}_{bn} = \mathrm{diag}\left(a_1^f \Omega_{bn}^2 \mathbf{I}_2,\ a_1^t \Omega_{bn}^2 \mathbf{I}_2\right) \quad \text{with} \quad \Omega_{bn} = 1\,\mathrm{Hz}. \tag{3.26}$$

This choice provides a crude approximation of the maximum spectral amplitude of the broadband noise and neglected harmonics based upon the main harmonic disturbances generated by the RW spinning at $\Omega_{bn} = 1\,\mathrm{Hz}$. This model can of course be refined based upon a more rigorous identification procedure of the broadband noise magnitude. However, for the purposes of this study, the simple model (3.26) is considered sufficient. Each of the weighting functions $\mathbf{W}_i(\Omega)$ with $i = \{1, \ldots, N\}$ has the role of modeling the amplitude spectrums and phase relationships between the different components of the harmonic disturbance vector $\mathbf{u}_w^i = \left[F_i^x \ \ F_i^y \ \ T_i^x \ \ T_i^y\right]^{\mathsf{T}}$ from (3.5). The internal structure of the $\mathbf{W}_i(\Omega)$ weights is illustrated in fig. 3.9. The system $F_{\text{peak}}(\Omega)$,

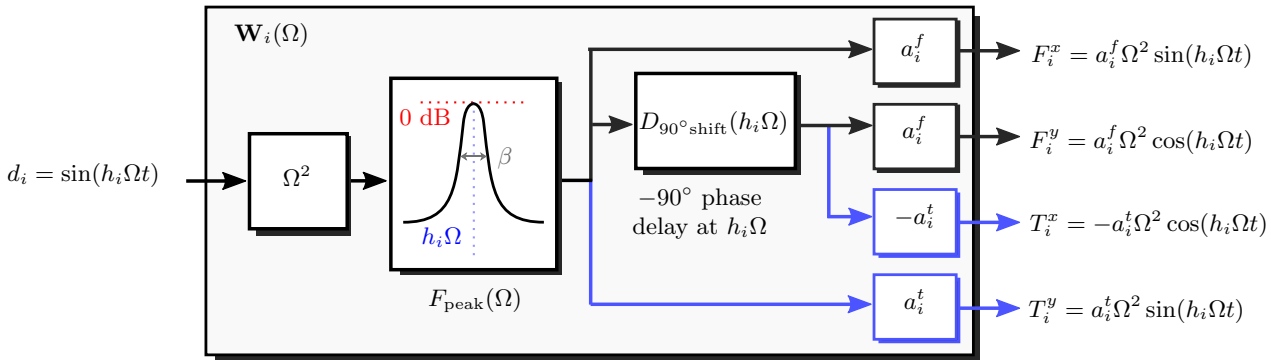


Figure 3.9: Internal structure of the weight $\mathbf{W}_i(\Omega)$ corresponding to the $i$-th harmonic disturbance. Note: outputs represent the steady state values when driven by the harmonic input $d_i(t) = \sin(h_i\Omega t)$.

contained within these weights, is chosen as the following second order unit gain bandpass filter:

$$F_{\text{peak}}(\Omega) = \frac{\beta s}{s^2 + \beta s + (h_i\Omega)^2} \quad \text{or in state space form} \quad F_{\text{peak}}(\Omega) = \left(\begin{array}{cc|c} -\beta & -h_i\Omega & \beta \\ h_i\Omega & 0 & 0 \\ \hline 1 & 0 & 0 \end{array}\right) \tag{3.27}$$

Together with the $\Omega^2$ and the $a_i^f, a_i^t$ scalings, its role is to provide for different spin rates $\Omega$, an approximation of the spectral amplitude corresponding to each of the RW harmonic force and torque components of $\mathbf{u}_w^i$. To do this, $F_{\text{peak}}(\Omega)$ is chosen to approximate the spectral amplitude of a unit

harmonic signal $\sin(h_i\Omega t)$. It can be seen that the parameter $\beta$ controls the filter bandwidth and is used to account for the way the disturbance energy is distributed around the central frequency $h_i\Omega$. If $F_{peak}(\Omega)$ is driven unit white noise, the power (or RMS value) of the resulting signal is equal to the $\mathcal{H}_2$ system norm of $F_{peak}(\Omega)$ given below:

$$\|F_{peak}\|_{\mathcal{H}_2} = \left(\frac{1}{2\pi}\int_{-\infty}^{\infty}\left|F_{peak}(j\omega)\right|^2 d\omega\right)^{1/2} = \sqrt{\frac{\beta}{2}} \tag{3.28}$$

In order to match this value with the RMS of a unit harmonic signal i.e. $1/\sqrt{2}$, the bandwidth $\beta$ is fixed to $\beta = 1$.

The $-90°$ phase delay between the components of the harmonic force $\begin{bmatrix}F_i^x & F_i^y\end{bmatrix}$ and torque $\begin{bmatrix}T_i^x & T_i^y\end{bmatrix}$ vectors is modeled using a first order time-delay filter:

$$D_{90°\text{shift}}(h_i\Omega) = \frac{-\tau_{\Omega i}s + 2}{\tau_{\Omega i}s + 2} = \left(\begin{array}{c|c} -2\tau_{\Omega i}^{-1} & 1 \\ \hline 4\tau_{\Omega i}^{-1} & -1 \end{array}\right) \quad \text{with} \quad \tau_{\Omega i} = (0.5h_i\Omega)^{-1} \tag{3.29}$$

Here, the delay is fixed to $\tau_{\Omega i} = (0.5h_i\Omega)^{-1}$ in order to introduce the corresponding $-90°$ phase delay at the harmonic frequency $h_i\Omega$ for any given wheel spin rate $\Omega$. With the previous considerations, it is possible to recast $\mathbf{W}_i$ as a system model affine in $\Omega$ and subsequently as an LFT, in the following way:

$$\begin{aligned}\mathbf{W}_i(\Omega) &= \begin{bmatrix} a_i^f & 0 \\ 0 & a_i^f \\ 0 & -a_i^t \\ a_i^t & 0 \end{bmatrix}\begin{bmatrix} 1 \\ \\ D_{90°\text{shift}}(\Omega) \end{bmatrix} F_{peak}(\Omega)\,\Omega^2 = \begin{bmatrix} a_i^f & 0 \\ 0 & a_i^f \\ 0 & -a_i^t \\ a_i^t & 0 \end{bmatrix}\left(\begin{array}{ccc|c} -\beta & -h_i\Omega & 0 & \beta\Omega \\ h_i\Omega & 0 & 0 & 0 \\ \Omega & 0 & -h_i\Omega & 0 \\ \hline \Omega & 0 & 0 & 0 \\ -\Omega & 0 & 2h_i\Omega & 0 \end{array}\right) \\ &= \mathcal{F}_u\left(\mathbf{W}_i, \Omega\mathbf{I}_3\right)\end{aligned} \tag{3.30}$$

**Remark 4.** *When driven by the normalized harmonic signal $d_i = \sin(h_i\Omega t)$, the steady-state outputs of this filter precisely match those of the i-th harmonic given in (3.5) when the force and torque vectors are perpendicular*[2] *i.e $\phi_i^f = \phi_i^t$. On the other hand if the input $d_i$ is set to unit white noise, the stochastic responses will have amplitude spectral densities matching the gains along each output channel of $\mathbf{W}_i$. Additionally, due to the bandwidth choice $\beta = 1$, the power of steady-state output is mainly focused within the narrow region around $h_i\Omega$ and equal to that of the harmonic signals (3.5). Therefore, in this stochastic context, the filter $\mathbf{W}_i$ can also be interpreted as an approximation in terms of power distribution of the deterministic sinusoidal perturbations.*

**Remark 5.** *A more refined amplitude spectrum of the unit harmonic signal can be obtained by replacing the peak filter $F_{peak}(\Omega)$ in (3.27) by a cascade of $n$ copies of itself. In this case, the overall filter deemed $F_{peak/n}(\Omega)$ of order $2n$ will have a sharper roll-off of $(20\,n)$ dB/decade and concentrate more of the signal energy around the central frequency $\Omega$.*

*In this work, a novel state space model of $F_{peak/n}(\Omega)$ for $n > 2$ is introduced. The representation*

[2]The filter can be adapted to include other phase relationships by introducing different delays or slightly altering the structure. For example if the phase relationship between the force and torque vectors is unknown, one possibility is to split the $\mathbf{W}_i$ weight into two copies of itself $\mathbf{W}_i = \begin{bmatrix}\mathbf{W}_i^f & \mathbf{W}_i^t\end{bmatrix}$ with the amplitude coefficients are fixed to $a_i^t = 0$ in $\mathbf{W}_i^f$ and $a_i^f = 0$ in $\mathbf{W}_i^t$. Afterwards the new weight is considered driven by two independent normalized force and torque signals $d_i^f$ and $d_i^t$.

*is affine in* $\Omega$ *and has the following recursive definition:*

$$F_{peak/n}(\Omega) := \left(\frac{\beta s}{s^2+\beta s+(h_i\Omega)^2}\right)^n = \left(\begin{array}{c|c}\mathbf{A}_n & \mathbf{B}_n \\ \hline \mathbf{C}_n & 0\end{array}\right) = \left(\begin{array}{c|c}\mathbf{A}_n & \begin{matrix}\beta\\ \mathbf{0}\end{matrix} \\ \hline \mathbf{0}\ 1\ 0 & 0\end{array}\right) \tag{3.31}$$

$$\textit{where}\quad \mathbf{A}_n = \begin{bmatrix}\mathbf{A}_1 & \mathbf{0}\\ \begin{bmatrix}\beta\\ \mathbf{0}\end{bmatrix}\begin{bmatrix}1 & 0\end{bmatrix} & \mathbf{A}_{n-1}\end{bmatrix} \quad \textit{and}\quad \mathbf{A}_1 = \begin{bmatrix}-\beta & -h_i\Omega\\ h_i\Omega & 0\end{bmatrix}$$

*In this case, the expression of the* $\mathcal{H}_2$ *norm can be calculated analytically from the state space matrices as*

$$\left\|F_{peak/n}\right\|_{\mathcal{H}_2} = \text{Trace}\left(\mathbf{B}_n^\mathsf{T}\mathbf{G}_o\mathbf{B}_n\right) \tag{3.32}$$

*where the matrix* $\mathbf{G}_o$ *represents the observability Gramian [ZDGO96] that is a solution of the following Lyapunov equation:*

$$\mathbf{A}_n^\mathsf{T}\mathbf{G}_o + \mathbf{G}_o\mathbf{A}_n + \mathbf{C}_n^\mathsf{T}\mathbf{C}_n = \mathbf{0} \tag{3.33}$$

*After solving equation (3.32) for different values of* $n$*, it is conjectured in this work that the* $\mathcal{H}_2$ *system norm of* $F_{peak/n}$ *is equal to:*

$$\left\|F_{peak/n}\right\|_{\mathcal{H}_2} = \sqrt{\frac{\beta\kappa_n}{2}} \quad \textit{with} \quad \kappa_n = \frac{(0.5)_{n-1}}{(1)_{n-1}} \tag{3.34}$$

*where* $(\cdot)_n$ *is the Pochhammer symbol (rising factorial). Matching the value of this norm with the RMS value* $1/\sqrt{2}$ *of a unit harmonic signal therefore requires the filter bandwidth to be* $\beta = \kappa_n^{-1}$ *for different values of* $n$*. These* $\beta$ *values for* $n = \{1,\dots,6\}$ *are given in table 3.3 and the singular*

Table 3.3: Necessary peak filter bandwidth $\beta$ of the filter $F_{peak/n}(\Omega)$ for values of $n$

| $n$ | 1 | 2 | 3 | 4 | 5 | 6 |
|---|---|---|---|---|---|---|
| Bandwidth $\beta = \kappa_n^{-1}$ | 1 | 2 | 8/3 | 16/5 | 128/35 | 256/63 |

*values and cumulative RMS of* $F_{peak/n}(\Omega)$ *for* $n = \{1,2,3\}$ *and* $\Omega = 10\,\text{Hz}$ *are shown in fig. 3.10. A slight increase in the gain around the central frequency* $\Omega$ *can be observed for higher* $n$ *values in order to keep power of the signal (*$\mathcal{H}_2$ *norm, i.e. area underneath the singular value plot) equal to* $1/\sqrt{2}$*.*

For the considered wheel model (adapted from [Kim14]), the main harmonic dominates in terms of amplitude over the other harmonics. As such, only the main harmonic weight $\mathbf{W}_1(\Omega)$ , parametrized by $h_1 = 1$, $a_1^f$ and $a_1^t$, will be considered in this study. The other harmonics are all lumped into the stochastic broadband disturbance signal shaped by $\mathbf{W}_{bn}$. With this choice, the complexity of the disturbance model and the subsequent system analysis is significantly reduced. Figure 3.11 shows the magnitude plot towards the first two outputs of this weight together with the phase difference plot between the same two responses across several $\Omega \in \mathbf{\Omega}$. It can be seen that both two outputs share the same peak amplitude of $a_1^f\Omega^2$ while the phase difference at the central frequency $\Omega$ remains at $-90°$ for all different values of $\Omega \in \mathbf{\Omega}$. 28+18 = 46

### Output weights and performance definitions

With the disturbance signals and the complex uncertainties properly scaled in the previous sections, the performance weights $\mathbf{W}_p$ and $\mathbf{W}_u$ can now be selected. These can be seen as specifications

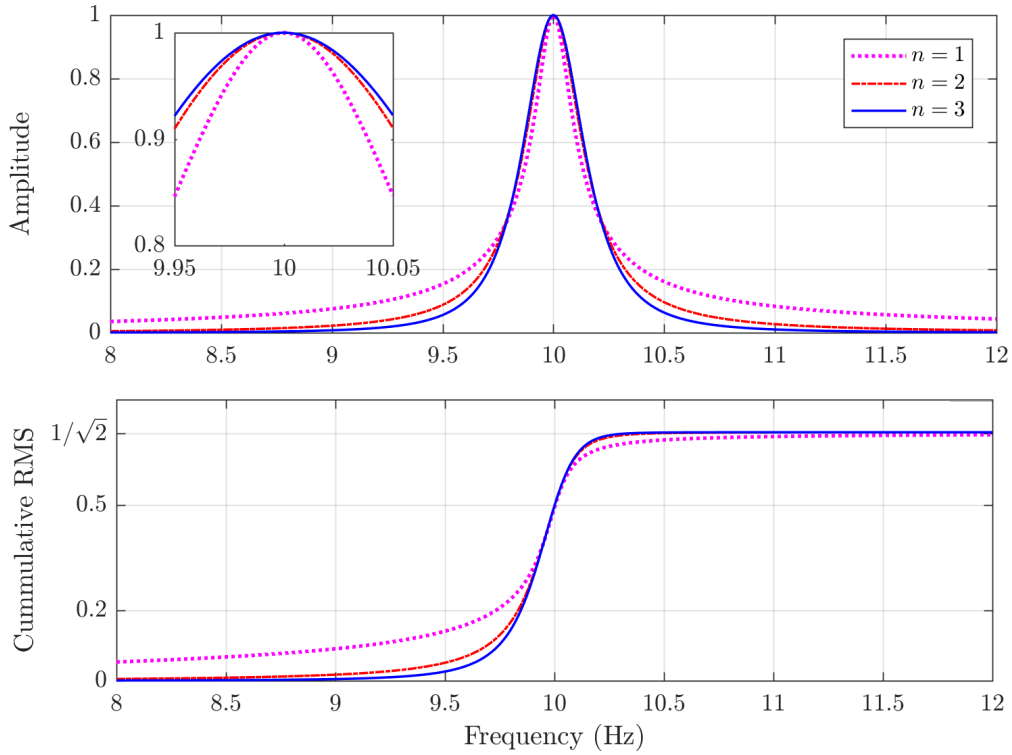


Figure 3.10: Singular values and cumulative RMS of $F_{peak/n}(\Omega)$ for $n = \{1, 2, 3\}$, bandwidth $\beta = \kappa_n^{-1}$ and $\Omega = 10\,\text{Hz}$.

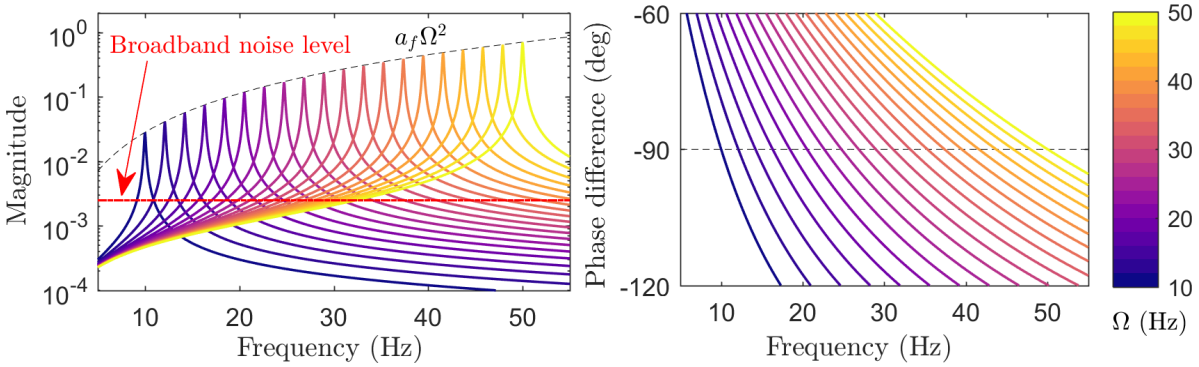


Figure 3.11: Magnitude and phase difference plots for the $F_x$ and $F_y$ outputs of the main harmonic disturbance model $\mathbf{W}_1(\Omega)$ for several wheel rates $\Omega \in [10, 50]\,\text{Hz}$ together with the broadband noise level $\mathbf{W}_{bn}$.

chosen to impose the performance requirements **(R2)** and their inverses represent the desired worst-case upper bounds on the amplitude spectral densities of the actuator control signals $\mathbf{u}_{pma}$ and pointing errors $\mathbf{p}$. In order to understand the limits of achievable performance and properly select these output weights, consider the nominal performance block $\mathbf{M}_{\mathbf{d}\to\mathbf{e}}$ of the closed-loop interconnection $\mathbf{M}(\Omega)$ given in (3.17). As previously stated, the nominal performance requirements are satisfied for a given controller $\mathbf{K}(\Omega)$ whenever the following conditions hold:

$$\left\|\mathbf{M}_{\mathbf{d}\to\mathbf{e}(i)}(\Omega)\right\|_{\mathcal{L}_{2i}} < 1 \quad \forall \Omega \in \mathbf{\Omega} \;\; ; \;\; i = \{1, \ldots, 8\} \;\; ; \;\; \mathbf{M}_{\mathbf{d}\to\mathbf{e}}(\Omega) = \begin{bmatrix} \mathbf{M}_{\mathbf{d}_w\to\mathbf{e}_p} & \mathbf{M}_{\mathbf{d}_n\to\mathbf{e}_p} \\ \mathbf{M}_{\mathbf{d}_w\to\mathbf{e}_u} & \mathbf{M}_{\mathbf{d}_n\to\mathbf{e}_u} \end{bmatrix} = \begin{bmatrix} \mathbf{W}_p & \\ & \mathbf{W}_u \end{bmatrix} \begin{bmatrix} \mathbf{G}_{pd} - \mathbf{G}_{pu}\mathbf{S}_i\mathbf{K}\mathbf{G}_{yd} & \mathbf{G}_{pu}\mathbf{S}_i\mathbf{K} \\ -\mathbf{S}_i\mathbf{K}\mathbf{G}_{yd} & \mathbf{S}_i\mathbf{K} \end{bmatrix} \begin{bmatrix} \mathbf{W}_d & \\ & \mathbf{W}_n \end{bmatrix} \tag{3.35}$$

Based on the control effort requirements **(R2)** the weight $\mathbf{W}_u$ is chosen as

$$\mathbf{W}_u = u_{max}^{-1}\mathbf{I}_6 \quad ; \quad u_{max} = 10\,\mathrm{V}/\sqrt{\mathrm{Hz}} \tag{3.36}$$

such that if the performance conditions $\left\|\mathbf{M}_{\mathbf{d}\to\mathbf{e}_u(\bullet)}(\Omega)\right\|_{\mathcal{L}_{2i}} < 1$ are satisfied an upper bound $u_{max}$ is guaranteed on the worst-case amplitude spectral density of each of the six control signals in $\mathbf{u}_{pma}$ in the presence wheel disturbances and sensor noise. However, compliance with these requirements further limits the achievable pointing performance by placing additional constraints on the maximum gains of the function $\mathbf{S}_i\mathbf{K}$.

The performance weight $\mathbf{W}_p$ is selected to ensure that the worst-case amplitude spectral density profiles of the absolute pointing errors $\mathbf{p} = \begin{bmatrix}\theta_a & \theta_b\end{bmatrix}^\mathsf{T}$ satisfy the pointing stability requirements **(R2)** if $\left\|\mathbf{M}_{\mathbf{d}\to\mathbf{e}_p(\bullet)}(\Omega)\right\|_{\mathcal{L}_{2i}} < 1$. In order to avoid placing contradictory requirements, consider the closed-loop transfer $\mathbf{M}_{\mathbf{d}_w\to\mathbf{e}_p} = \mathbf{W}_p(\mathbf{G}_{pd} - \mathbf{G}_{pu}\mathbf{S}_i\mathbf{K}\mathbf{G}_{yd})\mathbf{W}_d$ from normalized wheel disturbances $\mathbf{d}_w$ to pointing performance $\mathbf{e}_p$ and assume that the weight $\mathbf{W}_p$ has a high gain in a particular frequency region. In order to satisfy the requirements (3.35), the controller must shape the function $\mathbf{S}_i\mathbf{K}$ with sufficiently high gain in the same frequency range and decrease the open-loop disturbance contribution given by $\mathbf{P}_{\mathbf{d}_w\to\mathbf{e}_p} = \mathbf{W}_p\mathbf{G}_{pd}\mathbf{W}_d$ (see (3.16)). However, a high amplitude $\mathbf{S}_i\mathbf{K}$, will also cause an amplification of the noise contribution to the pointing errors $\mathbf{M}_{\mathbf{d}_n\to\mathbf{e}_p}$ and potentially conflict with the requirements on the robust stability and control effort performance. Based on the prior considerations, the pointing performance weight $\mathbf{W}_p$ was chosen as:

$$\mathbf{W}_p = \mathbf{W}_{pmax}\mathbf{W}_{\mathrm{RPE}} \quad \text{with} \quad \begin{matrix}\mathbf{W}_{pmax} = \epsilon_{max}^{-1}\mathbf{I}_2 \\ \epsilon_{max} = 0.65\,\mathrm{mas}/\sqrt{\mathrm{Hz}}\end{matrix} \quad ; \quad \begin{matrix}\mathbf{W}_{\mathrm{RPE}} = \frac{t_\Delta s\left(t_\Delta s+\sqrt{12}\right)}{(t_\Delta s)^2+6(t_\Delta s)+12}\mathbf{I}_2 \\ t_\Delta = 20\,\mathrm{ms}\end{matrix} \tag{3.37}$$

Here, $\mathbf{W}_{\mathrm{RPE}}$ calculates the RPE signals $\mathbf{p}_{\mathrm{RPE}}$ (shown in fig. 3.7) across a window time $t_\Delta = 20\,\mathrm{ms}$ based on the absolute pointing errors $\mathbf{p} = \begin{bmatrix}\theta_a & \theta_b\end{bmatrix}^\mathsf{T}$ using the frequency domain rational approximation given in [ECS11, PM12, OFBW13] . Subsequently, $\mathbf{W}_{pmax}$ is used to comply with the pointing stability requirements and guarantees, if (3.35) holds, an upper bound $\epsilon_{max}$ on the amplitude spectral density of the RPE signals $\mathbf{p}_{RPE}$.

### 3.3.4 Robust LPV controller synthesis

#### Problem setup

With the weights $\mathbf{W}_\bullet$ properly defined in the previous section, the challenge is now to synthesize an appropriate LPV controller $\mathbf{K}(\Omega) \in \boldsymbol{\mathcal{K}}$ that achieves a good trade-off between robustness and performance. Using the definitions given in table 3.2, the controller synthesis is expressed as the following multi-criteria optimization of the closed-loop matrix $\mathbf{M}(\Omega) = \mathcal{F}_l\left(\mathbf{P}(\Omega), \mathbf{K}(\Omega)\right)$:

$$\begin{aligned} &\text{minimize } \gamma \\ &\mathbf{K}(\Omega) \in \boldsymbol{\mathcal{K}}, \\ &\boldsymbol{\mathcal{D}}_s, \boldsymbol{\mathcal{D}}_1, \ldots, \boldsymbol{\mathcal{D}}_8 \in \mathbb{D} \end{aligned} \quad \text{s.t.} \quad \begin{aligned} &\gamma_{MC}(\Omega) = \left\|\mathrm{diag}\left(\begin{bmatrix}\boldsymbol{\mathcal{D}}_i\sqrt{\epsilon} & \\ & \boldsymbol{\mathcal{X}}(i)\end{bmatrix}\mathbf{M}(\Omega)\begin{bmatrix}\sqrt{\epsilon}\boldsymbol{\mathcal{D}}_i^{-1} & \\ & \mathbf{I}\end{bmatrix}\right)\right\|_{\mathcal{L}_{2i}} < \gamma \\ &\left\|\boldsymbol{\mathcal{D}}_s\mathbf{M}_{\mathbf{w}\to\mathbf{z}}(\Omega)\boldsymbol{\mathcal{D}}_s^{-1}\right\|_{\mathcal{L}_{2i}} < 1/\nu \\ &\forall\Omega \in \boldsymbol{\Omega} \qquad i \in \{1,\ldots,8\} \end{aligned} \tag{3.38}$$

with $\boldsymbol{\mathcal{X}}(i) = \begin{bmatrix}\mathbf{0}_{1\times(i-1)} & 1 & \mathbf{0}_{1\times(8-i)}\end{bmatrix}$. The constraint $\left\|\boldsymbol{\mathcal{D}}_s\mathbf{M}_{\mathbf{w}\to\mathbf{z}}(\Omega)\boldsymbol{\mathcal{D}}_s^{-1}\right\|_{\mathcal{L}_{2i}} < 1/\nu$ ensures that the resulting control law will be robustly stable with respect to any uncertainty $\Delta \in \boldsymbol{\Delta}$ with $\|\Delta\|_{\mathcal{L}_{2i}} < \nu$ and $\forall\Omega \in \boldsymbol{\Omega}$. The constraints containing the $\boldsymbol{\mathcal{D}}_i$ scalings are used to guarantee the robust performance requirements. More specifically, for fixed $\epsilon \in [0, 1]$, the constraints assure an $\mathcal{L}_2$

gain upper bound $\|\mathbf{d} \to \mathbf{e}(i)\|_{\mathcal{L}_{2i}} < \gamma$ with respect to any uncertainty $\Delta \in \mathbf{\Delta}$ with $\|\Delta\|_{\mathcal{L}_{2i}} < \epsilon/\gamma$. The $\epsilon$ parameter is used to adjust the trade-off between performance and robustness with higher values forcing the minimization problem to consider larger levels of uncertainty. The minimization problem (3.38), is known to be NP hard even for fixed values of $\Omega$ and is usually handled for the LPV case with heuristics (see [WPS16, VSK09, AA98]) based on the well-known DK-iteration [ZD98]. To overcome the disadvantage of high order controllers generated with these LPV synthesis methods when applied to high order non-academic systems and facilitate the controller implementation, the proposed method relies instead on nonsmooth $\mathcal{H}_\infty$ tools [ADN15, Apk11] to minimize $\gamma$ in (3.38) and synthesize a low order robust LPV controller. It is clear that the time-varying nature of $\Omega(t)$ is not explicitly taken into account in the synthesis phase. As such, the requirements are certified only for fixed $\Omega \in \mathbf{\Omega}$. However, the maximum RW accelerations $\dot{\Omega}(t)$, given in (2.4), are relatively small compared to the system dynamics and therefore, the possible discrepancies between the static and time-varying cases are assumed to be minor. This assumption will be rigorously verified a posteriori in the analysis section of the chapter.

### Controller structure

To increase the controller implementability, its structure is enforced to have the following affine dependency on $\Omega$:

$$\mathbf{K}(\Omega) = \mathbf{K}_{out}\widetilde{\mathbf{K}}(\Omega)\mathbf{K}_{in} \quad \text{where} \quad \begin{aligned}\widetilde{\mathbf{K}}(\Omega) &= \mathcal{F}_l\left(\left(\begin{array}{cc|c} \mathbf{A}_0 & \mathbf{B}_0 & \mathbf{A}_\Delta \\ \mathbf{C}_0 & \mathbf{D}_0 & \mathbf{B}_\Delta \\ \hline \mathbf{C}_\Delta & \mathbf{D}_\Delta & \mathbf{0} \end{array}\right), \Omega\mathbf{I}_{n_\Omega}\right) \\ &= \left(\begin{array}{c|c} \mathbf{A}_0 + \Omega\mathbf{A}_1 & \mathbf{B}_0 + \Omega\mathbf{B}_1 \\ \hline \mathbf{C}_0 + \Omega\mathbf{C}_1 & \mathbf{D}_0 + \Omega\mathbf{D}_1 \end{array}\right)\end{aligned} \tag{3.39}$$

where $\mathbf{A}_1 = \mathbf{A}_\Delta\mathbf{C}_\Delta$, $\mathbf{B}_1 = \mathbf{A}_\Delta\mathbf{D}_\Delta$, $\mathbf{C}_1 = \mathbf{B}_\Delta\mathbf{C}_\Delta$ and $\mathbf{D}_1 = \mathbf{B}_\Delta\mathbf{D}_\Delta$. The system $\widetilde{\mathbf{K}}(\Omega)$ of order $n_K$ forms the LPV part of the overall controller $\mathbf{K}(\Omega)$ and the size $n_\Omega$ of the scheduling block $\Omega\mathbf{I}_{n_\Omega}$ determines the maximum rank of the matrices $\mathbf{A}_1, \mathbf{B}_1, \mathbf{C}_1, \mathbf{D}_1$ in the affine [3] description (3.39). The fixed matrix $\mathbf{K}_{in} = \boldsymbol{\mathcal{X}}_y\mathbf{N}_r \in \mathbb{R}^{2\times 12}$ has the role of a sensor fusion block containing the force reconstruction matrix $\mathbf{N}_r$ defined in (2.33) and the selection matrix $\boldsymbol{\mathcal{X}}_y = \begin{bmatrix}\mathbf{0}_{2\times 3} & \mathbf{I}_2 & \mathbf{0}_{2\times 1}\end{bmatrix}$. The reduced vector $\mathbf{y}_k = \mathbf{K}_{in}\mathbf{y} \in \mathbb{R}^2$ will therefore represent, in the absence of sensor noise and placement uncertainty, a reconstruction of the torques $\begin{bmatrix}T_{su} & T_{sv}\end{bmatrix}$ in the vector $\mathbf{y}_s$ given in (2.20). Similarly, the control allocation block $\mathbf{K}_{out} = \mathbf{B}^+\boldsymbol{\mathcal{X}}_u \in \mathbb{R}^{6\times 4}$ contains the pseudoinverse of nominal PMA force projection matrix $\mathbf{B}$ given in (2.42) together with $\boldsymbol{\mathcal{X}}_u = \text{diag}\left(\begin{bmatrix}\mathbf{I}_2 \\ \mathbf{0}_{1\times 2}\end{bmatrix}, \begin{bmatrix}\mathbf{I}_2 \\ \mathbf{0}_{1\times 2}\end{bmatrix}\right)$. In this case, the actuator signal vector is $\mathbf{u} = \mathbf{K}_{out}\mathbf{u}_k$ where the reduced control vector $\mathbf{u}_k(t) \in \mathbb{R}^4$ can be thought, in the absence of actuator dynamics and uncertainties, as the desired values for the components $\begin{bmatrix}F_{asu} & F_{asv} & T_{asu} & T_{asv}\end{bmatrix}$ of the actuator force and torques vector $\mathbf{u}_s$ applied to the structural model. For clarity, the overall structure of $\mathbf{K}(\Omega)$ is also shown in fig. 3.12.

### Synthesis procedure

According to the controller structure given in (3.39), the goal is now to appropriately tune the LPV part $\widetilde{\mathbf{K}}(\Omega)$ of the controller and the D-scaling matrices such that for given $\epsilon, \nu$ the performance indicator $\gamma$ in (3.38) is minimized. To accomplish this, the following procedure is proposed:

[3] Although not strictly enforced in this study, it can be seen that the LPV structure can be further constrained to be strictly proper by fixing to zero the matrix $\mathbf{D}_0$ and either one of the two factors in $\mathbf{D}_1 = \mathbf{B}_\Delta\mathbf{D}_\Delta$.

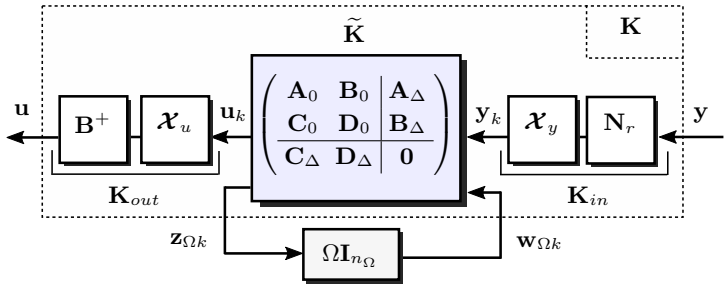


Figure 3.12: Internal structure of the LPV controller $\mathbf{K}(\Omega)$

**Step 1:** The original minimization problem given in (3.38) is reduced to the following simpler, but more conservative, single criteria optimization:

$$\underset{\mathbf{K}(\Omega)\in\boldsymbol{\mathcal{K}} \quad \boldsymbol{\mathcal{D}}\in\mathbb{D}}{\text{minimize}} \quad \gamma \quad \text{s.t.} \quad \gamma_{SC}(\Omega) = \left\| \begin{bmatrix} \boldsymbol{\mathcal{D}}\sqrt{\epsilon} & \\ & \mathbf{I} \end{bmatrix} \mathbf{M}(\Omega) \begin{bmatrix} \sqrt{\epsilon}\boldsymbol{\mathcal{D}}^{-1} & \\ & \mathbf{I} \end{bmatrix} \right\|_{\mathcal{L}_{2i}} < \gamma \quad \text{for} \quad \forall\Omega \in \boldsymbol{\Omega} \tag{3.40}$$

For fixed values of $\boldsymbol{\mathcal{D}}$, $\epsilon$ and $\Omega$, the previous minimization problem can be optimally solved using classical $\mathcal{H}_\infty$ tools. This generates an unstructured controller that has the same order as the augmented plant model $\mathbf{P}(\Omega)$. The performance obtained by such a pointwise optimal controller will afterwards be compared with the ones obtained using the low-order structured LPV controller calculated using non-smooth $\mathcal{H}_\infty$ techniques. This provides a clear measure of the performance penalty that must be paid to achieve the particular controller structure.

**Step 2:** In order to manage the trade-off between robustness and performance objectives, the optimization problem (3.40) is solved for multiple values of $\epsilon \in [0,\ 1]$ using nonsmooth $\mathcal{H}_\infty$ tools over a dense grid of wheel speeds $\Omega$ covering the set $\boldsymbol{\Omega}$. The decision variables are the controller matrices $\mathbf{A}_0 \in \mathbb{R}^{n_K \times n_K}$, $\mathbf{B}_0 \in \mathbb{R}^{n_K \times 2}$, $\mathbf{C}_0 \in \mathbb{R}^{4 \times n_K}$, $\mathbf{C}_\Delta \in \mathbb{R}^{n_\Omega \times n_K}$ and $\mathbf{D}_\Delta \in \mathbb{R}^{n_\Omega \times 2}$ together with the D-scales $\boldsymbol{\mathcal{D}} \in \mathbb{D}$. The orders $n_K$ and $n_\Omega$ are used as degrees of freedom controlling the complexity of the control law and are progressively increased up to a maximum value until the optimization procedure does not yield a significant improvement in $\gamma$. In the study case, the values of $n_K$ and $n_\Omega$ are fixed to $n_K = 6$ and $n_\Omega = 2$. This generates a family of controllers, each tuned for different levels of uncertainty $\epsilon$.

**Step 3:** The additional hard constraint $\left\|\boldsymbol{\mathcal{D}}_s \mathbf{M}_{\mathbf{w}\to\mathbf{z}} \boldsymbol{\mathcal{D}}_s^{-1}\right\|_{\mathcal{L}_{2i}} < 1/\nu$ with $\boldsymbol{\mathcal{D}}_s \in \mathbb{D}$ is added to the minimization problem (3.40) and Step 2 is re-executed for different $\nu \in [0,\ 1]$. This guarantees that each of the resulting controllers will also guarantee robust stability $\forall\Delta \in \boldsymbol{\Delta}$ with $\|\Delta\|_{\mathcal{L}_{2i}} < \nu$. Comparing the resulting performance indicators $\gamma$ with the ones obtained using the controllers generated at Step 2 easily highlights the additional performance cost that must be paid in order to enforce this additional stronger stability requirement.

**Step 4:** For each $\epsilon$ and $\nu$, the controller matrices and the D-scales obtained in the previous step are used to initialize and solve the full minimization problem (3.38). Compared to the previous step, the robust performance requirements are enforced separately only for a subset of output channels using different D-scales. As the optimization problem is less conservative and with more degrees of freedom compared with the previous step, it follows that the performances are guaranteed to improve.

The resulting performance levels $\gamma$ obtained at the end of **Step 4** are shown in fig. 3.13a. Each point maps different values of $\epsilon, \nu \in [0, 1]$ to a performance indication $\gamma$ and a corresponding controller.

Two of these controllers are highlighted in the figure and will be selected for further analysis. The first one, $\mathbf{K}_{performance}$ emphasizes performance over robustness with $\epsilon = 0.01\%$ ; $\nu = 25\%$ and resulted in a performance level $\gamma = 0.376$. The second highlighted controller is labeled as $\mathbf{K}_{robustness}$ and achieves a performance level of $\gamma = 0.955$ for $\nu = 100\%$ and $\epsilon = 5\%$. Compared to the previous controller, the new control law trades performance for guaranteed robustness by placing more demanding robust stability and performance constraints. In order to highlight how the LPV control laws adapts based on the wheel speed, the singular values and poles of $\mathbf{K}_{robustness}$ are shown in fig. 3.13b for different values of $\Omega$. It is clear that for each $\Omega$, the maximum gains follow the main harmonic disturbance and peak around the resonant frequencies of the passive isolator (14 Hz) and flexible attachment (36.5 Hz). The closed-loop stability and robust performances obtained using this controller will be analysed in-depth in section 3.4.

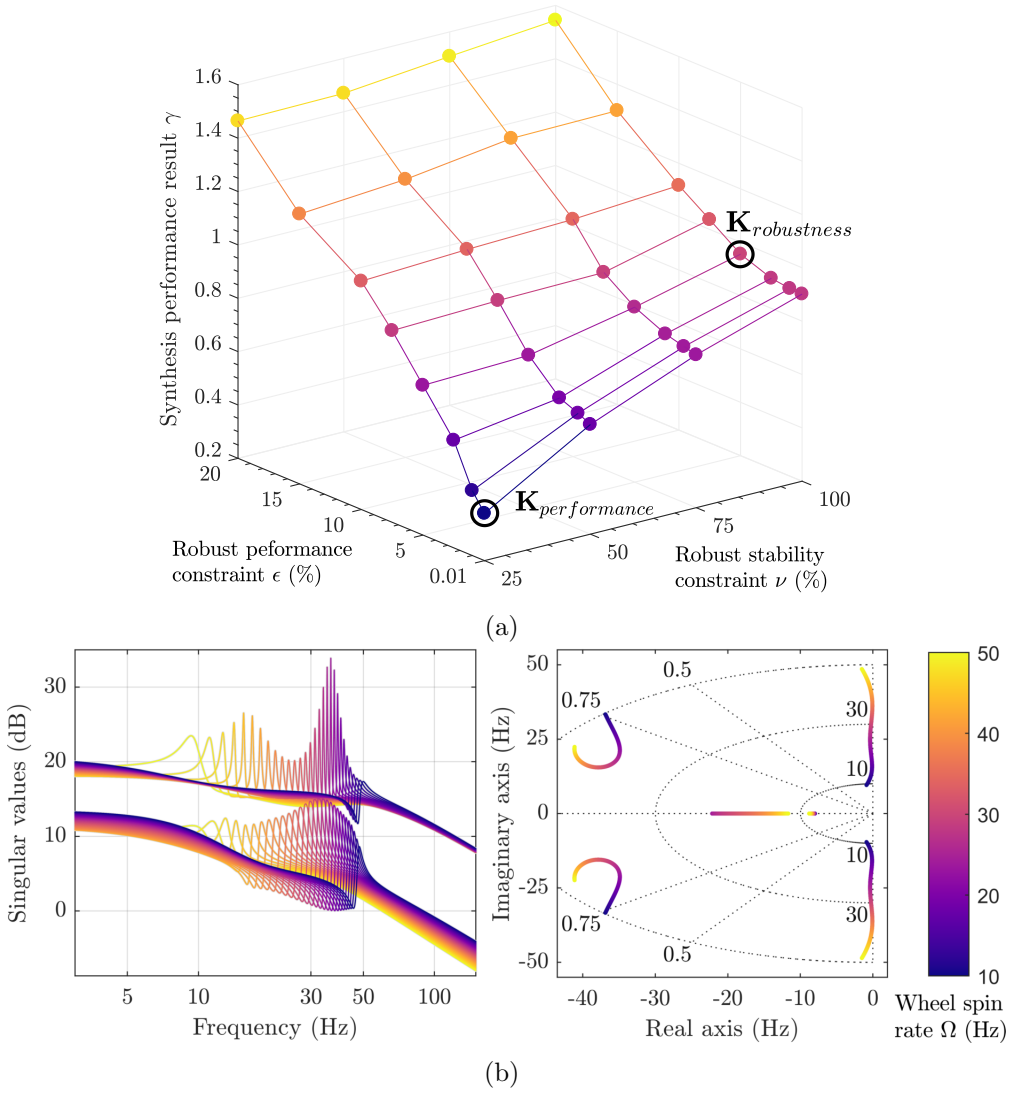


Figure 3.13: (a) Family of synthesized controllers with the corresponding performance indicator $\gamma$ for different $\epsilon$ and $\nu$ (b) Singular values and poles of the selected $\mathbf{K}_{robustness}$ controller across multiple fixed wheel speeds $\Omega \in \mathbf{\Omega}$.

### Performance penalty introduced by the structured LPV design

Imposing a fixed low-order LPV structure for the controller comes with a performance penalty compared to a full order optimal controller precisely tuned for a given $\Omega$. However, this penalty can

be rather small compared to the gains in simplicity and implementability offered by the proposed low-order LPV solution. In an effort to quantify this cost for the $\mathbf{K}_{robustness}$ controller, fig. 3.14 first shows a plot of the performance criterion $\gamma_{SC}(\Omega)$ from (3.40), calculated for multiple fixed $\Omega \in \mathbf{\Omega}$ using the LPV controller and D-scales generated at **Step 2** of the synthesis procedure. Afterwards, with both the D-scales and $\epsilon$ fixed, a set of optimal controllers minimizing the same single criteria (3.40) is calculated using classical $\mathcal{H}_\infty$ tools for each $\Omega$. Comparing the two curves, it can be seen that the single low-order LPV controller closely matches the optimal results with $\gamma_{SC}$ differences varying between $10^{-4}$ and $10^{-1}$. For the considered control problem, this close match is satisfactory and the performance trade-off is deemed acceptable. The additional small penalty needed to enforce the extra robust stability requirement associated with **Step 3** is highlighted by tracing the $\gamma_{SC}(\Omega)$ performance curve obtain using the LPV controller at this particular step. Finally, the curve $\gamma_{MC}(\Omega)$ reveals the value of full performance criteria given in (3.38) using the controller synthesized at **Step 4** of the procedure.

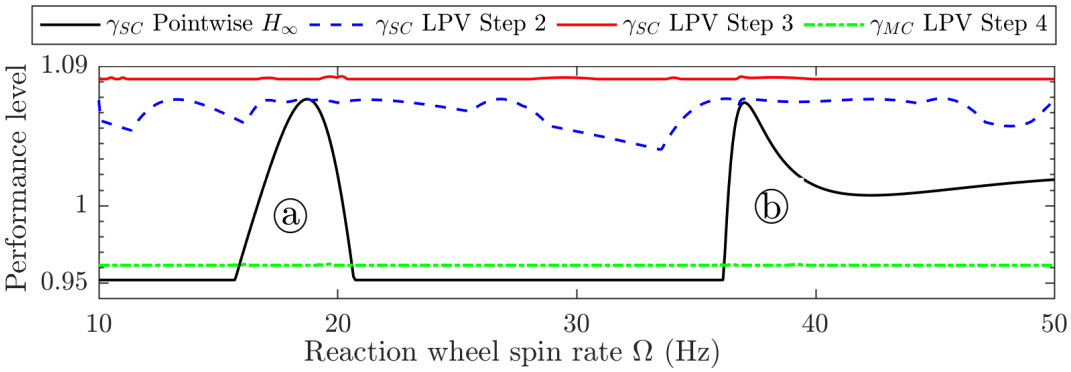


Figure 3.14: Single and multi-criteria performance level curves $\gamma_{SC}(\Omega)$ and $\gamma_{MC}(\Omega)$ obtained using the controller $\mathbf{K}_{robustness}$ at each step of the optimization procedure compared to the $\mathcal{H}_\infty$ optimal value of the single criteria $\gamma_{SC}$ obtained at each distinct value of $\Omega$ using the same fixed D-scales. Frequency regions where the optimal single criteria optimization can't guarantee both robust stability and robust performance requirements: ⓐ - actuator resonance and structural whirl modes; ⓑ - flexible attachment mode.

## 3.4 Performance and stability analysis

### 3.4.1 Nominal performance

The nominal performances using the previously designed LPV controller $\mathbf{K}_{robustness}$ are evaluated by first fixing the uncertainty blocks $\Delta_\bullet$ to zero in the control architecture pictured in fig. 3.7 . Additionally, the full order structural model $\widehat{\mathbf{G}}$ is used in place of the reduced one $\widehat{\mathbf{G}}_r$ employed during synthesis. Next, the singular values are calculated for the transfers from normalized disturbances $\mathbf{d} = \begin{bmatrix}\mathbf{d}_w & \mathbf{d}_w\end{bmatrix}^\mathsf{T}$ towards the pointing errors $\mathbf{p} = \begin{bmatrix}\theta_a & \theta_b\end{bmatrix}^\mathsf{T}$ and actuator control signals $\mathbf{u}$. These singular values are illustrated in fig. 3.15 for different fixed spin rates $\Omega$ in both open and closed-loop configurations. It can be seen that the closed-loop singular values lie below the specifications imposed by the performance weights. For every value of $\Omega$, each of the closed-loop responses shows a peak around the main harmonic disturbance. The peaks occurring around the 15 Hz and 37 Hz are due to the interaction between the main harmonic disturbance with the flexible modes of the passive isolators and those of the satellite attachment. In the case of the pointing errors, the slight amplification in the closed-loop high frequency spectrum can be explained by analyzing the transfer from each component of the disturbance $\mathbf{d}$ towards these performance channels. fig. 3.16a shows the contribution from the sensor noise $\mathbf{d}_n$, broadband perturbation vector $\mathbf{d}_{bn}$ and the main

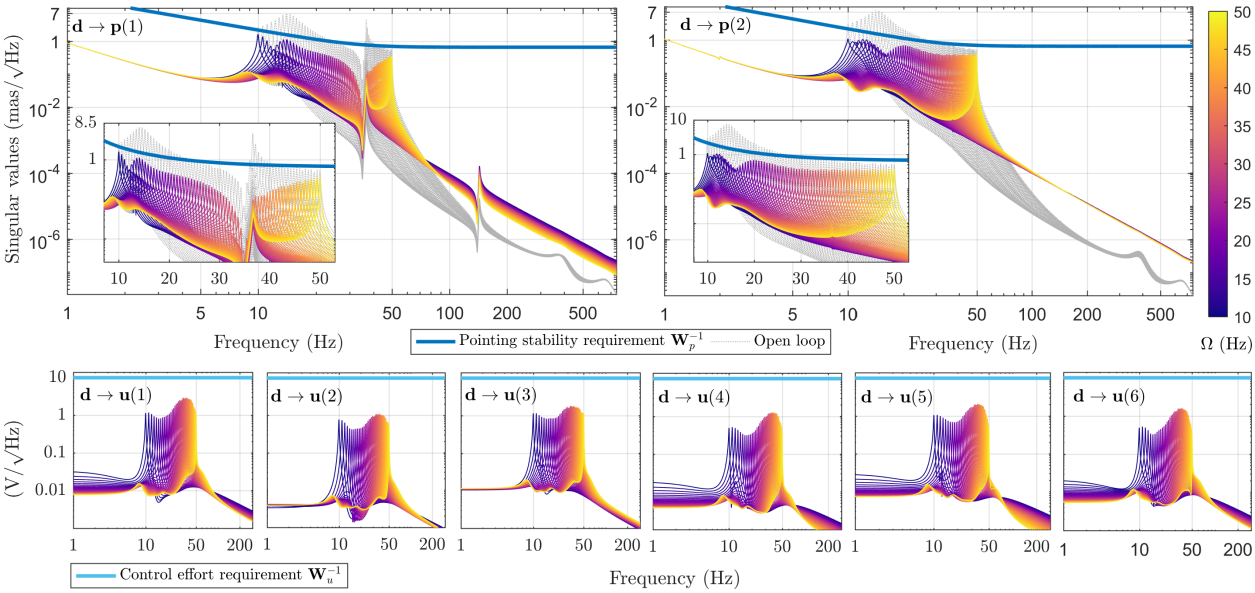


Figure 3.15: Singular values (representing the worst-case amplitude spectral densities) under nominal conditions from the normalized disturbances $\mathbf{d}$ towards the pointing errors $\mathbf{p}$ and control signals $\mathbf{u}$ for different spin rates $\Omega \in \mathbf{\Omega}$.

harmonic disturbance $d_1$ towards the closed-loop pointing error $\mathbf{p}(1)$. It is clear, that the high frequency contribution is largely due to the sensor noise while the mid-range is mostly dominated by the harmonic disturbance. The nominal system performance can also be visualized in terms of the $\mathcal{L}_2$ gain of the transfer $\mathbf{d} \to \mathbf{e}$ towards each of the weighted performance signals. This enables an easy evaluation of the $\mathcal{L}_2$ performance level relative to the specification corresponding to the gain of $\gamma = 1$. The open and closed-loop $\mathcal{L}_2$ gains are shown in fig. 3.16b for different output channels. For example, comparing the open and closed-loop $\mathcal{L}_2$ gains in the RPE channel $\mathbf{d} \to \mathbf{e}_p(1)$ around $\Omega = 37\,\text{Hz}$, it can be deduced that the peak RPE amplitude spectrum is attenuated by over 30 dB.

### 3.4.2 Robust stability and worst-case analysis

#### Analysis using the structured singular value

As previously explained in (2.56), the stability margin of the closed-loop interconnection with respect to the set of complex uncertainties $\Delta \in \mathbf{\Delta}$ can be evaluated at a given frequency $\omega \in \mathbb{R}$ and wheel spin rate $\Omega \in \mathbf{\Omega}$ by computing the structured singular value $\mu_{\mathbf{\Delta}}\left(\mathbf{M}_{\mathbf{w}\to\mathbf{z}}(\Omega, j\omega)\right)$. The upper bounds of this function using the $\mathbf{K}_{robustness}$ controller are shown in fig. 3.17a across a dense grid of reaction wheel spin rates $\Omega \in \mathbf{\Omega}$ and frequencies $\omega \in [5, 150]\,\text{Hz}$ encompassing the control bandwidth and main dynamics of the system [4]. It can be seen that the function peaks (i.e. the stability margin $1/\mu_{\mathbf{\Delta}}$ drops) in regions of high controller gain around frequencies equal to the wheel spin rate $\Omega$ or nearby the resonance frequencies of the actuators and passive isolators. To get a deeper insight into the sensitivity of the robust stability margin, fig. 3.17b shows for a given spin rate $\Omega \in \mathbf{\Omega}$, the maximum value of $\mu_{\mathbf{\Delta}}$ over all real frequencies $\omega$ i.e. $\sup_{\omega\in\mathbb{R}} \mu_{\mathbf{\Delta}}\left(\mathbf{M}_{\mathbf{w}\to\mathbf{z}}(\Omega, j\omega)\right)$ calculated for only certain uncertainty blocks.

[4] The bounds were calculated using the command robstab from MATLAB's Robust Control Toolbox [BCPS16]. The algorithm guarantees that the grid of frequencies includes the frequency at which the stability margin is smallest

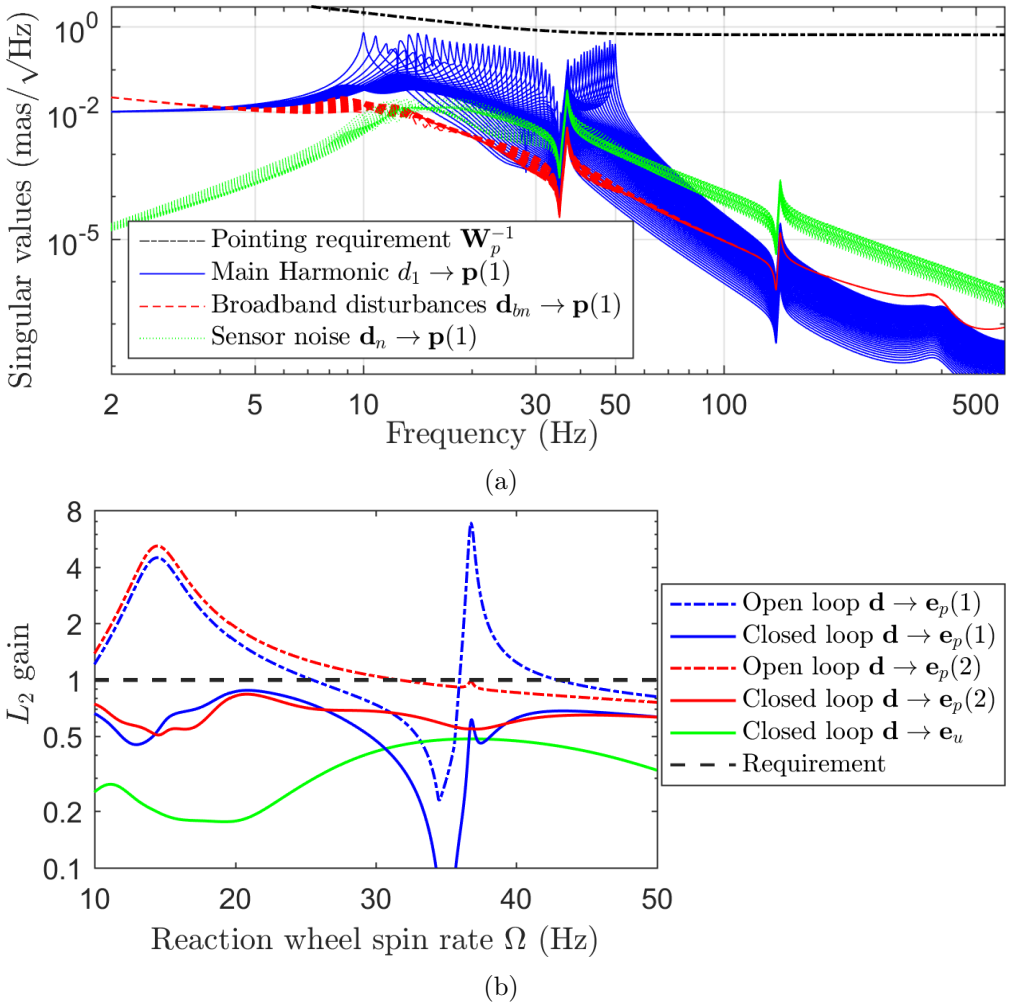


Figure 3.16: For different wheel spin rates $\Omega \in \mathbf{\Omega}$: (a) Contributions to the closed-loop pointing error spectrum $\mathbf{p}(1)$; (b) $\mathcal{L}_2$ gains across multiple performance transfers.

Noting that the peak values are below one in each case, it can be stated that the loop is guaranteed to remain stable for all the corresponding uncertainty blocks. This confirms that although the controller was synthesized to enforce robust stability only over the complex set $\mathbf{\Delta}$ given in (3.14), the coverage provided by this uncertainty model was wide enough to account for the real parametric set $\mathbf{\Delta}_{real}$. In the case of the combined complex uncertainties $\Delta = \text{diag}\,(\Delta_a, \Delta_y, \Delta_u)$, a 10% increase in the normalized uncertainty is enough to cause loop instability. This value is significantly lower than the 60% increase needed for the real uncertainties $\Delta_{real}$. The gap can be explained due to the fact that $\Delta$ also accounts for potential saturations or time-delays in the actuators.

The degradation of different performance indicators, under the influence of uncertainty, can also be systematically studied within the same framework. This is done by calculating an upper bound on the worst case $\mathcal{L}_2$ gain for several closed-loop performance transfers $\mathbf{d} \to \mathbf{e}(\bullet)$ across $\Omega \in \mathbf{\Omega}$ and with respect to different percentages $\epsilon \in [0, 1]$ of normalized complex uncertainty $\Delta \in \mathbf{\Delta}$, $\|\Delta\|_{\mathcal{L}_{2i}} < \epsilon$ , i.e. $\sup_{\Delta \in \mathbf{\Delta}, \|\Delta\|_{\mathcal{L}_{2i}} \leq \epsilon} \left\| \mathcal{F}_u \left( \mathbf{M}(\Omega), \Delta \right)_{\mathbf{d} \to \mathbf{e}(\bullet)} \right\|_{\mathcal{L}_{2i}}$. Numerically, this is efficiently performed using the MATLAB command wcgain [BCPS16]. The performance degradation curves for the pointing performance $\mathbf{e}_p(1), \mathbf{e}_p(2)$ and the control effort $\mathbf{e}_u$ channels with respect to the purely complex uncertainty set are shown in fig. 3.18a. The $\epsilon$ value at which each of these curve intersects the unit $\mathcal{L}_2$ gain represents the robust performance margin for that particular channel. This margin is equal to the maximum level of uncertainty for which the performance requirements are

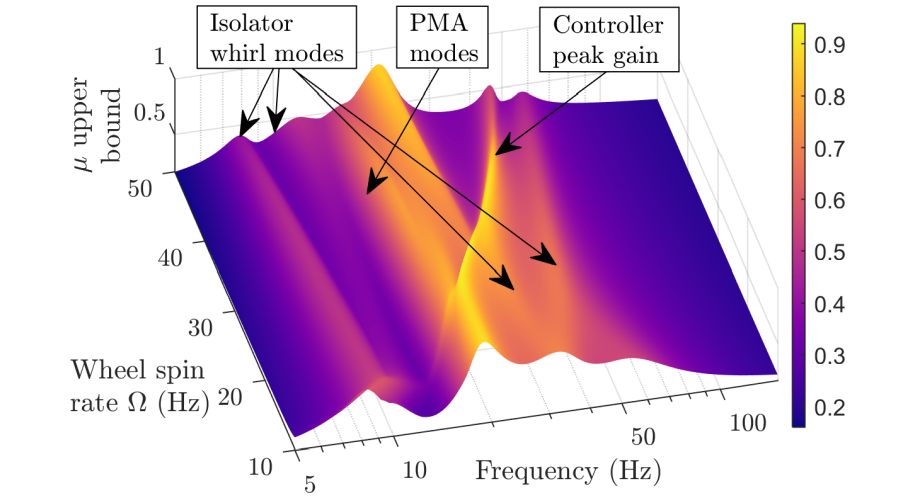


(a)

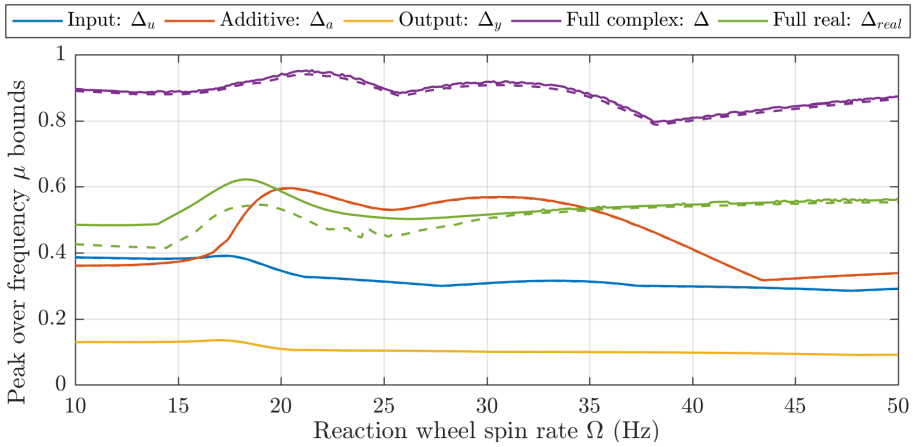


(b)

Figure 3.17: Robust stability results using $\mathbf{K}_{robustness}$ across different $\Omega \in \mathbf{\Omega}$. (a) Upper bound on $\mu_{\mathbf{\Delta}}\left(\mathbf{M}_{\mathbf{w}\to\mathbf{z}}(\Omega, j\omega)\right)$, i.e. the inverse robust stability margin, with respect to the full complex uncertainty $\Delta = \text{diag}\left(\Delta_u,\ \Delta_y,\ \Delta_a\right) \in \mathbf{\Delta}$ (see (3.14) for details). (b) Peak over frequency bounds of $\mu_{\mathbf{\Delta}}$ considering only certain uncertainty structures (solid lines for upper bounds and dashed for lower).

still met. For example, in the case of the RPE pointing performance channel $\mathbf{d} \to \mathbf{e}_p(1)$, about $\epsilon = 15.6\%$ of the normalized modeled uncertainty is sufficient to cause an amplification above unit $\mathcal{L}_2$ gain and therefore an invalidation of the requirement. Taking the uncertainties scaled near these robust performance margins, fig. 3.18b shows the upper bounds and worst case singular values calculated across multiple fixed $\Omega \in \mathbf{\Omega}$. For $\mathbf{e}_p(1)$, a value of $\epsilon = 15.6\%$ modeled uncertainty causes an amplification up to the maximum pointing error at $\Omega = 36.73\,\text{Hz}$ when the main harmonic disturbance interacts with the flexible mode of the satellite. Similarly for $\mathbf{e}_p(2)$, the amplification occurs at $\Omega = 12.81\,\text{Hz}$ and $\epsilon = 26\%$. Finally the gain of $\mathbf{d} \to \mathbf{e}_u$, corresponding to the combined control effort performance, is more robust to uncertainty and guaranteed to be below unit gain up to about $\epsilon = 97\%$.

It should be clear that the same type of analysis can be done for other uncertainty structures or performance transfers. For example, fig. 3.19 examines the worst-case gains at each frequency within the interval $\mathbf{\Omega} = [10, 50]\,\text{Hz}$ from main harmonic disturbance $w_1$ towards the two pointing errors $\mathbf{p} = \begin{bmatrix}\theta_a & \theta_b\end{bmatrix}^\mathsf{T}$. These are calculated with respect to different real uncertainty groups and compared to the nominal case. In this fashion, the sensitivity of the worst-case gain with respect

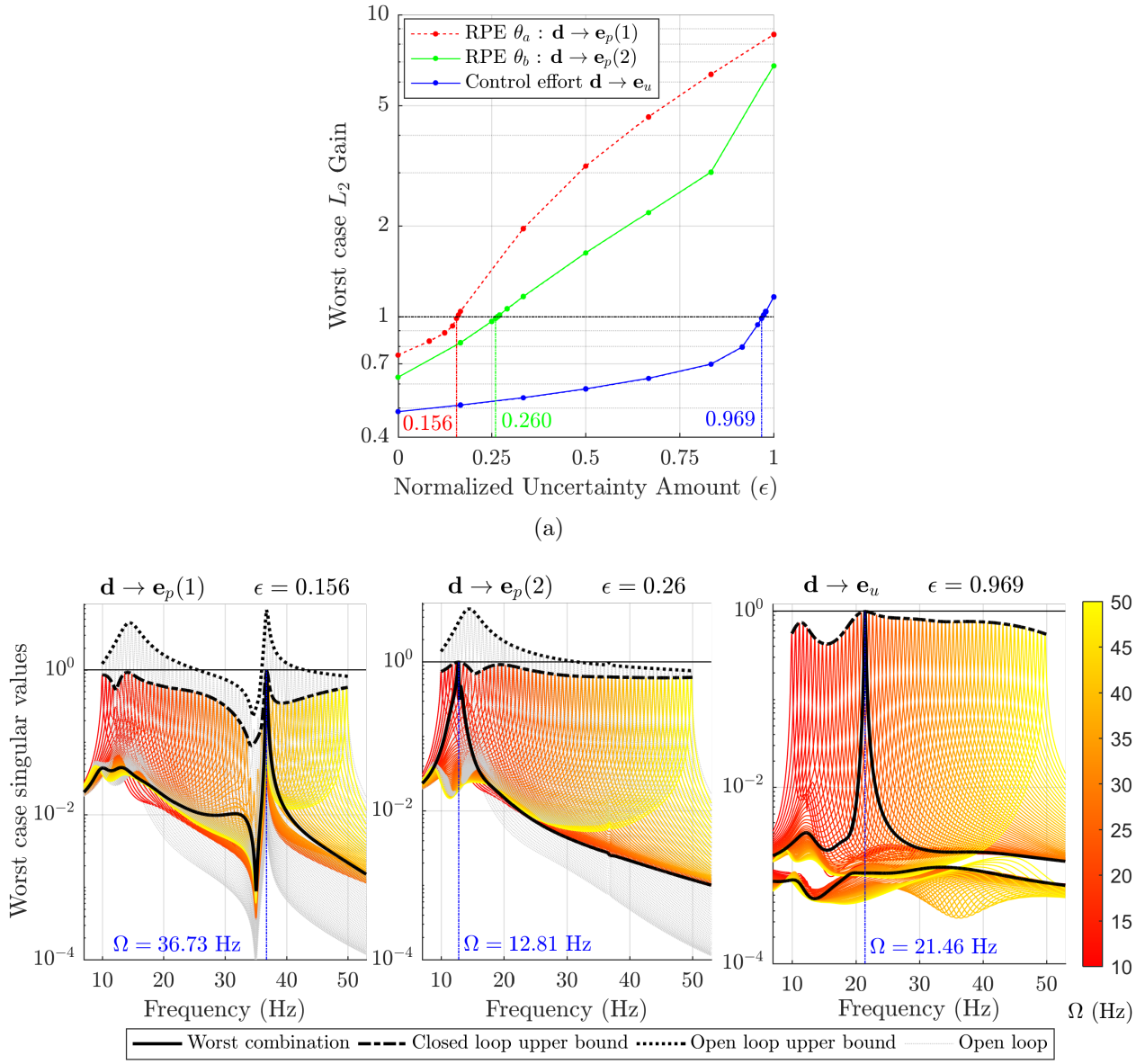


Figure 3.18: (a) Performance degradation curves. (b) Upper bounds and worst case combinations for different fixed $\Omega \in \mathbf{\Omega}$ and $\epsilon$ near the robust performance margins.

to each of parameter group is rigorously computed and the most significant driving uncertainties in each frequency range can be identified. For instance, actuator or isolator uncertainties alone are enough to cause a slight invalidation of the performance requirement around the 36 Hz modal frequency of the flexible attachment.

### Analysis via Integral Quadratic Constraints (IQC)

The previous $\mu$-analysis results relied on the underlying realistic assumption that the wheel speed $\Omega \in \mathbf{\Omega}$ is a slow-varying parameter in order to provide pointwise stability and performance guarantees. Whereas $\mu$-tools are restricted to LTI uncertainties, the more extensive IQC approach introduced in [MR97] can also handle a wide range of additional uncertainties such as linear time-varying (LTV) perturbations, time delays or sector-bounded non-linearities. A number of MATLAB

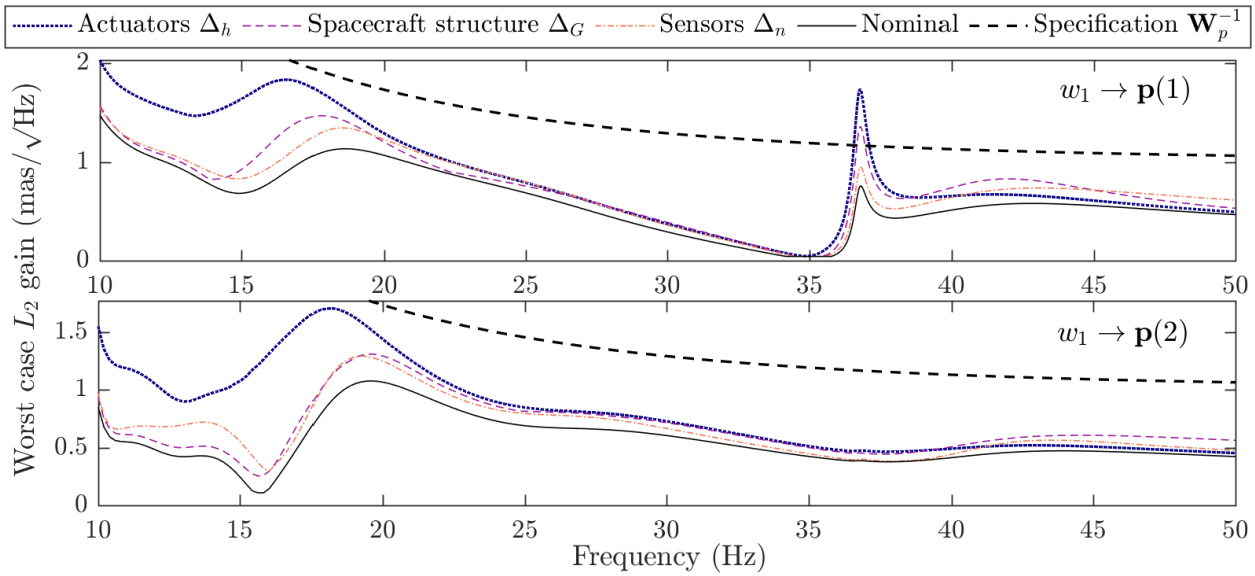


Figure 3.19: Closed-loop sensitivity analysis. Worst-case $\mathcal{L}_2$ gains from the main harmonic $w_1$ towards the two pointing errors $\mathbf{p} = \begin{bmatrix}\theta_a & \theta_b\end{bmatrix}^\mathsf{T}$ for different real uncertainty groups.

toolboxes [HSP15, KFS08, MKJR04] have been developed to facilitate the analysis using IQCs. A brief review of IQC theory is given in appendix A.2 and the reader can refer to [VSK16] for additional details. The flexibility of the IQC framework is leveraged to certify the robust stability and provide upper bounds on the worst case performances in the case time-varying $\Omega(t) \in \mathbf{\Omega}$, uncertain time-varying delays and actuator saturations. Consequently, the uncertainty introduced by the delay and saturation blocks (see fig. 3.6) is incorporated into the augmented plant model using the following two blocks, as shown in fig. 3.20:

$$\begin{aligned} &\Delta_\tau(t) = \operatorname{diag}\left[\left(\mathcal{D}_{\tau_i(t)} - 1\right)\frac{1}{s}\right];\ \ \tau_i(t) \in [0,\ \tau_{max}] && \\ &\mathcal{D}_{\tau_i(t)} := \left\{D_{\tau_i(t)} : \mathcal{L}_2 \to \mathcal{L}_2, D_{\tau_i(t)}\left(\xi(t)\right) = \xi\left(t - \tau_i(t)\right)\right\} && \text{and} \\ &\qquad\qquad \text{for} \quad i \in \{1, \ldots, 6\} && \end{aligned} \qquad \begin{aligned} &\Delta_{sat}(t) = \operatorname{diag}\left[\sigma_i(t)\right] \\ &\sigma_i(t) \in [0,\ \sigma_{max}] \end{aligned} \tag{3.41}$$

The operator $\Delta_\tau(t)$ accounts for the six different bounded time-varying delays $\tau_{1\ldots6}(t) \in [0,\ \tau_{max}]$, in a manner suitable for analysis via IQCs (see [VSK16, KR07] for details). Inspired by [PF16], the operator $\Delta_{sat}(t) \in \mathbb{R}^{6\times6}$ captures the effect of actuators saturations, using the simplified model $\text{sat}(u) \approx u - u \cdot \sigma(t)$ where $\sigma(t) \in [0,\ \sigma_{max}]$ is a time-varying uncertainty with arbitrarily fast variation rates and $\sigma_{max}$ is the maximum relative saturation level. Although this model is conservative, in the sense that it can be used to represent other uncertainties or nonlinearities, it offers the possibility to gain insight into the sensitivity and effects of the saturation on the performance of the system. The blocks $\Delta_\tau(t)$ and $\Delta_{sat}(t)$ together with ones containing the time-varying wheel speed $\Omega(t)$ can be aggregated into an overall time-varying uncertainty block $\Delta_{\text{IQC}}(t) = \operatorname{diag}\Big(\Omega(t)\mathbf{I}_7,\ \Delta_{sat}(t),\ \Delta_\tau(t)\Big) \in \mathbf{\Delta}_{\text{IQC}}$ in feedback with the closed-loop augmented system $\mathbf{M}$ (see fig. 3.20). In this case, the associated set of IQC multipliers that was chosen to analyze the closed-loop performances, combines the one defined for time-varying delay from in [KL04, KR07] with the multipliers for time-varying parameters with bounded rates given in [KS06]. With the structure in place, upper bounds on the worst-case $\mathcal{L}_2$ gains for any performance transfer, i.e. $\sup_{\Delta_{\text{IQC}}\in\mathbf{\Delta}_{\text{IQC}}} \left\|\mathcal{F}_u\left(\mathbf{M}, \Delta_{\text{IQC}}\right)_{\mathbf{d}\to\mathbf{e}(\bullet)}\right\|_{\mathcal{L}_{2i}}$ can be evaluated using the method outlined in appendix A.2. In this chapter, the analysis will focus solely on the control effort performance channel $\mathbf{d} \to \mathbf{e}_u$. To facilitate the identification of wheel speed ranges where the performance degradation is highest, the domain $\mathbf{\Omega}$ is subdivided into $N$ connected intervals such that $\mathbf{\Omega} = \bigcup_{i=1}^{N} \mathbf{\Omega}_i$. The

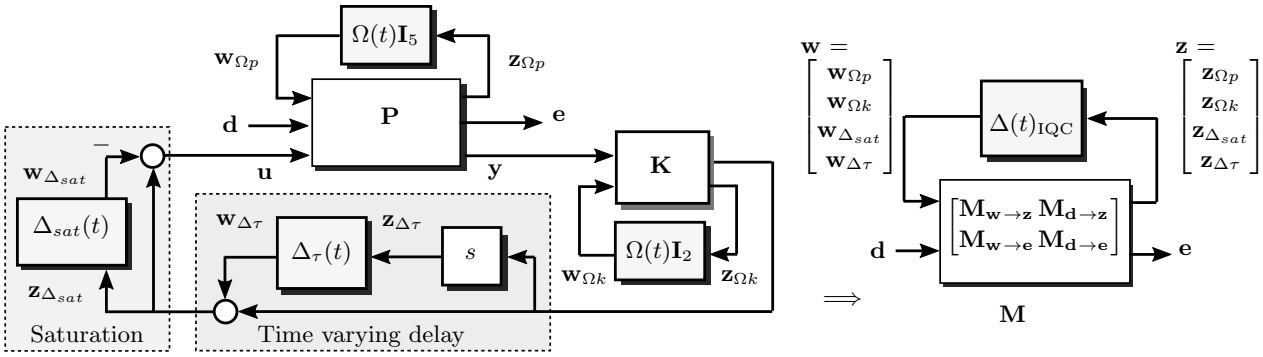


Figure 3.20: Loop transformations for IQC analysis.

bounds are afterwards calculated for each interval by restricting the domain of the smoothly-time varying wheel speed to $\Omega(t) \in \mathbf{\Omega}_i$. Following this methodology, fig. 3.21a shows the upper $\mathcal{L}_2$ bounds computed for different maximum acceleration $\dot{\Omega}_{max}$ and ignoring other uncertainties. The performances are rather insensitive to fast variations in $\Omega(t)$ with only a slight penalty compared to the fixed $\Omega$ case even for accelerations that are much higher than the typical ones given in (2.4).

The saturations effects are investigated by first fixing the maximum wheel acceleration $\dot{\Omega}_{max}$ to a low value ($10^{-4}$Hz/s) and ignoring the time-delays (fix $\Delta_\tau(t) = \mathbf{0}$). Next, the closed-loop $\mathcal{L}_2$ gain bounds for multiple maximum values $\sigma_{max}$ of the saturation block $\sigma_i(t) \in [0,\ \sigma_{max}]$ are evaluated and displayed in fig. 3.21b. As the $\mathcal{L}_2$ gain remains below one, closed-loop stability and robust control effort performance are guaranteed for any variation of the saturation levels within $\sigma_{max} \in [0, 100\%]$.

Finally, fig. 3.21c illustrates the performance degradation with respect to the combined effect of the six variable uncertain time-delays $\tau_{1\ldots6}(t) \in [0,\ \tau_{max}]$ up to the maximum value $\tau_{max} = 10\,\text{ms}$ for which the stability can still be guaranteed across $\mathbf{\Omega}$ . With respect to the current system, these time-delay stability margins are considered satisfactory. However, it should stressed that the computed $\mathcal{L}_2$ gain bounds can be overly pessimistic as the delays are assumed distinct and time-varying arbitrarily fast in each of the six actuators.

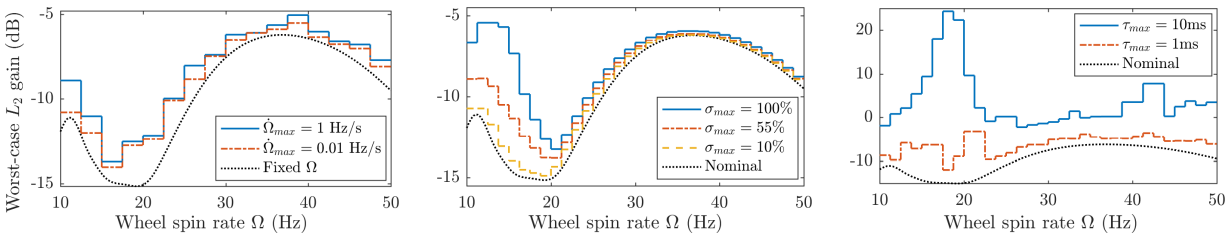


(a) (b) (c)

Figure 3.21: Upper bounds on the worst-case $\mathcal{L}_2$ gain for the combined control effort performance channel $\mathbf{d} \to \mathbf{e}_u$ for time-varying $\Omega(t)$ and different maximum: (a) accelerations $\dot{\Omega}_{max}$ (b) saturation levels $\sigma_{max}$ (c) time-varying uncertain delays $\tau_{max}$.

### 3.4.3 Time-domain simulations and comparative analysis

As part of the validation process, time-domain nonlinear simulations were performed using the $\mathbf{K}_{performance}$ and $\mathbf{K}_{robustness}$ controllers on a high-fidelity multi-body simulator developed with the expertise of ESA and Airbus Defence and Space. For the considered mission scenario, the reaction

wheel is accelerated using a constant torque from $\Omega = 10\,\text{Hz}$ at time $t = 0\,\text{min}$ to $\Omega = 50\,\text{Hz}$ at $t = 30\,\text{min}$. The simulator uses the disturbances model (3.5) and the amplitude coefficients given in table 3.1 to introduce the main reaction wheel harmonic disturbance. Stochastic broadband perturbations and sensor noise, with spectral densities bounded by the $\mathbf{W}_{bn}$ and $\mathbf{W}_{n}$weights described in the previous section, are also injected into the closed-loop system. The benefits of the proposed approach are highlighted by comparing open-loop results with the ones obtained in closed-loop using the two controllers. Figure 3.22 show the amplitudes and peak amplitude spectral density values of the relative pointing errors corresponding to each of the angular displacements $\mathbf{p} = \begin{bmatrix}\theta_a & \theta_b\end{bmatrix}^\mathsf{T}$ of the satellite main body in open-loop and in closed-loop with both the $\mathbf{K}_{robustness}$ and $\mathbf{K}_{performance}$ controllers. Figure 3.23 shows the full spectrograms of the RPE corresponding

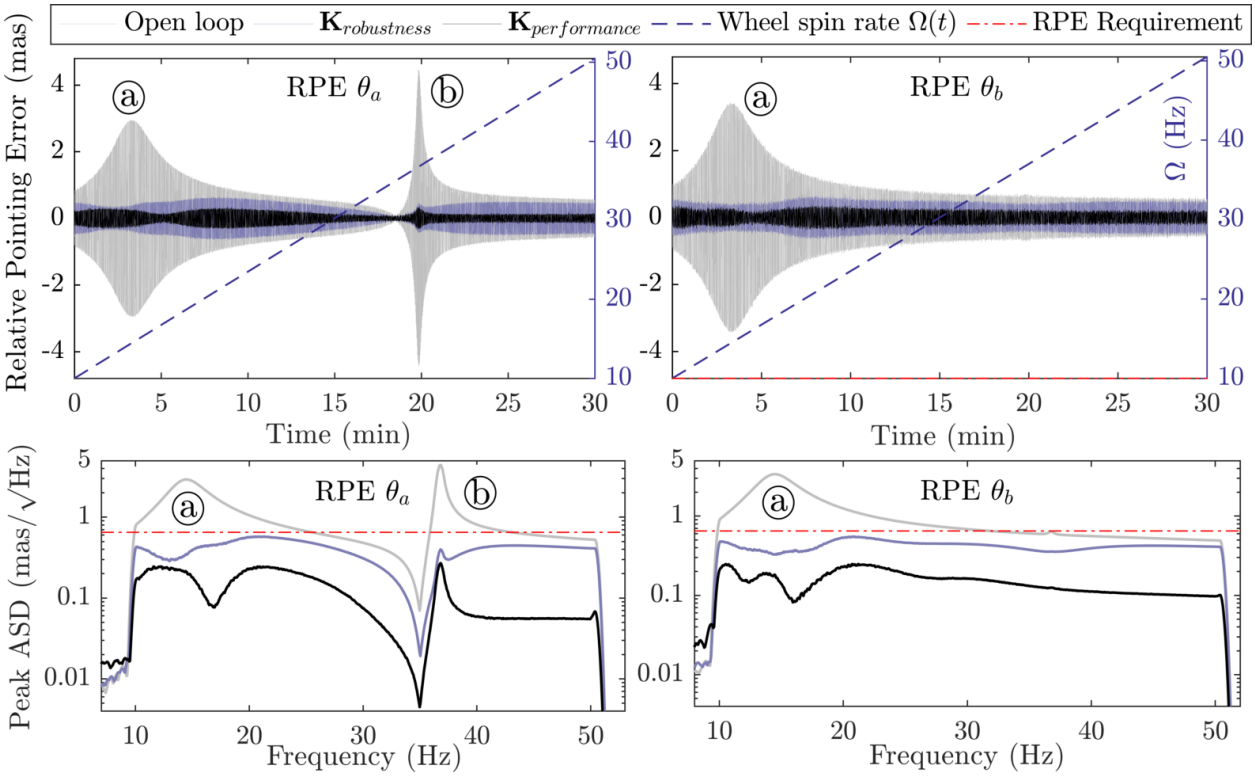


Figure 3.22: Relative Pointing Errors and peak amplitude spectral densities corresponding to each of the satellite's angular displacements $\mathbf{p} = \begin{bmatrix}\theta_a & \theta_b\end{bmatrix}^\mathsf{T}$ in open-loop and in closed-loop with both the $\mathbf{K}_{robustness}$ and $\mathbf{K}_{performance}$ controllers for a linear wheel spin variation of $\Omega(t) \in \mathbf{\Omega}$. Note: the peak at ⓐ coincides with the intersection between the main harmonic disturbance and the passive isolator mode while ⓑ occurs at the intersection with a mode of the flexible attachment.

to the relative pointing error associated with the $\mathbf{p}(1) = \theta_a$ angular displacement of the satellite are compared in open-loop and in closed-loop with both the $\mathbf{K}_{robustness}$ and $\mathbf{K}_{performance}$ controllers. One can easily observe that the contribution from the main harmonic disturbance towards the pointing error is significantly attenuated in closed-loop. On the other hand, a slight increase in the broadband pointing error response can be observed in the closed-loop scenarios. As previously shown in fig. 3.16a this is mainly the contribution from the sensor noise that propagates through the controller and into the actuator signals. This unavoidable effect is a well understood phenomenon that was taken into account and correctly predicted in both the controller design (section 3.3.2) and system analysis (section 3.4) phases.

In fig. 3.24 the six actuator control signals and their corresponding peak amplitude spectral densities are shown using both the $\mathbf{K}_{robustness}$ and $\mathbf{K}_{performance}$ controllers.

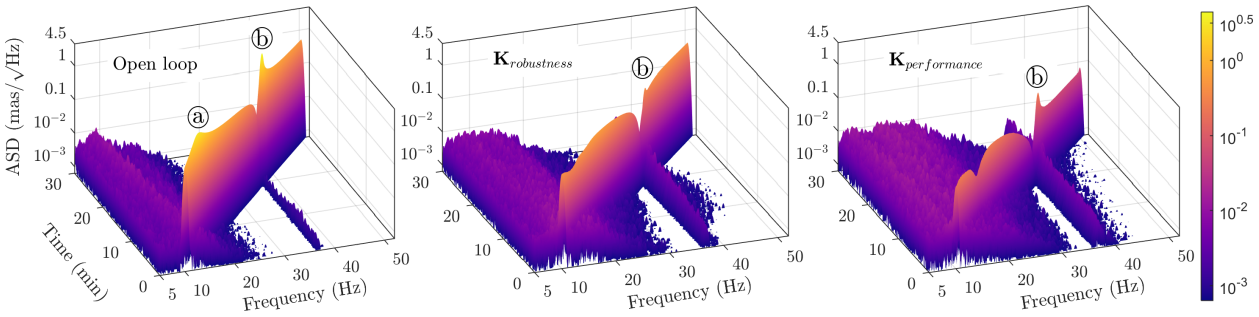


Figure 3.23: Spectrograms of the relative pointing error associated with the $\mathbf{p}(1) = \theta_a$ angular displacement of the satellite in open-loop and in closed-loop with both controllers. Note: labeled locations match those in fig. 3.22.

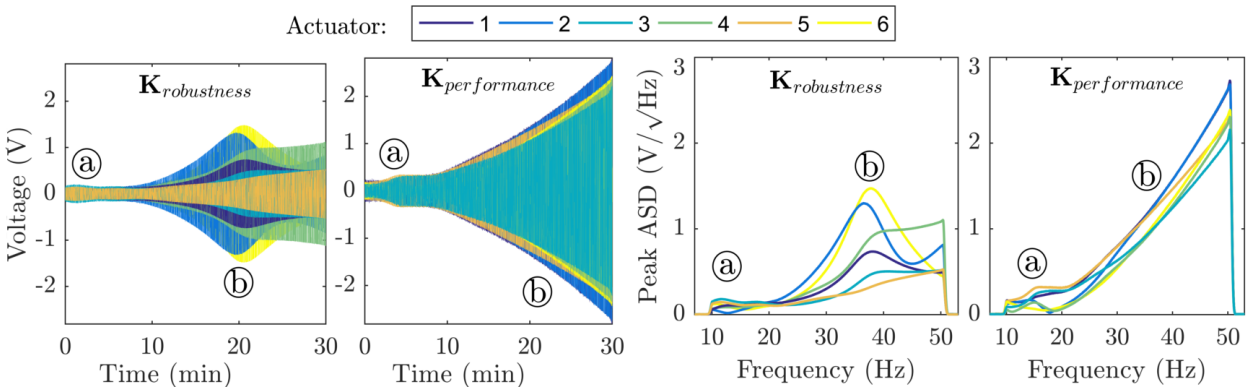


Figure 3.24: The six actuator control signals and their corresponding peak amplitude spectral densities using both controllers. Note: labeled locations match those in fig. 3.22

Overall, both the nominal pointing stability and control effort performances comply with the design requirements. Both controllers manage to significantly attenuate the pointing errors resulting from the interaction between the main harmonic disturbance and the isolator and flexible attachment modes. As expected from the $\gamma$ performance levels obtained during the synthesis phase (section 3.3.4), the controller $\mathbf{K}_{performance}$ manages to obtain higher attenuation levels using a more aggressive control signal.

Next, the robust performance of the two controllers is verified over a simplified real uncertainty set $\Delta \in \mathbf{\Delta}_{simple}$ of 26 real parameters that only includes variations in the stiffness and damping properties of the passive isolators and also uncertainty in the actuator coefficients, i.e. the parameters: $\{k_{pma1...6},\ c_{pma1...6},\ T_{pma1...6},\ k_u,\ k_{\theta u},\ k_v,\ k_{\theta v},\ c_u,\ c_{\theta u},\ c_v,\ c_{\theta v}\}$ defined in section 2.3. For this uncertainty model, fig. 3.25a illustrates the nominal and worst-case $\mathcal{L}_2$ gains between the normalized disturbances $\mathbf{d}$ and the relative pointing error $\mathbf{p}_{RPE}(2)$ of the closed-loop augmented system pictured in fig. 3.7. The values are calculated across different wheel spin rates $\Omega$ using the standard $\mu$-tools described earlier in the section and represent the predicted peak amplitude spectral density values of the closed-loop RPE $\theta_b$ signal. It is clear that while the nominal performances are better using $\mathbf{K}_{performance}$, the worst-case values peak to a much higher value compared to those obtained using $\mathbf{K}_{robustness}$.

The precise parameter combination $\Delta_{wc} \in \mathbf{\Delta}_{simple}$ that produces the peak at the spin rate $\Omega = 14.71$ Hz for the $\mathbf{K}_{performance}$ controller is also provided by the $\mu$-analysis procedure and shown in fig. 3.25b. These parameter values are subsequently fixed in the nonlinear simulator in order to compare the time domain data with the values predicted by $\mu$-analysis. Consequently, fig. 3.26 shows the amplitude, spectral density and cumulative RMS of the relative pointing error along

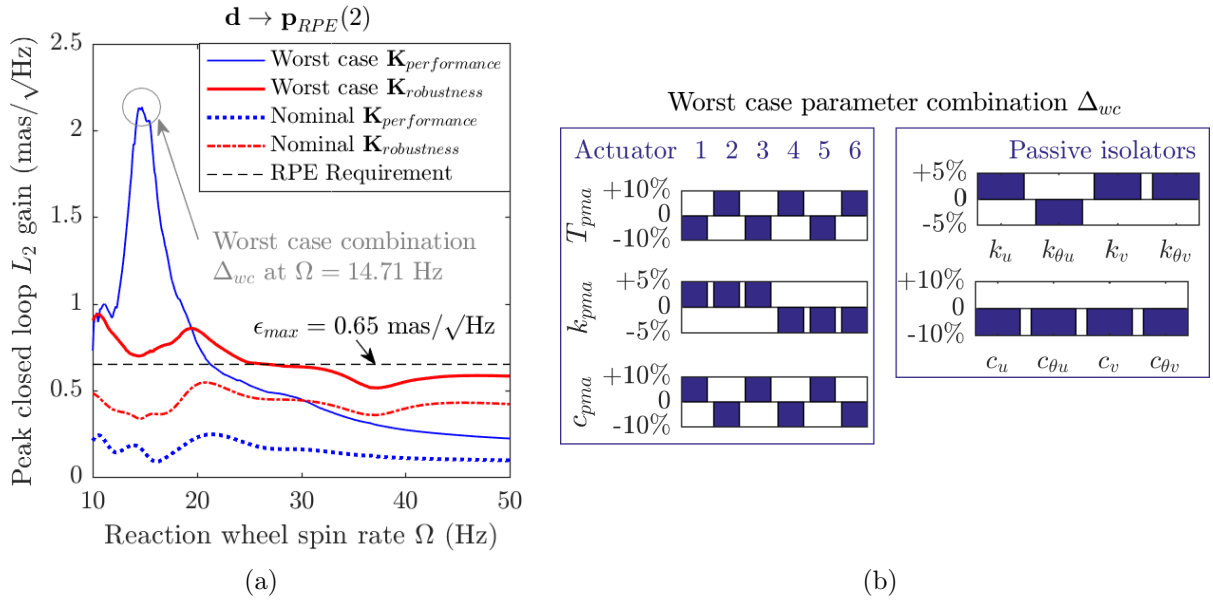


Figure 3.25: (a) Upper bounds on the worst-case closed-loop $\mathcal{L}_2$ gain of $\mathbf{d} \rightarrow \mathbf{p}_{RPE}(2)$ corresponding to the relative pointing error along the $\mathbf{p}(2) = \theta_b$ angular displacement for different wheel rates $\Omega \in \mathbf{\Omega}$ using both $\mathbf{K}_{robustness}$ and $\mathbf{K}_{performance}$ controllers ; (b) Parameter combination $\Delta_{wc}$ corresponding to the worst case $\mathcal{L}_2$ gain occuring at $\Omega = 14.71$ Hz using $\mathbf{K}_{performance}$.

the $\mathbf{p}(2) = \theta_b$ angular displacement in closed-loop using both controllers and running at a fixed $\Omega = 14.71$ Hz. The parameters are alternatively fixed to the worst-case parameter combination $\Delta_{wc}$ as well and to their nominal values. In this case, the simulation results precisely align with

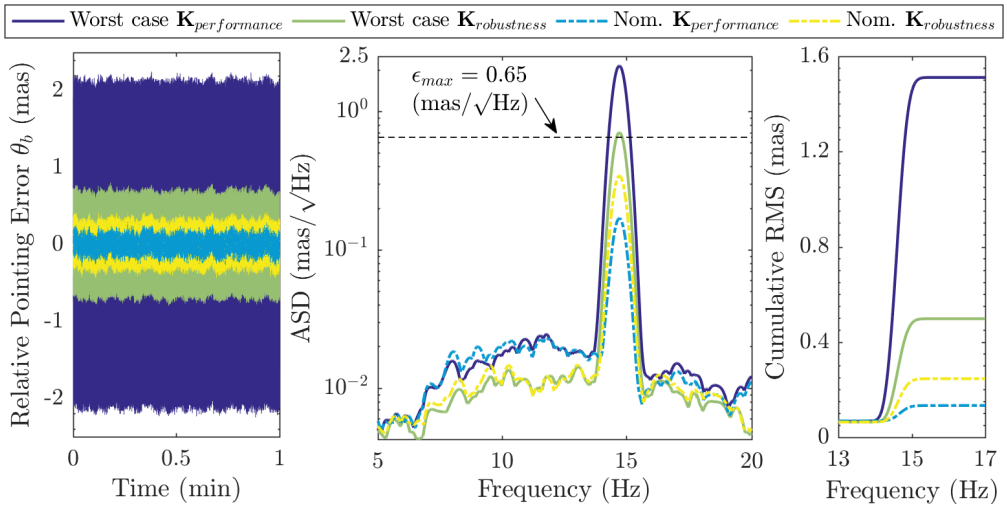


Figure 3.26: Time domain simulations of the closed-loop relative pointing error along the $\mathbf{p}(2) = \theta_b$ angular displacement (left) together with the amplitude spectral density (center) and cumulative RMS (right) at $\Omega = 14.71$ Hz using both controllers . Note: The various responses include those where the parameters are fixed to their nominal values and those where the parameters are fixed to the worst-case parameter combination $\Delta_{wc}$.

those predicted by $\mu$-analysis and highlight the efficiency of the proposed methodology in finding worst-case scenarios. It should be clear that the simplified real uncertainty set $\mathbf{\Delta}_{simple}$ contains a total of 26 real parameters and evaluating even the vertices of the hyperrectangle spanning this uncertainty space would involve a total of $2^{26}$ simulations for any given spin rate $\Omega \in \mathbf{\Omega}$. Monte Carlo campaigns would therefore quickly prove to be ineffective in finding particularly problematic

parameter combinations or spin rates while an analysis based on the structured singular value can be scaled to tens or even hundreds of uncertain parameters and provides guaranteed performance bounds.

## 3.5 Conclusions

The chapter outlines a unified and comprehensive methodology that can be used to perform rigorous control system design and validation for microvibration isolation systems with guaranteed pointing stability performance. To this end, an LFT model is first introduced in order to capture, in a common mathematical language, the complex dynamic interactions between the uncertain and time-varying structural dynamics of the spacecraft, the spinning reaction wheel, the attitude control systems as well as the hybrid isolation platform. This end-to-end analytical model is afterwards used to systematically synthesize, using structured $\mathcal{H}_\infty$ tools, a set of low-order LPV controllers that balance the trade-offs between robustness and performance. Finally, the work relies on the well-established structured singular value and IQCs in order to perform a detailed worst-case analysis of the system and obtain stability and performance certificates without relying on extensive Monte-Carlo simulations. It is hoped that the presented work can lead to a more widespread adoption of these powerful design and validation principles within the industry, raising the standards of performance and reliability of hybrid microvibration isolation systems.

---

"*If people do not believe that mathematics is simple, it is only because they do not realize how complicated life is.* "

John von Neumann

# 4 Worst case optical jitter analysis

## 4.1 Introduction

Predicting the dynamic opto-mechanical performance of complex spacecraft during the design phase is essential before investing considerable resources towards a particular architecture [MdWU+01]. Integrated dynamics and controls modeling provides the means of verifying the soundness of a particular spacecraft design and to identify crucial system parameters that are the main performance drivers. These multidisciplinary modeling approaches typically combine the dynamical model of the flexible spacecraft with that of the vibration isolation and optical sub-systems and have been researched in a number of studies such as [LYH12, MdWU+01, DGM12]. When combined with a disturbance model for the perturbations acting on the spacecraft, such as those produced by the reaction wheels, these approaches aim of predicting optical performance without relying on time-domain simulations. However, the problem of guaranteed worst-case bounds on the pointing errors resulting from reaction wheel microvibrations has not been investigated in these studies. This fact motivated the research presented in this chapter.

Previously, in chapter 3, it was shown how the dynamical model of the a flexible satellite actuated by a spinning reaction wheel can be integrated with the disturbance model for the wheel perturbations in order to tune an active vibration controller and improve the overall pointing performance. Using this integrated model as an example, one goal of this chapter is to highlight how the $\mathcal{H}_\infty/\mu$ framework can be used to make a rigorous and systematic assessment of the worst-case pointing errors of a general flexible spacecraft due to reaction wheel disturbances. The method provides accurate and non-conservative bounds on the time-domain performance solely based on values of various system norms and without any reliance of time-domain simulations.

Afterwards, the chapter will detail a novel method that can be used to simulate the image distortions occurring due to these disturbances based upon a solid mathematical framework. This is a problem of considerable industrial need as highlighted in [LYH12, PM16, PM12].

### 4.1.1 Chapter organization and main contributions

Section 4.1.2 begins with the a detailed presentation of the analysis architecture that can be used to assess the worst-case pointing stability of a general flexible spacecraft. To do this, the weighting functions previously described in section 3.3.3 will be employed to shape both the disturbance spectrum as well as to calculate the resulting relative pointing errors . The considered reaction wheel disturbance spectrum includes a number of harmonic signals plus an additional broadband

random perturbation. In section 4.2, it is shown how the $\mathcal{L}_2$ and $\mathcal{H}_2$ system norms can be used to make accurate worst-case time-domain predictions on both the $3\sigma$ amplitude as well as the RMS values resulting pointing errors without performing any simulations. Additionally, it is shown how the method can be adapted in a new way in order to assess the worst-case bounds and parametric sensitivities in various directions of the image plane. Finally section 4.3 will detail a novel method to compute the image distortions resulting from harmonic wheel perturbations. To this end, new analytical expressions for the Point Spread and Optical Transfer Functions are introduced in order to properly simulate and assess the elliptical image motion patterns resulting from harmonic wheel perturbations.

### 4.1.2 Analysis architecture

The analysis architecture that will be used throughout this chapter is shown in fig. 4.1 as $\mathbf{M}(\Omega, \Delta)$. For simplicity, the assumption is made that the spacecraft is actuated by a single reaction wheel

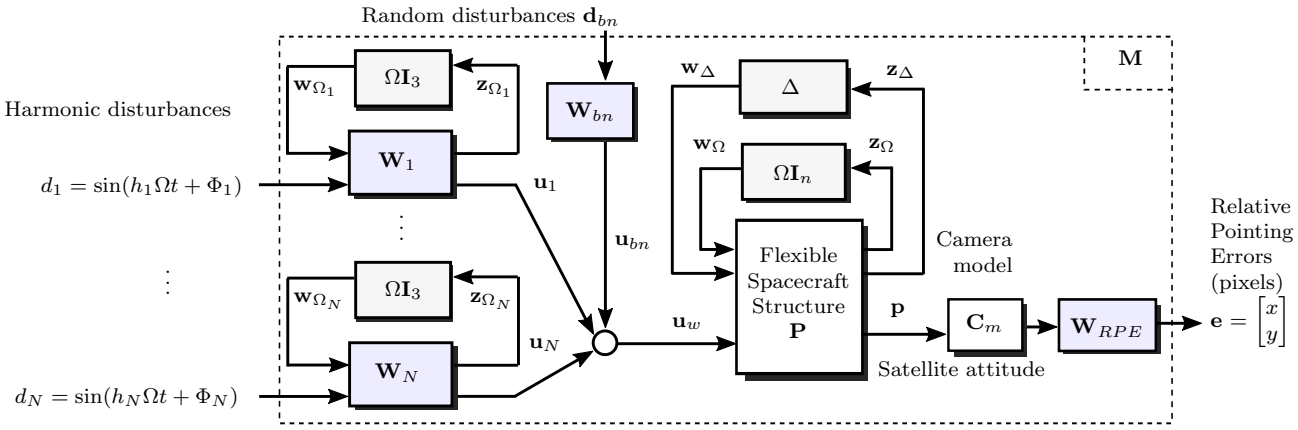


Figure 4.1: General system interconnection for jitter analysis.

spinning with a variable angular speed $\Omega \in \mathbf{\Omega}$. A second assumption is that the flexible spacecraft structure (the $\mathbf{P}$ block in fig. 4.1) can be written in LFT form with the dependency on the reaction wheel spin rate contained within the block $\Omega\mathbf{I}_n$ and the real and complex uncertainties isolated in the uncertainty block :

$$\Delta \in \mathbf{\Delta} \subset \mathbb{C}^{m \times m} \tag{4.1}$$

The results presented in this chapter are obtained using the plant model previously introduced in chapter 3, i.e. the flexible satellite coupled to the microvibration isolation architecture and using the controller $\mathbf{K}_{robustness}$. However, it should be stressed that the proposed analysis methodology can be applied to any other spacecraft models.

The structural model is considered perturbed by the reaction wheel's disturbance vector $\mathbf{u}_w = \begin{bmatrix} F_x & F_y & T_x & T_y \end{bmatrix}$ explained in (3.4) and composed of $N$ deterministic harmonic signals $\mathbf{u}_{1\ldots N}$ plus a stochastic broadband component $\mathbf{u}_{bn}$. Based on the method proposed in section 3.3.3, the filters $\mathbf{W}_{1\ldots N}$, detailed in (3.30), are used to capture the amplitude and phase correlation of the each harmonic disturbance at different wheel speeds $\Omega$. However, in this chapter, each of these weights is assumed to be driven by a corresponding harmonic signal:

$$d_i(t) = \sin\left(h_i\Omega t + \Phi_i\right) \text{ with fixed phase uniformly random in } \Phi_i \in [0, 2\pi) \tag{4.2}$$

Following the properties of the $\mathbf{W}_i(\Omega)$ weights summarized in remark 4 from chapter 3, it becomes clear that the steady states outputs in this case will precisely match those of the harmonic

components $\mathbf{u}_i$ given in (3.4). Similarly, the weight $\mathbf{W}_{bn}$ models the random broadband wheel disturbances when driven by unit white noise inputs $\mathbf{d}_{bn}$ (see (3.26) for the precise value used in this chapter).

The mission scenario that will be investigated is shown in fig. 4.2 and is made up of the flexible satellite model together with the isolation system previously illustrated in fig. 3.1. As explained in section 3.2.2, this satellite has a corresponding body fixed frame $\mathcal{F}_p := (o_p; \vec{a}, \vec{b}, \vec{c})$ attached at the CoM of its rigid body that describes its orientation with respect the an inertial reference frame $\mathcal{F}_{world} := (O; \vec{X}, \vec{Y}, \vec{Z})$. Initially, the rigid body is perfectly aimed at a particular target that is positioned along its negative $\vec{c}$ body axis. However, reaction wheel perturbations induce small angular displacements $\mathbf{p} = \begin{bmatrix}\theta_a & \theta_b\end{bmatrix}^\mathsf{T}$ around the $\vec{a}$ and $\vec{b}$ body axes. The absolute pointing error vector $\mathbf{p}$ is subsequently transformed into pixel errors corresponding to lateral translations of the target in the $xy$-plane [1] of the photodetector using the following simplified camera model

$$\underbrace{\begin{bmatrix}x\\y\end{bmatrix}}_{\mathbf{e}} = [\mathbf{W}_{RPE}\,\mathbf{C}_m] \underbrace{\begin{bmatrix}\theta_a\\\theta_b\end{bmatrix}}_{\mathbf{p}} \quad \text{where} \quad \mathbf{C}_m = \begin{bmatrix}\cos(\beta) & \sin(\beta)\\ -\sin(\beta) & \cos(\beta)\end{bmatrix}\begin{bmatrix}\alpha_x & \\ & \alpha_y\end{bmatrix} \tag{4.3}$$

where $\alpha_x = \alpha_y = 20\,\text{pixels/mas}$ are the pixel densities of the optical instrument in both directions and $\beta$ is the angle between the satellite and detector frames along the target pointing axis (see fig. 4.2 for clarity). Although, this angle is fixed to $\beta = 0$ for all simulations, variations within

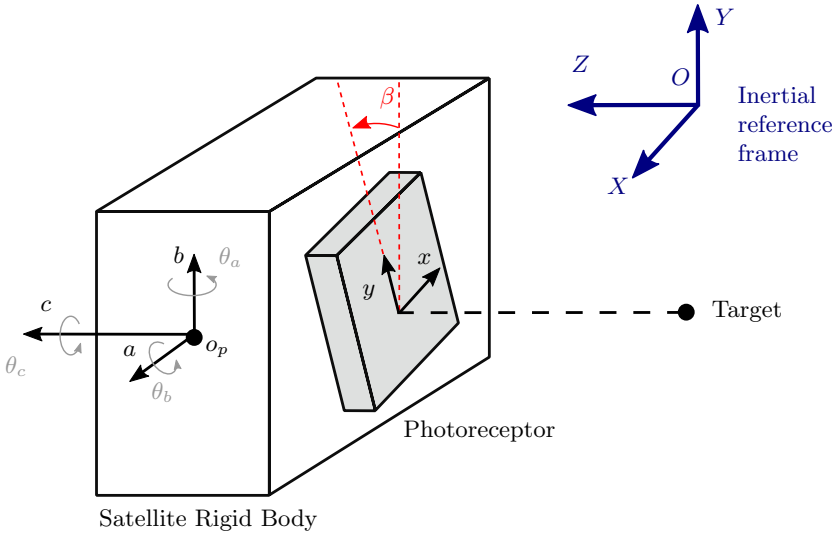


Figure 4.2: Simplified pointing scene considered in this study.

$\beta \in \begin{bmatrix}0, & 2\pi\end{bmatrix}$ will be used in subsequent mathematical calculations in order to examine pointing errors in different directions. The high-pass filter $\mathbf{W}_{RPE} = \frac{t_\Delta s\left(t_\Delta s + \sqrt{12}\right)}{(t_\Delta s)^2 + 6(t_\Delta s) + 12}\mathbf{I}_2$ is used to calculate the relative pointing error $\mathbf{e} = \begin{bmatrix}x & y\end{bmatrix}^\mathsf{T}$ within the exposure time $t_\Delta$ as detailed in (3.37). Obtaining accurate bounds and a deep understanding of these pointing errors is an issue of great importance for high stability space missions and represent the goal of the subsequent sections. This task is complicated by the variability of $\Omega \in \mathbf{\Omega}$ and also due to the presence of system uncertainty and the fact that external disturbances are both harmonic and stochastic in nature.

[1] The simplified model assumes that the effect on the pixel errors due to any satellite translation as well as due to rotations along the $c$-axis are negligible.

## 4.2 Pointing error analysis by means of system norms

For the overall interconnection $\mathbf{M}(\Omega, \Delta)$ that was described in the previous section,

Figure 4.3 shows the singular values of the transfer between the harmonic input $d_1$ and the broadband disturbances $\mathbf{d}_{bn}$ towards the two relative pointing errors $\mathbf{e} = \begin{bmatrix} x & y \end{bmatrix}^\mathsf{T}$ in the open-loop nominal case ($\Delta = 0$) and without any rotation in the photodetector ($\beta = 0$). It can be observed that due to the gyroscopic effect, the singular values from the broadband disturbances $\mathbf{d}_{bn}$ are slightly different across multiple spin rates $\Omega \in \mathbf{\Omega} = [10, 50]$ Hz. However, this variation is much more significant in the case of the input $d_1$ associated with the wheel's main harmonic perturbation. This results from the strong amplification of the filter $\mathbf{W}_1(\Omega)$ around its the central frequency. Consider the now

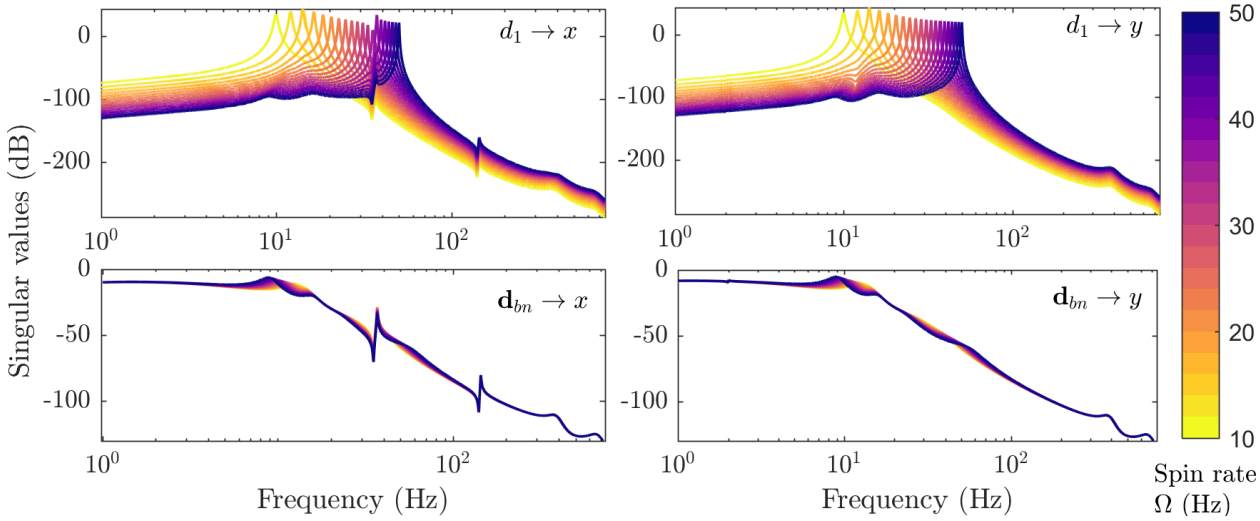


Figure 4.3: Open-loop singular values towards the relative pointing errors $\mathbf{e} = \begin{bmatrix} x & y \end{bmatrix}^\mathsf{T}$ for different $\Omega \in [10, 50]$Hz and in nominal conditions ($\Delta = \mathbf{0}$).

the following partition of the transfer matrix from external disturbances towards the pixel pointing error $\mathbf{e}(1) = x$:

$$x = \underbrace{\begin{bmatrix} \mathbf{M}_1 & \dots & \mathbf{M}_N & \mathbf{M}_{bn} \end{bmatrix}}_{\mathbf{M}_{\mathbf{d}\to x}(\Omega,\Delta)} \underbrace{\begin{bmatrix} d_1 & \dots & d_N & \mathbf{d}_{bn} \end{bmatrix}^\mathsf{T}}_{\mathbf{d}} \tag{4.4}$$

For fixed $\Delta \in \mathbf{\Delta}$ and $\Omega \in \mathbf{\Omega}$ the time-domain pointing error in the $x$-direction can be written as:

$$x(t) = x_{bn}(t) + \sum_{i=1}^{N} x_{\infty,i} \sin\left(h_i \Omega t + \psi_i\right) \tag{4.5}$$

where $x_{bn}$ is the stochastic component in response to the zero mean white noise unit covariance signals $\mathbf{d}_{bn}$. As these random disturbances are assumed to be Gaussian with zero mean and the system $\mathbf{M}_{bn}$ is LTI for any fixed values of $\Delta$ and $\Omega$, it follows that $x_{bn}$ is also Gaussian and its variance will be denoted by $\sigma_x^2$. The sinusoidal components with amplitude $x_{\infty,i}$ and phase $\psi_i$ are the result of the harmonic excitations $d_i(t)$ from (4.2). Both the variance $\sigma_x^2$ and the amplitudes[2] $x_{\infty,i}$ can be described in terms the system norms of $\mathbf{M}_{\mathbf{d}\to x}(\Omega)$ as:

$$x_{\infty,i} = \|\mathbf{M}_i\|_{\mathcal{L}_{2i}} \ , \ i = \{1, \dots, N\} \qquad ; \qquad \sigma_x^2 = \|\mathbf{M}_{bn}\|_{\mathcal{H}_2} \tag{4.6}$$

[2]This is the case if the harmonic filter $\mathbf{W}_i(\Omega)$ has sufficiently high gain at the central frequency $h_i\Omega$ compared to the adjacent frequencies and therefore $\|\mathbf{M}_i\|_{\mathcal{L}_{2i}} = |\mathbf{M}_i(jh_i\Omega)|$ holds.

where the notations $\|\cdot\|_{\mathcal{H}_2}$ denote the $\mathcal{H}_2$ system norm defined as

$$\sigma_x^2 = \|\mathbf{M}_{bn}\|_{\mathcal{H}_2} = \sqrt{\frac{1}{2\pi}\int_{-\infty}^{\infty} \text{Trace}\left[\mathbf{M}_{bn}^*(j\omega)\mathbf{M}_{bn}\right] d\omega} \tag{4.7}$$

Based on these norms, an upper bound $x_{3\sigma}$ on the predicted steady-state $3\sigma$ absolute value of $x(t)$ together with a corresponding measure $x_{rms}$ of the RMS value are provided by:

$$x_{3\sigma} = 3\sigma_x + \sum_{i=1}^{N} x_{\infty,i} \qquad ; \qquad x_{rms}^2 = \sigma_x^2 + \frac{1}{2}\sum_{i=1}^{N} x_{\infty,i}^2 \tag{4.8}$$

The same approach is applied for the other pointing error $y(t)$ in order to deduce $y_{\infty,i}$, $\sigma_y$ and afterwards $y_{3\sigma}$ and $y_{rms}$.

These norms can be used to make accurate and non-conservative time-domain predictions as shown in fig. 4.4. The image contains the relative pointing errors $\mathbf{e}(1) = x$ obtained using nonlinear industrial simulator for a linear spin rate variation within $\Omega(t) \in [10,\ 50]$Hz in both open and closed-loop scenarios. The data is afterwards superimposed with the predicted $3\sigma$ amplitude bounds $x_{3\sigma}$ and RMS values $x_{rms}$ calculated for the corresponding values of $\Omega$. It can be seen that the amplitude, RMS values and interactions with the flexible modes are correctly predicted in a non-conservative manner using the proposed approach.

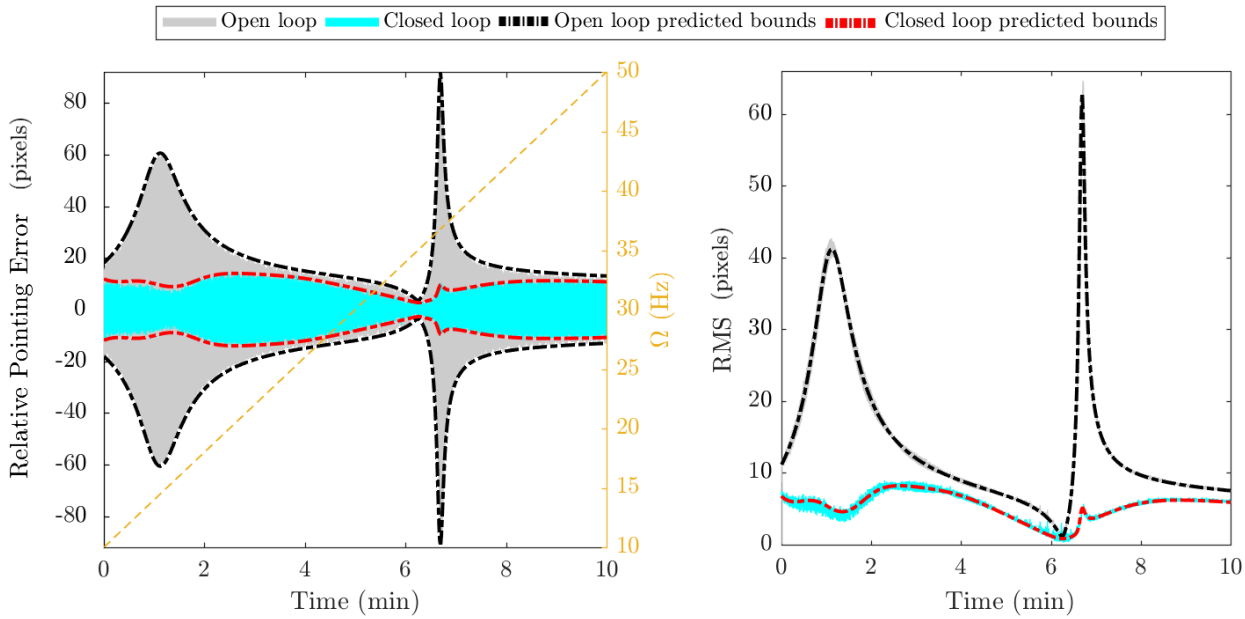


Figure 4.4: Predicted $3\sigma$ amplitude bounds and RMS values together with the simulated relative pointing errors in the nominal case ($\Delta = \mathbf{0}$) along the $x$-axis in both open and closed-loop for wheel rates $\Omega(t) \in \mathbf{\Omega}$ using the $\mathbf{K}_{robustness}$ controller designed in the previous chapter (for $\beta = 0$, this corresponds to the RPE $\theta_a$ measured in milliarcseconds that is shown in fig. 3.22 scaled by $\alpha_x$).

### 4.2.1 Geometry of the steady state pointing errors

Let $\mathbf{e}(t) = \begin{bmatrix} x(t) & y(t) \end{bmatrix}^\mathsf{T} \in \mathcal{C}_i \subset \mathbb{R}^2$ be the steady-state relative pointing error response due a single harmonic excitation $d_i = \sin(h_i\Omega t + \Phi_i)$ for fixed $\Omega$ and $\Delta$. If the phase $\Phi_i$ is assumed to be

uniformly random within $\Phi_i \in [0,\ 2\pi]$ then the set $\boldsymbol{\mathcal{C}}_i$ is an ellipse parametrized by:

$$\begin{aligned} \boldsymbol{\mathcal{C}}_i(\Theta) &= \begin{bmatrix} x_{\infty,i}\sin(\Theta) & y_{\infty,i}\sin(\Theta+\varphi_i) \end{bmatrix}^{\mathsf{T}} \quad \text{with} \quad \Theta \in [0, 2\pi) \\ \text{where} \quad \varphi_i &= \arg\left(\mathbf{M}_{d_i\to y}(j\omega)\right) - \arg\left(\mathbf{M}_{d_i\to x}(j\omega)\right) \quad \text{at frequency } \omega = h_i\Omega \end{aligned} \tag{4.9}$$

For clarity, the parameters characterizing the curve $\boldsymbol{\mathcal{C}}_1$ associated with the first harmonic signal $d_1$ are visible in the Bode plots shown in fig. 4.5 for $\Delta = \mathbf{0}$ and $\Omega = 34\,\text{Hz}$. If the stochastic distur-

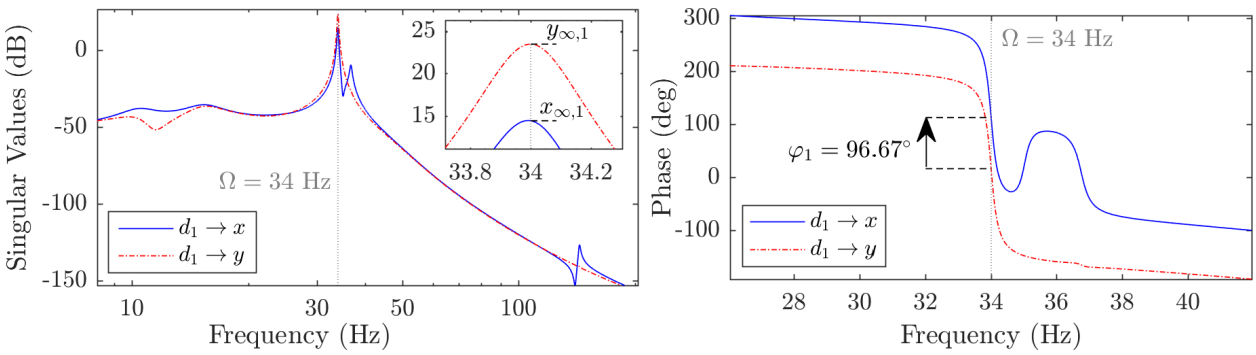


Figure 4.5: Bode plots of the transfers $\mathbf{M}_{d_1\to x}$ and $\mathbf{M}_{d_1\to y}$ and the parameters $\begin{bmatrix} x_{\infty,1} & y_{\infty,1} & \varphi_1 \end{bmatrix}$ of the ellipse $\boldsymbol{\mathcal{C}}_i$ associated harmonic signal $d_1$ for a spin rate $\Omega = 34\,\text{Hz}$.

bances $\mathbf{d}_{bn}$ are also introduced, the corresponding pointing error responses will have a distribution with variance $\sigma_x^2$ and $\sigma_y^2$ around the deterministic elliptical response. This fact is visible in fig. 4.6a, displaying the nominal closed-loop relative pointing errors obtained on the industrial simulator for fixed spin rate $\Omega = 36.4\,\text{Hz}$. The response perfectly aligns with the predicted geometry and therefore highlights the potential of the proposed method. Subsequently, the time-domain data is used to calculate the normalized histogram of the response, visible in fig. 4.6b, across a discrete pixel grid corresponding to the imaging sensor. This histogram is an empirical estimate of the probability density that a photon will hit a particular pixel. Due to its central role in simulating the effects of image motion, this function, also known as the Point Spread Function (PSF), will be studied in greater detail in the following section.

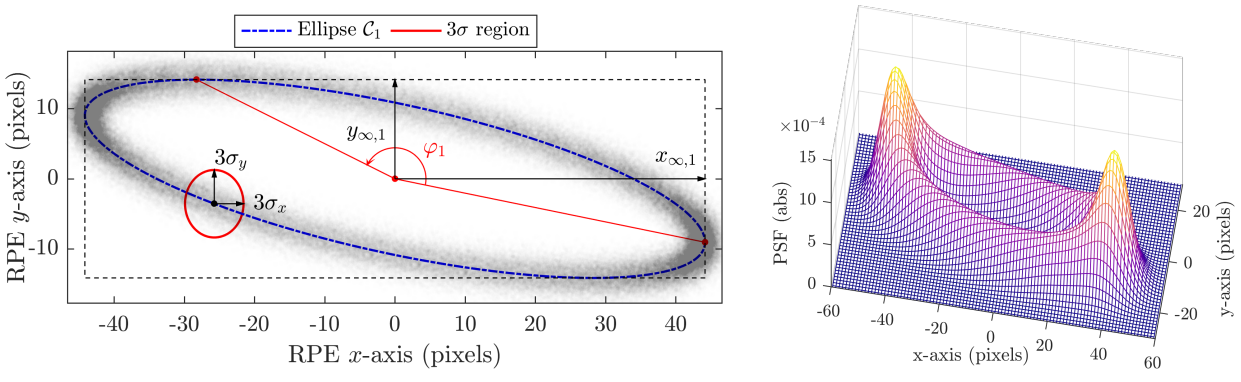


(a) (b)

Figure 4.6: a) Time domain samples of the open-loop simulator response for the wheel spin rate $\Omega = 36.4\,\text{Hz}$. b) Normalized histogram of the response across the pixel grid (corresponding to an empirical estimate of the Point Spread Function).

### 4.2.2 Worst-case pointing errors

The effect of the uncertainty $\Delta$ on the pointing errors, is evaluated by first replacing the norms $x_{\infty,i}$ with $i = \{1, \ldots, N\}$, given in (4.6), with the following upper bounds:

$$\widehat{x}_{\infty,i}(\Omega) \geq \max_{\Delta \in \mathbf{\Delta}} \|\mathbf{M}_i(\Omega, \Delta)\|_{\mathcal{L}_{2i}} \tag{4.10}$$

Each of these upper bounds can be determined using a variety of dedicated $\mu$-analysis tools such as MATLAB's *wcgain* command. These tools rely on calculating the structured singular value $\mu_{\mathbf{\Delta}}$ as outlined in (2.57) in order to guarantee tight upper bounds on the worst case $\mathcal{L}_2$ gains. In this case $\widehat{x}_{\infty,i}(\Omega)$ provides an upper bound on the maximum steady steady amplitude in response to the harmonic signal $d_1$ for a specific wheel spin $\Omega$ across all $\Delta \in \mathbf{\Delta}$ as seen in fig. 4.7a.

Considering now the effect of random disturbances, $\mathbf{d}_{bn}$, the upper bound $\widehat{\sigma}_x^2$ on the worst-case variance value[3] across all $\Omega \in \mathbf{\Omega}$ and $\Delta \in \mathbf{\Delta}$ satisfies:

$$\widehat{\sigma}_x^2 \geq \max_{\Delta \in \mathbf{\Delta}, \Omega \in \mathbf{\Omega}} \|\mathbf{M}_{bn}(\Omega, \Delta)\|_{\mathcal{H}_2} \tag{4.11}$$

Although dedicated algorithms exist to directly calculate upper bounds on the worst-case $\mathcal{H}_2$ system norm for an uncertain LTI model, the problem of computing worst-case $\mathcal{L}_2$ for both LTI and LPV systems has received considerably more attention in literature. Inspired by the Norm Bounding Problem (NBP) outlined in [OFBW13], the method proposed in this chapter will provide an upper bound on the worst-case $\mathcal{H}_2$ norm by reformulating it as a standard worst-case $\mathcal{L}_2$ gain calculation. To do this, consider stable strictly proper function $F_x(s)$ having a well defined $\mathcal{H}_2$ norm that satisfies:

$$\max_{\Delta \in \mathbf{\Delta}, \Omega \in \mathbf{\Omega}} \left\| F_x(s)^{-1} \mathbf{M}_{bn}(\Omega, \Delta) \right\|_{\mathcal{L}_{2i}} < 1 \tag{4.12}$$

Intuitively, this relationship guarantees that $F_x$ overbounds the maximum singular values of $\mathbf{M}_{bn}$ for any wheel spin rate $\Omega \in \mathbf{\Omega}$ and uncertainty $\Delta \in \mathbf{\Delta}$ and therefore

$$\widehat{\sigma}_x^2 = \|F_x(s)\|_{\mathcal{H}_2} \geq \max_{\Delta \in \mathbf{\Delta}, \Omega \in \mathbf{\Omega}} \|\mathbf{M}_{bn}(\Omega, \Delta)\|_{\mathcal{H}_2} \tag{4.13}$$

In this fashion, the computation of the upper bound on the $\mathcal{H}_2$ norm is transformed into the problem of finding an appropriate $F_x(s)$ that satisfies (4.12). Although a variety of methods exist to find an appropriate value for $F_x(s)$, the method of choice adopted in this work relies on solving the following optimization:

$$\underset{F_x \in \boldsymbol{\mathcal{F}}_x}{\text{minimize}} \quad \widehat{\sigma}_x^2 = \|F_x(s)\|_{\mathcal{H}_2} \quad \text{s.t.} \quad \max_{\Delta \in \mathbf{\Delta}, \Omega \in \mathbf{\Omega}} \left\| F_x(s)^{-1} \mathbf{M}_{bn}(\Omega, \Delta) \right\|_{\mathcal{L}_{2i}} < 1 \tag{4.14}$$

This class of mixed $\mathcal{H}_2/\mathcal{H}_\infty$ minimization problems can be efficiently handled by the same non-smooth $\mathcal{H}_\infty$ algorithms that were used to tune the controllers in sections 2.4.4 and 3.3.4. In this work, the structured set $\boldsymbol{\mathcal{F}}_x$ of possible transfer functions is specifically fixed to the set of all stable and strictly proper transfer functions of a given order $n_F$.

The minimization problem is challenging because it has to be optimized over all $\Delta \in \mathbf{\Delta}, \Omega \in \mathbf{\Omega}$. To tackle this issue, the optimization is converted into a finite dimensional problem using the following approach:

[3] The bound $\widehat{\sigma}_x^2$ is calculated as a single bound across all $\Omega \in \mathbf{\Omega}$ due to the fact that $\sigma_x$ doesn't significantly change for different wheel speeds.

**Step 1:** Fix the initial order $n_F$ of the stable and strictly proper filter $F_x(s) \in \boldsymbol{\mathcal{F}}_x$.

**Step 2:** Solve the original minimization problem given in (4.14) across a dense grid of $n_{samples}$ samples of $\mathbf{M}_{bn}(\Omega, \Delta)$ with $\Delta \in \boldsymbol{\Delta}, \Omega \in \boldsymbol{\Omega}$, i.e. solve the multi-model optimization problem:

$$\underset{F_x \in \boldsymbol{\mathcal{F}}_x}{\text{minimize}} \quad \widehat{\sigma}_x^2 = \|F_x(s)\|_{\mathcal{H}_2} \quad \text{s.t.} \quad \max_{i \in \{1,\ldots,n_{samples}\}} \left\{ \left\| F_x(s)^{-1} \mathbf{M}_{bn,i} \right\|_{\mathcal{L}_{2i}} \right\} < 1 \tag{4.15}$$

where $\mathbf{M}_{bn,i}$ with $i \in \{1, \ldots, n_{samples}\}$ represents one of the grid samples (with $n_{samples}$ initially fixed to $n_{samples} = 100$ in this study).

**Step 3:** With an the initial value of $F_x(s)$ obtained in the previous step, verify if condition (4.12) holds across all $\Delta \in \boldsymbol{\Delta}, \Omega \in \boldsymbol{\Omega}$ by computing the worst-case $\mathcal{L}_2$ gain using standard $\mu$ calculations (MATLAB's *wcgain* command). If this condition does not hold, then add the worst case combination to the set of grid samples $\mathbf{M}_{bn,i}$ and re-exectute **Step 2**.

**Step 4:** Increase the order $n_F$ of the filter $F_x(s)$ and re-execute starting from **Step 1** until there is no significant decrease in the value of $\widehat{\sigma}_x^2$ calculated in **Step 2** over each iteration.

**Result:** The filter $F_x(s)$ overbounding the singular value of $\mathbf{M}_{bn,i}$ across $\Delta \in \boldsymbol{\Delta}, \Omega \in \boldsymbol{\Omega}$ and the corresponding worst case variance $\widehat{\sigma}_x^2 = \|F_x(s)\|_{\mathcal{H}_2}$.

Figure 4.7b shows an example of one filter $F_x(s)$ of order $n_F = 4$ that was calculated using the previously described method. It can be seen that $F_x(s)$ provides a tight overbound over all the sampled values $\mathbf{M}_{bn,i}$ of $\mathbf{M}_{bn}(\Omega, \Delta)$.

The same approach can be employed for worst-case pointing error in other directions of the image plane. To do this, the camera rotation angle $\beta$ in (4.3) is varied within $\beta \in [0, \ \pi]$ and the worst-case bounds (4.10) are recomputed. Following this approach a convex polygon can be generated that encapsulates the set of possible steady state system ellipsoidal responses associated with a harmonic excitation $d_i$. The polygons for the main harmonic disturbance, calculated for $n = \{2, \ 3, \ 30\}$ directions are shown in fig. 4.8 for both open and closed-loop systems and at wheel speeds $\Omega = \{14.44, \ 36.4\}$ Hz close to the modal frequencies of the system. The various ellipses (4.9), corresponding to different samples of the uncertainty $\Delta \in \boldsymbol{\Delta}$ are used to illustrate how the proposed method can be employed to obtained a tight envelope on the possible system responses. The same procedure is also used for sensitivity analysis by only considering subsets of the total system uncertainties and fixing the rest to the nominal values. Figure 4.8 illustrates this method for applied to the closed-loop system spinning with $\Omega = 14.44$ Hz. For sufficiently high number of edges, the inner polygon, corresponding to the nominal condition ($\Delta = \mathbf{0}$), converges to the same nominal ellipse $\boldsymbol{\mathcal{C}}_1$ defined in (4.9). The bounds on this domain are slightly enlarged when uncertainties in the stiffness and damping characteristics of the passive isolators are introduced due to shifts in frequency and damping characteristics of the corresponding isolator mode. Additionally, when uncertainties in the tangential actuators (T-Group) or vertical actuators (V-Group) are considered (see the actuator arrangement in fig. 2.2), a slight shift in the direction of maximum gain can also be observed. The proposed analysis methodology therefore allows the systematic identification of both the magnitude and the direction in which the uncertain parameters contribute to the overall pointing error.

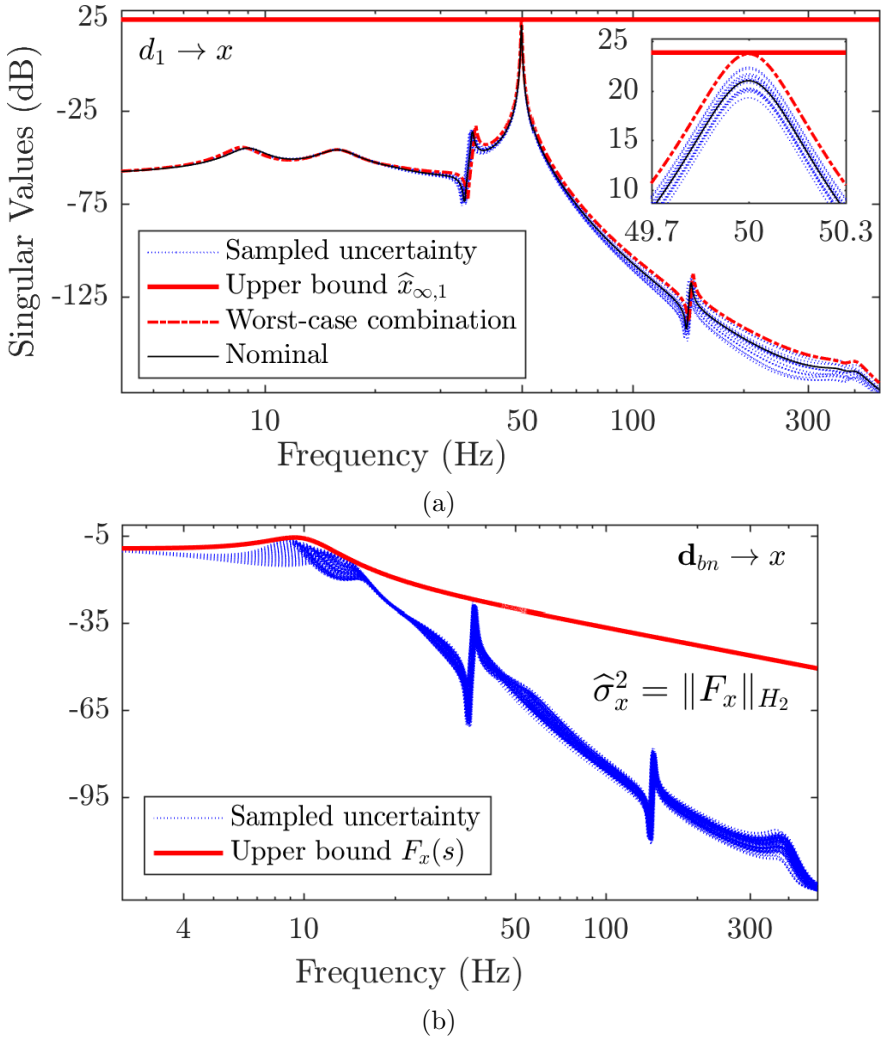


Figure 4.7: Singular values, uncertainty samples and worst case bounds on the transfer towards the pointing error $x$ from a) main harmonic $d_1$ at $\Omega = 50\,\text{Hz}$ b) stochastic noise $\mathbf{d}_n$.

## 4.3 Image jitter simulation

### 4.3.1 Description of the Optical Transfer Function (OTF)

An important performance measure for imaging spacecraft is the Point Spread Function (PSF) that describes the response of an imaging system to a point source. The Optical Transfer Function (OTF) is the two-dimensional spatial Fourier transform of the PSF and describes the spatial frequency response of an optical system analogous to the transfer function of a mechanical system [DGM12]. The main use of the OTF is to predict and analyze optical system performance, to specify requirements and tolerances or to perform image reconstruction.

The Fourier transform of an object imaged through an incoherent and isoplanic optical system is the product between the system OTF and the Fourier transform of the object projected onto the detector, i.e.

$$\mathbf{FT}_{image}(\boldsymbol{\xi}) = \mathbf{OTF}_{system}(\boldsymbol{\xi})\mathbf{FT}_{object}(\boldsymbol{\xi}) \tag{4.16}$$

where $\boldsymbol{\xi} = \begin{bmatrix}\xi_x & \xi_y\end{bmatrix}$ is 2D spatial frequency (in cycles per pixels for example). For space applications, the overall system OTF can be decomposed as the element-wise product of several OTFs, such as

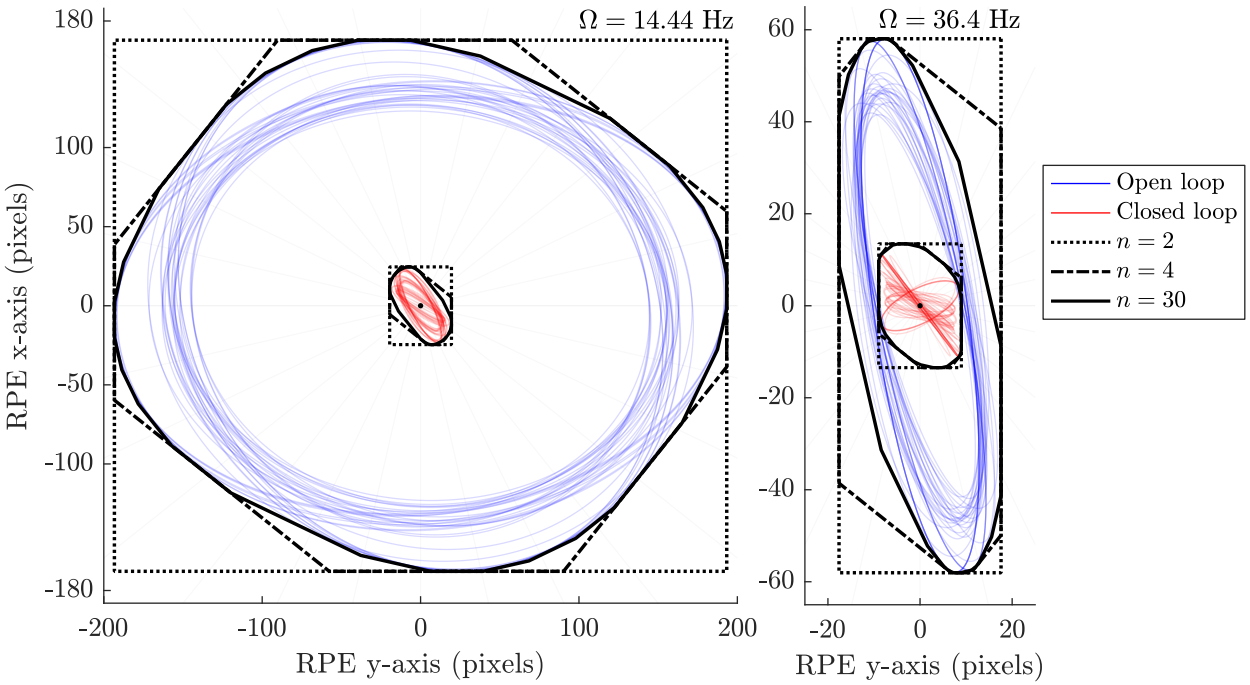


Figure 4.8: Worst-case bounds in $n \in \{2, 4, 30\}$ directions. The resulting polygons encapsulate the possible ellipsoidal responses caused by main harmonic disturbance for any values of the uncertain parameters.

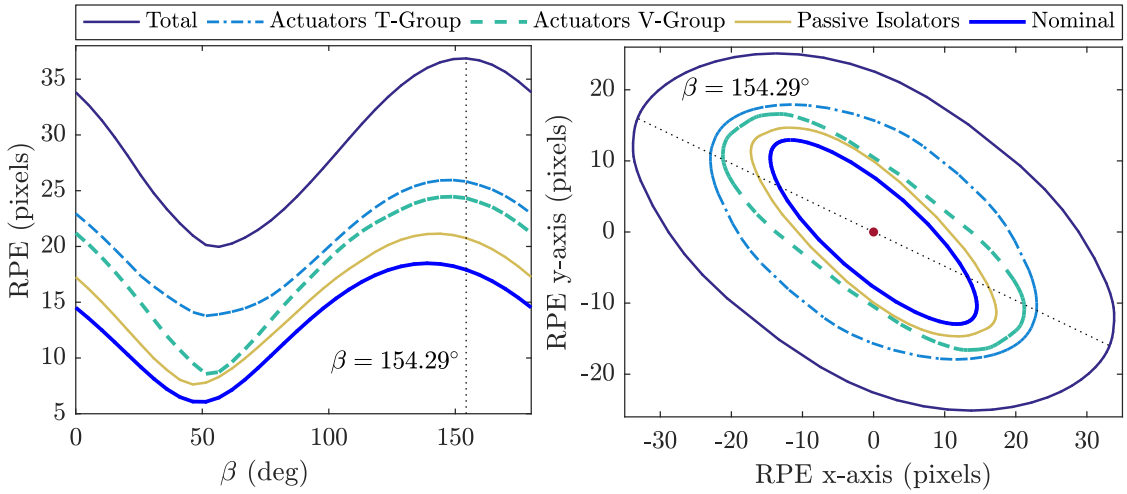


Figure 4.9: Sensitivity analysis of the worst-case pointing error polygonal bounds with respect to different uncertainty groups (closed-loop model with $\Omega = 14.44\,\text{Hz}$)

the one due to image motion, the optics, or the atmospheric distortions [PM12, PM16]. A typical system OTF can therefore be given by:

$$\mathbf{OTF}_{system}(\boldsymbol{\xi}) = \mathbf{OTF}_{motion}(\boldsymbol{\xi})\mathbf{OTF}_{optics}(\boldsymbol{\xi})\mathbf{OTF}_{atmosphere}(\boldsymbol{\xi}) \tag{4.17}$$

The focus of this study is only the contribution $\mathbf{OTF}_{motion}$ due to image motion. In this case, various closed-form expressions exist to compute the OTF for different types of one-dimensional image motion such as sinusoidal, Gaussian random or constant velocity [DGM12, PM16]. Although methods to derive the OTF for two-dimensional line-of-sight motion have been presented in works such as [PM16, LYH12], to the best of the authors' knowledge, these methods don't cover the case where the image motion follows an average Gaussian distribution along a main elliptical path as is

the case for the response pictured in fig. 4.6a. The focus of this work is therefore on deriving two-dimensional analytical expressions for $\mathbf{OTF}_{motion}$ as well as the associated point spread function $\mathbf{PSF}_{motion}$ for these types of motions with the final goal of better simulating the corresponding jitter effects due to microvibrations.

### 4.3.2 Analytical expressions for the OTF resulting from reaction wheel microvibrations

As previously mentioned, the two-dimensional pointing error motion is a superposition of elliptical responses due to the harmonic signals overlapped with gaussian random noise contributions. If the exposure time $t_\Delta$ is much longer than the harmonic perturbations and all of the random disturbances are assumed to be zero-mean Gaussian signals, then the steady state relative pointing errors in the detector plane, for fixed $\Omega$, can be described in a statistical framework as:

$$\begin{bmatrix} x \\ y \end{bmatrix} = \begin{bmatrix} x_{bn} \\ y_{bn} \end{bmatrix} + \sum_{i=1}^{N} \begin{bmatrix} x_{\infty,i} \sin(\Theta_i) \\ y_{\infty,i} \sin(\Theta_i + \varphi_i) \end{bmatrix} \tag{4.18}$$

where $\Theta_i \in \begin{bmatrix} 0, & 2\pi \end{bmatrix}$ are uniformly random phase angles , $x_{bn}$, $y_{bn}$ are zero mean Gaussian random signals with variance $\sigma_x$, $\sigma_y$ and the fixed constants $x_{\infty,i}$, $y_{\infty,i}$,$\varphi_i$ describe the geometry of the $i$-th harmonic ellipse (4.9). The total motion point spread function $\mathbf{PSF}_{motion}$ is equal to the joint probability distribution in the two directions and quantifies the probability associated with a photon hitting the detector at a particular location. The probability density function $\mathbf{PSF}_i(x, y)$ associated with the elliptical motion along the curve $\boldsymbol{\mathcal{C}}_i$ can be written as:

$$\mathbf{PSF}_i(x, y) := \begin{cases} \dfrac{1}{2\pi\sqrt{x_{\infty,i}^2 + y_{\infty,i}^2 - x^2 - y^2}} & \text{for} \quad \begin{bmatrix} x & y \end{bmatrix} \in \boldsymbol{\mathcal{C}}_i \\ 0 \quad \text{otherwise} \end{cases} \tag{4.19}$$

and represents[4] an extension to the two-dimensional case of the probability density associated with uni-dimensional random phase sinusoidal motion. The probability density corresponding to the Gaussian random variations[5] around the elliptical path are provided by:

$$\mathbf{PSF}_{jitter}(x, y) := \frac{1}{2\pi\sigma_x\sigma_y} \exp\left(-\frac{x^2}{2\sigma_x^2} - \frac{y^2}{2\sigma_y^2}\right) \tag{4.20}$$

The total joint probability distribution, i.e. $\mathbf{PSF}_{motion}$, requires the convolution of all the previous probability density functions as follows:

$$\mathbf{PSF}_{motion} := \mathbf{PSF}_{jitter} * \mathbf{PSF}_1 * \cdots * \mathbf{PSF}_N \tag{4.21}$$

The calculations are greatly simplified if the convolutions are replaced by multiplications in the Fourier domain. In this case, the overall motion OTF is rewritten as:

$$\mathbf{OTF}_{motion}(\boldsymbol{\xi}) = \mathbf{OTF}_{jitter}(\boldsymbol{\xi}) \prod_{i=1}^{N} \mathbf{OTF}_i(\boldsymbol{\xi}) \tag{4.22}$$

where $\mathbf{OTF}_{jitter}$ is the result of the Gaussian random pointing error motion while $\mathbf{OTF}_i$ quantifies the image degradation due to the high-frequency sinusoidal motion resulting from the $i$-th harmonic

[4] It can be verified that the function satisfies $\int_{-\infty}^{\infty}\int_{-\infty}^{\infty} \mathbf{PSF}_i(x, y)\, dx\, dy = \int_0^{2\pi} \mathbf{PSF}_i\left(\boldsymbol{\mathcal{C}}_i(\theta)\right) \left|\boldsymbol{\mathcal{C}}_i'(\theta)\right| d\theta = \int_0^{2\pi} \frac{1}{2\pi} = 1$

[5] under the simplifying assumption that the random motions $x_{bn}$ and $y_{bn}$ in the $xy$ plane are not correlated.

motion. Let the functions $\mathbf{x}_{\infty,i}(\beta)$ and $\boldsymbol{\sigma}_x(\beta)$ denote harmonic amplitudes and standard deviations along the detector $x$-axis, calculated using the system bounds (4.6), for all angles $\beta \in [0, \ \pi]$ of the detector in the camera model (4.3). In this case, the two-dimensional expressions of $\mathbf{OTF}_{jitter}(\boldsymbol{\xi})$ and $\mathbf{OTF}_i(\boldsymbol{\xi})$ can be written in polar form in terms of the one-dimensional OTFs given in [DGM12] as:

$$\mathbf{OTF}_{jitter}(\beta, \xi) = \exp\left(-2(\pi\xi\boldsymbol{\sigma}_x)^2\right) \quad ; \quad \mathbf{OTF}_i(\beta, \xi) = J_0\left(2\pi\xi\mathbf{x}_{\infty,i}\right) \tag{4.23}$$

where $J_0$ is the zero-order Bessel function and $\xi$ is the spatial frequency along a any given angle $\beta$. Multiplying these functions gives rise to the total $\mathbf{OTF}_{motion}(\beta, \xi)$ along that particular $\beta$-direction. An example of this particular OTF calculation process is illustrated in fig. 4.10. Here we consider the open-loop system running at $\Omega = 18.3\,\text{Hz}$ perturbed by the first two harmonic excitations centered at $\Omega$ and $2\Omega$ Hz. It can be observed that the function $\mathbf{OTF}_1$ displays a high degree of radial symmetry as the response caused by the first harmonic is mainly circular in nature. However, the asymmetry visible in the case of $\mathbf{OTF}_2$ is due to the interaction of the second harmonic with the flexible mode at 36.75 Hz. This causes primarily oscillations in the direction of the flexible mode. The combined effect of these two possible motions is also visible in general shape of $\mathbf{PSF}_{total}$ where a mainly circular distribution is spread across the direction of the flexible mode.

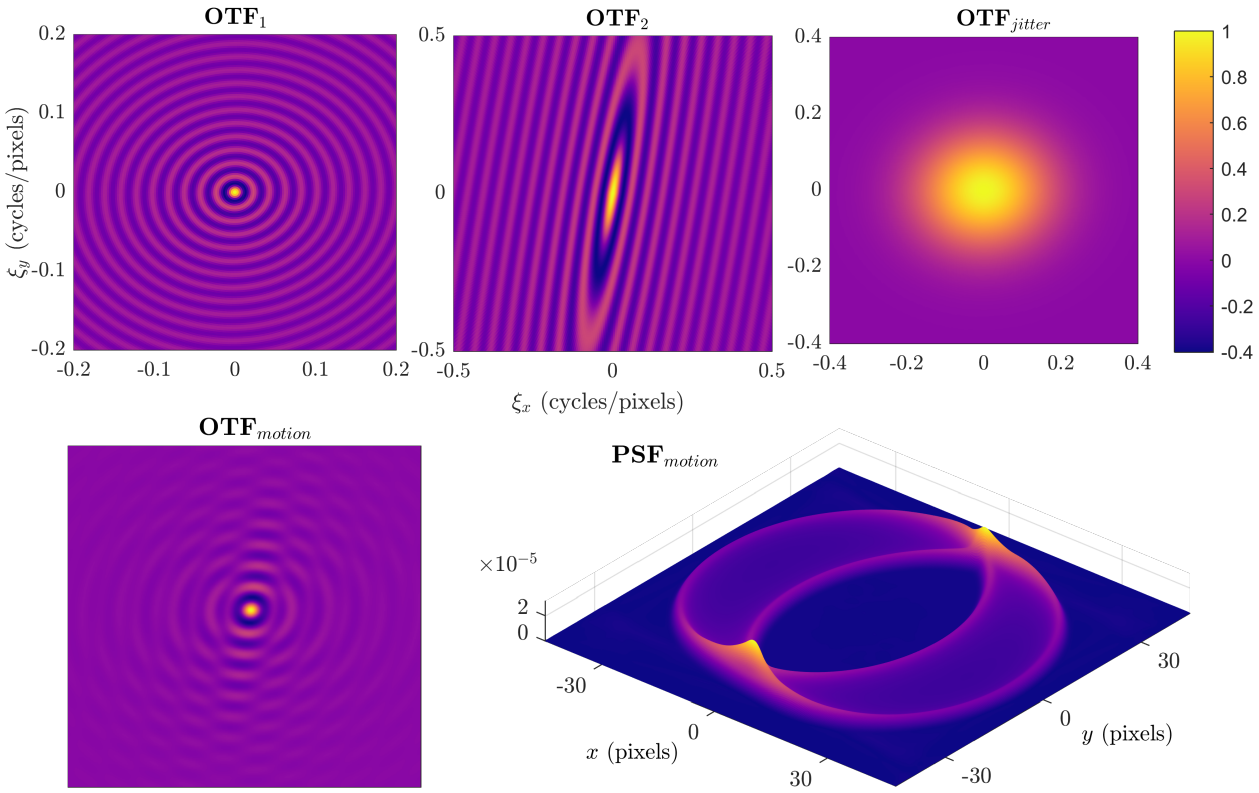


Figure 4.10: Components of the total $\mathbf{OTF}_{motion}$ for the main and second harmonic excitations at $\Omega = 18.3\,\text{Hz}$ and the corresponding $\mathbf{PSF}_{motion}$.

Based on the relationship (4.16), the newly computed motion OTF can be used as a Fourier domain image filter in order to perform jitter simulation and a visual assessment of the picture degradation. The outline of this process is shown in fig. 4.11. It is easy to see how the spatial frequencies for which $\mathbf{OTF}_{motion}$ has zero magnitude are completely eliminated from the image spectrum, resulting in loss of information. Applying this method for different reaction wheel speeds in both open and closed-loop settings provides an illustration of the benefits of the proposed active vibration control solution. This is visible in the results presented in fig. 4.12 for wheel rates $\Omega$ close to some flexible modes of the system. The filter image correctly captures the motion blur associated with the particular movement induced by the wheel disturbances. For example, at

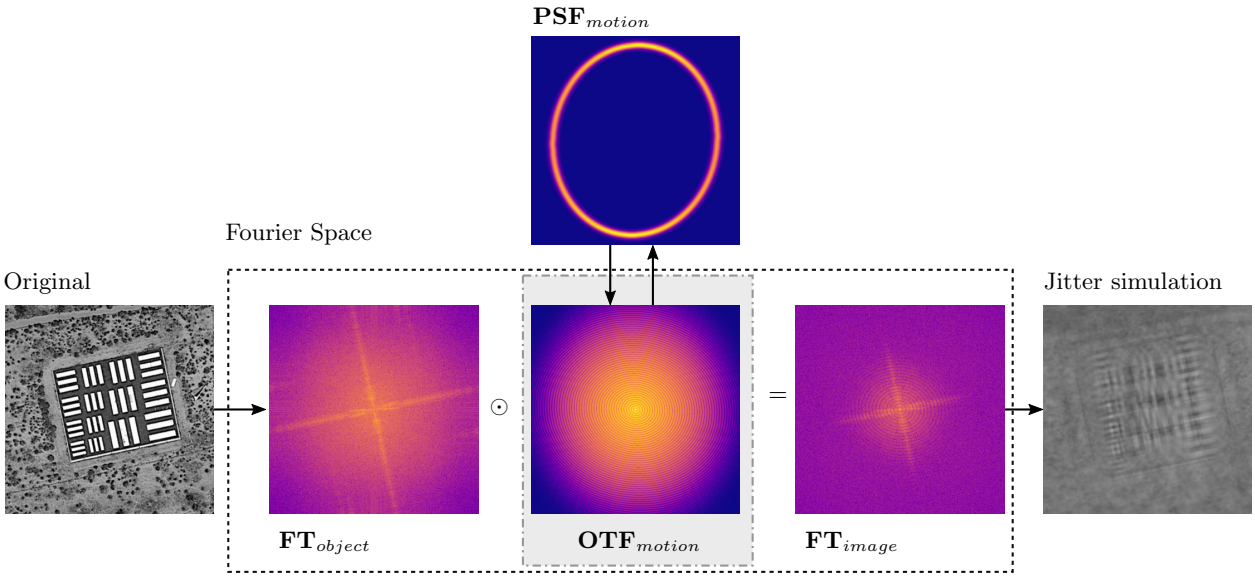


Figure 4.11: Outline of the jitter simulation process. Note: only the spectral magnitudes are shown, however **OTF**$_{motion}$ also acts upon the phase component.

$\Omega = 14.5\,\text{Hz}$, the movements in the two imaging axis are almost in quadrature, leading to a circular PSF and a circular blurring features in the resulting images. In contrast, at $\Omega = 36.75\,\text{Hz}$, the main harmonic disturbance intersects with the flexible mode, leading to in-phase motions primarily along the direction of resonant mode. This is visible both in the corresponding PSF and in the resulting image that displays sinusoidal motion blur along that particular direction.

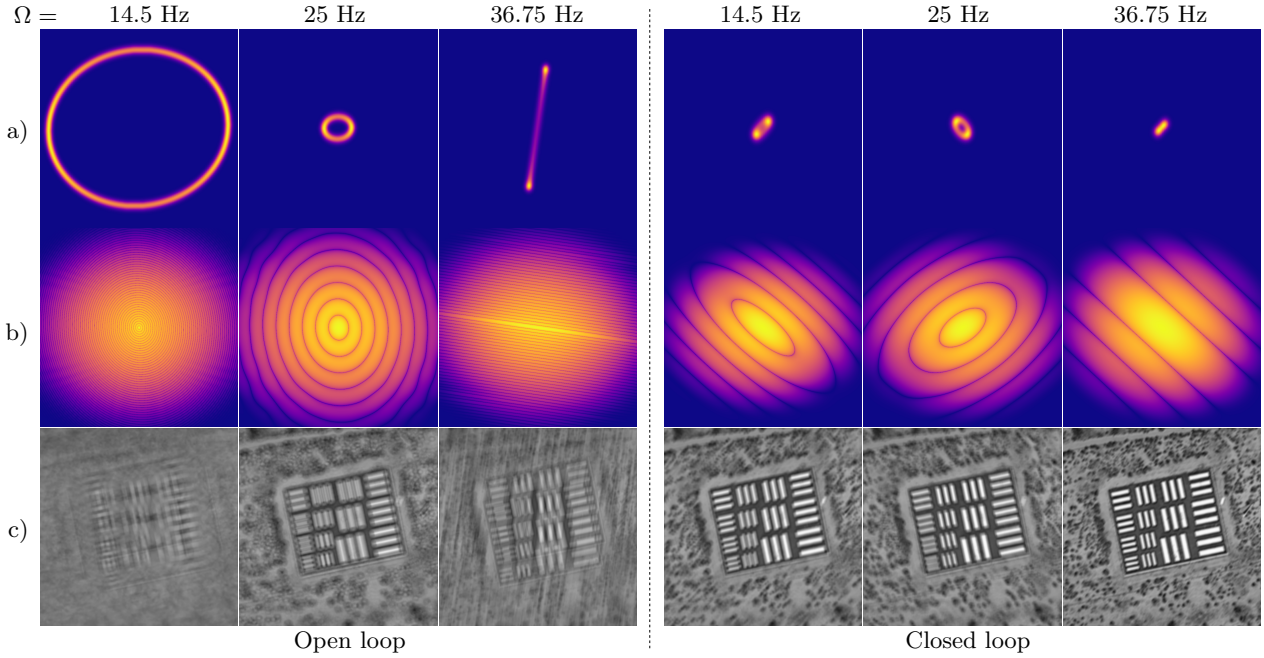


Figure 4.12: Jitter simulation results $\Omega = \{14.5,\ 25,\ 36.75\}$ Hz in open and closed-loop scenarios. a) Point Spread Functions b) Magnitudes of the OTF c) Filtered images.

### 4.3.3 Image reconstruction

Besides enabling more accurate jitter simulations, knowledge about the optical transfer function can also be used perform deblurring on the resulting image. For example, consider that in addition to the detector motion, the image is also corrupted by additive white Gaussian noise, i.e.

$$\mathbf{FT}_{image}(\boldsymbol{\xi}) = \mathbf{OTF}_{motion}(\boldsymbol{\xi})\mathbf{FT}_{object}(\boldsymbol{\xi}) + \mathbf{N}(\boldsymbol{\xi}) \tag{4.24}$$

where $\mathbf{N}(\boldsymbol{\xi})$ is mean power spectral density of the noise. The goal is to find a filter $\mathbf{G}_{deconv}(\boldsymbol{\xi})$ so that $\mathbf{FT}_{object}$ can be estimated as follows:

$$\widehat{\mathbf{FT}}_{object}(\boldsymbol{\xi}) = \mathbf{G}_{deconv}(\boldsymbol{\xi})\mathbf{FT}_{image}(\boldsymbol{\xi}) \tag{4.25}$$

where $\widehat{\mathbf{FT}}_{object}(\boldsymbol{\xi})$ is an estimate of $\mathbf{FT}_{object}$ that minimizes the mean square error. One possible way to obtain such an estimate is to employ a Wiener deconvolution filter that is described in the frequency domain as:

$$\mathbf{G}_{deconv}(\boldsymbol{\xi}) = \frac{\mathbf{OTF}^{*}_{motion}(\boldsymbol{\xi})}{|\mathbf{OTF}_{motion}(\boldsymbol{\xi})|^2 + \mathbf{NSR}(\boldsymbol{\xi})} \tag{4.26}$$

where the term $\mathbf{NSR}(\boldsymbol{\xi}) = \mathbf{N}(\boldsymbol{\xi})/\mathbf{FT}_{object}(\boldsymbol{\xi})$ is the noise-power-to-signal-power ratio. When the signal is very strong relative to the noise, $\mathbf{NSR} \to \mathbf{0}$ and the Wiener filter becomes simply the inverse of the system. Conversely, when the signal-to-noise ratio drops $\mathbf{NSR} \to \infty$ it follows that $\mathbf{G}_{deconv} \to \mathbf{0}$. In most practical situations, the quantity $\mathbf{NSR}(\boldsymbol{\xi})$ is rarely known to a high degree of accuracy. Therefore, it is usually estimated using empirical models. Figure 4.13 shows how this filter could be employed to recover significant spatial information from an image deteriorated by both the previously described motion blur as well as uniform additive Gaussian noise (with variance equal to 1% of that of the original image). The effectiveness of this image restoration approach opens up the possibility for a different kind of control philosophy. In this alternative approach, the focus is shifted from minimizing the pointing error, to the problem of forcing the system response along a known trajectory even in the presence of model uncertainty. Afterwards, restoration algorithms, like the ones previously introduced, could be used to achieve higher levels of image quality then the ones attainable with a strategy solely based on minimizing the pointing error.

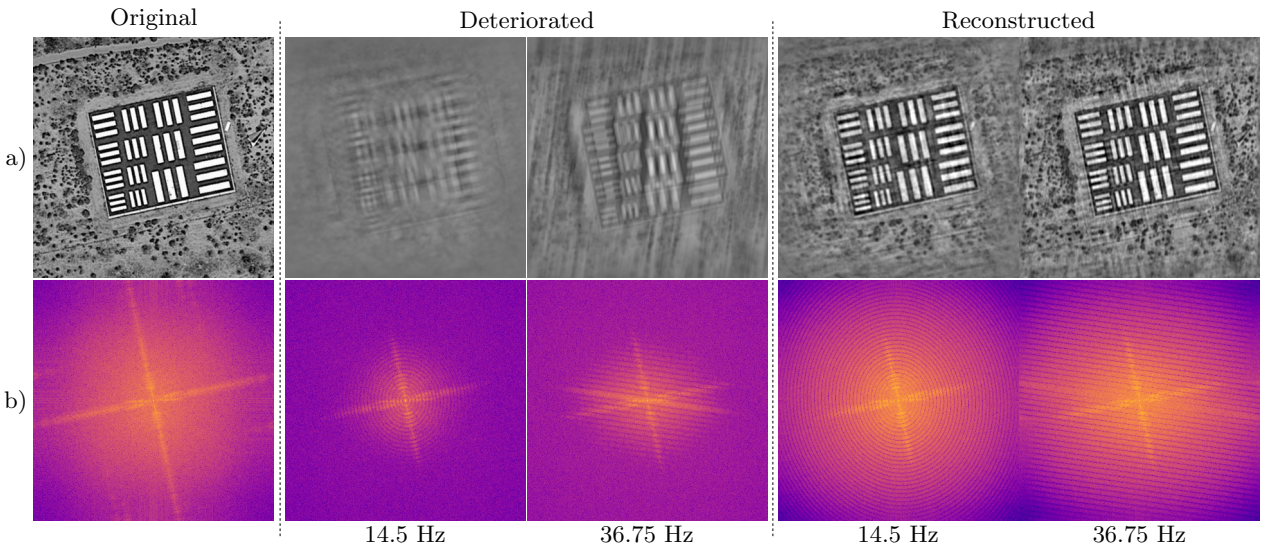


Figure 4.13: Image reconstruction in open-loop configuration for $\Omega = \{14.5,\ 36.75\}$ Hz. a) Image space b) Fourier power spectrum.

## 4.4 Conclusions

The chapter highlights a systematic microvibration analysis framework that relies on system norms and $\mathcal{H}_\infty/\mu$ concepts to guarantee end-to-end pointing error performance in the presence of system uncertainty. To this end, the novel disturbance model is used to capture the harmonic disturbance spectrum generated by a spinning reaction wheel. The disturbance model is linked to an uncertain structural model of the spacecraft and used to provide key details about the geometry of the resulting steady-state pointing error trajectories.

Secondly, the chapter proposes a detailed and comprehensive worst-case pointing error analysis of the uncertain system. The method relies on $\mu$-tools in order to guarantee a tight polygonal envelope around the set of possible steady-state responses and also to extract parametric sensitives of the resulting bounds.

Finally, the chapter also presents a powerful new jitter simulation procedure that takes into account the two-dimensional phase correlation between the movements in the detector plane. This method provides a deeper understanding into the nature of the image distortions introduced by the harmonic microvibrations. A potential image restoration procedure is used to highlight how this understanding could be put to use in the form of a deconvolution filter.

---

" *Nobody ever figures out what life is all about, and it doesn't matter. Explore the world. Nearly everything is really interesting if you go into it deeply enough.* "

Richard Feynman

# 5 Conclusions and recommendations

## 5.1 Thesis summary

Next generation satellite missions will have to meet extremely challenging pointing stability requirements. Even low levels of vibration can introduce enough jitter in the optical elements to cause a significant reduction in image quality. The success of these projects is therefore constrained by the ability of on-board vibration isolation and optical control techniques to keep stable the structural elements of the spacecraft in the presence of external and internal disturbances. This problem becomes increasingly more complex as modern space structures become more lightweight and flexible, leading to a problem of great importance in this industry. Although a variety of on-board equipment generate these microvibrations, by far the largest anticipated disturbance source is the reaction wheel assembly that is used to control spacecraft attitude by acting as a momentum exchange device. These devices provide significant cost and mass savings when compared to the Cold Gas Micro Propulsion Systems that are currently employed for attitude control during very high stability missions. For this reason, a variety of passive,active or hybrid isolation strategies have been developed to specifically target the disturbances produced by these wheels with the hopes of rivaling the performances achieved using Micro Propulsion Systems. However, the vast majority of such isolation systems are calibrated based on a combination of empirical tuning and time-consuming Monte Carlo campaigns on high fidelity simulators. In most cases, these provide only stochastic guarantees and give no direct relation between the analysis and the control design phases. This often leads to large redesign and verification efforts in case of minor changes to the system design or performance objectives. These issues have been outlined in detail in chapter 1.

Within the space industry, the trend is to increasingly rely on analytical tools during the development and verification phases of modern spacecraft. Nevertheless, prior to the research work carried out in this thesis, no integrated end-to-end framework existed for the purposes of tuning modern active microvibration isolation architectures. In this case end-to-end refers to an uncertain model that combines the optical and structural models of a flexible satellite actuated by a spinning reaction wheel together with the microvibration isolation system and a disturbance model of the reaction wheel perturbations. This motivated the main objective of the thesis which was the development of an Integrated Modeling, Control and Analysis framework for microvibration isolation systems. This framework incorporates uncertainty modeling via LFTs, robustness analysis via the Structured Singular Value $\mu$ and IQCs and modern robust control synthesis techniques such as structured $\mathcal{H}_\infty$ and $\mu$ methods. In order to reach this goal, chapter 2 introduces the hybrid microvibration isolation platform developed by Airbus Defence and Space and subsequently transfered to ESA. The setup combines the usage of passive isolators together with active control law to perform broadband microvibration isolation. The class of perturbations that are specifically

targeted are the ones that are typically generated by the spinning reaction wheels during operation. The capabilities of this platform were demonstrated in preliminary studies however, the controller synthesis procedures relied on a black box model that didn't provide a lot of physical insight into the dynamics. To alleviate these issues, the chapter begins by first extracting, in agreement with the industrial partners, a new uncertain model of the platform that is based upon the physical equations of the system. This model is expressed as an LFT and captures in an unified manner the dependency on various parametric uncertainties as well as the gyroscopic effects induced by the spinning motion of the wheel. This LFT model serves as the starting point for all further research presented in the thesis. Afterwards, based on this model, the active isolation controller is tuned to minimize the elastic forces that get transmitted through the passive isolators using a systematic control design procedure based on $\mathcal{H}_\infty/\mu$ techniques. In order to increase performance , the proposed controller is chosen to adapt based upon the current operating spin rate of the reaction wheel. Finally, the robust performances of the isolation architecture are assessed with the help of the structured singular value $\mu$. Furthermore, the same $\mu$-techniques are shown to provide parametric sensitivity with respect each of the uncertain elements and help identify the driving parameters of the overall setup. Finally, the method enabled the possibility of calculating worst-case combinations without the reliance on the classical and expensive Monte Carlo campaigns. Time domain simulations based on a nonlinear high-fidelity industrial simulator are included as a final verification step of the worst-case parameter combinations identified using $\mu$ methods.

Motivated by the previous results, chapter 3 established an Integrated Modeling, Control and Analysis framework for a typical space observation mission that incorporates the previous microvibration platform. To do this, the LFT model of isolation setup, established earlier in chapter 2, is integrated with that of simplified model of a flexible spacecraft stabilized using an attitude control system. The main goal was to show how modern robust control methods can be employed to tune the isolation platform in order to guarantee improved pointing stability performance during closed-loop operation even in the presence of uncertainties. Weighting functions are used to specify the frequency domain profile of external disturbances and also set the desired bounds on the pointing stability and actuator control signals. These weights include an improved disturbance model for the multi harmonic perturbation spectrum produced by the reaction wheel. Afterwards, the robust stability and performance objectives are expressed in as bounds on the worst-case $\mathcal{L}_2$ gains of certain scaled closed-loop transfers. These gains are optimized in the subsequent robust synthesis procedure. Here, multiple LPV controllers, scheduled by the wheel spin rate, are designed for different levels of system uncertainty in order to highlight the performance trade-offs inherent in the design. It was shown how this approach can be employed to synthesize an active vibration control strategy that significantly improves the pointing stability of the overall mission while also being robust to model uncertainty. Lastly, the third part of chapter 3 establishes the $\mu$ and IQC analysis framework that is used to validate the proposed isolation design. The framework provided accurate and guaranteed bounds on the worst-case pointing performance in the presence of parametric uncertainty, time-varying actuator delays and saturations as well as variable spin rates. The predicted worst-case scenarios showed almost perfect agreement with the results obtained on the high-fidelity industrial simulator.

Chapter 4 takes the previous analysis one step forward and uses it to predict, in a rigorous way, the worst-case pointing errors of a general flexible spacecraft in response to reaction wheel disturbances. It was shown how both the pointing error amplitude in various directions of the image plane due to the harmonic perturbations as well as the variance in response to the Gaussian noise can be bounded by certain $\mathcal{L}_2$ gains of the system. Based on these bounds, the geometry of the pointing error response for different reaction wheel spin rates is established and used to simulate the image distortions resulting from such jitter motions. This is done with the aid of new analytical expressions for the Point Spread and Optical Transfer Functions that correctly handle the 2-D image motion induced by the wheel perturbations.

## 5.2 Main achievements

All of the objectives listed in the introduction chapter of the thesis have been achieved and the contributions to the state of the art can be grouped as follows:

**Integrated modeling**

- the thesis established an Integrated Modeling, Control and Analysis framework for a typical space observation mission composed of a flexible satellite mode, a hybrid isolation platform and a reaction wheel assembly. The overall system is assembled by combining the LFT models of each sub-component. In this fashion, the uncertainty in each subcomponent naturally combines in a representative and physical uncertainty model at system level. The proposed LFT representation is also parameterized by the spin rate of the reaction wheel and is capable of correctly capturing the gyroscopic coupling induced by wheel into the overall system. The integrated end-to-end uncertain system model fully captures the disturbance propagation from the reaction wheels, through the isolation system and flexible spacecraft structure towards the sensitive instruments.
- a new disturbance model for reaction wheel perturbations is convinced by taking into account the multi-harmonic noise spectrum generated by any typical reaction wheel during operation. The model takes into considerations the phase correlation that exists between the harmonic components in an effort to make the disturbance model as accurate as possible. The model is shown to have an LFT representation that is parameterized by the wheel's spin rate and can seamlessly integrate into the overall end-to-end model of the plant in order to make non-conservative predictions about the resulting pointing errors.

**Control system design**

- With the structural and disturbance models in place, the work describes how fundamental results from $\mathcal{H}_\infty/\mu$ theory can be used to reformulate the stability requirements and isolation performance objectives into bounds on the $\mathcal{L}_2$ gain of certain scaled closed-loop transfers. These $\mathcal{L}_2$ gains are subsequently minimized by means of structured LPV controllers that are tuned using multi-objective non-smooth $\mathcal{H}_\infty$ techniques. Two novel active isolation strategies are proposed and demonstrated in chapter 2 and chapter 3 that are based on different assumptions. The first one described in chapter 2 employs an adaptive pre-filter block parameterized by the reaction wheel spin rate together with a tunable LTI block to significantly decrease the force and torque transmissibility around the main harmonic disturbance. In this case, the tuning procedure relies on a very simplified model of the reaction wheel perturbations. The second control strategy presented in chapter 3 employs the integrated model of the flexible satellite together with the accurate disturbance model of the reaction wheel perturbations. In this case, a low-order structured LPV controller is directly tuned to push the predicted open-loop pointing error spectrum below a certain threshold. Both of these strategies also take into account the system uncertainties and employ D-scales in the optimization procedure in an effort to reduce conservatism at guarantee the robust performance requirements.
- In section 3.3.4 the proposed synthesis procedure generates a set of controllers each optimized for the same performance criteria but employing different levels of uncertainty. Analyzing the resulting performance levels across the set of controllers reveals the trade-off between robustness and performance. Additionally, a methodology is proposed to visualize the performance

penalty introduced by the low-order structured LPV design compared to a full order optimal controller tuned to a specific value of the scheduling parameter.

**Worst case analysis**

- both chapter 3 and chapter 2, describe new analysis methodologies in the field of microvibration control that are based on analytical tools such as the structured singular value $\mu$ and IQCs. These are used to certify the microvibration isolation architectures without relying on Monte-Carlo campaigns. Once the LFT models are assembled, the $\mu$ computations were proven essential in identifying worst-case combinations for different performance objectives even for numerous uncertain parameters. These were subsequently validated on the industrial simulator to highlight the soundness of this approach. IQCs provided the means to extend the worst-case analysis methodology to also include the effects of actuator saturation, time-varying reaction wheel spin rates and uncertain time-varying delays.
- new analytical expressions are introduced for the Point Spread and Optical Transfer Functions associated with the elliptical 2-D motion induced by the wheel's harmonic perturbations. These are used to simulate the image distortions resulting from such jitter motions in a manner that correctly handles the phase relations between the motions along each imaging axis. Based on these expressions, an algorithm is proposed that could be used to perform image reconstruction for this class of image deformation.

## 5.3 Future work

Research into microvibration isolation technology is a topic that will only grow in interest in the coming years, especially with the emergence of smallsat and nanosatellite platforms. The trend towards lighter space structures further motivates active research in this field. What follows is a list of recommendations for future work in certain subjects addressed in this thesis for which further research is deemed necessary:

- The IQC analysis performed in section 3.4.2 with respect to actuator saturation showed that the closed-loop remains stable for any loss of efficiency in the PMAs. Therefore, taking only stability into account, the system is inherently fault tolerant with respect to any number of failures in the actuators. However, in order to achieve such robustness, the uncertainty domain used in the synthesis procedure had to account for high simultaneous variations in the actuator gains. Such a scenario is not very likely to occur in practice and it could be argued that the previous solution is overly conservative. In order to maximize performance, future research could investigate the possibility of directly synthesizing a robust controller that is passively fault tolerant only with respect to a single actuator failure. Another alternative is to design a complete Fault Detection, Isolation, and Recovery (FDIR) unit that runs in parallel with a controller designed solely to maximize performance. In case of a failure this FDIR unit could perform the switch to a backup controller. Although this strategy would probably perform the best in terms of isolation, it would introduce a lot of complexity to the overall isolation architecture. A proper trade-off analysis of these aspects would be an interesting future study.
- Inspired by the works of [PPAL16, ALdPC13], the controller synthesis procedure could be extended to tune certain structural parameters at the same time. Such an integrated control/structure co-design would allow in the case of this thesis for simultaneous tuning of the

attitude control and hybrid isolation systems. Additionally, the same methodology could be employed to optimally place the sensor and actuator blocks in order to achieve super isolation performance or increase system robustness.

- The current thesis only focused on the disturbance effects induced by a single reaction wheel, however it is suspected that the presented techniques can scaled to multiple wheel configurations without significant difficulty. This could be accomplished by first modeling each of the $N$ wheels as a separate LFT scheduled by a corresponding spin rate $\Omega_i$ with $i = \{1, \ldots, N\}$. Afterwards for each wheel, the disturbances must be correctly rotated and projected into the supporting frame to account for the mounting direction. As many of the current and future spacecraft are equipped with a cluster of reaction wheels, analyzing the vibration interaction between the multiple connected flywheels is a matter of significant industrial relevance. For example, in [FB12], it has been shown that resonant vibration of flywheel whirl at non-spin speeds can be caused by the synchronous imbalance-induced vibration input of another flywheel in the system. These sort of interactions are especially relevant in the case of smallsat or nanosats platforms for which reaction wheels are relatively inexpensive. For instance, in [NAS16], the GEMINI Stability Control (GSC) concept makes use of extra reaction wheels combined with precision speed control to maintain reaction wheel speeds on the "sweet spot" of their passive vibration isolators and therefore optimize disturbance attenuation. To do this, the study proposes to install two reaction wheels per axis (six reaction wheels total) on a smallsat plaform. This simplifies the arrangement, and also enabled the torque to be commanded using either common mode control (i.e., commanding the wheels to accelerate in the same direction), or speed commanded using differential-mode control (i.e., commanding the wheels to accelerate opposite each other). The methodology presented in this thesis could be adapted to such system in order to provide additional analytical insight into the coupled dynamics.

- the use magnetically suspended bearings instead of ball-bearings to support the flywheels offers a number of significant advantages. These Magnetic bearing reaction wheels (MBRW) may be operated at much higher speeds and therefore improve the momentum-to-mass ratio compared to traditional ball-bearing flywheels which are limited to around 10 000 rpm. For example, in [ZBK14] a reaction wheel demonstrator is presented that employs a high-speed, magnetically levitated electrical drive system, to reach spin rates of over 200 000 rpm. Such systems could potentially be investigated within the analysis framework introduced in this thesis. To do this, one would have to replace the dynamics of wheel flexible support in table 2.2 with the closed-loop dynamics of the magnetically levitated system (such as the one proposed in [XFLC13]). Afterwards, both the magnetic levitation system and the hybrid isolation platform proposed in the thesis can be tuned at the same time in order to achieve state-of-the-art isolation performance.

- all the results presented in this thesis are based on the assumption that the passive isolators behave like a 6-DoF viscoelastic joint with linear stiffness and damping and ignore any non-linear effects. This is a safe assumption for current elastomers undergoing small amplitude deformations. However, the true mechanical properties of elastomeric dampers are relatively complicated and may vary with environment temperature and excitation frequency [HS96]. Therefore the linear model that was employed in this thesis has some serious shortcomings which could become increasingly more apparent in future years. For example, the shear stiffness value of the elastomers varies with the frequency, temperature, deformation and amplitude of excitation. Hence, there exists a real need for a reliable, usable, non-linear theory that includes consideration of nonlinear effects. Currently, fractional derivative models such as the one presented in [SPA11] offer the best compromise between complexity and predictive capacity [Ibr08]. In this context, future research might investigate if the techniques based

on Integral Quadratic Constraints that were used in this thesis could provide an alternative way to analyze the dynamical properties of these nonlinear dampers. A good starting point for this potential study would be to use the IQC multipliers introduced in [Jön98, PH98] to model the elastic hysteresis effects commonly observed in elastomeric materials.

In conclusion, the work carried out in this thesis has been shown to significantly improve the previous techniques in the field of active microvibration isolation, especially with respect to the issue of uncertainty management. In particular the work demonstrated the powerful capabilities of an integrated end-to-end modeling framework in which to perform worst-case analysis and system design of reaction wheel microvibration isolation systems. However, one must remember that the results presented in this thesis are a preliminary study and require further exploration. A number of possible future developments have thus been suggested based on the currently unsolved issues and for which this thesis can be used as an initial reference.

---

" *Deep in the human unconscious is a pervasive need for a logical universe that makes sense. But the real universe is always one step beyong logic.* "

Frank Herbert

# Appendix

## A.1 Morton's method for affine parameter dependent matrices

Consider $\mathbf{\Phi}$ a parameter vector of length $k$ and a parameter dependent matrix $\mathbf{A}(\mathbf{\Phi}) \in \mathbb{R}^{n\times m}$ affine in $\mathbf{\Phi}$. Each parameter $\Phi_i \in \mathbf{\Phi}$ is considered uncertain and bounded by $\Phi_i \in [\alpha_i,\ \beta_i]$ with a nominal value $\Phi_i^0 = (\alpha_i + \beta_i)/2$. With a prior normalization of $\Phi_i \in \mathbf{\Phi}$ such as $\Phi_i = \Phi_i^0 + v_i\delta_i$ where $v_i = (\beta_i - \alpha_i)/2$ and $|\delta_i| \leq 1$, it is possible [Mor85, HO06] to write the matrix $\mathbf{A}(\mathbf{\Phi})$ as

$$\mathbf{A}(\mathbf{\Phi}) = \mathbf{A}_o + \sum_{i=1}^{k} \delta_i \mathbf{A}_i \tag{1}$$

with constant matrices $\mathbf{A}_i \in \mathbb{R}^{n\times m}, i = \{1,\dots,k\}$ . Let $\mathbf{A}_i = \mathbf{L}_i\mathbf{R}_i$ be a full rank factorization of $\mathbf{A}_i$ with $\mathbf{L}_i \in \mathbb{R}^{n\times r_i}$ and $\mathbf{R}_i \in \mathbb{R}^{r_i\times m}$. Then $\mathbf{A}(\mathbf{\Phi})$ can be rewritten as

$$\mathbf{A}(\mathbf{\Phi}) = \mathbf{A}_0 + \sum_{i=1}^{k} \mathbf{L}_i\delta_i\mathbf{I}_{r_i}\mathbf{R}_i = \mathcal{F}_u\left(\left[\begin{array}{ccc|c} 0 & \dots & 0 & \mathbf{R}_1 \\ \vdots & \ddots & \vdots & \vdots \\ 0 & \dots & 0 & \mathbf{R}_k \\ \hline \mathbf{L}_1 & \dots & \mathbf{L}_k & \mathbf{A}_0 \end{array}\right], \left[\begin{array}{ccc} \delta_1\mathbf{I}_{r_1} & & \\ & \ddots & \\ & & \delta_k\mathbf{I}_{r_k} \end{array}\right]\right) = \mathcal{F}_u \tag{2}$$

## A.2 Performance Analysis using IQCs

Two finite energy signals $\mathbf{w} \in \mathcal{L}_2^{n_w}, \mathbf{z} \in \mathcal{L}_2^{n_z}$ whose Fourier transforms are denoted as $\hat{\mathbf{w}}$ and $\hat{\mathbf{z}}$ are said to satisfy the frequency domain IQC defined by a multiplier $\mathbf{\Pi}$ if

$$\int_{-\infty}^{\infty} \begin{bmatrix}\hat{\mathbf{z}}(\mathrm{j}\omega)\\ \hat{\mathbf{w}}(\mathrm{j}\omega)\end{bmatrix}^* \mathbf{\Pi}(\mathrm{j}\omega) \begin{bmatrix}\hat{\mathbf{z}}(\mathrm{j}\omega)\\ \hat{\mathbf{w}}(\mathrm{j}\omega)\end{bmatrix} d\omega \geq 0,\ \mathbf{\Pi} = \begin{bmatrix}\mathbf{\Pi}_{11} & \mathbf{\Pi}_{12}\\ \mathbf{\Pi}_{12}^* & \mathbf{\Pi}_{22}\end{bmatrix}. \tag{3}$$

where $\mathbf{\Pi}(\mathrm{j}\omega) : \mathrm{j}\mathbb{R} \to \mathbb{C}^{(n_w+n_z)\times(n_w+n_z)}$ can be any measurable Hermitian-valued function, although it is usually chosen among the rational functions bounded on the imaginary axis. The uncertainty domain $\mathbf{\Delta}_{\mathrm{IQC}}$ introduced by a causal and bounded operator $\Delta_{\mathrm{IQC}} : \mathcal{L}_2^{n_v} \to \mathcal{L}_2^{n_w}$ is said to be described by an IQC of this form, provided that the inequality (3) holds for all $\mathbf{z} \in \mathcal{L}_2^{n_z}$ and $\mathbf{w} = \Delta_{\mathrm{IQC}}(\mathbf{z})$ (where $\Delta_{\mathrm{IQC}}(\mathbf{z})$ represents the output of $\Delta_{\mathrm{IQC}}$ when excited by $\mathbf{z}$). For a given uncertainty description, the set $\mathbf{D}_\Pi$ of all suitable multiplier $\mathbf{\Pi}$ is therefore given by:

$$\mathbf{D}_\Pi := \left\{\mathbf{\Pi} : \int_{-\infty}^{\infty} \begin{bmatrix}\hat{\mathbf{z}}(\mathrm{j}\omega)\\ \epsilon\hat{\mathbf{w}}(\mathrm{j}\omega)\end{bmatrix}^* \mathbf{\Pi}(\mathrm{j}\omega) \begin{bmatrix}\hat{\mathbf{z}}(\mathrm{j}\omega)\\ \epsilon\hat{\mathbf{w}}(\mathrm{j}\omega)\end{bmatrix} d\omega \geq 0, \forall\epsilon \in [0,1], \forall\mathbf{z} \in \mathcal{L}_2^{n_z}, \mathbf{w} = \Delta_{\mathrm{IQC}}(\mathbf{z}), \Delta_{\mathrm{IQC}} \in \mathbf{\Delta}_{\mathrm{IQC}}\right\} \tag{4}$$

where the term $\epsilon$ needs to be introduced due to the fact that the IQC theory requires the set of uncertain perturbations to be star-shaped with respect to the origin (i.e. if $\Delta_{\mathrm{IQC}} \in \mathbf{\Delta}_{\mathrm{IQC}}$,

then $\epsilon\Delta_{\text{IQC}} \in \mathbf{\Delta}_{\text{IQC}}, \forall \epsilon \in [0,1]$). With the multipliers chosen from this set and for a nominally stable system $\mathbf{M}$, analyzing whether $\mathcal{F}_u(\mathbf{M}, \Delta_{\text{IQC}})$ has a robust performance of level $\gamma$, i.e. $\sup_{\Delta_{\text{IQC}} \in \mathbf{\Delta}_{\text{IQC}}} \mathcal{H}_\infty[\mathcal{F}_u(\mathbf{M}, \Delta_{\text{IQC}})] < \gamma$, is reduced to verifying whether the following inequality holds:

$$\begin{bmatrix} \mathbf{M}(\mathrm{j}\omega) \\ \mathbf{I} \end{bmatrix}^* \widetilde{\mathbf{\Pi}}(\mathrm{j}\omega) \begin{bmatrix} \mathbf{M}(\mathrm{j}\omega) \\ \mathbf{I} \end{bmatrix} \prec 0, \forall \omega \in \mathbb{R} \cup \{\infty\}, \text{ where } \widetilde{\mathbf{\Pi}} = \begin{bmatrix} \mathbf{\Pi}_{11} & \mathbf{0} & \mathbf{\Pi}_{12} & \mathbf{0} \\ \mathbf{0} & \mathbf{I} & \mathbf{0} & \mathbf{0} \\ \mathbf{\Pi}_{12}^* & \mathbf{0} & \mathbf{\Pi}_{22} & \mathbf{0} \\ \mathbf{0} & \mathbf{0} & \mathbf{0} & -\gamma^2\mathbf{I} \end{bmatrix} \tag{5}$$

The previous inequality can be efficiently verified by expressing it as a single Linear Matrix Inequality (LMI) [VSK16] using the Kalman-Yakubovich-Popov (KYP) lemma [IH05]. To accomplish this, the multipliers are first parameterized as $\mathbf{\Pi}(s) = \mathbf{\Psi}(s)^* \mathbf{S} \mathbf{\Psi}(s)$ where $\mathbf{S}$ is a matrix variable and $\mathbf{\Psi}(s)$ is a tall transfer-matrix constructed from pre-selected basis transfer functions. The structure of both $\mathbf{\Psi}(s)$ and $\mathbf{S}$ is chosen based on the type of uncertainty being investigated.

# References


[AA98] Pierre Apkarian and Richard J. Adams. Advanced gain-scheduling techniques for uncertain systems. *IEEE Transactions on Control Systems Technology*, 6(1):21–32, 1998.

[Add17] Daniele Addari. *A Semi-empirical approach for the modelling and analysis of microvibration sources on-board spacecraft.* PhD thesis, University of Surrey, 2017.

[ADN15] Pierre Apkarian, Minh Ngoc Dao, and Dominikus Noll. Parametric Robust Structured Control Design. *IEEE Transactions on Automatic Control*, 60(7):1857–1869, jul 2015.

[AG03] Rabih Alkhatib and M. F. Golnaraghi. Active structural vibration control: a review. *Shock and Vibration Digest*, 35(5):367, 2003.

[Agr09] Brij Agrawal. Jitter control for imaging spacecraft. In *2009 4th International Conference on Recent Advances in Space Technologies*, pages 615–620. IEEE, jun 2009.

[ALdPC13] Daniel Alazard, Thomas Loquen, Henry de Plinval, and Christelle Cumer. Avionics/Control co-design for large flexible space structures. In *AIAA Guidance, Navigation, and Control (GNC) Conference*, Reston, Virginia, aug 2013. American Institute of Aeronautics and Astronautics.

[AN07] Pierre Apkarian and Dominikus Noll. Nonsmooth optimization for multiband frequency domain control design. *Automatica*, 43(4):724–731, apr 2007.

[Apk11] Pierre Apkarian. Nonsmooth mu-synthesis. *International Journal of Robust and Nonlinear Control*, 21(13):1493–1508, sep 2011.

[BCPS16] Gary Balas, Richard Chiang, Andy Packard, and Michael Safonov. Robust Control Toolbox User's Guide, 2016.

[Bia97] B. Bialke. A compilation of reaction wheel induced spacecraft disturbances, 1997.

[BMSL11] Fabrice Boquet, Florence Malric-Smith, and Jean-Pascal Lejault. Active and passive microvibration mitigation system for earth observation and space science missions. *Advances in the Astronautical Sciences*, 141:461–480, 2011.

[BR16] Jean-Marc Biannic and Clement Roos. Generalized State Space: a new Matlab class to model uncertain and nonlinear systems as Linear Fractional Representations, 2016.

[Bro06] Allen J. Bronowicki. Vibration Isolator for Large Space Telescopes. *Journal of Spacecraft and Rockets*, 43(1):45–53, jan 2006.

[CDS96] D Cunningham, P Davis, and F Schmitt. A multi-axis isolation system for the French earth observation satellite's magnetic bearing reaction wheel. In *DPA/AIAA/ASME/SPIE Conference on Active Materials and Adaptive Structures*, 1996.

[CRS13] A Calvi, N Roy, and ECSS Secretariat. Spacecraft mechanical loads analysis handbook, 2013.

[CSD+99] Richard G Cobb, Jeanne M Sullivan, Alok Das, L Porter Davis, T Tupper Hyde, Torey Davis, Zahidul H Rahman, and John T Spanos. Vibration isolation and suppression system for precision payloads in space. *Smart Materials and Structures*, 8(6):798–812, dec 1999.

[DC93] P. Davis and D.C. Cunningham. A multiaxis passive isolation system for a magnetic bearing reaction wheel, 1993.

[DCH94] P. Davis, D. Cunningham, and J. Harrell. Advanced 1.5 Hz passive viscous isolation system, 1994.

[DCH95] L. Porter Davis, Delano R. Carter, and Tristram Tupper Hyde. Second-generation hybrid D-strut. In Conor D. Johnson, editor, *Proceedings of SPIE - The International Society for Optical Engineering*, volume 2445, pages 161–175. Society of Photo-Optical Instrumentation Engineers, may 1995.

[DGM12] Keith B. Doyle, Victor L. Genberg, and Gregory J. Michels. *Integrated Optomechanical Analysis*, volume 58. SPIE press Bellingham, 2012.

[DPZ91] J. Doyle, A. Packard, and K. Zhou. Review of LFTs, LMIs, and mu. In *Conference on Decision and Control*, pages 1227–1232. IEEE, 1991.

[DQGL08] K. Dong, N. M. Qi, J. J. Guo, and Y. Q. Li. An estimation approach for propellant sloshing effect on spacecraft GNC. In *2008 2nd International Symposium on Systems and Control in Aerospace and Astronautics, ISSCAA 2008*, 2008.

[DWJR86] L.P. Davis, J.F. Wilson, R.E. Jewell, and J.J. Roden. Hubble space telescope reaction wheel assembly vibration isolation system, 1986.

[ECS08] ECSS. Pointing Performance Standard ECSS-E-ST-60-10C, 2008.

[ECS11] ECSS. ESA pointing error engineering handbook ESSB-HB-E-003, 2011.

[EM02] L.M. Elias and D.W. Miller. A coupled disturbance analysis method using dynamic mass measurement techniques. In *Proceedings of the 43rd Annual AIAA/ASME/ASCE/AHS/ASC Structures, Structural Dynamics, and Materials Conference*, pages 22–25, 2002.

[FB12] Jordan Firth and Jonathan Black. Vibration interaction in a multiple flywheel system. *Journal of Sound and Vibration*, 331(7):1701–1714, mar 2012.

[FBBH14] Alexandre Falcoz, Fabrice Boquet, Samir Bennani, and David Henry. Active Vibration Control and Isolation: The LPV Way. In *ESA-CNES-DLR Workshop "Linear Parameter Varying Control: A Framework for Adaptable Space Systems"*, Netherlands, 2014.

[FSBW07] Walter Fichter, Alexander Schleicher, Samir Bennani, and Shufan Wu. Closed Loop Performance and Limitations of the LISA Pathfinder Drag-Free Control System. In *AIAA Guidance, Navigation and Control Conference and Exhibit*, Reston, Virigina, aug 2007. American Institute of Aeronautics and Astronautics.

[FTD91] M.K.H. Fan, A.L. Tits, and J.C. Doyle. Robustness in the presence of mixed parametric uncertainty and unmodeled dynamics. *IEEE Transactions on Automatic Control*, 36(1):25–38, 1991.

[GA94] Pascal Gahinet and Pierre Apkarian. A linear matrix inequality approach to H infinity control. *International Journal of Robust and Nonlinear Control*, 4(4):421–448, 1994.

[GACC14] Nicolas Guy, Daniel Alazard, Christelle Cumer, and Catherine Charbonnel. Dynamic Modeling and Analysis of Spacecraft With Variable Tilt of Flexible Appendages. *Journal of Dynamic Systems, Measurement, and Control*, 136(2):021020, jan 2014.

[GMGB14] S. Aglietti Guglielmo, Remedia Marcello, Richardson Guy, and LePage Brian. Inspecting the Characterisation of Microvibration Sources. In *65th International Astronautical Congress*, 2014.

[GV03] J. Gerrits and A. E P Veldman. Dynamics of liquid-filled spacecraft. *Journal of Engineering Mathematics*, 45(1):21–38, 2003.

[GW00] Carlos M. Grodsinsky and Mark S. Whorton. Survey of Active Vibration Isolation Systems for Microgravity Applications. *Journal of Spacecraft and Rockets*, 37(5):586–596, sep 2000.

[Has86] M D Hasha. Reaction wheel mechanical noise variations. *Space Telescope Program Engineering Memo SSS*, 218:175–183, 1986.

[HO06] Simon Hecker and Others. *Generation of low order LFT representations for robust control applications*. PhD thesis, Technische Universit{ä}t M{ü}nchen, 2006.

[HS96] A.M. Horr and L.C. Schmidt. Frequency Domain Dynamic Analysis of Large Space Structures with Added Elastomeric Dampers. *International Journal of Space Structures*, 11(3):279–289, sep 1996.

[HSP15] Arnar Hjartarson, Peter Seiler, and Andrew Packard. LPVTools: A toolbox for modeling, analysis, and synthesis of Parameter Varying control systems. *IFAC-PapersOnLine*, 48(26):139–145, 2015.

[Ibr08] R.A. Ibrahim. Recent advances in nonlinear passive vibration isolators. *Journal of Sound and Vibration*, 314(3-5):371–452, jul 2008.

[IH05] T. Iwasaki and S. Hara. Generalized KYP lemma: unified frequency domain inequalities with design applications. *IEEE Transactions on Automatic Control*, 50(1):41–59, jan 2005.

[Jön98] Ulf Jönsson. Stability of uncertain systems with hysteresis nonlinearities. *International Journal of Robust and Nonlinear Control*, 8(3):279–293, mar 1998.

[KFS08] H Köroglu, M Farhood, and C W Scherer. LPVMAD, the iqc analysis tool. Technical report, Technical report, Delft University of Technology, The Netherlands, 2008.

[Kim14] Dae-kwan Kim. Micro-vibration model and parameter estimation method of a reaction wheel assembly. *Journal of Sound and Vibration*, 333(18):4214–4231, sep 2014.

[KL04] Chung-Yao Kao and Bo Lincoln. Simple stability criteria for systems with time-varying delays. *Automatica*, 40(8):1429–1434, aug 2004. *A.2.*

[KPG10] D. Kamesh, R. Pandiyan, and Ashitava Ghosal. Modeling, design and analysis of low frequency platform for attenuating micro-vibration in spacecraft. *Journal of Sound and Vibration*, 329(17):3431–3450, 2010.

[KPG12] D. Kamesh, R. Pandiyan, and Ashitava Ghosal. Passive vibration isolation of reaction wheel disturbances using a low frequency flexible space platform. *Journal of Sound and Vibration*, 331(6):1310–1330, mar 2012.

[KR07] Chung-Yao Kao and Anders Rantzer. Stability analysis of systems with uncertain time-varying delays. *Automatica*, 43(6):959–970, jun 2007.

[KS06] Hakan Koroglu and Carsten W. Scherer. Robust Stability Analysis against Perturbations of Smoothly Time-Varying Parameters. In *Proceedings of the 45th IEEE Conference on Decision and Control*, pages 2895–2900. IEEE, 2006.

[KU14] Keiji Komatsu and Hideki Uchida. Microvibration in spacecraft. *Mechanical Engineering Reviews*, 1(2):SE0010–SE0010, 2014.

[Lau16] Philippe Laurens. Vibration isolating device, 2016.

[Le17] M.P. Le. *Micro-disturbances in reaction wheels*. PhD thesis, Technische Universiteit Eindhoven, 2017.

[LJDL15] Chunchuan Liu, Xingjian Jing, Steve Daley, and Fengming Li. Recent advances in micro-vibration isolation. *Mechanical Systems and Signal Processing*, 56-57:55–80, may 2015.

[LKM+07] Kuo-Chia Liu, Thomas Kenney, Peiman Maghami, Pete Mule, Carl Blaurock, and William B Haile. Jitter test program and on-orbit mitigation strategies for solar dynamic observatory. In *20th International Symposium on Space Flight Dynamics. NASA Goddard Space Flight Center, Annapolis*, 2007.

[LLJ14] Qing Luo, Dongxu Li, and Jianping Jiang. Coupled dynamic analysis of a single gimbal control moment gyro cluster integrated with an isolation system. *Journal of Sound and Vibration*, 333(2):345–363, 2014.

[LLZ13a] Q. Luo, D. Li, and W. Zhou. Studies on vibration isolation for a multiple flywheel system in variable configurations. *Journal of Vibration and Control*, 21(1):105–123, jul 2013.

[LLZ+13b] Qing Luo, Dongxu Li, Weiyong Zhou, Jianping Jiang, Guang Yang, and Xinsheng Wei. Dynamic modelling and observation of micro-vibrations generated by a Single Gimbal Control Moment Gyro. *Journal of Sound and Vibration*, 332(19):4496–4516, sep 2013.

[LMB08] Kuo-Chia Liu, Peiman Maghami, and Carl Blaurock. Reaction Wheel Disturbance Modeling, Jitter Analysis, and Validation Tests for Solar Dynamics Observatory. In *AIAA Guidance, Navigation and Control Conference and Exhibit*, pages 1–18, Reston, Virigina, aug 2008. American Institute of Aeronautics and Astronautics.

[LPD10] Charles F Lillie, Ronald S Polidan, and Dean R Dailey. Key enabling technologies for the next generation of space telescopes. In *Space Telescopes and Instrumentation*, volume 7731, page 773102, jul 2010.

[LS89] R.A. Laskin and M. San Martin. Control/structure system design of a spaceborne optical interferometer. In *Proceedings of the AAS/AIAA Astrodynamics Specialist Conference*, pages 369–395, 1989.

[LTD00] Craig T. Lawrence, André L. Tits, and Paul Van Dooren. A fast algorithm for the computation of an upper bound on the mu-norm. *Automatica*, 36(3):449–456, mar 2000.

[LYH12] Dae-Oen Lee, Jae-San Yoon, and Jae-Hung Han. Integrated Framework for Jitter Analysis Combining Disturbance, Structure, Vibration Isolator and Optical Model. In *Proceedings of SPIE - The International Society for Optical Engineering*, pages 834126–834126–8, apr 2012.

[Mag06] Jean-François Magni. User manual of the linear fractional representation toolbox. Technical report, ONERA, Toulouse, France, 2006.

[Mas99] Rebecca Ann Masterson. *Development and validation of empirical and analytical reaction wheel disturbance models*. phdthesis, Massachusetts Institute of Technology, 1999.

[Mas02] R Masterson. Development and Validation of Reaction Wheel Disturbance Models: Empirical Model. *Journal of Sound and Vibration*, 249:575–598, 2002.

[MCCCMC01] Christelle Manceaux-Cumer, Jean-Pierre Chrétien, J.-P. Chretien, and Christelle Manceaux-Cumer. Minimal LFT form of a spacecraft built up from two bodies. In *AIAA Guidance, Navigation, and Control Conference and Exhibit*, volume 1, pages 1–9, Reston, Virigina, aug 2001. American Institute of Aeronautics and Astronautics.

[MdWU+01] D.W. Miller, O.L. de Weck, S.A. Uebelhart, R. Grogan, and I. Basdogan. Integrated dynamics and controls modeling for the Space Interferometry Mission (SIM). In *2001 IEEE Aerospace Conference Proceedings (Cat. No.01TH8542)*, volume 4, pages 4/2089–4/2102. IEEE, 2001.

[MKJR04] A Megretski, C Kao, U Jonsson, and A Rantzer. A guide to IQC $\beta$: A matlab toolbox for robust stability and performance analysis. *Technical Report, MIT*, 2004.

[MKS07] Scott Miller, Paul Kirchman, and John Sudey. Reaction Wheel Operational Impacts on the GOES-N Jitter Environment. In *AIAA Guidance, Navigation and Control Conference and Exhibit*, Guidance, Navigation, and Control and Co-located Conferences. American Institute of Aeronautics and Astronautics, aug 2007.

[Mor85] Blaise Morton. New applications of mu to real-parameter variation problems. In *Conference on Decision and Control*, pages 233–238. IEEE, dec 1985.

[MR97] Alexandre Megretski and Anders Rantzer. System analysis via integral quadratic constraints. *IEEE Transactions on Automatic Control*, 42(6):819–830, jun 1997.

[NAS16] NASA's Jet Propulsion Laboratory. GEMINI Stability Control for Reducing Pointing Jitter in CubeSats and Smallsats, 2016.

[OFBW13] T. Ott, W. Fichter, S. Bennani, and S. Winkler. Precision pointing H infinity, and stability-time errors. *CEAS Space Journal*, 4(1-4):13–30, jun 2013.

[PBLJ00] A. Packard, G. Balas, R. Liu, and Jong-Yeob Shin. Results on worst-case performance assessment. In *Proceedings of the American Control Conference*, pages 2425–2427 vol.4, Chicago, 2000. IEEE.

[PCH+15a] Valentin Preda, Jérôme Cieslak, David Henry, Samir Bennani, and Alexandre Falcoz. LPV Control for Active Vibration Mitigation in High Stability Space Missions: A Comparative Study. In *8th IFAC Symposium on Robust Control Design*, 2015.

[PCH+15b] Valentin Preda, Jerome Cieslak, David Henry, Samir Bennani, and Alexandre Falcoz. LPV Control for Multi-harmonic Microvibration Attenuation: Application to High Stability Space Missions. *IFAC-PapersOnLine*, 48(26):127–132, 2015.

[PCH+15c] Valentin Preda, Jerome Cieslak, David Henry, Samir Bennani, and Alexandre Falcoz. Microvibration Attenuation based on H-infinity/LPV Theory for High Stability Space Missions. In *Journal of Physics: Conference Series*, volume 659, page 012026, nov 2015.

[PCH+17a] Valentin Preda, Jérôme Cieslak, David Henry, Samir Bennani, and Alexandre Falcoz. A H-infinity/mu solution for microvibration mitigation in satellites: A case study. *Journal of Sound and Vibration*, 399:21–44, jul 2017.

[PCH+17b] Valentin Preda, Jérôme Cieslak, David Henry, Samir Bennani, and Alexandre Falcoz. Robust Control Design in a Non-Smooth H-infinity / mu setting for Spacecraft Microvibration Attenuation. In *10th International ESA Conference on Guidance, Navigation & Control Systems*, Salzburg, Austria, may 2017. European Space Agency.

[PCH+17c] Valentin Preda, Jérôme Cieslak, David Henry, Samir Bennani, and Alexandre Falcoz. Robust Microvibration Control and Worst-case Analysis for High Pointing Stability Space Missions. *Submitted to: International Journal of Robust and Nonlinear Control*, 2017.

[PD93] A. Packard and J. Doyle. The complex structured singular value. *Automatica*, 29(1):71–109, jan 1993.

[PdBB+16] T. Prusti, J. H. J. de Bruijne, A. G. A. Brown, A. Vallenari, C. Babusiaux, C. A. L. Bailer-Jones, U. Bastian, and M. Biermann. The Gaia mission. *Astronomy & Astrophysics*, 595:A1, nov 2016.

[PF16] Mark C. Palframan and Mazen Farhood. An IQC analysis framework for small fixed-wing UAS. In *Proceedings of the American Control Conference*, volume 2016-July, pages 6754–6759. IEEE, jul 2016.

[PH98] T.E. Pare and J.P. How. Robust stability and performance analysis of systems with hysteresis nonlinearities. In *Proceedings of the 1998 American Control Conference. ACC (IEEE Cat. No.98CH36207)*, pages 1904–1908 vol.3. IEEE, 1998.

[PHR+07] A. Preumont, M. Horodinca, I. Romanescu, B. de Marneffe, M. Avraam, A. Deraemaeker, F. Bossens, and A. Abu Hanieh. A six-axis single-stage active vibration isolator based on Stewart platform. *Journal of Sound and Vibration*, 300(3-5):644–661, mar 2007.

[PM12] Mark Pittelkau and William McKinley. Pointing Error Metrics: Displacement, Smear, Jitter, and Smitter with Application to Image Motion MTF. In *AIAA/AAS Astrodynamics Specialist Conference*, Reston, Virigina, aug 2012. American Institute of Aeronautics and Astronautics.

[PM16] Mark E. Pittelkau and William G. McKinley. Optical transfer functions, weighting functions, and metrics for images with two-dimensional line-of-sight motion. *Optical Engineering*, 55(6):063108, jun 2016.

[PPAL16] J. Alvaro Perez, Christelle Pittet, Daniel Alazard, and Thomas Loquen. Integrated Control/Structure Design of a Large Space Structure using Structured H$\infty$ Control. *IFAC-PapersOnLine*, 49(17):302–307, 2016.

[Pre11] André Preumont. Vibration Control of Active Structures , An Introduction. *Vibration Control of Active Structures , An Introduction*, page 199, 2011.

[RDR+86] J J Rodden, H J Dougherty, L F Reschke, M D Hasha, and L P Davis. Line-of-sight performance improvement with reaction-wheel isolation. *Guidance and Control*, pages 71—-84, 1986.

[Riv04] EI Rivin. Passive Vibration Isolation. In *Applied Mechanics Reviews*, volume 57, chapter 1-2, page B31. 2004.

[RLD10] Mike Ruth, Kenneth Lebsock, and Cornelius Dennehy. What's New is What's Old: Use of Bode's Integral Theorem (circa 1945) to Provide Insight for 21st Century Spacecraft Attitude Control System Design Tuning. In *AIAA Guidance, Navigation, and Control Conference*, Virigina, 2010.

[Sec13] Federico Secondi. *Robust active control for microvibration mitigation in high stability space missions*. PhD thesis, Politecnico di Milano, 2013.

[SNG08] S. Shankar Narayan, P. S. Nair, and Ashitava Ghosal. Dynamic interaction of rotating momentum wheels with spacecraft elements. *Journal of Sound and Vibration*, 315:970–984, 2008.

[SPA11] M. Sasso, G. Palmieri, and D. Amodio. Application of fractional derivative models in linear viscoelastic problems. *Mechanics of Time-Dependent Materials*, 15(4):367–387, nov 2011.

[TCVV02] Doug Thayer, Mark Campbell, Juris Vagners, and Andrew Von Flotow. Six-axis vibration isolation system using soft actuators and multiple sensors. *Journal of Spacecraft and Rockets*, 39(2):206–212, 2002.

[TN85] Vassilios D Tourassis and Charles P Neuman. The inertial characteristics of dynamic robot models. *Mechanism and Machine Theory*, 20(1):41–52, jan 1985.

[TO03] Shigemune Taniwaki and Yoshiaki Ohkami. Experimental and numerical analysis of reaction wheel disturbances. *JSME International Journal Series C*, 46(2):519–526, 2003.

[VGL+07] A. E P Veldman, J. Gerrits, R. Luppes, J. A. Helder, and J. P B Vreeburg. The numerical simulation of liquid sloshing on board spacecraft. *Journal of Computational Physics*, 224(1):82–99, 2007.

[VP99] L Vaillon and C Philippe. Passive and active microvibration control for very high pointing accuracy space systems. *Smart Materials and Structures*, 8(6):719–728, dec 1999.

[VSK09] Joost Veenman, Carsten Scherer, and Hakan Koroglu. IQC-Based LPV Controller Synthesis for the NASA HL20 Atmospheric Re-entry Vehicle. In *AIAA Guidance, Navigation, and Control Conference*, Reston, Virigina, aug 2009. American Institute of Aeronautics and Astronautics.

[VSK16] Joost Veenman, Carsten W. Scherer, and Hakan Köroğlu. Robust stability and performance analysis based on integral quadratic constraints. *European Journal of Control*, 31:1–32, sep 2016.

[WC03] Michael F Winthrop and Richard G Cobb. Survey of state-of-the-art vibration isolation research and technology for space applications. volume 5052, pages 134–26, jul 2003.

[WHX+13] Li Weipeng, Huang Hai, Zhou Xubin, Zheng Xintao, Bai Yang, Weipeng Li, Hai Huang, Xubin Zhou, Xintao Zheng, and Yang Bai. Design and Experiments on an Active Isolator for Satellite Micro-Vibration. *Chinese Journal of Aeronautics*, 27(6):1461–1468, dec 2013.

[Wij09] Jaap J Wijker. *Random vibrations in spacecraft structures design: theory and applications*, volume 165. Springer Science \& Business Media, 2009.

[WLS94] Zi-Qin Wang, Petter Lundström, and Sigurd Skogestad. Representation of uncertain time delays in the H infinity framework. *International Journal of Control*, 59(3):627–638, mar 1994.

[WPS16] Shu Wang, Harald Pfifer, and Peter Seiler. Robust synthesis for linear parameter varying systems using integral quadratic constraints. In *Automatica*, volume 68, pages 111–118. IEEE, dec 2016.

[WWE05] T. Wacker, L. Weimer, and K. Eckert. GOCE platform micro-vibration verification by test and analysis. In *European Space Agency, ESA SP*, number 581, pages 733–740, 2005.

[XFLC13] X. Xu, J. Fang, H. Li, and P. Cui. Active suppression of imbalance vibration in the magnetically suspended control moment gyro. *Journal of Vibration and Control*, 21(5):989–1003, jul 2013.

[YD90] P.M. Young and J.C. Doyle. Computation of mu with real and complex uncertainties. In *29th IEEE Conference on Decision and Control*, pages 1230–1235 vol.3. IEEE, 1990.

[YD96] P.M. Young and J.C. Doyle. Properties of the mixed $\mu$ problem and its bounds. *IEEE Transactions on Automatic Control*, 41(1):155–159, 1996.

[YND95] Peter M. Young, Matthew P. Newlin, and John C. Doyle. Computing bounds for the mixed mu problem. *International Journal of Robust and Nonlinear Control*, 5(6):573–590, 1995.

[ZAZ11] Wei Yong Zhou, Guglielmo S. Aglietti, and Zhe Zhang. Modelling and testing of a soft suspension design for a reaction/momentum wheel assembly. *Journal of Sound and Vibration*, 330(18-19):4596–4610, 2011.

[ZBK14] Christof Zwyssig, Thomas Baumgartner, and Johann W. Kolar. High-speed magnetically levitated reaction wheel demonstrator. In *2014 International Power Electronics Conference (IPEC-Hiroshima 2014 - ECCE ASIA)*, pages 1707–1714. IEEE, may 2014.

[ZD98] Kemin Zhou and John Comstock Doyle. *Essentials of Robust Control*. Prentice Hall, New Jersey, 1998.

[ZDGO96] Kemin Zhou, John Comstock Doyle, Keith Glover, and Others. *Robust and Optimal Control*, volume 40. Prentice Hall, New Jersey, 1996.

[ZL12] Wei-Yong Yong Zhou and Dong-Xu Xu Li. Design and analysis of an intelligent vibration isolation platform for reaction/momentum wheel assemblies. *Journal of Sound and Vibration*, 331(13):2984–3005, jun 2012.

[ZLLJ12] W.-Y. Zhou, D.-X. Li, Q. Luo, and J.-P. Jiang. Design and test of a soft suspension system for cantilevered momentum wheel assembly. *Proceedings of the Institution of Mechanical Engineers, Part G: Journal of Aerospace Engineering*, 227(7):1144–1160, jun 2012.

[ZLLL12] Weiyong Zhou, Dongxu Li, Qing Luo, and Kun Liu. Analysis and Testing of Microvibrations Produced by Momentum Wheel Assemblies. *Chinese Journal of Aeronautics*, 25(4):640–649, aug 2012.

[ZYP09] Zhen-hua Zhang, Lei Yang, and Shi-wei Pang. Jitter environment analysis for micro-precision spacecraft. *Spacecraft Environment Engineering*, 26(6):528–534, 2009.

"*So long and thanks for all the fish.*"

Douglas Adams, The Hitchhiker's Guide to the Galaxy